Yongming Yang
Master in Structural Engineering

Bond behavior and durability of CFRP-to-steel bonded joints under cyclic loading and freeze-thaw and salt fog

Dissertation for obtaining the Doctor degree in Civil Engineering
Specialty Structures

Adviser: Manuel Américo de Jesus Gonçalves da Silva,
Retired Full Professor, Universidade Nova de Lisboa
Co-adviser: Carlos Manuel Chastre Rodrigues,
Associate Professor, Universidade Nova de Lisboa
Co-adviser: Hugo Emanuel Charrinho da Costa Biscaia,
Researcher, Universidade Nova de Lisboa

Examination Committee
Chairman : Prof. Doutor Jorge Joaquim Pamies Teixeira
Examiners: Prof. Doutor Luís Filipe Pereira Juvandes
Prof. Doutor José Manuel de Sena Cruz
Co-examiners: Prof. Doutor Manuel Américo de Jesus Gonçalves da Silva
Prof. Doutor João Carlos Gomes Rocha de Almeida

FACULDADE DE CIÊNCIAS E TECNOLOGIA
UNIVERSIDADE NOVA DE LISBOA

December, 2018

Yongming Yang
Master in Structural Engineering

Bond behavior and durability of CFRP-to-steel bonded joints under cyclic loading and freeze-thaw and salt fog

Dissertation for obtaining the Doctor degree in Civil Engineering
Specialty Structures

Adviser: Manuel Américo de Jesus Gonçalves da Silva,
Retired Full Professor, Universidade Nova de Lisboa
Co-adviser: Carlos Manuel Chastre Rodrigues,
Associate Professor, Universidade Nova de Lisboa
Co-adviser: Hugo Emanuel Charrinho da Costa Biscaia,
Researcher, Universidade Nova de Lisboa

Chairman of the
Examination Committee: Prof. Doutor Jorge Joaquim Pamies Teixeira
Examiners: Prof. Doutor Luís Filipe Pereira Juvandes
Prof. Doutor José Manuel de Sena Cruz
Co-examiners: Prof. Doutor Manuel Américo de Jesus Gonçalves da Silva
Prof. Doutor João Carlos Gomes Rocha de Almeida

FACULDADE DE CIÊNCIAS E TECNOLOGIA
UNIVERSIDADE NOVA DE LISBOA

December, 2018

Bond behavior and durability of CFRP-to-steel bonded joints under cyclic loading and freeze-thaw and salt fog

Copyright © Yongming Yang, Faculdade de Ciências e Tecnologia, Universidade Nova de Lisboa.
A Faculdade de Ciências e Tecnologia e a Universidade Nova de Lisboa têm o direito, perpétuo e sem limites geográficos, de arquivar e publicar esta tese através de exemplares impressos reproduzidos em papel ou de forma digital, ou por qualquer outro meio conhecido ou que venha a ser inventado, e de divulgar através de repositórios científicos e de admitir a sua cópia e distribuição com objectivos educacionais ou de investigação, não comerciais, desde que seja dado crédito ao autor e editor.

Acknowledgements

This work has been conducted during the years 2015 and 2018 at the department of Civil engineering at Faculdade de Ciências e Tecnologia, Universidade Nova de Lisboa, Portugal. At the moment, after finishing the Ph.D. thesis, I wish to express my sincere gratitude to whom without their help during those three years, the thesis is not possible.

Firstly and also foremost, I would like to thank my advisor, Prof. Manuel A G Silva, for giving me the opportunity to join his team, for his patience and for his invaluable inputs to all the aspects on living and studying during those years. I also like to acknowledge my co-advisor, Prof. Carlos Chastre, for his meaningful suggestion on experiment methods design, and for his very helpful comments on the manuscript of the publications. Furthermore, I give my sincere thanks and gratitude to another co-advisor, Prof. Hugo Biscaia, for his valuable and indispensable topic discussion every time, for his pursuit of perfection, for his help to the improvements of the publications writing.

I also would like to thank Prof. Guijun Xian of Harbin Institute of Technology, China, for providing the HIT CFRP laminates to support my Ph.D. work.

I also thank the technicians, Eng. Victor Silva, Mr. Gaspar and Mr. Jorge at the structures laboratory of the department of Civil engineering.

Finally, my deepest gratitude to my parents and sister for their continuous support and encouragements throughout these years.

Abstract

There are many structural members of metallic bridges, namely girders and trusses, requiring rehabilitation and strengthening in a large number of countries. The utilization of polymers reinforced with carbon fibers (CFRP) has been considered of great potential for that purpose and many laboratorial tests have been made in the past 30 years to study the behavior of structural members strengthened with CFRP, based on which structural solutions have been designed and built. Despite that, more research is necessary to obtain data on the mechanical response and durability of those composite materials and structures, as well as on the CFRP/steel joints, to improve design procedures and define more suitable strengthening methodologies.

One of the topics of the thesis is the study of the bond behavior of CFRP/steel joints under mechanical or thermal loading. In a first phase, tests of double-strap joints, with several different bonded lengths were subjected to monotonic loading and a simplified method was developed to estimate the responses and compare with the experimental results. Following that phase, pseudo-cyclic and cyclic tests were made to examine the capacity of the joints for those types of loading. The damage developed in the interface was analyzed in a way that allowed the calculation of the dissipated energy and related it to the slip between the CFRP strips and the steel plates.

The durability of the bonded CFRP/steel joints was also studied. The joints as well as adhesive coupons, separately, were exposed to accelerated aging imposed by (i) temperature cycles between -20ºC and +20ºC with testing of effects at selected stages (1,000h, 2,500h, 3,500h, 5,000h and 10,000h), and (ii) salt fog cycles lasting for 5,000h. Both monotonic and cyclic tests were made to evaluate the deterioration caused by aging and different mechanisms were identified. Stresses due to resistance to free thermal expansion and due to galvanic corrosion were also addressed.

Analytical solutions based on local bond laws, either bilinear or tri-linear, were used to estimate the debonding of the CFRP laminates from steel. It was also confirmed that the capacity of the joint is associated with the initiation of damage in the adhesive caused by steel corrosion. A “loading threshold” was detected approximately equal to 50% of the ultimate monotonic loading capacity of the joints, below which cyclic loading does not damage the CFRP/steel integrity. Experimental results showed that the normalized slip at the interface ($\Delta S/\Delta S_{ult}$) and the normalized dissipated energy, local and global (w_d/G_f and E_d/E_t, respectively), may be inter-related both for reference, unaged samples, and aged samples. Moisture is a critical factor in temperature cycles around 0ºC, called freeze-thaw for simplicity, while temperature effects alone for cycles between -20ºC and +20ºC were negligible. Galvanic corrosion between CFRP and steel is generated by the accumulation of corrosion products in the joints, creating electric bridges that lead to deterioration of the CFRP laminates. Local corrosion of steel causes stress concentrations that may lead to brittle failure under monotonic or cyclic loading.

Resumo

Em todo o mundo existem muitos elementos estruturais em pontes metálicas, especialmente vigas e treliças, que necessitam de ser reabilitados ou reforçados. A técnica de reforço com polímeros reforçados com fibras de carbono (CFRP) tem sido considerada como uma técnica com bastante potencial para solucionar alguns desses problemas, e por isso, nos últimos 30 anos têm sido realizados em laboratório muitos ensaios experimentais para estudar o comportamento de diversos elementos estruturais reforçados com CFRP e variadíssimas soluções de reforço têm sido aplicadas em obra com base nesse conhecimento. No entanto, continua a ser necessário desenvolver mais investigação para estudar aspetos relacionados com a resposta mecânica e com a durabilidade desses materiais compósitos, bem como das respetivas ligações coladas com ele realizadas, no sentido de contribuir com diretrizes de projeto mais confiáveis e encontrar métodos de reforço mais eficazes.

Um dos tópicos desta tese é o estudo do comportamento da aderência em ligações coladas CFRP/aço submetidas a ações mecânicas e/ou térmicas. Para compreender melhor esse comportamento, numa primeira fase foram realizados ensaios monotónicos com diferentes comprimentos de colagem por forma a avaliar o comportamento de dois tipos de ligações duplas CFRP/aço, tendo sido desenvolvido um modelo simplificado com capacidade de estimar o desempenho da ligação, o qual foi comparado com os ensaios experimentais. Em seguida foram realizados ensaios cíclicos e pseudo-cíclicos por forma a avaliar o comportamento da ligação a diferentes tipos de ações cíclicas. A análise dos resultados foi baseada na análise do dano da interface, o que permitiu estabelecer uma relação da energia dissipada em função do deslizamento a que está sujeita a ligação.

Outro tópico abordado nesta tese é o estudo da durabilidade de ligações coladas CFRP/aço. As ligações CFRP/aço bem como a resina utilizada para colar o CFRP ao aço foram expostas a dois tipos de envelhecimento: (i) ciclos de temperatura entre -20 e 20ºC, variando o período de exposição (1000h; 2500h; 3500h; 5000h e 10000h); e (ii) ciclos de nevoeiro salino, com um período de exposição de 5000h. Em seguida essas ligações foram sujeitas a ensaios mecânicos, monotónicos e cíclicos para avaliar a degradação da ligação CFRP/aço. Vários mecanismos de degradação foram encontrados e associados aos materiais utilizados na ligação. As tensões desenvolvidas na ligação devido a impedimento de deformação térmica e a corrosão galvânica são dois assuntos importantes neste campo e que também foram analisados na tese.

Verificou-se que podem ser utilizadas soluções analíticas com base em modelos locais de aderência bi ou tri-lineares para estimar o descolamento do CFRP do aço. Verificou-se igualmente, que a tensão máxima da ligação está associada ao início do dano no adesivo provocado pela corrosão do aço. Foi detetado um "limite de carga" de 50% da capacidade máxima da carga monotónica das ligações, abaixo do qual, o carregamento cíclico não causa danos à ligação CFRP/aço. Os resultados experimentais mostraram que o incremento normalizado do deslizamento da interface ($\Delta S/\Delta S_{ult}$) e a energia dissipada normalizada, local e global (w_d/G_f e E_d/E_t, respetivamente) podem ser relacionados entre si, tanto para as amostras não envelhecidas como para as envelhecidas. A humidade é um fator crítico nos ciclos de gelo degelo mas o impacto de ciclos térmicos, entre -20ºC e 20ºC, no dano da ligação CFRP/aço pode ser ignorado, tendo por base os ensaios realizados. A corrosão galvânica entre o CFRP e o aço desenvolve-se devido ao depósito de produtos da corrosão na ligação, que atuam como pontes elétricas, levando à degradação dos laminados de CFRP. Tendo-se constatado que os pontos de concentração de tensões que ocorrem devido à corrosão local do aço podem levar a roturas frágeis sob carregamento monotónico ou cíclico.

Keywords

CFRP-to-steel bonded joints

Adhesive

CFRP laminates

Cyclic test

Freeze-thaw

Salt fog

Damage

Corrosion

Palavras-chave

Juntas de CFRP e aço

Adesivo

Laminados de CFRP

Ensaios cíclicos

Gelo-degelo

Nevoeiro salino

Dano

Corrosão

Table of contents

List of Figures

List of Tables

Nomenclature

$F_{exp,\,j}$ = maximum experimental loads obtained in the j^{th} sample
$F_{pred,\,j}$ = maximum predicted loads obtained in the j^{th} sample
n = sequential ID number in each class of tests
L_b = CFRP bond length
L_{eff} = effective bond length
d_1 and d_2 = distance between consecutive strain guages
β = axial stiffness ratio
β_{HIT} = axial stiffness ratio for HIT bonded joints
β_{SIKA} = axial stiffness ratio for SIKA bonded joints
b_{CFRP} = width of the CFRP laminates
t_{CFRP} = thickness of the CFRP laminates
E_{CFRP} = Young's modulus of the CFRP laminates
b_{steel} = width of the steel plate
t_{steel} = thickness of the steel plate
E_{steel} = Young's moudulus of the steel plate
σ_{max} = tensile strength of the materials
σ_y = yield strength of steel
ε_u = ultimate strain of adhesive and CFRP
F_{max} = maximum load transmitted to single CFRP laminates
F_{CFRP} = load transmitted to the CFRP laminates
F_{steel} = load transferred to the steel plate
$F_{threshold}$ = no interfaical damage occured before the load
A_{CFRP} = cross section of the CFRP laminate
A_{steel} = cross section of the steel plate
u_{CFRP} = displacement in the CFRP laminate
u_{steel} = displacement in the steel plate
τ = bond stress within the interface
τ_1 = maximum bond stress
$\tau_{critical}$ = maximum bond stress at the loaded end
s = relative displacements between the bonded materials (or slip)
s_{max} = slip correspond the maximum bond stress
s_{ult} = slip when the interface starts debonding
σ_{CFRP} = axial stress in the CFRP laminate
σ_{steel} = axial stress in the steel plate
ε_{CFRP} = axial strain in the CFRP laminate
ε_{steel} = axial strain in the steel plate
K_e = initial interfacial stiffness
D = damage parameter
w_d = local interfacial energy dissipated at a particular cycle
G_f = local the total fracture energy
E_d = global interfacial energy dissipated at a partical cycle
E_t = global total interfacial energy dissipated

D_{limit} = damage limit of the bonded interface
T_g = glass transition temperature
α_{CFRP} = linear thermal expansion coefficient of CFRP laminates
α_{steel} = linear thermal expansion coefficient of steel plate
ΔT = uniform temperature variation
T_i = initial temperature
T_f = final temperature
Tan δ_{int} = value of energy dissipated at the fiber-matrix interface
Tan δ_c = value of energy dissipated in the FRP composite
Tan δ_{mat} = value of energy dissipated in the matrix
v_f = fiber fraction
E_c = elastic modulus of composites
E_m = elastic modulus of matrix

Chapter 1

Introduction

1.1 Brief considerations

There has been a lot of research on the application of FRP composites in civil engineering in the past 30-40 years, but only more recently the subject of strengthening of steel structures with CFRP composites has attracted the attention of researchers, which justifies the low number of publications available in the scientific community. In addition, the behavior of steel structures adhesively bonded with CFRP material is often dominated by the bonded CFRP-to-steel interface since most failures are known to take place at the interface between these two materials. For that reason, the literature review presented in the thesis is devoted to the summary of published data on bond aspects associated to the mechanical response and durability. Thus, some data on global behavior of the CFRP strengthening steel structural elements, e.g., girder, truss et al. are not emphasized in the present topic. In this section, a brief literature review is provided to give a general overview regarding some important studies of the thesis topic, i.e. on the "behavior and durability of CFRP-to-steel bonded joints under repeated loading and freeze-thaw and salt fog". Of course, a more comprehensive literature review will be presented in each of the following chapters.

1.2 Motivation

A lot of steel bridges were built a few decades ago worldwide, which inevitably require strengthening or rehabilitation with the extending of the service life. It has been estimated e.g.

that more than 300,000 railway bridges exist in Europe in 2007, 22% of steel beam type and 14% steel/concrete composite bridges [1]. Overall, 35% of those bridges were more than 100 years old and only 11% less than 10 years old in 2007. The US Department of Transportation [2] estimated that almost 68.5 % of the Nation's 604,493 bridges were 26 years old or older in 2010, with 11.5% of total bridges classified as structurally deficient, and 12.8 % of bridges were functionally obsolete. As an additional indicator, in 2013, out of 607,380 bridges, 200,000 bridges were steel bridges.

In China, steel bridges are widely used in railway infrastructure, which included 6550 steel girder bridges by the end of 2010 [3]. There are 4547 steel girder bridges that have serviced for more than 50 years under railway traffic in 2010, including 3884 steel plate girder bridges and 484 steel truss girder bridges [3].

All steel structures deteriorate with time, due to the service condition to which they are subjected. The reasons for deficiencies in steel structures placed in a civil infrastructure can be divided into two main aspects: (i) changes in the use of a structure, (ii) degradation of a structure. The former may be due to (a) increased live load, (b) increased dead load, (c) increased dead and live load; The latter may be caused by (a) corrosion (b) fatigue (c) impact vandalism, fire, blast loading or inappropriate structural alterations during maintenance, (d) design or construction errors [4].

According to the statistics on the main causes of damage of steel bridges, fatigue and environment accounted for 49% and 41% respectively. In general, weld defects, bolted or riveted details are stress raisers from which fatigue cracking may initiate and propagate. And corrosion is the another main cause for the degradation of a structure, leading to the reduction in the cross section of a steel part in the steel structures [4].

The traditional strengthening or rehabilitation technologies, namely welding, bolting and riveting as well as externally adhesive bonding with structural steel plate, have many disadvantages [5], namely (i) introduction of residual stresses to the steel elements; (ii) increase of localized stresses; (iii) extra weight added; and (iv) further corrosion. Therefore, a new and alternative technology to the traditional methods is needed for strengthening or rehabilitation of steel structures.

Carbon fiber reinforced polymer (CFRP) composites have numerous advantages that might be interesting to explore in order to positively respond to this real need of strengthening steel structures, such as: (i) light weight; (ii) high strength and stiffness; (iii) excellent fatigue [6, 7]; and (iv) good long-term performance [8, 9]. Compared to traditional strengthening technology using steel material, CFRP adhesively bonding technology has some advantages such as easy construction and maintenance as well as a more uniform stress distribution over the bonded area [10]. Although it is expected to be used as an externally strengthening material for civil engineering structures, and many studies have been published devoted to different aspects of design and durability of reinforced concrete elements, much scarcer data are found when the members to be strengthened are built with structural steel.

Recently, studies on application of CFRP laminates in steel bridges have been focused on some possibilities, including: (i) increase or restore the tensile or flexural capacity of steel elements, for example, bond to the steel truss element and the tension flange of the steel girder due to corrosion damage, (ii) increase fatigue resistance of steel elements, for example, strengthening of riveted elements against fatigue crack propagation [11].

It is known that the primary challenge towards the successful implementation of FRP materials for strengthened steel structures is the performance of the bond due to the premature debonding of the CFRP laminate from the substrate. Thus, it is of extreme importance to improve the actual knowledge of the bond stress transfer and failure mechanism between both bonded materials. Moreover, the behavior of the strengthened structures is important when one has to consider and support complicated loading conditions, namely repeated loading (e.g., earthquake excitation, traffic load and long-term temperature changes) and face long-term service environments (freeze-thaw and salt-fog).

1.3 State of the Art

In the scientific community, behavior of bonded CFRP/steel interface often has been evaluated through examining the response of CFRP-to-steel bonded joints. These bonded joints models have been made either through attaching CFRP laminates/sheets to the surface of steel blocks

(direct-shear tests model), as well as fabricating two steel plates together with CFRP composites (double-strap bonded joints model). With the bonded joints models mentioned above, considerable works have been done to examine the bond carry capacity and failure modes under monotonic loading [12-15]. Some variations also were considered to ascertain the effects of the properties of CFRP, e.g., modulus and width of CFRP [12], and of properties of the adhesive, namely its ductility and layer thickness [13, 14], as well as of the treated surface of the adherent materials [15].

The bond properties are often directly related to a local bond stresses developed in the interfacial and corresponding relative displacement between the adherents, i.e., CFRP composite and steel. However, the axial stresses transfer in the bonded materials and the bond shear stress transfer within the bonded interface are different on the direct-shear tests model and the double-strap bonded joints model caused the latter is made without constrain of the steel substrate.

Yu et al. [13] experimentally studied the bond response of the CFRP-to-steel bonded joints through testing series of direct-shear bonded joints (i.e., pull-push tests) with different type of adhesive and CFRP laminates. Local bond-slips were obtained and the bond stresses transfer mechanisms were interpreted. Further, Fernando et al. [16] derived closed-form solutions based on the bond-slip model associated with a ductile adhesive to interprete the bond stresses transfer process within the bonded interface. However, there are some experimental studies have been conducted for double strap tests (i.e., pull-pull tests) [12, 17, 18] but very few bond-slip curves were obtained from this loading condition [17, 18]. Moreover, the calculation method of these bonds-slip curves has not considered the effects of the deformation of steel plate, in this case, on the relative deformation of the bonded materials, i.e., CFRP and steel (slip).

Repeated loading lower than the monotonic strength capacity adopted in the design guideline leads to bond accumulative damage and may produce catastrophic failure of the reinforced system without pre-inspection. Currently, the global response (force vs. deformation of the bonded joints) of the CFRP-to-steel boned joints under fatigue loading has been studied in [19-21]. Colombi and Fava [19] assessed the fatigue behavior of CFRP-to-steel double strap joints through observing crack initiation, progression and debonding up to failure, and associated it

to the reduction of global stiffness (force vs. deformation of the bonded joints) of bonded joints with fatigue load. It was observed that the crack initiation was associated with a stiffness reduction of 98%, after subsequent gradual crack progression, quicker debonding and final sudden failure when stiffness reduced to 95% and 90% of the initial value. Other two fatigue studies conducted by Liu et al. [20] and Wu et al. [21] focused on the effects of the different level fatigue loads on the residual strength capacity.

Freeze-thaw is a common operating condition for outdoor structures and requires attention to the behavior/durability of externally bonded reinforced systems. Freeze-thaw cycles act on the CFRP-steel bonded system primarily via degrading the adhesive and the interfaces between adhesive and the bonded materials. Not many studies regarding adhesive exposure to freeze-thaw cycles exist, one being authored by Agarwal *et al*. [22] who exposed adhesive coupons of SIKA-30 and SIKA-330, to 40 cycles of 16h at -18°C followed by 8h at 38°C and 100% relative humidity and found 9% and 19% reduction, respectively, on the tensile strength and elastic modulus of SIKA-330 and no significant degradation of strength and 14% reduction of the elastic modulus for SIKA-30. The degradation of the interfaces has often been found to be significantly more important than that of the adhesive [23]. Kim *et al*. [24] showed that steel-to-steel double lap shear joints subjected to 100 freeze/thaw cycles (8h -20°C, 16h room temperature per cycle) had their failure mode changed from cohesive (in the adhesive) at 0 h to adhesive failure.

One of the studies from Heshmati *et al*. [25] reported that the initial slope of the bond shear stress vs. slip (relative deformation between the adherents) after freeze-thaw aging remained the same for all the specimens irrespective of the aging condition (pre-conditioned in distilled water or salt water or humidity prior to freeze-thaw aging), or the presence of moisture (without preconditioned prior to freeze-thaw aging). Another study conducted by Heshmati *et al*. [26] indicated that moisture had not evident effect on the bond capacity and failure mode for aging by freeze-thaw cycles.

Another concern results from the eventual contact of carbon fiber reinforced polymer composite materials (acting as a cathode) with most metals as anodes in the presence of an electrolyte e.g.

from salt water, and the creation of galvanic coupling [27-30]. Galvanic coupling has been found to degrade the CFRP composite itself besides resulting in more severe metallic corrosion [27-30].

Kim, Bumadian and Park [31] investigated the effects of galvanic coupling on the bond durability of CFRP-to-steel joints and found that the steel acting as anode was significantly corroded in the edges of the bonded areas and debonding failure of CFRP took place. The authors indicated that the adhesive layer impeded galvanic interaction between the steel and conductive carbon fibers. Recent studies on accelerated corrosion of CFRP-to-steel bonded joints by Batuwitage et al. [32, 33] found that failure of the joints changed from interfacial failure between adhesive and steel to CFRP rupture failure, and a significant reduction occurred in the tensile strength of CFRP. Increasing the number of CFRP layers increased the durability of the bonded joints.

1.4 Thesis objectives

The bond properties of the CFRP-to-steel interface subjected to service loadings and bond durability of the CFRP-to-steel exposed to long-term service environments are, therefore, important concerns and the results of the studies developed worldwide by the researchers on these subjects should firstly point out to the improvement of national and international codes, which are quite useful for designers.

Regarding what is mentioned above, this thesis includes the study of the bond behavior and durability of CFRP-to-steel bonded joints under repeated loading and aggressive conditions namely freeze-thaw and salt fog.

The main objectives of this work are as follows:

- Develop an experimental program of mode-II monotonic testing on CFRP-to-steel double strap bonded joints with different bond lengths. Propose a mathematical model for the bond response and derive closed-form solutions to compare with the experimental results;
- Develop an experimental program of cyclic testing on CFRP-to-steel double strap

bonded joints with two different CFRP laminates. Obtain results capable of explaining the bond cumulative damage mechanism and enabling the proposal of a based on which to propose a fatigue limit for CFRP-to-steel bonded joints under Mode-II loading;

- Make an assessment of the bond durability of CFRP-to-steel bonded joints subjected to freeze-thaw cycles for a relative long time and ascertain the bond degradation mechanism through materials characterization and thermal stress analysis;
- Make an assessment of the durability of CFRP/steel bonded system subjected to salt fog spray through the degradation mechanism of the materials and bond response;

1.5 Organization of the thesis

The objectives presented above required the treatment of issues and procedures that are organized in different chapters as follows. A flow chart of the thesis structure is illustrated (Figure 1.1) to facilitate understanding of organization of the thesis.

Chapter 1

In this chapter the motivation of the study is presented in a summarized way. A brief literature review is provided also to give a general overview on some important studies of the thesis topic. The objectives that are intended and a brief description of the organization of the thesis are conducted.

Chapter 2

The content of this chapter is essentially part of a published article: Yang YM, Biscaia HC, Chastre C, Silva, MAG. Bond characteristics of CFRP-to-steel bonded joints. J Constr Steel Res 2017;138:401-419, DOI: 10.1016/j.jcsr.2017.08.001.

A series of CFRP-to-steel double-strap bonded joints with different bond length are tested under monotonic loading. A mathematical model capable of reflecting on the bond response of CFRP-to-steel boned joints is proposed. Based on the model, closed-form solutions are derived to better understand the full-range debonding process for double-strap bonded joints (i.e., pull-pull tests) and compared with the experimental results.

Chapter 3

The content of this chapter is essentially part of a published article: Yang YM, Silva MAG, Biscaia HC, Chastre C. CFRP-to-steel bonded joints subjected to cyclic loading: An experimental study. Compos Part B: Engineering 2018;146:28-41, DOI: 10.1016/j.compositesb.2018.03.039.

Pseudo-cyclic and cyclic loading are applied in CFRP-to-steel bonded joint with two different CFRP laminates to examine the bond response. Pseudo-cyclic and cyclic bond vs. slip and force vs. slip curves are obtained, based on which, local and global interfacial cumulative damage are deeply analyzed.

Chapter 4

The content of this chapter is essentially part of the manuscript under review in Composites Structure (Elsevier) under the title “Bond durability of CFRP-to-steel bonded joints subjected to freeze-thaw”. The authors are Yongming Yang, Manuel A G Silva, Hugo Biscaia and Carlos Chastre.

This chapter presents the degradation data regarding CFRP-to-steel bonded joints and adhesive subjected to 10,000h freeze-thaw aging (833 freeze-thaw cycles, each cycle includes 6h freeze at -20°C followed by 6h thaw at 20°C). Degradation mechanism is deeply discussed through relating failure modes of bonded joints, bond capacity and properties of adhesive as well as the thermal stress developed within the bonded interface during the freeze-thaw aging.

Chapter 5

The content of this chapter is essentially part of the manuscript under review in Composite Part B: Engineering (Elsevier) under the title “Monotonic and cyclic bond response of CFRP-to-steel joints after salt fog exposure”. The authors are Yongming Yang, Hugo Biscaia, Manuel A G Silva and Chastre Carlos.

The studies in this chapter focused on the bond response of CFRP-to-steel joints under loading after salt fog exposure, as a complementary to the works conducted in chapter 3 and chapter 6.

Chapter 6

The content of this chapter is essentially part of the manuscript under review in Composite Part B: Engineering (Elsevier) under the title “Material degradation of CFRP-to-steel joints subjected to salt fog”. The authors are Yongming Yang, Manuel A G Silva.

This chapter presents the degradation data regarding CFRP-to-steel bonded joints and adhesive subjected to 10,000h salt fog aging (each cycle includes 18h salt spray followed by 6h dry at 35°C). This study focuses on the degradation of materials namely CFRP and adhesive. The degradation mechanisms of CFRP laminates and adhesive are described.

Chapter 7

This chapter presents conclusions regarding each analyzed subject, some recommendation based on the knowledge obtained and also some issues that may be the aim of further research.

Chapter 8

This chapter presents all the references cited in the thesis

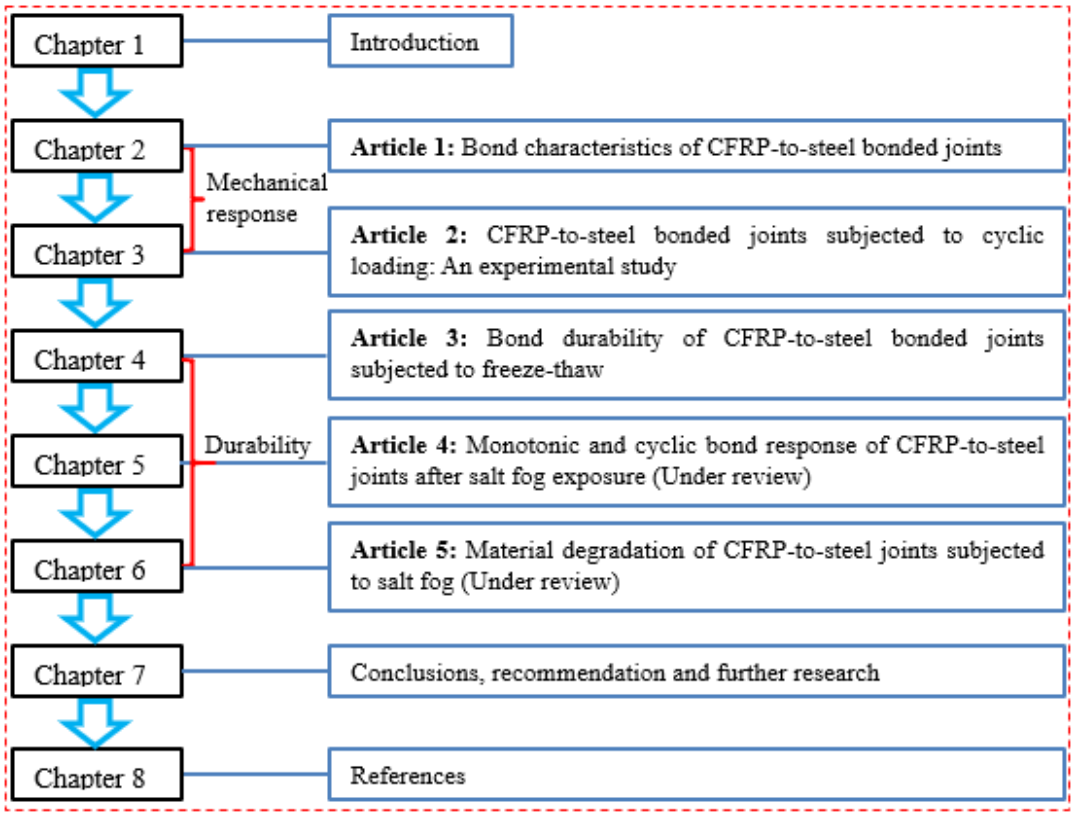

Figure 1.1 – Flow chart of the thesis structure

Chapter 2

Bond characteristics of CFRP-to-steel bonded joints

2.1 Introduction

Fiber Reinforced Polymer (FRP) sheets and strips, if adequately bonded to steel structures, have been shown to be effective enough on the enhancement of both the mechanical characteristics and fatigue life. Some research shows that significant increase in the stiffness and strength of the repaired beams can be achieved through the use of CFRP laminates [34-38]. A state-of-the-art review on steel beams externally strengthened with FRP composites under fatigue loading was published in 2014 [39], in which different rehabilitation techniques were discussed and the experimental results from previous research were summarized. In that study [39], it was shown that the mechanical properties of beams strengthened with FRP composites actually improved when compared to the unstrengthened beams. Among other aspects, it was found that the use of FRP composites can delay the initial cracking, reduce the crack growth rate, extend the fatigue life and decrease the stiffness decay with residual deflection.

As is well known, the primary challenge to the successful implementation of FRP composites for the strengthening of steel structures is the performance of the bond between both materials, which is susceptible to premature debonding. Premature debonding of the CFRP laminate from the substrate puts the bond stress transfer between materials at risk. This is an important failure mode that has recently attracted attention to national and international codes by adding useful guidelines for designers. The complexity of the mechanical response of a full-scale reinforced section does not allow the bond debonding mechanism to be clearly investigated. Thus, as a first step, more research [13, 14, 40-42] has been conducted with direct-shear tests of CFRP laminates/sheets attached to the surface of steel blocks (i.e., pull-push test), as well as double-strap bonded joints by putting together two steel plates with CFRP composites (pull-pull test) [12, 17, 18, 43] in order to enhance the understanding and modeling of the debonding failure mechanism coincident with a fracture Mode II loading.

Understanding and analyzing those failure modes is very important in seeking the control methods that can improve the reliability of the reinforced system. Even so, appropriate surface preparation of the steel and CFRP has been imposed to ensure that the failure will not occur within the interface between materials [44]. The failure modes associated to CFRP-to-steel bonded joints may have many possibilities such as: (i) the properties of the adhesive; (ii) the adhesive layer thickness; (iii) the stiffness of CFRP composites; and (iv) the bond length. Generally, brittle adhesive with low strength leads to cohesive failure, whereas high strength [41], ductility adhesive [13, 41] or thicker adhesive [14] leads to the delamination of the CFRP composite, whilst a high modulus CFRP seems to induce either the delamination or the rupture of CFRP composite [12, 18]. It should be noted that the change of the failure mode with different bond lengths was reported in [12, 18].

Like concrete [45], an interesting aspect of the bond behaviour of the CFRP-to-steel interface is that there is an effective bond length beyond which an extension in the bond length cannot increase the ultimate capacity of the joint. In fact, the correct evaluation of the effective bond length is an important part of the whole strengthening design, which can avoid the waste of composite materials in strengthening projects. Therefore, Sweedan et al. [46] studied the influence of using mechanical fasteners on CFRP-to-steel bonded joints to improve their strength. However, they found that when the distance between bolts increased from 100 mm to 168 mm, the influence of the bolts on the final strength was almost insignificant [46].

Knowledge of the interfacial behaviour of the joint plays an important role. Usually, this interfacial behaviour is quantified with a local relationship of the joint through the relation between the bond stress developed within the joint and the relative displacements (or slips) between bonded materials. The shape of the bond-slip curves is closely related to the properties of the adhesive (linear or nonlinear) [13, 41] with the failure mode and the geometric conditions of the specimens being relegated to a second plan. A considerable number of bond-slip curves of CFRP-to-steel bonded joints were obtained from pull-push tests and the derivation of closed-form solutions can be helpful for the understanding of the full-range debonding process [16, 47, 48]. To the best of the authors' knowledge, a lot of experimental studies have been conducted for double strap tests (i.e., pull-pull tests) [12, 17, 18, 43] but very few bond-slip curves were obtained from this loading condition [17, 18]. An excellent review by Zhao [49] also suggested that further research is required to determine bond-slip relationships based on those tests.

In the present chapter, a series of CFRP-to-steel double-strap bonded joints (pull-pull tests), with different bond lengths, was carried out. The failure modes are herein reported and the bond-slip relationship in each test was obtained. Based on the experimental results, a tri-linear bond-slip model is proposed and it is used for the determination of a closed-form solution that, despite easy implementation, provided accurate results when compared with those of the

experiments. The strength of the CFRP-to-steel interface, the distribution of the slips, strains in the CFRP laminate or in the steel and bond stresses within the interface are analyzed and discussed.

2.2 Experimental program and failure modes

2.2.1 Materials

Pultruded unidirectional CFRP laminates, steel plates and adhesive to bond the structures were used to make the specimens for testing. The CFRP laminate, which was 1.26 mm thick and 10 mm wide, was bought from a SIKA supplier as well as the bonding agent, a two-part room-temperature curable bonding agent, SIKADUR-30. The steel plate was 5 mm thick and 50 mm wide and it was cut in different lengths, as required by the different bonding lengths. The main mechanical properties of these three materials were experimentally obtained from tensile tests of flat coupons in accordance with standards ASTM D 3039 [50], ISO 527-2-1993 [51] and EN 10025:2004 [52]. The average values obtained from these tests are reported in Table 2.1. The coefficients of variation, cov, are shown in the same table.

Table 2.1 - Material properties of the CFRP laminate, adhesive and steel.

Materials	Young's modulus E (MPa)		Tensile strength σ_{max} (MPa)		Yield strength σ_y (MPa)		Ultimate strain ε_u (%)	
	Mean	cov	Mean	cov	Mean	cov	Mean	cov
SIKA laminate	163,300	4.2	1840	2.8	N/A	N/A	1.13	9.6
SIKA-30 adhesive	8432	3.0	21.76	7.64	N/A	N/A	0.34	12.5
Steel	210,000	N/A	540	N/A	400	N/A	N/A	N/A

2.2.2 Preparation of the specimens and test setup configuration

The double strap test was selected to study the bond properties of the CFRP-to-steel interface. The tests were conducted on specimens with the dimensions and configurations shown schematically in Figure 2.1. There are several advantages of the geometry chosen for the specimens. The mechanical clamping with two steel plates fastened with metallic bolts, applied on one side of the sample, ensured that the debonding failure would occur on the monitored side of the sample. Moreover, the 10 mm long gap at the center of the specimen could minimize or even prevent localized effects such as stress concentrations due to the external pressure applied to the clamped steel plates.

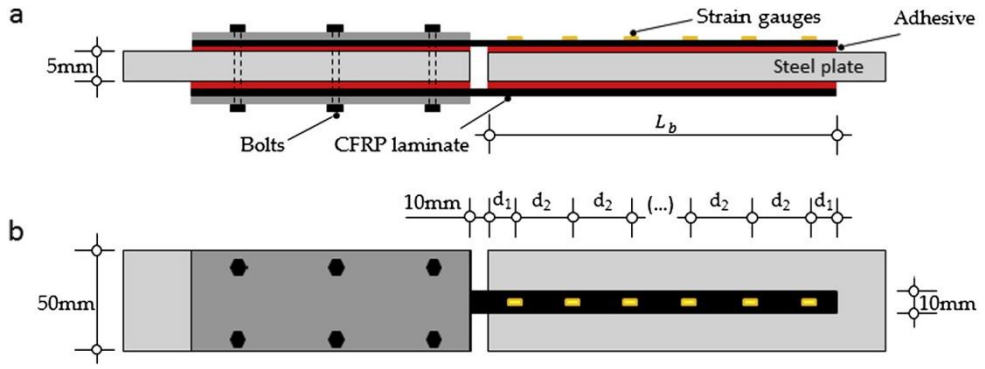

Figure 2.1 - Scheme of the specimens: (a) lateral view; and (b) front view.

The steel plates were grit-blasted and then cleaned with acetone to remove dust, grease and other contaminants before bonding the joints using a SIKA bonding agent, as recommended by the supplier. Two plastic 2.26 mm bars were used as bearing plates to make sure that a uniform 1 mm constant thickness of the adhesive was applied in all specimens. An illustration of process of preparation of CFRP-to-steel bonded joints is presented in Figure 2.2, in order to facilitate understanding. At end, the specimens were cured at room temperature (~24ºC) for 2 weeks before testing.

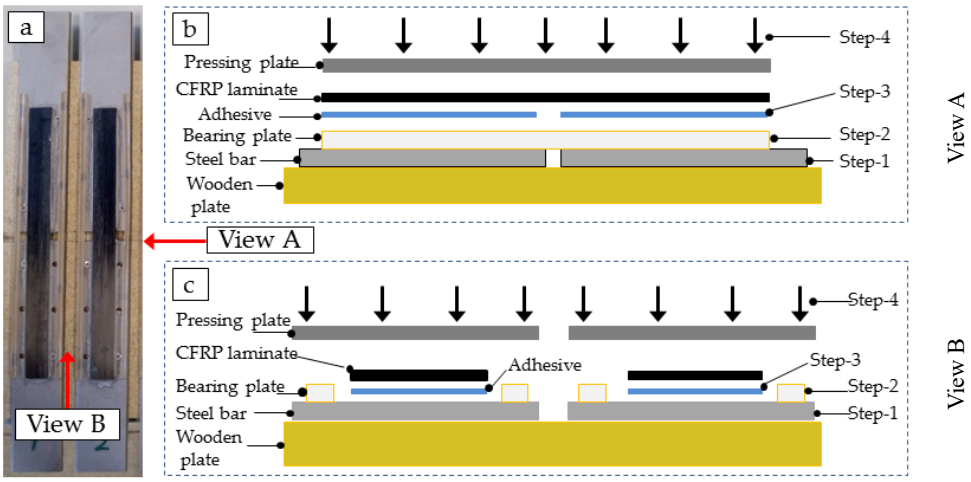

Figure 2.2 - Process of preparation of CFRP-to-steel bonded joints: (a) bonded joints, (b) Schematic view of preparation process from view A and (c) from View B

A total of 35 specimens with different bond lengths were prepared and tested under a pulled shear load in order to create a debonding failure mode consistent with the fracture Mode II. Different bond lengths were considered to analyze the differences between load-slip responses and to find out the effective bond length (L_{eff}) of the CFRP-to-steel interface, which is known in the literature, e.g. [53-56], by the length beyond which the strength of the interface can increase no further. The axial stiffness ratio of the specimens is defined as:

$$\beta = \frac{b_{CFRP} \cdot t_{CFRP} \cdot E_{CFRP}}{b_{steel} \cdot t_{steel} \cdot E_{steel}} \quad (2.1)$$

where b_{CFRP}, t_{CFRP} and E_{CFRP} are the width, the thickness and the Young's modulus of the CFRP laminate, respectively; and b_{steel}, t_{steel} and E_{steel} are the width, the thickness and the Young's modulus of the steel plate, respectively. For the values of the materials used, the axial stiffness β defined in (2.1) is equal to 0.039, which is an important parameter on the debonding behaviour in pull-pull tests as proved in [57]. The identification of the specimens and the bonded lengths used in the experimental program are presented in Table 2.2. For instance, S-10-25a/b/c, the initial letter "S" means that the CFRP laminate used is from SIKA supplier; the first number, "10", corresponds to the width of the CFRP laminate and the second number, "25", represents the bonded length; the letters "a", "b" and "c" at the end of the reference code means that the same test with the same characteristics was repeated three times.

The CFRP laminates of the specimens with different bond lengths, L_b, were set up with strain gauges as shown schematically in Figure 2.1. The first strain gauge and the last one were bonded 12.5 mm from the CFRP loaded and free ends but the intermediate strain gauges were all bonded at an interval of 25 mm. All tests were performed on a universal tensile machine with a maximum capacity of 50 kN. The tensile force transmitted to the specimens was monotonically imposed with a displacement rate of 1 mm/min. Figure 2.3 shows an overview of the test setup configuration used for testing the CFRP-to-steel interface under those conditions.

Table 2.2 - Summarized test results of the double strap bonded joints.

Designation of the specimens	Bond length, L_b (mm)	Average debonding load per interface, F_{max} (N)	Instrumentation (strain gauges)	Observed failure modes
S-10-10a/b/c	10	958	Not instrumented	A
S-10-25a/b/c	25	2822	Not instrumented	A
S-10-50a/b/c	50	5594	2 (d_1 = 12.5 mm; d_2 = 25 mm)	A
S-10-60a/b/c	60	6068	3 (d_1 = 10.0 mm; d_2 = 20 mm)	A
S-10-75a/b/c	75	5180	3 (d_1 = 12.5 mm; d_2 = 25 mm)	A
S-10-90a/b/c	90	7156	4 (d_1 = 7.5 mm; d_2 = 25 mm)	A
S-10-100a/b/c	100	5661	4 (d_1 = 12.5 mm; d_2 = 25 mm)	A
S-10-110a/b/c	110	6247	5 (d_1 = 5.0 mm; d_2 = 25 mm)	A
S-10-125a/b/c	125	6102	5 (d_1 = 12.5 mm; d_2 = 25 mm)	A
S-10-135a/b	135	7117	6 (d_1 = 5.0 mm; d_2 = 25 mm)	A
S-10-150a/b/c	150	5836	6 (d_1 = 12.5 mm; d_2 = 25 mm)	A
S-10-200a/b/c	200	6591	8 (d_1 = 12.5 mm; d_2 = 25 mm)	A

Note: A means that the failure mode occurred within the CFRP laminates and the adhesive interface (CFRP/Adhesive Interface Debonding); d_1 and d_2 – distances between consecutive strain gauges as shown in Figure 2.1.

Figure 2.3 - Overview of the test setup.

2.2.3 Failure modes

Zhao and Zhang [49] have described the possible failure modes that can be observed in CFRP-to-steel interfaces. Among all the failure modes described [49], in the current work the debonding of the interface between the CFRP composite and the adhesive was usually observed in all samples. However, in some parts of the bond length, a small and very thin surface of the resin remained bonded to the CFRP laminate after its complete separation from the resin. Therefore, in Table 2.2, it is stated that the failure mode is adhesive. As an example, Figure 2.4 shows this typical failure mode on four different samples with different bonded lengths randomly selected from the batch of 35 specimens. This figure shows two different perspectives: one is the failure mode observed from the side of the CFRP laminate, whereas the other is the perspective given of the failure mode observed from the steel plate. It is also important to mention that visible cracks or parts of the bonding agent debonded from the steel plates were never observed in the tests herein performed.

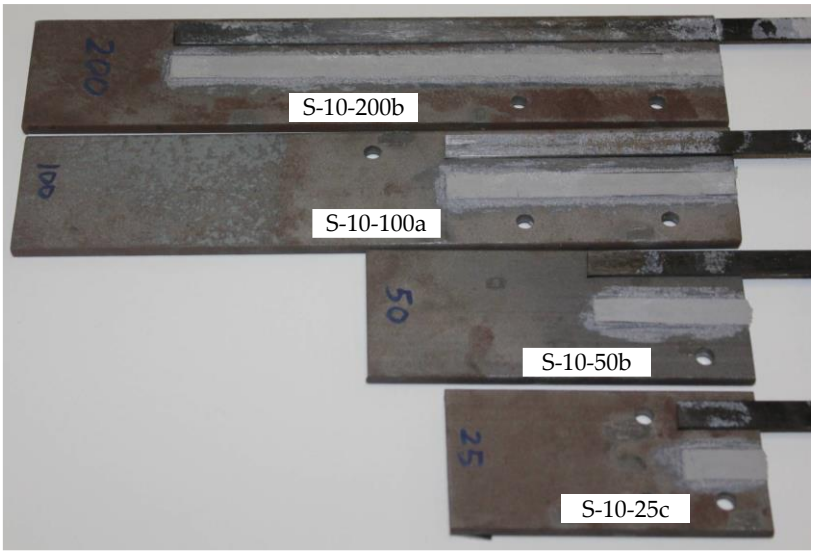

Figure 2.4 - Overall overview of the typical failure modes observed on some samples with different bonded lengths.

2.3 Local bond-slip behavior

2.3.1 Experimental bond-slip relationship

The bond-slip relationship of the CFRP-to-steel interface was obtained from the data collected by the strain gauges bonded on the CFRP laminate along the bond length. The bond stresses developed within the interface were calculated by assuming that between two consecutive strain gauges, the bond stress is constant according to [13, 41, 18, 58-61]:

$$\tau\left(x_{i+1/2}\right)=E_{CFRP}\cdot t_{CFRP}\frac{\varepsilon_{CFRP,i+1}-\varepsilon_{CFRP,i}}{x_{i+1}-x_i} \tag{2.2}$$

where $\varepsilon_{CFRP,i+1}$ and $\varepsilon_{CFRP,i}$ are, respectively, the strains in the CFRP laminate at point i+1 and point i; and the difference (x_{i+1} - x_i) is the distance between two consecutive points. As will be shown later, the bond stresses developed along the bond length are not constant and, therefore, the distances between strain gauges should be as small as possible in order to improve accuracy. On the other hand, the determination of the relative displacements (or slips) between the CFRP laminate and the steel plate assumed a linear distribution of the strains between two consecutive points [59] and in the present work they were determined as follows:

$$s\left(x_i\right)=\int_{x_i}^{x_{i+1}}\left(\varepsilon_{CFRP}-\varepsilon_{steel}\right)dx+s\left(x_{i+1}\right)=\frac{\varepsilon_{CFRP,i+1}+\varepsilon_{CFRP,i}}{2}\cdot\left(x_{i+1}-x_i\right) \\ -\frac{\varepsilon_{steel,i+1}+\varepsilon_{steel,i}}{2}\cdot\left(x_{i+1}-x_i\right)+s\left(x_{i+1}\right) \tag{2.3}$$

where $s(x_{i+1})$ is the slip at point x_{i+1} and $\varepsilon_{steel,i+1}$ and $\varepsilon_{steel,i}$ are the strains in the steel plate at the points i+1 and i, respectively. It should be noted also that, for the determination of Eq. (2.3), the region of zero slip was firstly identified from the bond stress distribution determined from

Eq. (2.2). Thereof, where the bond stress is zero it means that slip is zero as well and Eq. (2.3) can be derived and used towards the CFRP loaded end (centre of the double strap bond joint). Furthermore, the strains in the steel plate (ε_{steel}) can be found from the equilibrium condition of the test, i.e. using the loads measured from the tensile machine and from the loads in the CFRP composite. Due to the determination of the bond stresses at point i+1/2, an average value of the slips determined from Eq. (2.3) should be made between two consecutive points:

$$s\left(x_{i+1/2}\right)=\frac{s\left(x_{i+1}\right)+s\left(x_i\right)}{2} \tag{2.4}$$

The bond-slip relationship is finally determined by associating the average bond stress calculated from Eq. (2.2) and the average slip calculated from Eq. (2.4). However, due to the slips developed in both CFRP ends, the determination of the slips must firstly be made by the identification of a point (or points) of the bond length where the bond stress is zero, so the slip is zero as well. From that point forward, Eq. (2.3) should then be used without affecting the outcome of the interfacial bond-slip relationship [62, 63].

Figure 2.5 shows the differences between the interfacial bond-slip relationships obtained when the sample has a short (Figure 2.5a) or a long (Figure 2.5b) bonded length. From these results, it can be noticed that only from the samples with a sufficient bond length is it possible to fully define the interfacial bond-slip relationship. In this case of bond between the CFRP laminate and the steel plate, three different and distinct stages can be distinguished in the bond-slip relationship. The bond-slip relationship of the CFRP-to-steel interface can first be characterized by small slips and an almost linear increase of the bond stress, until a maximum bond stress value is reached. From this point on, the increase of the slips originates a decrease in the bond stress until a lower and constant bond stress is reached. Then, after this constant bond stress, a sudden and noisy rupture of the CFRP-to-steel interface was observed and heard and, therefore, no further data was collected from the samples.

The definition of the nuclear points of the interfacial bond-slip model can be made only if the interface has a sufficiently long bond length [59, 62-64]. Therefore, only the specimens with the longest bond lengths (S-10-200a, S-10-200b and S-10-200c) were chosen to define those points and their average values were calculated. Thus, the maximum bond stress τ_1 and the corresponding slip s_1 were found to be 11.55 MPa and 0.015 mm, respectively, whereas bond stress τ_2 and the corresponding slip s_2 were set at equal to 1.40 MPa and 0.085 mm, respectively. The ultimate slip and the last nuclear point in the proposed bond-slip relationship was s_3 = 0.300 mm.

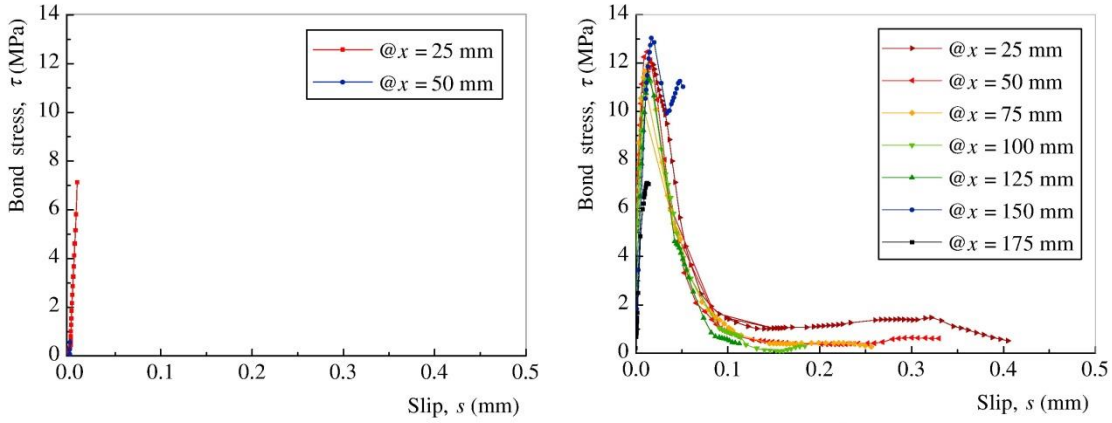

Figure 2.5 - Experimental bond-slip relationship obtained from the specimens with: (a) a short bond length (S-10-75a); and (b) the longest bond length (S-10-200b)

2.3.2 Proposed bond-slip model

Based on the experiments, a tri-linear bond-slip model is proposed for the simulation of the local behaviour of the CFRP-to-steel interface in CFRP/steel double strap joints which is quite similar to the local behaviour observed by Ren *et al*. [65] for grouted rockbolts. The interfacial bond-slip model is, therefore, built with an initial Elastic stage (E), followed by a linear Softening (S) stage that ends when a stage (C) of constant shear stress initiates. The interfacial bond-slip model can be mathematically defined as follows:

$$\tau(s) = \begin{cases} \frac{\tau_1}{s_1} \cdot s & \text{if} \quad 0 \le s \le s_1 \\ \frac{\tau_2 - \tau_1}{s_2 - s_1} \cdot s + \frac{\tau_1 \cdot s_2 - \tau_2 \cdot s_1}{s_2 - s_1} & \text{if} \quad s_1 < s \le s_2 \\ \tau_2 & \text{if} \quad s_2 < s \le s_3 \\ 0 & \text{if} \quad s > s_3 \end{cases} \tag{2.5}$$

where τ_1 and τ_2 are, respectively, the maximum bond stress and the bond stress corresponding to the constant stage; s_1, s_2 and s_3 are, respectively, the slip at maximum bond stress, the slip at the end of the linear softening stage and the ultimate slip which represents the end of the constant stage and from that point forward the complete debonding between materials initiates.

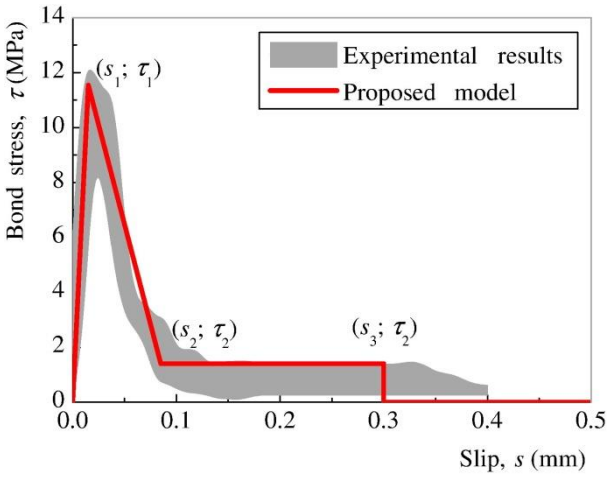

Figure 2.6 - Comparison between the experimental and the proposed bond-slip relationships.

2.4 Analysis of the debonding failure process

2.4.1 Main hypotheses and equilibrium conditions

In the formulation of the model leading to a closed-form solution, the following assumptions were made:

- the strain distribution across the width of the CFRP composite is constant and, consequently, the bond stresses developed along the width of the bonded length are constant;
- the cross section of the FRP composite stays unchanged during the full debonding failure process;
- a sufficiently long bond length is assumed, which means that the maximum strength of the interface is always reached and the effective bond length is ensured;
- the load applied to the FRP composite induces interfacial shear on the FRP-to-steel interfaces, which is consistent with the fracture Mode II debonding process and resulting into rupture modes that are in agreement with this fracture mode;
- the debonding failure process to be modeled is consistent with that observed from the tests, which means that other possible debonding failure processes lie outside of the scope of the proposed model and, consequently, of this work.

In addition to the above assumptions, it should be noted that the closed-form solution intends to simulate the debonding failure process of the double strap joints tested accordingly to the experimental program. Despite the fact of the same methodology could be used to predict the debonding failure process of other test setup configurations, adequate boundary conditions (see Appendix A) should be used for each case.

The proposed model, assuming a segment length *dx* of the double strap joint bonded length as

shown in Figure 2.7, leads to the following equilibrium equations:

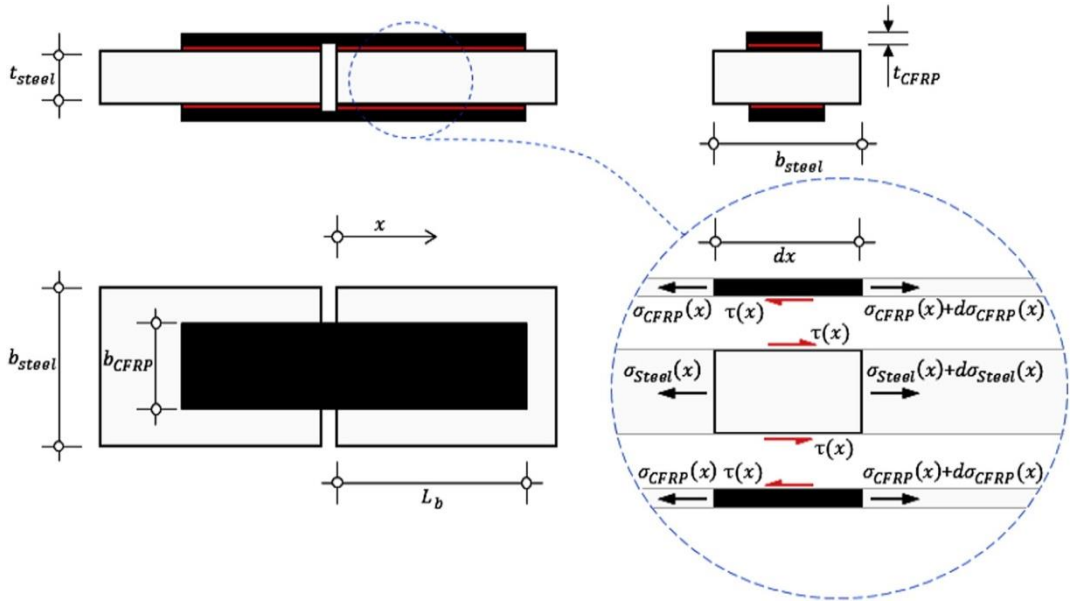

Figure 2.7 - Equilibrium of forces in an infinitesimal length *dx* of the CFRP-to-steel interface.

$$F = F_{steel} + F_{CFRP} \tag{2.6}$$

$$\frac{d\sigma_{CFRP}}{dx} + \frac{\tau(x)}{t_{CFRP}} = 0 \tag{2.7}$$

and

$$\frac{d\sigma_{steel}}{dx} - \frac{2\tau(x)\cdot b_{CFRP}}{b_{steel}\cdot t_{steel}} = 0 \tag{2.8}$$

where F_{CFRP} and F_{steel} are the loads transmitted to the CFRP laminate and to the steel, respectively; τ is the bond stress developed within the CFRP-to-steel interface; and σ_{CFRP} and σ_{steel} are the axial stresses in the CFRP laminate and in the steel, respectively. It should be noted that Eq. (2.6) was used to calculate the loads/strains in the steel plate (see Eq. (2.3)). Assuming an elastic and linear constitutive behaviour for the CFRP laminate and for the steel, the axial stresses in both materials can be defined as:

$$\sigma_{CFRP} = E_{CFRP}\cdot\frac{du_{CFRP}}{dx} \tag{2.9}$$

and

$$\sigma_{steel} = E_{steel}\cdot\frac{du_{steel}}{dx} \tag{2.10}$$

where u_{CFRP} and u_{steel} are, respectively, the displacements in the CFRP laminate and in the steel. Hence, the first derivative of the CFRP and steel displacements with respect to x, du_{CFRP}/dx and du_{steel}/dx, represent the strains in the CFRP laminate and in the steel, respectively.

The relative displacements between bonded materials (or slips), i.e. between the CFRP laminate and the steel, are determined according to:

$$s = u_{steel} - u_{CFRP} \tag{2.11}$$

Differentiating Eq. (2.11) with respect to x yields:

$$\frac{ds}{dx} = \frac{du_{steel}}{dx} - \frac{du_{CFRP}}{dx} \tag{2.12}$$

Introducing Eqs. (2.9) and (2.10) into (2.12), the following equation is obtained:

$$\frac{ds}{dx} = \frac{\sigma_{steel}}{E_{steel}} - \frac{\sigma_{CFRP}}{E_{CFRP}} \tag{2.13}$$

which when differentiated with respect to x yields:

$$\frac{d^2s}{dx^2} = \frac{1}{E_{steel}} \cdot \frac{d\sigma_{steel}}{dx} - \frac{1}{E_{CFRP}} \cdot \frac{d\sigma_{CFRP}}{dx} . \tag{2.14}$$

In the equilibrium of the segment dx, the interfacial bond-slip model defined in (2.5) can be used, i.e. $\tau(x) \equiv \tau(s)$. When Eqs. (2.7) and (2.8) are introduced in Eq. (2.14), the second order differential equation is obtained:

$$\frac{d^2s}{dx^2} - \lambda \cdot \tau(s) = 0 \tag{2.15}$$

where

$$\lambda = \frac{1}{E_{CFRP} \cdot t_{CFRP}} + \frac{2b_{CFRP}}{E_{steel} \cdot b_{steel} \cdot t_{steel}} \tag{2.16}$$

2.4.2 Description of the states of the interface

Depending on the stage of the bond-slip model, Eq. (2.15) leads to different slip distributions, $s(x)$ and depending on the state of the interface Eq. (2.15) provides a single solution for each one. However, before trying to find these solutions, it is important to identify and understand first what these states are or represent. Hence, until the complete debonding of an interface with a sufficiently long bonded length, for the current test conditions, there is only one possible path to reach the complete debonding of the CFRP-to steel interface. The different states that the interface undergoes until its complete debonding are briefly described next:

- Elastic (E): at this initial state, the full bond length has an elastic performance in which the slips developed within the interface are lower than the slip s_1 (see Eq. (2.5)). The most

loaded end of the CFRP laminate shows the largest slips, which tend to decrease towards the CFRP free end, but at the closest regions of the CFRP free end, the slips tend to increase once again in a much smaller proportion than that developed in the opposite bonded region;

- Softening-Elastic (S-E): in this state, the most CFRP loaded end softens, which means that the maximum bond stress has already been reached at that point. As the load is being transmitted to the CFRP laminate, the maximum bond stress migrates from the CFRP loaded end to the centre of the bonded region. In this softening area of the interface, the slips developed in it are now higher than the maximum slip s_1 but smaller than s_2, which is the maximum slip of the softening stage, as defined in the proposed bond-slip model. Naturally, when s_2 is reached, this state will end and the next one will begin to develop;
- Constant-Softening-Elastic (C-S-E): in this state, the three stages defined in the proposed bond-slip model are developed within the CFRP-to-steel interface. Despite the fact the slips in both CFRP ends have increased so far, the bond stress distribution has a different trend. At the CFRP loaded end, a constant bond stress τ_2 develops in a bonded length where the slips are higher than s_2 but lower than s_3, which is the slip beyond which the complete detachment between the CFRP laminate and the steel plate occurs. After that point, the bond stress increases until its peak value, i.e. maximum bond stress τ_1, is reached and the softening bonded region is delimited by s_1 and s_2. The remaining bonded regions of the interface are in an elastic state that won't change before the strength of the interface is reached;
- Debonded-Constant-Softening-Elastic (D-C-S-E): in this state, the most loaded end has already debonded. The maximum strength of the interface is reached and, depending on the bond length, this state performs as if it is yielding, i.e. with the same load there is an increase in the slips at the CFRP loaded end. Also, excluding the debonded region, the bond stress distribution in this state has the same configuration. Still, as the slips increase, the elastic region will tend to decrease until its complete disappearance, which represents the beginning of a new state;
- Debonded-Constant-Softening (D-C-S): two regions of the bonded area are responsible for the transfer of stresses between materials. The softening region is localized at the closest region of the CFRP free end and at this point, the slips are increasing between s_1 and s_2. Of course, when slip s_2 is reached at the CFRP free end, the softening region vanishes from the interface and a new state will then begin;
- Debonded-Constant (D-C): only the region corresponding to a constant bond stress is still transferring stresses between materials. From the point of view of equilibrium of the CFRP laminate, the load at this stage is easily determined by multiplying the bond stress τ_2 with

the remaining bonded area.

Figure 2.8 shows the debonding failure process of the case under analysis, i.e. for the test setup configuration (double strap test), where a small axial stiffness rate is used and with a sufficiently long bond length. Figure 2.8 illustrates, therefore, the bond stress transfer throughout the debonding failure process and, albeit schematically, shows development of the bond stress distribution in the load-slip response of the interface at the CFRP loaded end (at $x = 0$).

Next, taking into account the states previously described, the corresponding closed-form solution for each state is presented. The determination of the load-slip curve as well as the distributions of slips developed within the interface, the strains in the CFRP laminate and in the steel plate and the bond stresses are all reported in detail in the following subsections.

2.4.3 Solution for the Elastic state

To find the closed-form solution for the Elastic state, the equilibrium differential equation stated in (2.15) is solved by considering the corresponding elastic stage of the bond-slip model defined through Eq. (2.5), yielding:

$$\frac{d^2 s}{dx^2} - \alpha_1^{\,2} \cdot s = 0 \tag{2.17}$$

where:

$$\alpha_1^{\,2} = \frac{\tau_1}{s_1} \cdot \lambda \tag{2.18}$$

Considering the boundary conditions and the integration constants in this state presented in Appendix A.1, the solution of Eq. (2.17) is:

$$s_E(x) = \frac{F}{\alpha_1 \cdot \sinh(\alpha_1 \cdot L_b) \cdot E_{CFRP} \cdot A_{CFRP}} \cdot [\beta \cdot \cosh(\alpha_1 \cdot x) + \cosh(\alpha_1 \cdot (x - L_b))] \tag{2.19}$$

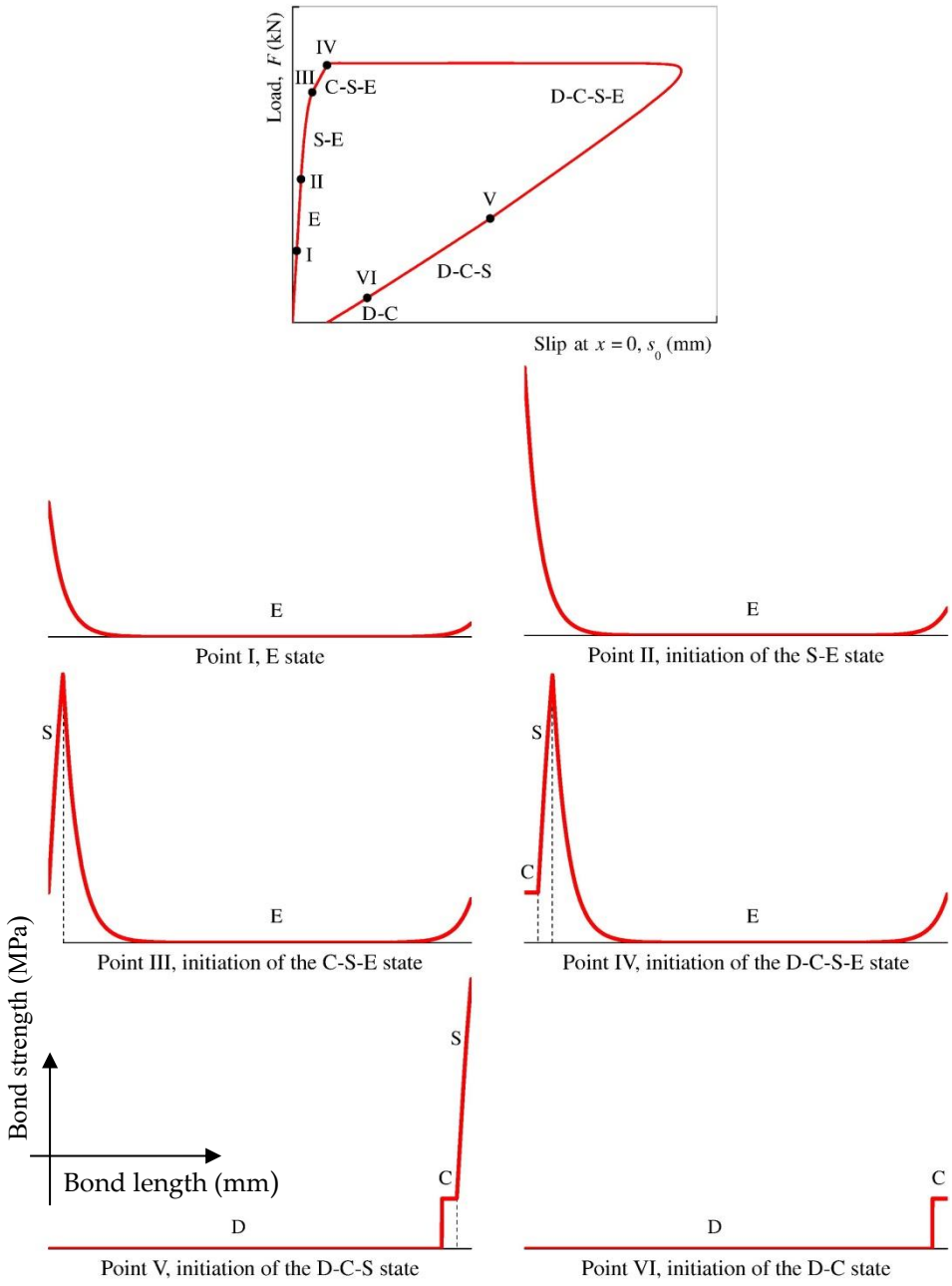

Figure 2.8 - Scheme of the full debonding process of the CFRP-to-steel interface with a small value of the axial stiffness rate.

The corresponding elastic load-slip response either at $x = 0$ or $x = L_b$ can be now obtained from Eq. (2.19) , leading to:

$$s_E(x=0) = \frac{F}{\alpha_1 \cdot \sinh(\alpha_1 \cdot L_b) \cdot E_{CFRP} \cdot A_{CFRP}} \cdot [\beta + \cosh(\alpha_1 \cdot L_b)] \tag{2.20}$$

and

$$s_E(x=L_b) = \frac{F}{\alpha_1 \cdot \sinh(\alpha_1 \cdot L_b) \cdot E_{CFRP} \cdot A_{CFRP}} \cdot [\beta \cdot \cosh(\alpha_1 \cdot L_b) + 1] \cdot \tag{2.21}$$

Based on the elastic stage of the bond-slip model, the bond stress distribution can be determined as follows:

$$\tau_E(x) = \frac{\tau_1 \cdot F}{s_1 \cdot \alpha_1 \cdot \sinh(\alpha_1 \cdot L_b) \cdot E_{CFRP} \cdot A_{CFRP}} \cdot [\beta \cdot \cosh(\alpha_1 \cdot x) + \cosh(\alpha_1 \cdot (x - L_b))] \cdot \tag{2.22}$$

To determine the strains in the CFRP laminate and in the steel plate, Eqs. (A.4) and (A.5) (both in Appendix A.1), should be introduced into Eq. (2.6) leading, therefore, to the strains in the CFRP laminate and in the steel plate, respectively:

$$\varepsilon_{CFRP}(x) = \gamma - \frac{1}{1+\beta} \cdot \frac{ds}{dx} \tag{2.23}$$

and

$$\varepsilon_{steel}(x) = \gamma + \frac{\beta}{1+\beta} \cdot \frac{ds}{dx} \tag{2.24}$$

where

$$\gamma = \frac{F}{E_{CFRP} \cdot A_{CFRP} + E_{steel} \cdot A_{steel}} \cdot \tag{2.25}$$

Hence, introducing the first derivative of Eq. (2.19) with respect to x, the strains in the CFRP laminate and in the steel plate in the elastic stage are respectively calculated according to:

$$\varepsilon_{CFRP,E}(x) = \gamma \cdot \left\{ 1 - \frac{1}{\beta \cdot \sinh(\alpha_1 \cdot L_b)} \cdot [\beta \cdot \sinh(\alpha_1 \cdot x) + \sinh(\alpha_1 \cdot (x - L_b))] \right\} \tag{2.26}$$

and

$$\varepsilon_{steel,E}(x) = \gamma \cdot \left\{ 1 + \frac{1}{\sinh(\alpha_1 \cdot L_b)} \cdot [\beta \cdot \sinh(\alpha_1 \cdot x) + \sinh(\alpha_1 \cdot (x - L_b))] \right\} \cdot \tag{2.27}$$

The maximum load reached in this state can be determined when the CFRP loaded end, i.e. at $x = 0$, reaches the slip s_1 and, therefore, when this condition is introduced into Eq. (2.20), the load F corresponds to the maximum elastic load $F_{E,\max}$ given by:

$$F_{E,\max} = \frac{s_1 \cdot \alpha_1 \cdot \sinh(\alpha_1 \cdot L_b) \cdot E_{CFRP} \cdot A_{CFRP}}{\beta + \cosh(\alpha_1 \cdot L_b)} \cdot \tag{2.28}$$

For an infinite bond length, i.e. $L_b \to \infty$, the limit of Eq. (2.28) gives:

$$F_{E,\max} = \lim_{L_b \to \infty} \frac{s_1 \cdot \alpha_1 \cdot E_{CFRP} \cdot A_{CFRP}}{\tanh(\alpha_1 \cdot L_b)} = s_1 \cdot \alpha_1 \cdot E_{CFRP} \cdot A_{CFRP} \cdot \tag{2.29}$$

Denoting the elastic fracture energy, $G_{F,E}$, as the area limited by the elastic stage of the bond-slip relationship and regarding Eq. (2.18), the maximum elastic load transmitted to the CFRP

laminate is finally determined according to:

$$F_{E,\max} = b_{CFRP} \cdot \sqrt{2G_{F,E} \cdot E_{CFRP} \cdot t_{CFRP} \cdot (1+2\beta)} \tag{2.30}$$

where:

$$G_{F,E} = \frac{\tau_1 \cdot s_1}{2}. \tag{2.31}$$

Moreover, the length beyond which the elastic load cannot increase (or the elastic effective bond length), can be found from the limit stated in (2.29) by assuming that when $\tanh(\alpha_1 \cdot L_b) = 1$ the bond length and the effective bond length are the same and the approximation $\alpha_1 \cdot L_b \approx 2$ is valid. Thus, regarding Eq. (2.18), the effective bond length associated to the elastic stage of the tri-linear bond-slip model is:

$$L_{eff,E} = s_1 \cdot \sqrt{\frac{2E_{CFRP} \cdot t_{CFRP}}{G_{F,E} \cdot (1+2\beta)}}. \tag{2.32}$$

2.4.4 Solution for the Softening-Elastic state

For the Softening-Elastic state, besides the second order differential equation in (2.17), which governs the equilibrium of the bonded length under an elastic stage, the second order differential equation that governs the softening region is derived by introducing the softening stage defined in Eq. (2.5) (between slip s_1 and slip s_2) into Eq. (2.15), leading to:

$$\frac{d^2 s}{dx^2} + \alpha_2{}^2 \cdot s = a \tag{2.33}$$

where:

$$\alpha_2{}^2 = \frac{\tau_1 - \tau_2}{s_1 - s_2} \cdot \lambda \tag{2.34}$$

and

$$a = \frac{\tau_1 \cdot s_2 - \tau_2 \cdot s_1}{s_1 - s_2} \cdot \lambda. \tag{2.35}$$

For the boundary conditions defined in Appendix A.2 and assuming an infinite bond length, the slips developed within the elastic and the softened region of the CFRP-to-steel interface are, respectively, determined according to:

$$s_E(x) = \frac{s_1 \cdot \cosh(\alpha_1 \cdot (x - L_b))}{\cosh(\alpha_1 \cdot (L_b - L_S))} + \frac{\gamma \cdot (1+\beta) \cdot \sinh(\alpha_1 \cdot (x - L_S))}{\alpha_1 \cdot \cosh(\alpha_1 \cdot (L_b - L_S))} \tag{2.36}$$

and

$$s_S(x)=\left(\frac{s_1\cdot\alpha_1}{\alpha_2\cdot\sin(\alpha_2\cdot L_S)}-\frac{\gamma\cdot(\beta+1)}{\alpha_2\cdot\tan(\alpha_2\cdot L_S)\cdot\beta}\right)\cdot\cos(\alpha_2\cdot x)-\frac{\gamma\cdot(\beta+1)}{\alpha_2\cdot\beta}\cdot\sin(\alpha_2\cdot x)+\frac{a}{{\alpha_2}^2} \tag{2.37}$$

The load-slip response in this state can be found by using Eqs. (2.36) and (2.37). In the case of Eq. (2.36), the load-slip response at $x = L_b$ is obtained whereas Eq. (2.37) gives the load-slip response at $x = 0$. Hence, the load-slip responses at $x = L_b$ and $x = 0$ are, respectively:

$$s_E(x=L_b)=\frac{s_1}{\cosh(\alpha_1\cdot(L_b-L_S))}+\frac{\gamma\cdot(\beta+1)\tanh(\alpha_1\cdot(L_b-L_S))}{\alpha_1} \tag{2.38}$$

and

$$s_S(x=0)=\left(\frac{s_1\cdot\alpha_1}{\alpha_2\cdot\sin(\alpha_2\cdot L_S)}-\frac{\gamma\cdot(\beta+1)}{\alpha_2\cdot\tan(\alpha_2\cdot L_S)\cdot\beta}\right)+\frac{a}{{\alpha_2}^2}\cdot \tag{2.39}$$

The bond stress distributions in the elastic and softened regions are respectively determined from the bond-slip model defined in (2.5), which leads to:

$$\tau_E(x)=\frac{\tau_1\cdot\cosh(\alpha_1\cdot(x-L_b))}{\cosh(\alpha_1\cdot(L_b-L_S))}+\frac{\gamma\cdot(\beta+1)\cdot\tau_1\cdot\sinh(\alpha_1\cdot(x-L_S))}{s_1\cdot\alpha_1\cdot\cosh(\alpha_1\cdot(L_b-L_S))} \tag{2.40}$$

and

$$\tau_S(x)=\left\{\left(\frac{s_1\cdot\alpha_1}{\alpha_2\cdot\sin(\alpha_2\cdot L_S)}-\frac{\gamma\cdot(\beta+1)}{\alpha_2\cdot\tan(\alpha_2\cdot L_S)\cdot\beta}\right)\cdot\cos(\alpha_2\cdot x)-\frac{\gamma\cdot(\beta+1)}{\alpha_2\cdot\beta}\cdot\sin(\alpha_2\cdot x)\right\}\cdot\frac{{\alpha_2}^2}{\lambda}-\frac{a}{\lambda}\cdot \tag{2.41}$$

The strains in the CFRP laminate and in the steel plate can be determined by using Eqs. (2.23) and (2.24), respectively. Thus, when the first derivative of Eq. (2.36) with respect to x is introduced into Eqs. (2.23) and (2.24), the strains in the CFRP laminate and in the steel plate along the elastic region of the interface are, respectively:

$$\varepsilon_{CFRP,E}(x)=\gamma\cdot\left[1-\frac{\cosh(\alpha_1\cdot(x-L_S))}{\cosh(\alpha_1\cdot(L_b-L_S))}\right]-\frac{\alpha_1\cdot s_1\cdot\sinh(\alpha_1\cdot(x-L_b))}{(1+\beta)\cdot\cosh(\alpha_1\cdot(L_b-L_S))} \tag{2.42}$$

and

$$\varepsilon_{steel,E}(x)=\gamma\cdot\left[1+\frac{\beta\cdot\cosh(\alpha_1\cdot(x-L_S))}{\cosh(\alpha_1\cdot(L_b-L_S))}\right]+\frac{\beta\cdot\alpha_1\cdot s_1\cdot\sinh(\alpha_1\cdot(x-L_b))}{(1+\beta)\cdot\cosh(\alpha_1\cdot(L_b-L_S))}\cdot \tag{2.43}$$

If the first derivative of Eq. (3.37) with respect to x is now introduced into Eqs. (2.23) and (2.24), and assuming an infinite bond length, the strains in the CFRP laminate and in the steel plate along the softened region of the CFRP-to-steel interface are obtained according to:

$$\varepsilon_{CFRP,S}(x)=\gamma\cdot\left[1-\frac{\sin(\alpha_2\cdot x)}{\beta\cdot\tan(\alpha_2\cdot L_S)}+\frac{\cos(\alpha_2\cdot x)}{\beta}\right]+\frac{\alpha_1\cdot s_1\cdot\sin(\alpha_2\cdot x)}{(1+\beta)\cdot\sin(\alpha_2\cdot L_S)} \tag{2.44}$$

and

$$\varepsilon_{steel,S}(x)=\gamma\cdot\left[1+\frac{\sin(\alpha_2\cdot x)}{\tan(\alpha_2\cdot L_S)}-\cos(\alpha_2\cdot x)\right]-\frac{\alpha_1\cdot s_1\cdot\beta\cdot\sin(\alpha_2\cdot x)}{(1+\beta)\cdot\sin(\alpha_2\cdot L_S)}. \tag{2.45}$$

To determine the equations derived in this subsection, the softened length L_S is needed. Thus, the slip s_1 can always be found at $x = L_S$ and introducing this condition into Eq. (2.37), the softened length is defined according to:

$$L_S=-\frac{2}{\alpha_2}\cdot\arctan\left\{\frac{\sqrt{s_1^{\,2}\cdot\left(\alpha_1^{\,2}+\alpha_2^{\,2}\right)+a\cdot\left(\frac{a}{\alpha_2^{\,2}}-2\cdot s_1\right)-\left(\frac{\gamma\cdot(\beta+1)}{\beta}\right)^2}+\alpha_2\cdot s_1-\frac{a}{\alpha_2}}{\alpha_1\cdot\left(\frac{\gamma\cdot(\beta+1)}{\alpha_2\cdot\beta}+s_1\right)}\right\}. \tag{2.46}$$

As already shown in the literature [66], the shape of the bond-slip model has no influence on the calculation of the maximum load and, therefore, its maximum value at the end of this S-E state can be obtained from Eq. (2.30). However, the elastic fracture energy ($G_{F,E}$) in Eq. (2.30) should be replaced by the fracture energy of the current S-E state. Thus, the maximum load in this current S-E state is defined as:

$$F_{E,\max}=b_{CFRP}\cdot\sqrt{2G_{F,S-E}\cdot E_{CFRP}\cdot t_{CFRP}\cdot(1+2\beta)} \tag{2.47}$$

where:

$$G_{F,S-E}=\frac{\tau_1\cdot s_2}{2}+\frac{\tau_2\cdot(s_2-s_1)}{2}. \tag{2.48}$$

2.4.5. Solution for the Constant-Softening-Elastic state

For this C-S-E state, another second order differential equation must be added to Eqs. (2.17) and (2.33). This additional equation should govern the equilibrium of the CFRP-to-steel interface along the bonded length with a constant bond stress τ_2. Hence, introducing the constant bond stress τ_2 into Eq. (2.15), yields:

$$\frac{d^2s}{dx^2}=\alpha_3 \tag{2.49}$$

where:

$$\alpha_3=\tau_2\cdot\lambda \tag{2.50}$$

Taking into account the boundary conditions defined in Appendix A.3, the solution of Eq. (2.49)

for the elastic bonded region is:

$$s_E(x)=\frac{s_1\cdot\cosh\left(\alpha_1\cdot\left(x-L_b\right)\right)}{\cosh\left(\alpha_1\cdot\left(L_b-L_{S,\max}-L_C\right)\right)}+\frac{\gamma\cdot(\beta+1)\cdot\sinh\left(\alpha_1\cdot\left(x-L_{S,\max}-L_C\right)\right)}{\alpha_1\cdot\cosh\left(\alpha_1\cdot\left(L_b-L_{S,\max}-L_C\right)\right)} \tag{2.51}$$

whereas the slip distributions along the softening and the constant regions are, respectively:

$$s_S(x)=\frac{a}{{\alpha_2}^2}+\frac{\gamma\cdot(\beta+1)\cdot\left[-\beta\cdot\cos\left(\alpha_2\cdot\left(x-L_C\right)\right)-\cos\left(\alpha_2\cdot\left(x-L_{S,\max}-L_C\right)\right)\cdot\cosh\left(\alpha_1\cdot\left(L_b-L_{S,\max}-L_C\right)\right)\right]}{\alpha_2\cdot\beta\cdot\sin\left(\alpha_2\cdot L_{S,\max}\right)\cdot\cosh\left(\alpha_1\cdot\left(L_b-L_{S,\max}-L_C\right)\right)}$$
$$+\frac{L_C\cdot\alpha_3\cdot\cos\left(\alpha_2\cdot\left(x-L_{S,\max}-L_C\right)\right)\cdot\cosh\left(\alpha_1\cdot\left(x-L_{S,\max}-L_C\right)\right)+s_1\cdot\alpha_1\cdot\cos\left(\alpha_2\cdot\left(x-L_C\right)\right)\cdot\sinh\left(\alpha_1\cdot\left(L_b-L_{S,\max}-L_C\right)\right)}{\alpha_2\cdot\sin\left(\alpha_2\cdot L_{S,\max}\right)\cdot\cosh\left(\alpha_1\cdot\left(L_b-L_{S,\max}-L_C\right)\right)} \tag{2.52}$$

and

$$s_C(x)=\frac{\alpha_3}{2}\cdot\left(x^2-{L_C}^2\right)+\frac{\gamma\cdot(\beta+1)}{\beta}\cdot\left(L_C-x\right)+s_2\cdot \tag{2.53}$$

The load-slip responses in this state, Eqs. (2.51) and (2.53) should be used and the corresponding load-slip response at the CFRP free and loaded ends are, respectively:

$$s_E\left(x=L_b\right)=\frac{s_1}{\cosh\left(\alpha_1\cdot\left(L_b-L_{S,\max}-L_C\right)\right)}+\frac{\gamma\cdot(\beta+1)\cdot\tanh\left(\alpha_1\cdot\left(L_b-L_{S,\max}-L_C\right)\right)}{\alpha_1} \tag{2.54}$$

and

$$s_C(x=0)=-\frac{\alpha_3\cdot{L_C}^2}{2}+\frac{\gamma\cdot(\beta+1)\cdot L_C}{\beta}+s_2\cdot \tag{2.55}$$

Once again, the bond stress developed within the interface and along the bond length is determined by introducing the corresponding bond stress defined in (2.5) into the corresponding Eqs. (2.51)-(2.53):

$$\tau_E(x)=\frac{\tau_1\cdot\cosh\left(\alpha_1\cdot\left(x-L_b\right)\right)}{\cosh\left(\alpha_1\cdot\left(L_b-L_{S,\max}-L_C\right)\right)}+\frac{\gamma\cdot(\beta+1)\cdot\tau_1\cdot\sinh\left(\alpha_1\cdot\left(x-L_{S,\max}-L_C\right)\right)}{s_1\cdot\alpha_1\cdot\cosh\left(\alpha_1\cdot\left(L_b-L_S-L_C\right)\right)}, \tag{2.56}$$

$$\tau_S(x)=-\frac{a}{\lambda}+\frac{{\alpha_2}^2}{\lambda}\cdot\left\{\frac{\gamma\cdot(\beta+1)\cdot\left[-\beta\cdot\cos\left(\alpha_2\cdot\left(x-L_C\right)\right)-\cos\left(\alpha_2\cdot\left(x-L_{S,\max}-L_C\right)\right)\cdot\cosh\left(\alpha_1\cdot\left(L_b-L_{S,\max}-L_C\right)\right)\right]}{\alpha_2\cdot\beta\cdot\sin\left(\alpha_2\cdot L_{S,\max}\right)\cdot\cosh\left(\alpha_1\cdot\left(L_b-L_{S,\max}-L_C\right)\right)}\right.$$
$$\left.+\frac{L_C\cdot\alpha_3\cdot\cos\left(\alpha_2\cdot\left(x-L_{S,\max}-L_C\right)\right)\cdot\cosh\left(\alpha_1\cdot\left(x-L_{S,\max}-L_C\right)\right)+s_1\cdot\alpha_1\cdot\cos\left(\alpha_2\cdot\left(x-L_C\right)\right)\cdot\sinh\left(\alpha_1\cdot\left(L_b-L_{S,\max}-L_C\right)\right)}{\alpha_2\cdot\sin\left(\alpha_2\cdot L_{S,\max}\right)\cdot\cosh\left(\alpha_1\cdot\left(L_b-L_{S,\max}-L_C\right)\right)}\right\} \tag{2.57}$$

and

$$\tau_C(x)=\tau_2\cdot \tag{2.58}$$

The strains in the CFRP laminate along the bond length in each stage can be found, once more,

with Eq. (2.23) and therefore, in the Elastic, Softening and Constant regions of the CFRP-to-steel interface. The strains in the CFRP laminate for an infinite bond length are:

$$\varepsilon_{CFRP,E}(x)=\gamma\cdot\left[1-\frac{\cosh\left(\alpha_1\cdot\left(x-L_{S,\max}-L_C\right)\right)}{\cosh\left(\alpha_1\cdot\left(L_b-L_{S,\max}-L_C\right)\right)}\right]-\frac{\alpha_1\cdot s_1\cdot\sinh\left(\alpha_1\cdot\left(x-L_b\right)\right)}{(1+\beta)\cdot\cosh\left(\alpha_1\cdot\left(L_b-L_{S,\max}-L_C\right)\right)}, \quad (2.59)$$

$$\varepsilon_{CFRP,S}(x)=\gamma\cdot\left[1+\frac{\sin\left(\alpha_2\cdot\left(L_C+L_{S,\max}-x\right)\right)}{\beta\cdot\sin\left(\alpha_2\cdot L_{S,\max}\right)}\right]+\frac{\alpha_1\cdot s_1\cdot\sin\left(\alpha_2\cdot\left(x-L_C\right)\right)+L_C\cdot\alpha_3\cdot\sin\left(\alpha_2\cdot\left(x-L_C-L_{S,\max}\right)\right)}{(1+\beta)\cdot\sin\left(\alpha_2\cdot L_{S,\max}\right)} \quad (2.60)$$

and

$$\varepsilon_{CFRP,C}(x)=\frac{\gamma\cdot(\beta+1)}{\beta}-\frac{\alpha_2\cdot x}{1+\beta}. \quad (2.61)$$

On the other hand, the strains in the steel plate are determined from Eq. (2.24). Considering the three stages developed within the CFRP-to-steel interface, the strains in the Elastic, Softening and Constant regions, are:

$$\varepsilon_{steel,E}(x)=\gamma\cdot\left[1+\frac{\beta\cdot\cosh\left(\alpha_1\cdot\left(x-L_{S,\max}-L_C\right)\right)}{\cosh\left(\alpha_1\cdot\left(L_b-L_{S,\max}-L_C\right)\right)}\right]+\frac{\beta\cdot\alpha_1\cdot s_1\cdot\sinh\left(\alpha_1\cdot\left(x-L_b\right)\right)}{(1+\beta)\cdot\cosh\left(\alpha_1\cdot\left(L_b-L_{S,\max}-L_C\right)\right)} \quad (2.62)$$

$$\varepsilon_{steel,S}(x)=\gamma\cdot\left[1+\frac{\sin\left(\alpha_2\cdot\left(x-L_C-L_{S,\max}\right)\right)}{\sin\left(\alpha_2\cdot L_{S,\max}\right)}\right]+\frac{\beta}{1+\beta}\cdot\frac{\alpha_1\cdot s_1\cdot\sin\left(\alpha_2\cdot\left(L_C-x\right)\right)+L_C\cdot\alpha_3\cdot\sin\left(\alpha_2\cdot\left(L_C+L_{S,\max}-x\right)\right)}{\sin\left(\alpha_2\cdot L_{S,\max}\right)} \quad (2.63)$$

and

$$\varepsilon_{steel,C}(x)=\frac{\beta\cdot\alpha_2\cdot x}{1+\beta}. \quad (2.64)$$

It is worth noting that the calculation of the slips, bond stresses and strains requires the determination of the length corresponding to the region with a constant bond stress τ_2, which can be found by fixing slip s_2 at $x = L_C$ in Eq. (2.52):

$$L_C=\frac{\tan\left(\alpha_2\cdot L_{S,\max}\right)}{\alpha_3}\cdot\left(s_2\cdot\alpha_2-\frac{a}{\alpha_2}\right)+\frac{\gamma\cdot(\beta+1)}{\alpha_3\cdot\beta}-\frac{s_1\cdot\alpha_1}{\alpha_3\cdot\cos\left(\alpha_2\cdot L_{S,\max}\right)}. \quad (2.65)$$

Furthermore, the strength of the interface is reached at the end of this C-S-E state, i.e. when the last slip s_3 reaches the CFRP loaded end. In such case, and as already mentioned before, the maximum load can be determined from Eq. (2.30). However, the complete fracture energy (G_F), i.e. the area limited by the complete bond-slip model defined in (2.5), should be used instead of $G_{F,E}$, which leads to:

$$F_{E,\max}=b_{CFRP}\cdot\sqrt{2G_F\cdot E_{CFRP}\cdot t_{CFRP}\cdot(1+2\beta)} \quad (2.66)$$

where:

$$G_F = \frac{\tau_1 \cdot s_2}{2} + \frac{\tau_2 \cdot (2s_3 - s_2 - s_1)}{2}. \quad (2.67)$$

2.4.6. Solutions for the other post-peak states (D-C-S-E, D-C-S and D-C)

From the latter state on, the load decreases and the slip at the CFRP loaded end decreases as well. Since the bond length (L_b) is replaced by L_b - L_d, the solutions derived previously can be used on these states developed after the peak load (maximum strength of the CFRP-to-steel interface). Of course, each solution for each stage must be respected. The state D-C-S-E ends and the state D-C-S begins when the following equality is verified:

$$L_d = L_b - L_{S,\max} - L_{C,\max} \quad (2.68)$$

where $L_{C,\max}$ is the maximum length corresponding to a region where the bond length is under a constant bond stress. Also, the D-C-S state will end and the D-C state will initiate when:

$$L_d = L_b - L_{C,\max}. \quad (2.69)$$

During the last state, only a debonded region and another bonded area under a constant bond stress persist. Thus, the increase of the debonded length originates the decrease of the length L_C until zero and the equality stated in (2.69) becomes $L_d = L_b$, which means that the initial bond length is completely ruined. At this ultimate point, the strains in the CFRP laminate as well as the strain in the steel plate and the bond stresses are all zero. However, it is worth noting that from a theoretical point of view, the slips along the CFRP-to-steel interface have the same value s_3 at any point of the interface.

2.5 Experimental verifications

In this section, an analysis of the experimental results is developed. Complementarily, the closed-form solutions herein proposed are also reason for different comparisons made with the experiments. The validation of the proposed closed-form solution is shown through its capability and accuracy of predicting the debonding process of the experimental samples. For the simplicity of showing either the experimental or the analytical results, a restricted number of specimens were selected for presentation. Moreover, the results to be presented for each specimen followed a slip criterion shown by the 7 points marked in Figure 2.9b, i.e. approximately at one half of s_1 (Point 1), s_1 (Point 2), the average value between s_1 and s_2 (Point 3), s_2 (Point 4), the average value between s_2 and s_3 (Point 5), s_3 (Point 6) and the highest slip experimentally registered during the test s_{hst} (Point 7). Of course, depending on the conditions and specificity of the test, this criterion may not be fully accomplished and some points may not be shown due to the failure of the specimens at an earlier state.

2.5.1 Load-slip curves

Among other factors such as the interfacial bond-slip behaviour of the interface or the axial stiffness of the bonded materials, the bonded length influences the load-slip response of the CFRP-to-steel interface [62]. So, as the bonded length of an interface increases, the possibility of observing a plateau in the load-slip response increases as well and it is very well-defined, as long as the bonded length increases. In these circumstances, the post-peak behaviour of the interface shows a snap-back behaviour, e.g. [67-69]. However, for short bonded lengths, the strength of the interface is either reduced or the post-peak behaviour vanishes. From the experiments, the followed monotonic displacement only allowed the observation of this reduction in strength of the CFRP-to-steel interface (see Figure 2.9a) but the snap-back behaviour was not captured during the experiments because the slips at $x = 0$ do not have a monotonic trend [70, 71].

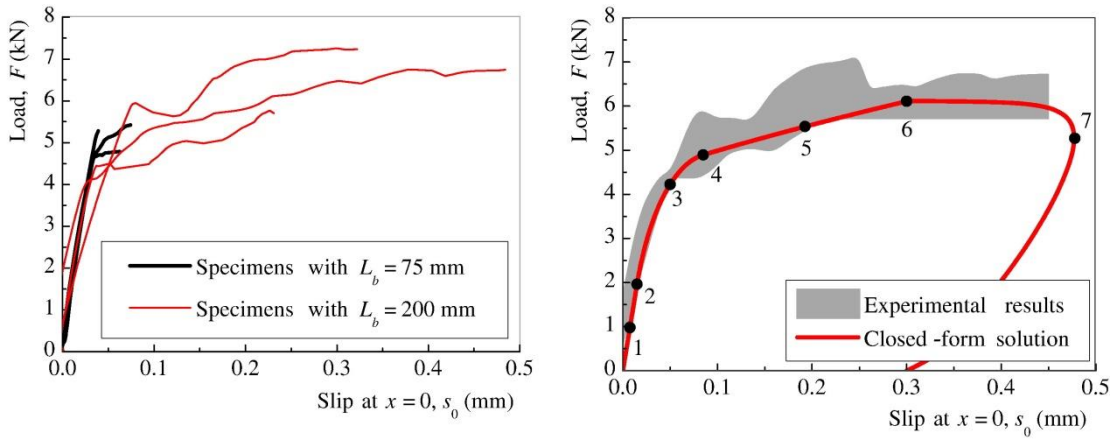

Figure 2.9 - Load-slip responses at the CFRP loaded end: (a) obtained from the experiments; and (b) comparison between the specimens with the longest bond length and the closed-form solution.

The load-slip responses either experimentally or analytically obtained from the specimens with the longest bond length (S-10-200a, S-10-200b and S-10-200c) are shown in Figure 2.8b, in which the gray area represents the range of values obtained experimentally, whereas the solid line corresponds to the closed-form solution. Also, satisfactory agreement of the closed-form solution with the experiments can be seen in Figure 2.8b.

2.5.2 Slip distributions

The experimental slip distributions along the CFRP-to-interface with different bonded lengths are shown in Figure 2.10. In the circumstances under analysis, the slip distributions show a significant increase at the CFRP loaded end as the load transmitted to the CFRP laminate increases. Unlike other experimental results reported in the literature (e.g. [18, 59, 72]), the

slips at the CFRP free end are almost zero and have a marginal influence on the final performance of the CFRP-to-interface because along that region of the bond length the bond stresses developed there should be almost zero as well, respecting, therefore, the initial Elastic stage of the bond-slip model.

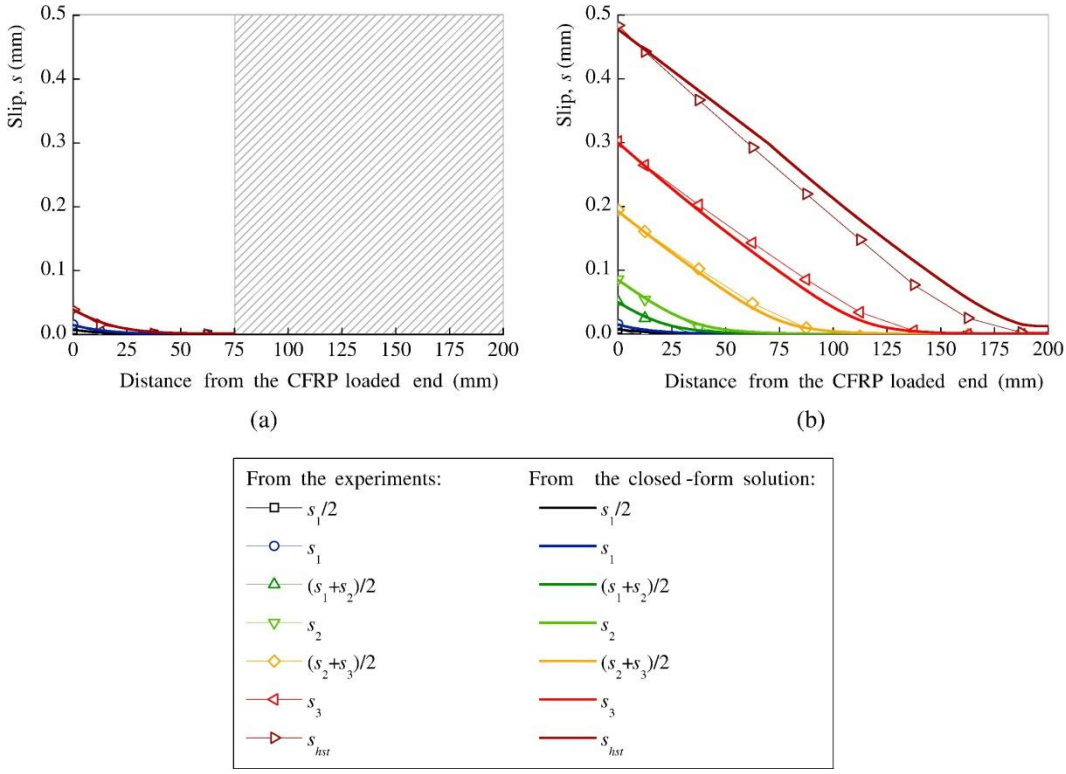

Figure 2.10 - Slip distributions at different states of the debonding process of the specimens: (a) S-10-75a; and (b) S-10-200b.

Regarding the comparison between the closed-form solution and the experimental results shown in Figure 2.10, it can be seen that the slips are quite accurately predicted for the range of values obtained for the specimens S-10-75a and S-10-200b.

2.5.3 Strains in the CFRP laminate

The characteristics of the strain distributions obtained from the double strap tests are quite different from those obtained from double-lap shear tests or double pull tests [73]. Unlike the strains obtained from double-lap or double pull tests, where the bonded region closest to the CFRP free end has almost no strains (the same for slips and bond stresses), in the present case, the equilibrium condition in (2.6) requires that in the double strap test, the strains in the CFRP laminate are not zero along the whole bond length except, of course, at the CFRP free end, where the strain is free of any mechanical deformation. Besides that, the strains in the CFRP laminates are always higher in the regions closest to the CFRP loaded end. When the CFRP begins to separate from the steel plate, the strain in the CFRP laminate is constant and then

decreases, remaining constant for a certain length and dropping to zero at $x = L_b$.

Figure 2.11 shows the strains at different slips (Points 1 to 7), obtained from the experiments where the strain characteristics described above can be seen. In particular, Figure 2.11b makes the comparison between the closed-form solution and the range of values obtained from one specimen with a bond length of 200 mm (S-10-200b). As shown in this particular figure, the accuracy of the closed-form solution is quite remarkable in all the seven points shown here.

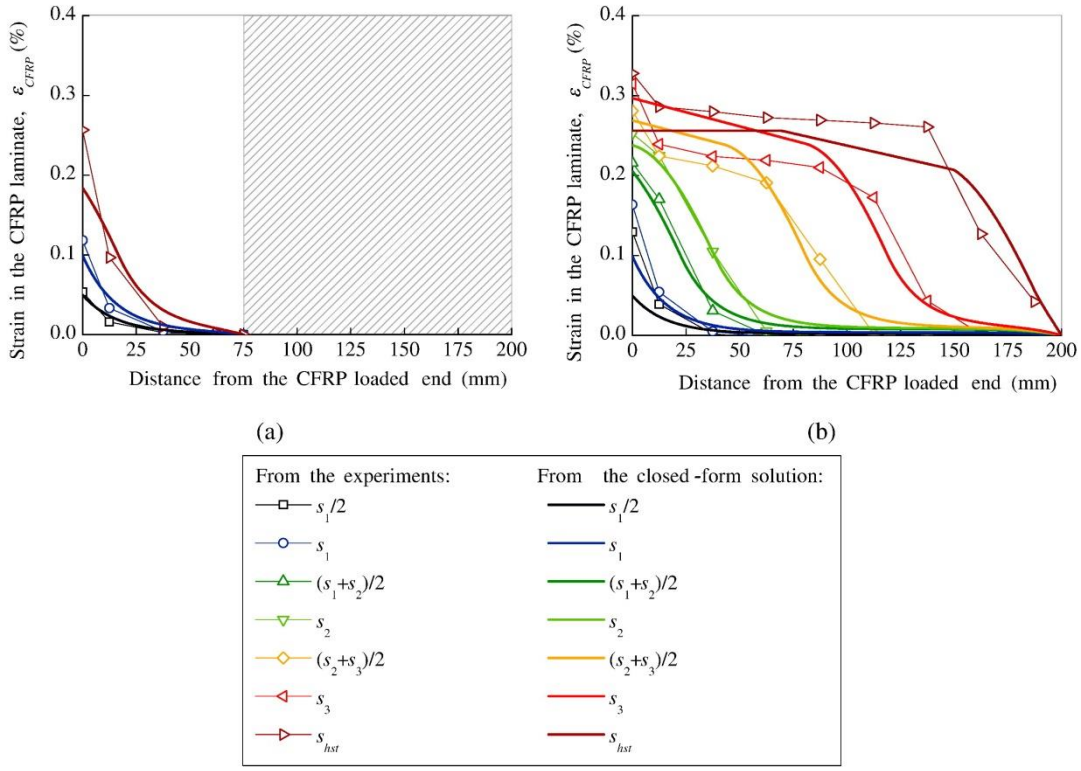

Figure 2.11 - Strain developed in the CFRP laminate at different states of the debonding process of the specimens: (a) S-10-75a; and (b) S-10-200b.

2.5.4 Bond stresses within the interface

The four stages previously defined in the bond-slip model should be seen in the specimens with the longest bond length. Therefore, as the load increases the bond stress at the CFRP loaded end also increases until a peak value is reached. Afterwards, this maximum value tends to migrate from the CFRP loaded end towards the CFRP free end. Along the region limited by the CFRP loaded end until the localization of the maximum bond stress, the values of the bond stresses tend to decrease (softened region). Close to failure, a constant bond stress seems to develop along a short length near the CFRP loaded end. However, all these characteristics cannot be seen in the samples with shorter bonded lengths. For instance, in the specimen chosen in Figure 2.12a, only the Elastic and the Softening stages could be predicted by the closed-form solution, whilst the experiments captured only the Elastic stage.

Regarding the closed-form solution, the range of values obtained from specimens S-10-75a and S-10-200b seemed to be quite well simulated despite the conditioning of the determination of the bond stresses already mentioned in Section 2.4.

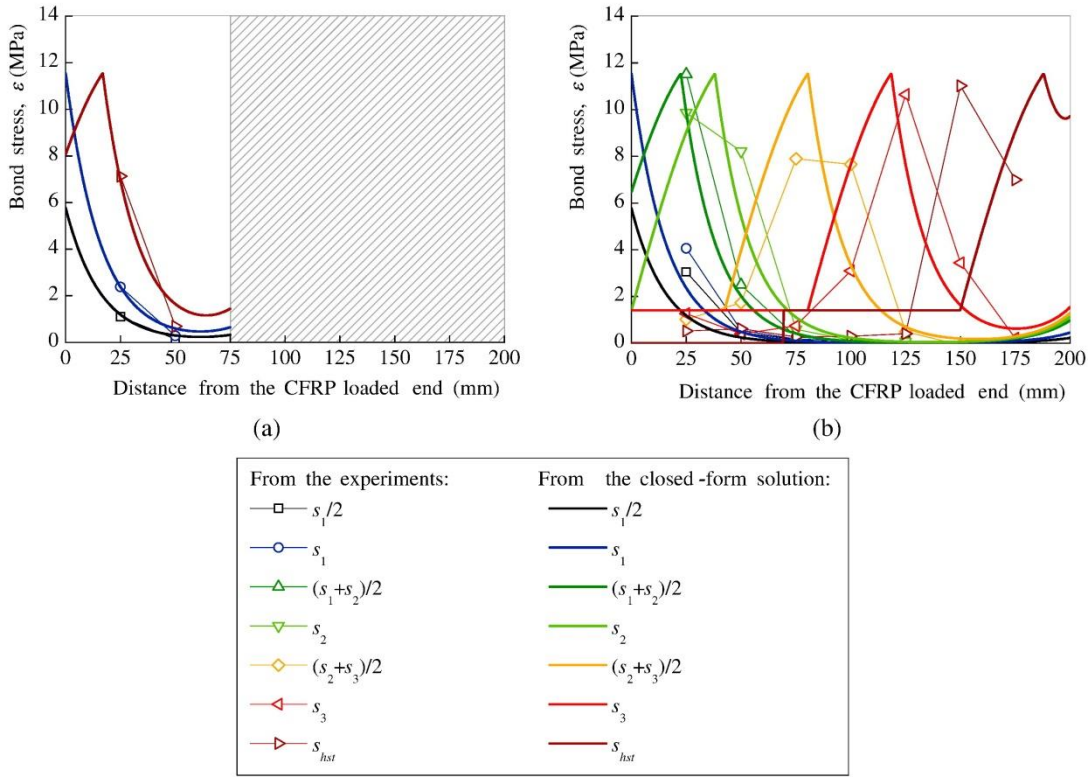

Figure 2.12 - Bond stresses developed along the bond length at different states of the debonding process of the specimens: (a) S-10-75a; and (b) S-10-200b.

2.5.5 Debonding loads and effective bond length

The determination of the effective bond length can be obtained from Figure 2.13, i.e. from a debonding load (or maximum load) vs. bond length graph. In this case, a trend line was obtained in order to predict the debonding loads for several bonded lengths with the least error possible. For this purpose, it was established that the sum of the quadratic differences between the experimental loads and the loads obtained from a trend line was found from the following minimization process:

$$\min_{F_{\max},L_{eff}} = \sum_{j=1}^{n}\left(\frac{F_{\exp,j}}{F_{pred,j}} - \beta_L\right)^2 \tag{2.70}$$

where $F_{exp,j}$ and $F_{pred,j}$ are, respectively, the maximum experimental and predicted loads obtained in the j^{th} sample; and

$$\beta_L = \begin{cases} \dfrac{L_b}{L_{eff}} \cdot \left(2 - \dfrac{L_b}{L_{eff}}\right) & \text{if} \quad \dfrac{F_{\exp}}{F_{pred}} < 1 \\ 1 & \text{if} \quad \dfrac{F_{\exp}}{F_{pred}} \geq 1 \end{cases} . \tag{2.71}$$

Parameter β_L is, in fact, a factor that affects the strength of an interface with a bonded length shorter than the effective bond length but, on the other hand, it assumes a unitary value if the bonded length is higher than the effective bond length.

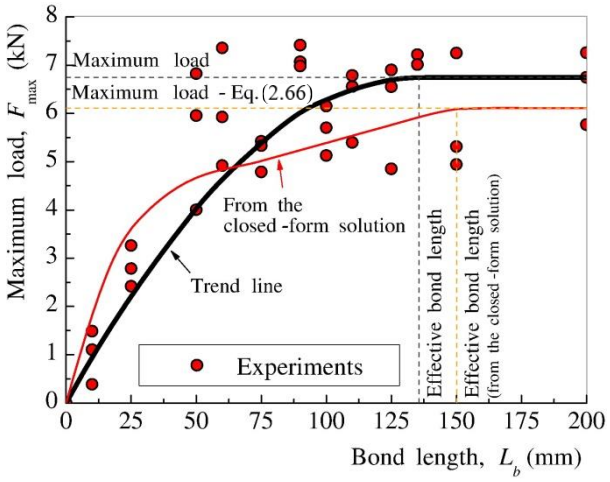

Figure 2.13 - Definition of the effective bond length through the debonding load vs. bond length relationship.

Thus, two variables are identified and are also estimated within this minimization procedure: (i) the debonding or maximum load F_{pred}; and (ii) the effective bond length, L_{eff}. At the same time, the proposal made by Neubauer and Rostásy [74] is assumed when the bonded length is pointedly shorter than the estimated effective bond length, as can be seen from the first line of Eq. (2.71). Figure 2.13 shows both the predicted maximum load and the effective bond length of the CFRP-to-steel interface as well as the results obtained from the closed-form solutions. From both predictions, the results show that the effective bond length and the maximum strength ranged from 135 mm to 150 mm and from 6.1 kN to 6.7 kN, respectively. Unlike the trend line which assumes a parabolic function for the representative samples with a bond length shorter than the effective bond length, the curve obtained from the closed-form solution shows four distinct paths. The first is linear and corresponds to those cases where only the Elastic stage of the bond-slip relationship develops within the interface. The second path is nonlinear and coincides with the development of a Softening region within the CFRP-to-steel interface. After this, and before the last path, where the maximum strength of the interface was defined as well as the effective bond length, another linear path is observed, due to the appearance of the Constant stage within the interface before the debonding failure.

2.6 Remarks

The aim of the present work was to characterize the bond behaviour of CFRP-to-steel plates by way of a series of double strap tests where the bonded length varied from 10 mm to 200 mm. The interfacial bond-slip behaviour was determined and a simplified tri-linear bond-slip model was proposed. Then, a simple yet accurate closed-form solution was proposed, based on the tri-linear bond-slip model. All the results were analyzed and discussed and the main conclusions achieved are as follows:

- The interfacial bond-slip behaviour of the CFRP-to-steel interface presented four distinct stages. In ascending order of slip: Elastic; Softening; Constant; and Debonded. The first is characterized by an increase of the bond stress with the slips in an almost linear way until a peak value is reached. The second stage is characterized by linear softening that ends when a constant bond stress starts to develop within the interface at a lower bond stress value when compared with the maximum value of bond stress. The last stage corresponds to the complete separation between materials, which is traduced by a zero bond stress transfer;
- All the failure modes observed in the tests were quite similar. In all the samples, an adhesive failure type between the CFRP laminate and the bonding agent was observed. Nevertheless, the failure modes also allowed small quantities of resin bonded to the surface of the CFRP laminate to be observed. It should also be noted that rupture or cracking of the bonding agent was never observed;
- The closed-form solution herein proposed has some versatility due to its tri-linear based definition, i.e. it can be used in other cases (unless there are other specificities not included in this closed-form solution), where the interfacial bond-slip behaviour can be approximated to other shapes namely the bi-linear, rigid with linear softening, elastic-plastic, rigid with linear softening followed by a constant stage, etc. For this purpose, the corresponding values in each stage should be refined in order to reproduce, if only approximately, the shapes of these bond-slip models;
- The closed-form solutions provide a valuable contribution to the prediction of the debonding failure of the CFRP-to-steel interface. Despite their simple derivation and hypotheses, the conjunction of equations derived here can be easily implemented in standards or rules, helping designers to predict the interface strength and to understand the failure process of bonded joints between an FRP composite and steel;
- Unlike double pull tests or double-lap shear tests, the slips, the strains and the bond stresses developed along the bonded length have different characteristics. For instance, the slips and

the bond stresses developed at the CFRP free end are not zero. Depending on the value of the axial stiffness ratio, these differences can be significant. In the present case, this was not quite so relevant since the value of the axial stiffness ratio was low, $\beta = 0.039$;

- The effective bond length of the interface was also defined. Based on the experiments carried out in the present work, the effective bond length of the CFRP-to-steel interface may range between 135 mm and 150 mm.

2.7 Summary of this chapter

In this chapter, the work done on bond characteristics of CFRP-to-steel joints in pull-pull loaded conditions is presented (see the illustration of the bond reponse of CFRP-to-steel double strap bonded joints, in Figure 2.14). Monotonic loading of the double strap joints with different bond lengths was applied and the failure modes and interfacial bond-slip curves were obtained. A tri-linear bond slip model is proposed, derived from experimental data. A closed-form solution approach is also proposed based on the tri-linear bond-slip model.

The strength of the CFRP-to-steel interface (Table 2.2), the distribution of the relative displacements (Figure 2.10) between bonded materials, the strains (Figure 2.11) developed in the CFRP laminate and the bond stresses along the interface (Figure 2.12) are reported and the closed-form solution is compared with the experimental results (Figure 2.10-2.12).

Two cases are selected for presentation: (i) one with a bond length greater than the effective bond length; and, inversely, (ii) one with a bond length shorter than the effective bond length. The results predicted by the closed-form solutions are shown to be accurate enough when compared to the experiments. The effective bond lengths of CFRP-to-steel double strap bonded joints defined by experiments and closed-form solution are compared, as illusrated in Figure 2.13.

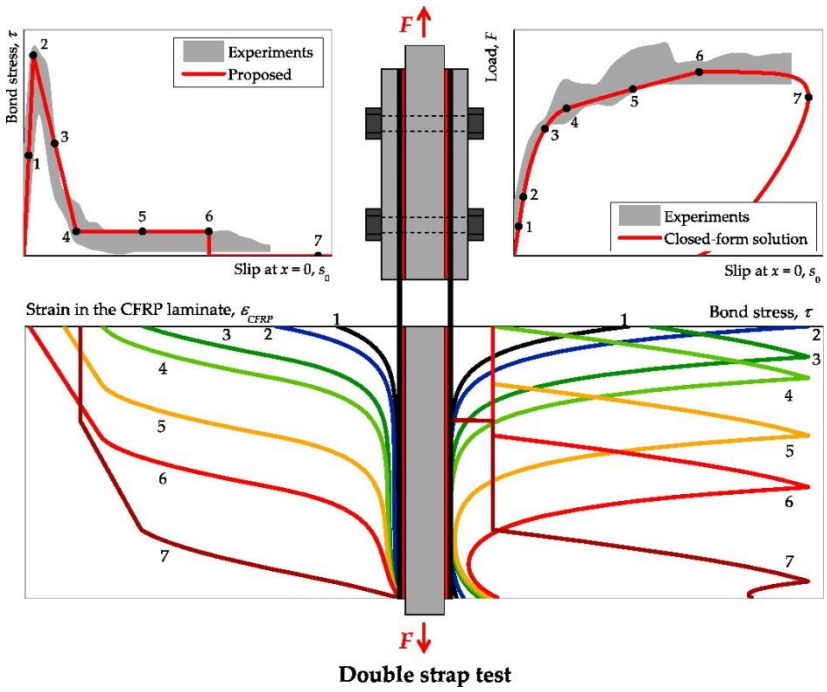

Figure 2.14 - Illustration of the bond reponse of CFRP-to-steel double strap bonded joi

Chapter 3

CFRP-to-steel bonded joints subjected to cyclic loading：An experimental study

3.1 Introduction

Recent research addressed the problem of steel structures externally strengthened with Carbon FRP (CFRP) composites, namely examining the response of CFRP-to-steel bonded joints subjected to mechanical loading [49], but notwithstanding such and similar efforts the number of studies is still scarce, especially for cyclic loading that frequently acts on rehabilitated structures [75] as is the case of earthquake loading (few cycles of high amplitude), traffic on bridges or viaducts (fatigue load) and temperature variation (high-cycles under low loading amplitude). Concurrently, there are numerous steel bridges that require rehabilitation worldwide [1-5] e.g. due to inadequate maintenance, corrosion and increase of traffic volume, being possible their strengthening by using CFRP composites [11]. Systematic research on the performance of CFRP-to-concrete joints shed some light on the topic, but generalization to CFRP-to-steel joints is difficult due to the recognized differences posed by steel [76], failures being absent in the substrate case in the latter bonded joints.

However, a brief review of CFRP-to-concrete joints subjected to cyclic loading shows that: (i) low cyclic loads do not influence the bond capacity of the joints, if the residual bond length, i.e. the length measured excluding the damaged area due to cyclic loading near the loaded end, is longer than the effective bond length; and (ii) the behavior of the bonded interface is closely related to the cyclic maximum load. Studies of creep-fatigue report tests on FRP-to-concrete double-lap shear specimens for Mode-II fatigue loading with maximum load varying from 30% to 80% of the static bond capacity can be found in the literature, e.g. [77]. The model used by Diab et al. [77] assumed the degradation of stiffness and strength of the interface before debonding started, keeping the fracture energy constant since earlier findings established that

the post-fatigue static capacity is not affected if the residual bond length is sufficiently long. The results indicated that the debonding growth rate along the interfaces decreased with the number of fatigue cycles and that 30% of the static bond capacity of the FRP-concrete interface could be considered the endurance limit of fatigue loading for FRP-strengthened beams since no debonding occurred under this load level after 2,000,000 cycles. In addition, 50% of the static ultimate capacity could be considered as the fatigue threshold value, seeing that no failure occurred at this load level after 3,000,000 cycles. The authors [77] concluded that for the bonded lengths considered, the fatigue life of FRP-concrete interfaces increased.

Nigro et al. [78] performed a series of single shear tests under both monotonic and cyclic loadings and three different bonded lengths, respectively, higher, about equal to, and lower than the calculated effective bond length. The results showed that the reduction in bond length up to one half the theoretical effective bond length induced a comparable reduction in the maximum debonding load both for monotonic and cyclic action. For load-unload cycles up to 70% of the static monotonic ultimate load, the influence on the bond stiffness and strength was negligible, whereas for a loading of 90% of the static monotonic capacity forty cycles were sufficient to induce a reduction in peak shear.

Bizindavyi et al. [79] also found that the fatigue life increased with the FRP bonded length. Still for concrete as the main adherend, a number of experimental and theoretical studies showed that the stiffness of the bond load-slip decreased with the number of cycles [77-82]. As mentioned before, there are few publications on CFRP-to-steel joints subjected to cyclic or fatigue loads. Nevertheless, full-scale steel beams strengthened with CFRP composites under fatigue exist; in particular, Kamruzzaman et al. [39] present a review on which CFRP debonding failure was the primary failure mode and showed that the fatigue properties of steel beams are improved by using CFRP reinforcement**.** The numerous recommendations for future research presented in this review confirm that many questions remain unsolved and FRP-to-steel joints under fatigue loading require further studies. Liu et al. [20] reported tests on both normal modulus (240 GPa) and high modulus (640 GPa) CFRP double strapped bonded steel plate joints subjected to fatigue loading and found that there is no fatigue failure for a maximum applied load less than 40% of the ultimate static strength. For a maximum applied load less than approximately 35% of the ultimate static strength, the influence on the bond strength was below 10%.

Wu et al. [21] performed a series of static and fatigue tests on UHM CFRP laminate and steel plate double strap joints testing specimens under fatigue loading with load ratios of the maximum fatigue load to the average static bond strength of control specimens between 0.2 and 0.6. After a selected number of fatigue cycles, the specimens were tensioned to failure under static loading. The failure modes, residual bond strength and residual bond stiffness of such

specimens were compared with those of the control specimens. It was found that fatigue loading introduced damage restricted to a very small zone close to the loaded end, which was called "fatigue damage zone", and 99% of the bond-line remained intact, i.e. the bond behavior was not much affected.

Colombi et al. [19] equally performed fatigue tests on CFRP-to-steel double-strap bonded joints and found that the stiffness of the joints decreased with fatigue load due to progressive debonding of the CFRP strips, serving as an indicator for the subsequent progressive global failure. Crack initiation was associated with a stiffness reduction to 98%, quicker debonding when stiffness reduced to 95% and final sudden failure when the stiffness dropped to 90% of the initial value.

A bond-slip model for FRP-to-steel interfaces subjected to cyclic loading is a key element in fatigue life prediction of FRP-strengthened steel structures [48]. In this study, some CFRP-to-steel bonded joints were tested under monotonic, pseudo-cyclic and cyclic loadings, and the CFRP-to-steel interfacial bond-slip curves were obtained and systematically compared. Furthermore, an estimate of bond fatigue characteristics was conducted based on bond-slip curves obtained with a limited number of cycles. The damage analysis of the CFRP-to-steel bonded interface was carried out considering local and global points of view, which also allowed to compare and correlate them.

3.2 Experimental program

3.2.1 Materials

In present studies, two kinds of pultruded CFRP laminates were used; one was produced at Harbin Institute of Technology (HIT) laboratory, hereafter designated as HIT CFRP; another one were same as adopted in the chapter 2, i.e., the CFRP laminates acquired from the local industry in Lisbon and designated as SIKA CFRP hereafter. The HIT CFRP laminates had a cross-sectional area of 20×1.46 mm^2. The SIKA CFRP laminates had a cross-sectional area of 20×1.26 mm^2, which differs with that in chapter 2 (in that case with 10×1.26 mm^2) though the same CFRP laminates were adopted.

The adhesive (Sikadur-30) and steel materials adopted here are the same as in chapter 2.

In the following, the measurement methods to obtain the mechanical properties of materials (CFRP laminates, adhesive and steel) are described and more data on mechanical properties are presented here, though some data on the mechanical properties of SIKA CFRP laminates, adhesive and steel were already listed in a table in Chapter 2.

The mechanical properties of the two kinds of CFRP laminates, HIT and SIKA, were obtained

according to standard ASTM D 3039 [50]. Based on ten HIT CFRP laminate coupon tests, the mean tensile modulus, tensile strength and ultimate strain were, respectively, 180.5 GPa with a coefficient of variation (COV) of 2.5%, 1,824 MPa with COV = 4.1% and 1.00% with COV = 5.1%. Also based on the test of five CFRP coupons from SIKA laminates, the mean tensile modulus, tensile strength and ultimate strain were, respectively, 163.3 GPa with COV = 4.2%, 1,836 MPa with COV = 2.8% and 1.13% with COV = 9.6%. All adhesive coupons used for tensile tests were made by pouring the homogeneous mixture into stainless steel molds, cured for 2 weeks at ambient temperature and tested according to ISO527-2-1993 [51]. Based on four adhesive coupon tensile tests, the mean tensile modulus, tensile strength and ultimate strain of the adhesive were 8.4 GPa with COV = 3.0%, 21.76 MPa with COV = 7.64% and 0.33% with COV = 12.5%, respectively. The mild steel plates used in the samples had a rectangular cross-section with thickness of 5 mm and width of 50 mm. The mechanical properties of the steel used in this study were assumed the same as those provided by the local steel supplier, whose measurements followed the standard EN10025:2004 [52]. Therefore, the mean tensile modulus, tensile strength and yield strength of the steel are 210.0 GPa, 540 MPa and 400 MPa, respectively.

Table 2.1 - Material properties of the CFRP laminate, adhesive and steel.

Materials	Tensile modulus E (MPa)	Tensile strength σ_{max} (MPa)	Yield strength σ_y (MPa)	Ultimate strain, ε_u (%)
SIKA laminate	163,300	1840	N/A	1.13
SIKA-30 adhesive	8432	21.76	N/A	0.34
Steel	210,000	540	400	N/A

3.2.2 Geometry of the samples

The schematic view of double strap CFRP-to-steel bonded joints adopted in the present experimental study is shown in Figure 3.1, where their geometry is defined. To ensure that the samples had a sufficient long bond length, i.e. a bond length longer than the effective bond length, a bonded length of 150 mm was chosen, which, according to Wu et al.'s model [57], is longer than the effective bond length as it will be evaluated and discussed in the subsequent section. Strain gauges with a length of 5 mm were mounted on the top surface of the CFRP laminate, as also shown in Figure 3.1. The strain gauges at the extreme locations were bonded at 5 mm of the CFRP loaded or free ends whereas the strain gauges nearer to each of those were bonded at 20 mm. The remaining intermediate gauges were 25 mm spaced apart. A data logger was used to collect the axial strains developed throughout the CFRP laminate during the test.

The importance of surface treatment to enhance the behavior of bond is known, e.g. [15], and

the surfaces of the steel plates were prepared by grit-blasting, dust removing and cleaning with acetone to eliminate grease and other contaminants prior to bonding of the adherends. For greater consistency of the specimens to be tested, two plastic bars with 2.26 mm of thickness for SIKA material and 2.46 mm for HIT material, were used so that the adhesive layer had a uniform thickness of 1.00 mm. The specimens were cured at room temperature (~25ºC) for 2 weeks prior to testing.

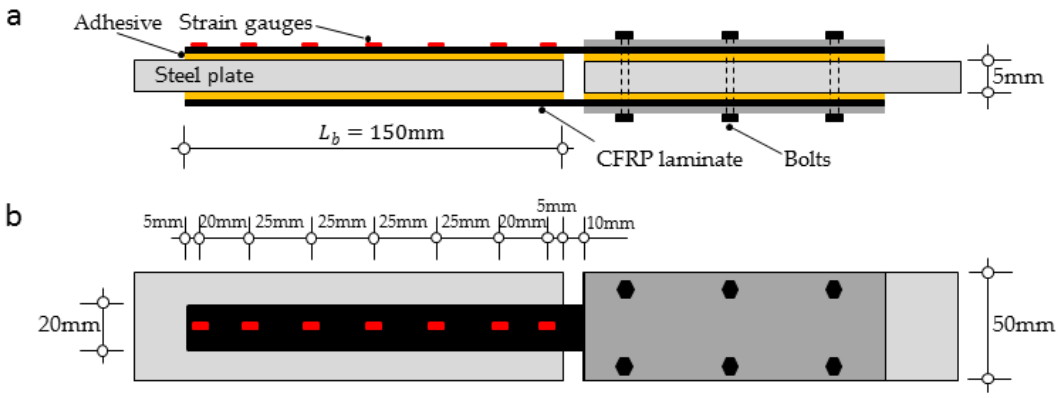

Figure 3.1 - CFRP-to-steel bonded joints: (a) side view; and (b) front view.

A total of eighteen CFRP-to-steel bonded joints were made, nine of which were produced with HIT CFRP laminates and the other nine with SIKA CFRP laminates. Three specimens were prepared per loading type considered (monotonic, pseudo-cyclic, and cyclic). Given that the six specimens tested under cyclic loading did not fail until the end of the load history scheduled, those specimens were subjected after that to monotonic loading until rupture (monotonic after cyclic). Table 3.1 presents the CFRP-to-steel bonded joints tested, the type of loading, the failure load and the corresponding mode of failure obtained in the twenty-four tests performed. The designations of specimens used are listed in Table 3.1, where "X-Y-n" indicates X the type of CFRP (H = Harbin, S = SIKA), Y the type of loading (M = Monotonic, PC = Pseudo-cyclic, C = Cyclic, CM = Monotonic applied after cyclic test) and n is a sequential ID number in each class of tests, i.e. H-PC-03 refers to specimen 3, made with HIT CFRP and subjected to pseudo-cyclic loading, and S-M-01 designates specimen 1, SIKA and monotonic loading.

3.2.3 Estimation of the effective bond length

Some expressions can be been found in the literature [15, 16, 57] suggesting how to estimate the effective bond length. The proposal made by Wu et al. [57] is followed hereafter and in the basis of this formulation the interfacial bond-slip model has a bi-linear shape. Hence, the determination of the effective bond length can be predicted according to:

$$L_{eff} = \frac{1}{\gamma_1} \cdot \operatorname{acosh}\left[\frac{2\beta \cdot \left(0.97^2 + \sqrt{0.97^4 + (1-0.97^2)\cdot(\beta^2 - 0.97^2)}\right)}{(1-0.97^2)}\right] + \frac{1}{\gamma_2} \cdot \operatorname{atan}\left(\frac{\gamma_1}{\gamma_2}\right) \quad (3.1)$$

where the parameter β is the axial stiffness ratio defined as:

$$\beta = \frac{b_{CFRP} \cdot E_{CFRP} \cdot t_{CFRP}}{b_{steel} \cdot E_{steel} \cdot t_{steel}} \quad (3.2)$$

and

$${\gamma_1}^2 = \frac{\tau_1}{s_{max}} \cdot \gamma^2 \quad (3.3.a)$$

$${\gamma_2}^2 = \frac{\tau_1}{s_{ult} - s_{max}} \cdot \gamma^2 \quad (3.3.b)$$

where t_{CFRP}, b_{CFRP} and b_{steel}, t_{steel} are the thickness and the width of the CFRP laminate and steel plate, respectively; E_{CFRP} and E_{steel} are the tensile modulus of the CFRP laminate and the steel plate, respectively; τ_1 and s_{max} are, respectively, the maximum bond stress and the corresponding slip value; s_{ult} is the ultimate slip, i.e. the slip beyond which the CFRP laminate completely detaches from the steel plate and no further bond stresses are transferred between materials; and

$$\gamma^2 = \frac{1}{E_{CFRP} \cdot t_{CFRP}} - \frac{2 \cdot b_{CFRP}}{E_{steel} \cdot b_{steel} \cdot t_{steel}} \quad (3.4)$$

Table 3.1 - CFRP-to-steel bonded joints tested and ultimate load.

CFRP materials	Specimen	Loading type	Number of cycles	Failure Load F (kN)	Avg. Failure Loads (kN)	Failure mode
HIT	H-M-01	Monotonic	-	16.20	17.00	C
HIT	H-M-02		-	17.90		
HIT	H-M-03		-	16.89		
HIT	H-PC-01	Pseudo-cyclic	21	18.19	17.78	C
HIT	H-PC-02		18	16.77		
HIT	H-PC-03		21	18.40		
HIT	H-C-01	Cyclic	600	N/A	N/A	No Failure
HIT	H-C-02		600	N/A		
HIT	H-C-03		600	N/A		
HIT	H-CM-01	Monotonic after cyclic	-	16.49	17.03	C
HIT	H-CM-02		-	17.51		
HIT	H-CM-03		-	17.07		
SIKA	S-M-01	Monotonic	-	12.00	12.57	A+C
SIKA	S-M-02		-	13.70		
SIKA	S-M-03		-	12.00		
SIKA	S-PC-01	Pseudo-cyclic	16	12.59	11.94	A+C
SIKA	S-PC-02		16	11.60		
SIKA	S-PC-03		16	11.64		
SIKA	S-C-01	Cyclic	600	N/A	N/A	No Failure
SIKA	S-C-02		600	N/A		
SIKA	S-C-03		1000	N/A		
SIKA	S-CM-01	Monotonic after cyclic	-	12.96	12.76	A+C
SIKA	S-CM-02		-	12.22		
SIKA	S-CM-03		-	13.10		

Note 1: C means that the rupture occurred inside the adhesive (Cohesive failure); A means that it occurred within the interface between CFRP and adhesive (Adhesive failure).

Note 2: The failure load, F, in this table corresponds to the load transmitted to one single CFRP laminate

Based on a study carried out by Biscaia et al [42] with CFRP laminates externally bonded to steel, the effective bond length was initially estimated by assuming the following parameters needed to define the bi-linear bond-slip relationship: s_{max} = 0.096 mm, τ_1 = 13.27 MPa and, s_{ult} = 0.256 mm. The axial stiffness ratios for the HIT and SIKA CFRP joints were β_{HIT} = 4.98 and β_{SIKA} = 6.38. Although the definition of the bond-slip relationship may be affected by the surface conditions, type of adhesive agent, thickness of adhesive or the type of FRP laminate, by adopting these parameters it was possible to estimate effective bond lengths of 133 mm and 119 mm for HIT and SIKA joints, respectively. Therefore, to ensure that the current specimens would have a sufficiently long bond length and the complete bond-slip relationship could be obtained, a bonded length of 150 mm was adopted for all the samples.

3.2.4 Load history and test set up

The specimens were subjected to different loading types - monotonic, pseudo-cyclic, cyclic, and monotonic after cyclic - having been used for each loading type, three HIT and three SIKA CFRP joints. Pseudo-cyclic loading is defined in Figure 3.2a showing a finite sequence of sets of three cycles of the same amplitude each, and each set was followed by another one with larger amplitude. The average value of maximum monotonic load was defined as the reference load, F_{ref}; the normalized loading force was calculated by F/F_{ref}, where F is the loading force. All cycles started at zero load and the number of sets of three cycles applied until the previously obtained ultimate monotonic capacity was exceeded. The cyclic loading as shown in Figure 3.2b, was chosen with the purpose of attempting to examine the bond response of joints subjected to repeated loading. The results obtained as shown in the following meet the expectation, though the number of cycles is not high compared with fatigue tests, due mainly to two causes. One cause is the limitation of the available equipment, and the other one is the absence of expectation of different results for a feasible increase of number of tests.

The pseudo-cyclic tests were run in order to find, in an expedite manner, the levels beyond which there was damage accumulation and to record data on the stress strain paths of loading-unloading.

All the tests, i.e. monotonic, pseudo-cyclic, cyclic, and monotonic after cyclic tests, were performed with a Zwick 50 kN tensile machine as shown through Figure 3.3. The rate of application of the tensile force corresponded to a displacement of 1 mm/min.

3.3 Results and discussion

3.3.1 Load-slip curves

The curves of external load vs. slip at the CFRP loaded end, both for monotonic and pseudo-cyclic loading are shown in Figure 3.4. As shown, the envelope at the loaded end for the specimens tested under the pseudo-cyclic loading history can be traced from the monotonic response, e.g. in Figure 3.4a for HIT bonded joints and in Figure 3.4b for SIKA bonded joints. Similar results were also reported by Ko et al. [82] for CFRP-to-concrete in the case of force-deformation curves of the bonded joints.

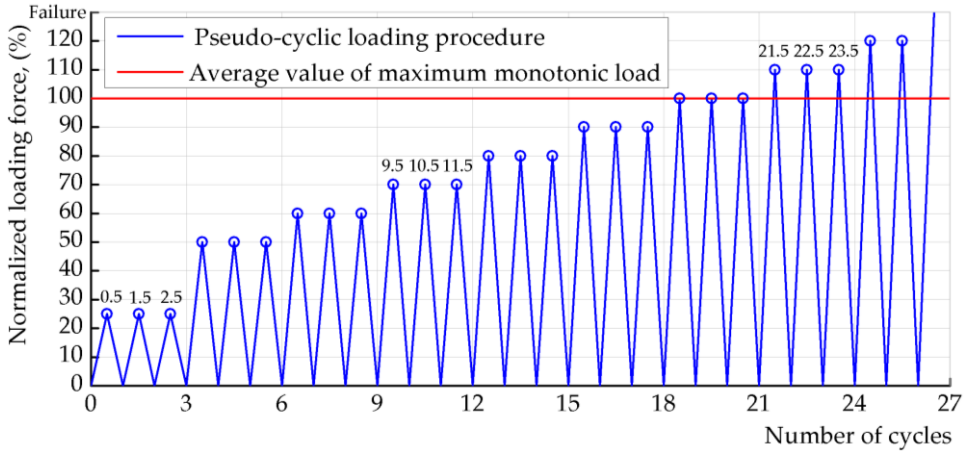

(a)

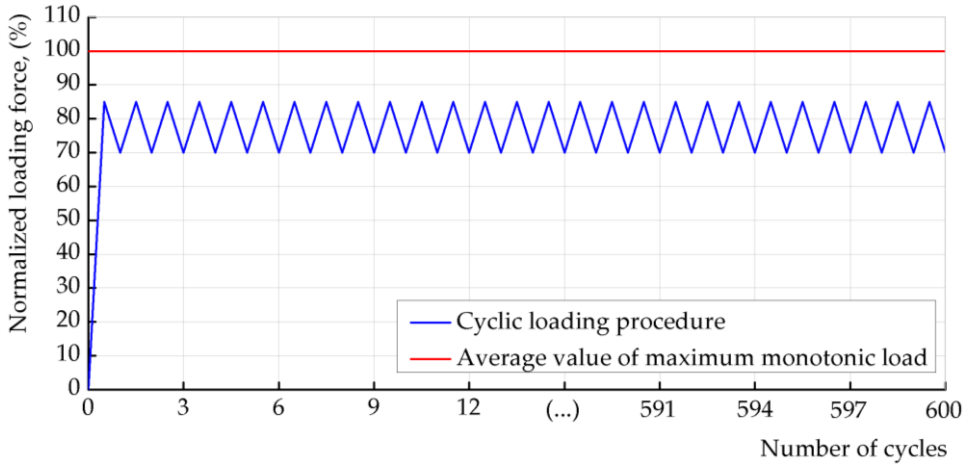

(b)

Figure 3.2 - Definition of: (a) pseudo cyclic; and (b) cyclic loading.

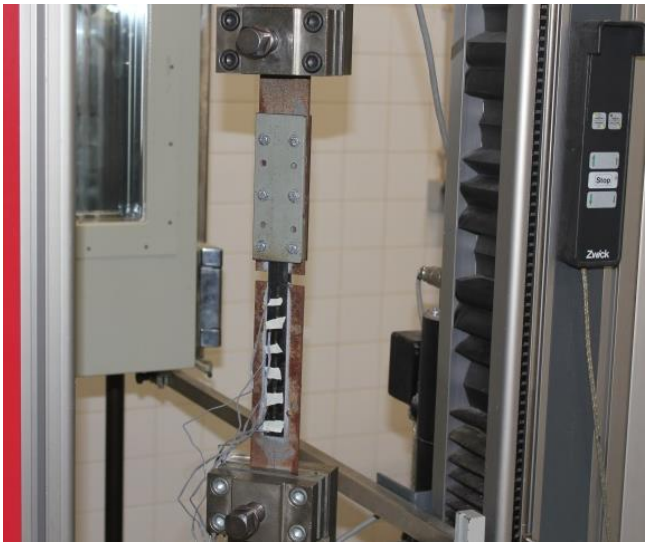

Figure 3.3- Overview of the test setup.

In every comparison of load vs. slip, the pseudo-cyclic curves and monotonic curves are similar for the first several cycles, presenting the same stiffness; at a later stage the degradation of stiffness at the loaded end became more evident with the number of cycles. This degradation of stiffness is attributed to the deterioration of bond around the loaded end, which increases with more cycles and larger load amplitude.

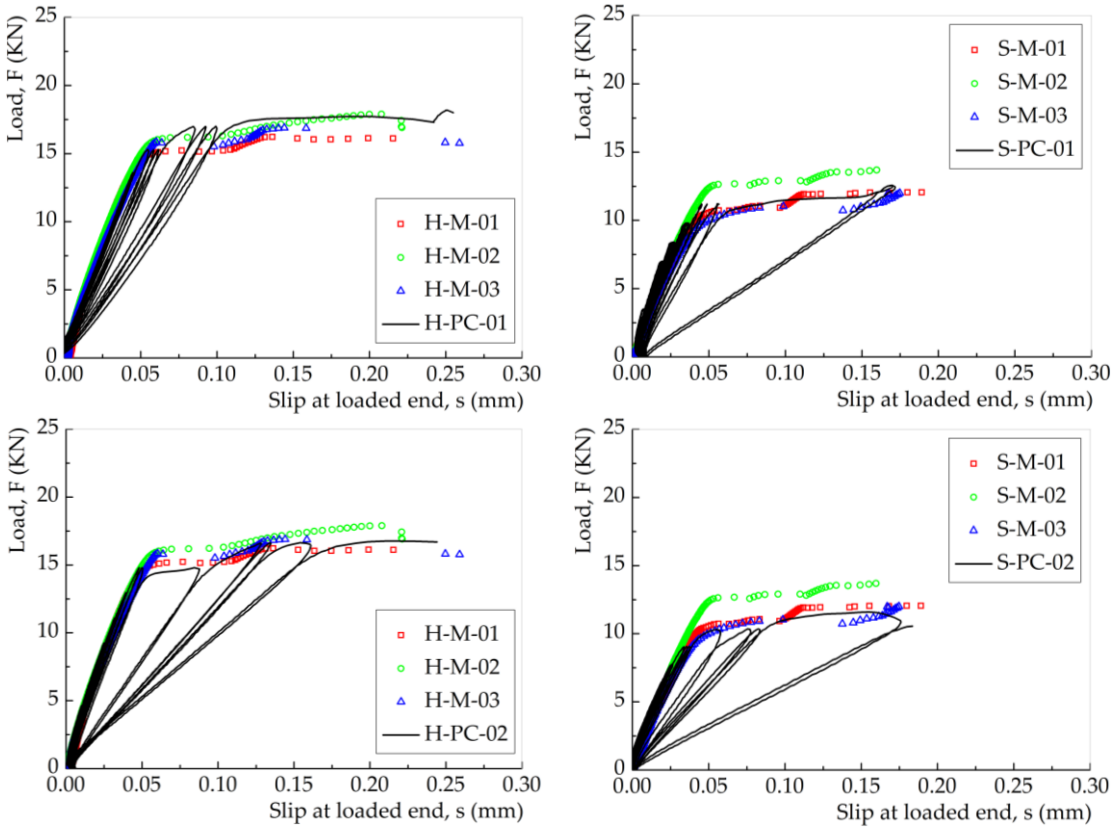

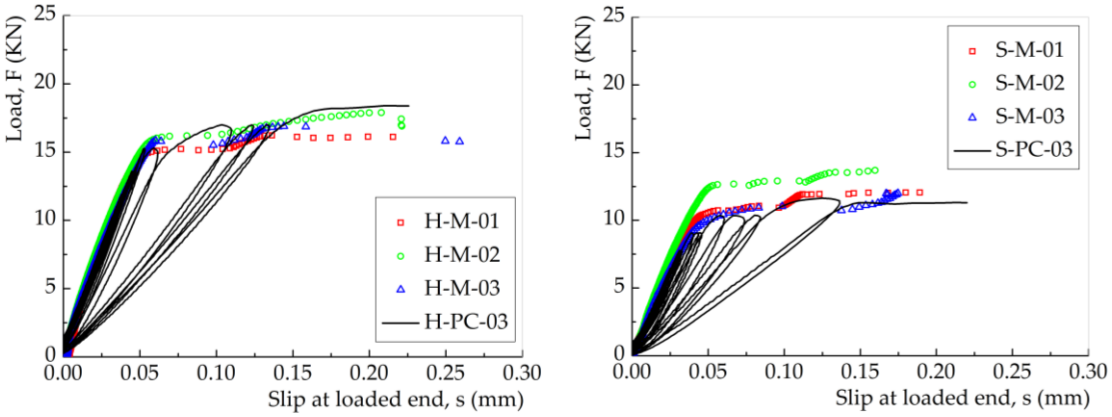

(a) (b)

Figure 3.4 - Load-slip at the loaded end for: (a) HIT; and (b) SIKA bonded joints.

In order to obtain a closer view on the bond response of the CFRP-to-steel joints under loading cycles at a higher maximum load and with a high number of cycles, 600 cycles were chosen and applied to the bonded joints with the exception of specimen S-C-03 where 1,000 cycles were carried out.. The long time period needed to carry out each test caused some failure on the data acquisition during the tests of three specimens which did not allow to record the strains provided from the strain gauges bonded throughout the bonded length. For this reason, the load vs. slip curves of samples H-C-03, H-CM-03, H-CM-01 and S-CM-01 are not shown here. For the same reason, the corresponding bond vs. slip curves presented in the next subsection couldn't be herein presented as well.

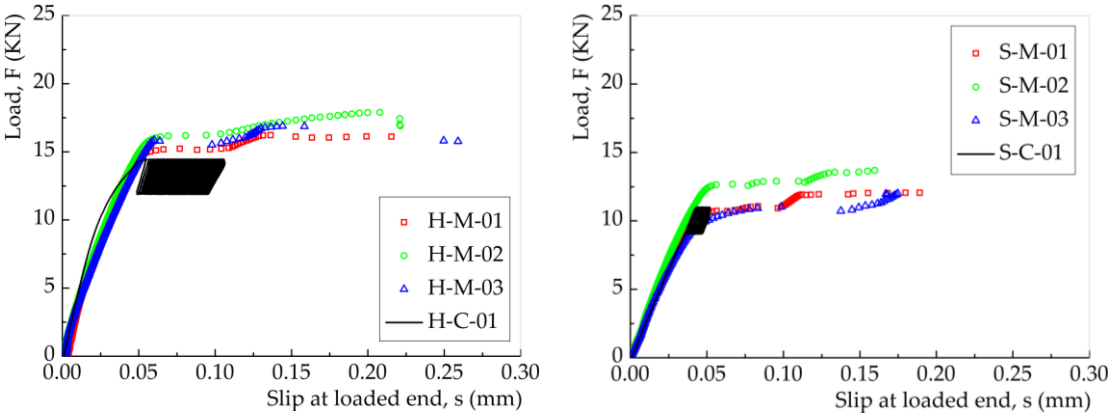

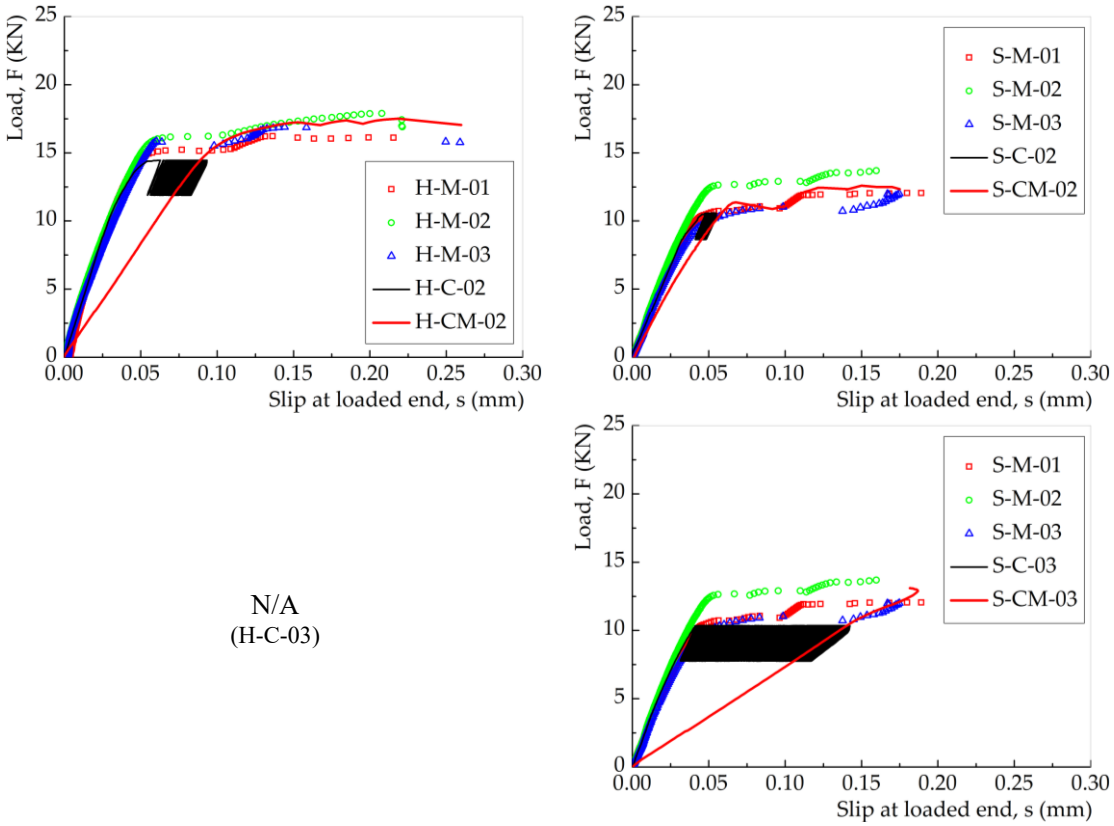

Figure 3.5 - Load vs. slip at the loaded end: (a) HIT; and (b) SIKA bonded joints.

Still, for the available data, Figure 3.5 makes the comparison between the load-slip behavior obtained from the cyclic tests with the monotonic ones (before and after cyclic loading). Particularly, Figure 3.5a shows the results obtained with the CFRP laminates from HIT whereas Figure 3.5b shows the results obtained from the samples where the CFRP from SIKA supplier was used. From the load-slip response it can be seen that the cycles caused a gradual reduction to the stiffness of the bonded joints, which is in accordance to what has been reported in another study available in the literature [20].

It is also clear that the stiffness of the monotonic load-slip response of the specimens previously subjected to the cyclic loading history almost followed the same stiffness obtained at the end of the loading cycles. Therefore, the results obtained from specimens H-CM-02, S-CM-02 and S-CM-03 indicate that the damage induced to those bonded interfaces due to the cyclic tests was irrecoverable.

3.3.2 Failure modes and load carrying capacity

Results obtained in addition to those summarized in Table 3.1 are shown next. Table 3.1 also correlates the failure modes of all adhesively bonded joints to acronyms explained earlier. Failure modes are closely related to the materials used and typical situations are illustrated in Figure 3.6. Cohesive failure mode within the adhesive is seen in specimens H-M-01, H-PC-03

and H-CM-02 whereas a hybrid failure mode (i.e., A+C accordingly to the definition in Table 3.1) could be observed from specimens S-M-01, S-PC-02 and S-CM-02. The failure modes are not directly associated with the loading history. Joints with HIT CFRP laminates, where cohesive failure took place in the adhesive indicated good bond properties in the interface between steel or CFRP and the adhesive layer, whereas for SIKA CFRP laminates, mixed failure mode indicated that the interface between CFRP and adhesive was not so strong.

It was found that HIT bonded joints have larger maximum load capacity than SIKA bonded joints, as detailed in Table 3.1, namely, with average capacities of 17.0 kN and 12.9 kN, respectively, for monotonic loading. The causes are presumably the different bond strengths and to a smaller degree, elastic modulus and thickness of laminates. The strength capacity of each type of joint differed only slightly between the different loading types applied - monotonic, pseudo-cyclic and monotonic after cyclic loading, which can be attributed to a longer residual bond length than the effective bond length. The residual bond length is defined as the length measured excluding the damaged area due to cyclic loading near the loaded end. Detailed analysis of the damage near the loaded end under pseudo-cyclic and cyclic loading will be shown in the following section.

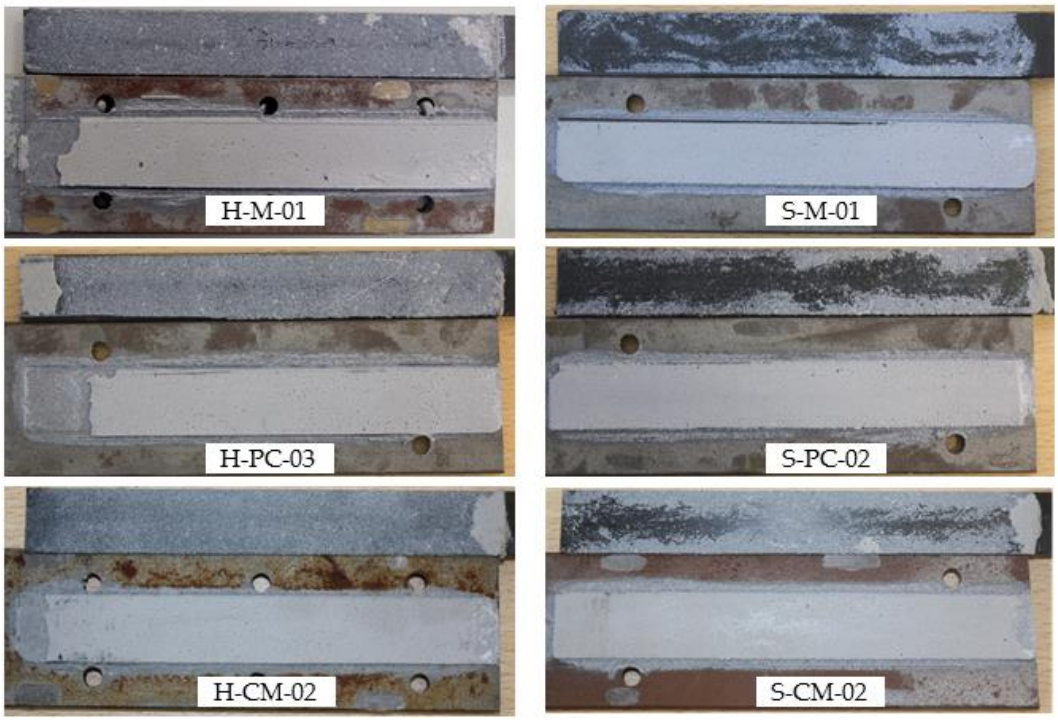

Figure 3.6 - Some specimens after failure – cohesive in adhesive or hybrid in adhesive and CFRP-to-adhesive interface.

3.3.3 Bond-slip curves

Strain gauges bonded onto the CFRP laminate were used to generate data from which the interfacial bond-slip relationship was found. The bond stresses developed within the interface were calculated by assuming that the bond stress is constant between two consecutive strain gauges and the following expression was used:

$$\tau(x_{i+1/2}) = E_{CFRP} \cdot t_{CFRP} \frac{\varepsilon_{CFRP,i+1} - \varepsilon_{CFRP,i}}{x_{i+1} - x_i} \quad (3.5)$$

where $\varepsilon_{CFRP,i+1}$ and $\varepsilon_{CFRP,i}$ are, respectively, the strains in the CFRP laminate at points x_{i+1} and x_i. The relative displacement between the CFRP and the steel plate allows the determination of the slip in the interface which can be determined as

$$s(x) = u_{CFRP}(x) - u_{steel}(x) \quad (3.6)$$

where $u_{CFRP}(x)$ and $u_{steel}(x)$ are the displacements in the CFRP laminate and in the steel plate, respectively. The first derivative with respect to x of Eq. (3.6) is:

$$\frac{ds}{dx} = \frac{du_{CFRP}}{dx} - \frac{du_{steel}}{dx} \quad (3.7)$$

where du_{CFRP}/dx and du_{steel}/dx are the strains in the CFRP laminate and in the steel, respectively. Therefore, the integration of Eq. (3.7) with respect to x allow the determination of the slips developed within the bonded interface from the strains developed on the CFRP laminates and on the strains in the steel plate. The slips developed within the CFRP-to-steel interface can be numerically determined as:

$$s(x_i) = \int_{x_i}^{x_{i+1}} (\varepsilon_{CFRP} - \varepsilon_{steel})\, dx + s(x_{i+1}) \approx$$

$$\approx \left[\frac{\varepsilon_{CFRP,i+1} + \varepsilon_{CFRP,i}}{2} - \frac{\varepsilon_{steel,i+1} + \varepsilon_{steel,i}}{2}\right] \cdot (x_{i+1} - x_i) + s(x_{i+1}) \quad (3.8)$$

where $s(x_{i+1})$ is the slip at point x_{i+1} and $\varepsilon_{steel,i+1}$ and $\varepsilon_{steel,i}$ are the strains in the steel plate at points x_{i+1} and x_i, respectively. The slip at any point requires the knowledge of the slip at an "initial" point as seen in Eq. (3.8), more commonly starting from the point where slip is zero. Therefore, for the calculation of the slips developed within the interface, it was firstly identified the region of zero slip from the bond stress distribution and identified the region of zero bond stress. Since the bond length adopted for the samples is expected to be longer than the effective bond length, the identification of this region should be easy to make and then the slips should be calculated into the direction of the center of the double strap bond joint. The calculation of the strains in the steel plate (ε_{steel}) was made by equilibrium using the loads registered by the tensile machine and the loads in the CFRP laminates obtained from the strain gauges.

Due to the calculation of the bond stresses at midpoints, the corresponding average value of the slip was also considered:

$$s(x_{i+1/2}) = \frac{1}{2}(s_{x_{i+1}} + s_{x_i}) \quad (3.9)$$

The bond-slip relationship associates the average bond stress calculated from Eq. (3.5) and the average slip calculated from Eq. (3.9). The largest slip occurred at the CFRP loaded end where the data for the complete bond-slip curve should be obtained. Typical bond-slip curves at 12.5 mm from the loaded end were thus chosen for reporting here.

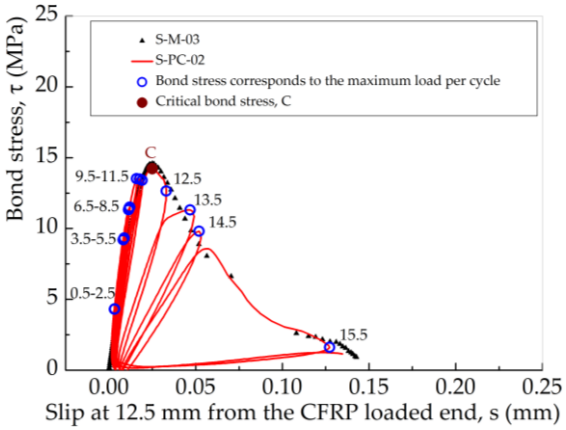

Figure 3.7 - Monotonic (S-M-03) and pseudo-cyclic (S-PC-02) bond-slip curves.

As an example, it is shown in Figure 3.7, the comparison between the bond-slip curves of the monotonic test S-M-03 and the pseudo-cyclic test S-PC-02. The shape of the monotonic bond-slip relationship may be defined between a bi-linear and a linear with an exponential softening, as described in the literature for brittle substrates such as concrete [83, 84], but a simple bi-linear shape is, in fact, consistent with some previous findings reported in the literature for CFRP-to-steel interfaces [13, 17, 85]. The envelope curve of the pseudo-cyclic test is basically bounded by the monotonic curve. The ascending and descending branches of the pseudo-cyclic test in the earlier cycles, before Point C, i.e. at maximum bond stress (see Figure 3.7), and of the monotonic bond-slip curve are almost coincident. However, beyond point C the loading-unloading associated with the pseudo-cycles follows paths that differ from the monotonic bond-slip curve.

From Figure 3.8a to 3.8d, the bond-slip curves corresponding to pseudo-cyclic loading are divided into different stages according to four increasing amplitudes. For each of the three initial cycles with the same load amplitude, the loading paths till a point of "maximum" bond stress were followed by unloading, as shown in Figure 3.8a-d, travelled in the direction opposite to that of loading, and associated with the same maximum stress and slip. The points in these graphs correspond to the maximum bond stress and slip developed in each cycle and actually represent one-half of cycle. These points are identified by the corresponding semi cycle number which, in the cases of semi cycles, e.g. 0.5, 1.5 and 2.5 (see Figure 3.2a) represent the peak

loads reached at the same position of the cyclic loads for the points in the three initial cycles during the first amplitude. Along the Elastic stage of the bond-slip relationship, i.e. for the initial ascending stage of the bond-slip relationship, the points associated with the same amplitude are coincident because the elastic stiffness (k_e) remains almost unaltered leading to a situation of no damage of the adhesively bonded interface, as it can be seen from Figure 3.8a-d.

Figure 3.8e corresponds to a set of cycles of higher amplitude and starts with the stiffness k_e until the bond stress exceeds the maximum bond stress at point C hereafter designated as "critical bond stress" and corresponding to the "critical loading". Beyond this "critical bond stress", the bond stress decreases to Point 12.5, corresponding to the 12.5th cycles (first peak load in fifth amplitude as it can be seen from Figure 3.2a), and then unloads with a residual slip at zero load and stiffness $k_{d,1}$. The new cycle of this pack of 3 cycles started with stiffness $k_{d,2}$ until a new and smaller maximum bond stress is reached at Point 13.5 corresponding to the 13.5th cycles (second peak load of the fifth amplitude), and then unloaded with a reduced stiffness causing a new larger residual slip for zero load. The process successively continued and induced a degradation of the stiffness and residual slip. Figure 3.8f shows the bond response to the cycles at the last load amplitude. The first cycle of this set started with a similar stiffness as that of the most recent unloading path until bond stress at Point M is reached and the debonding proceeds like before.

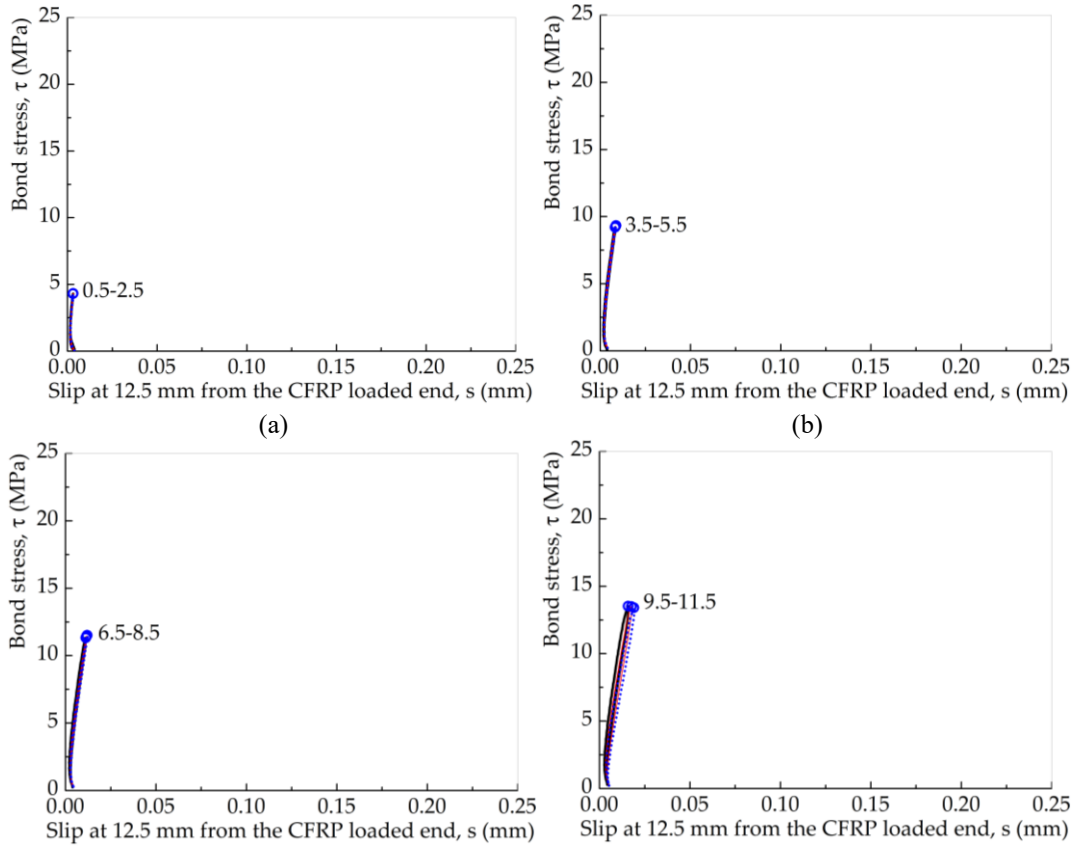

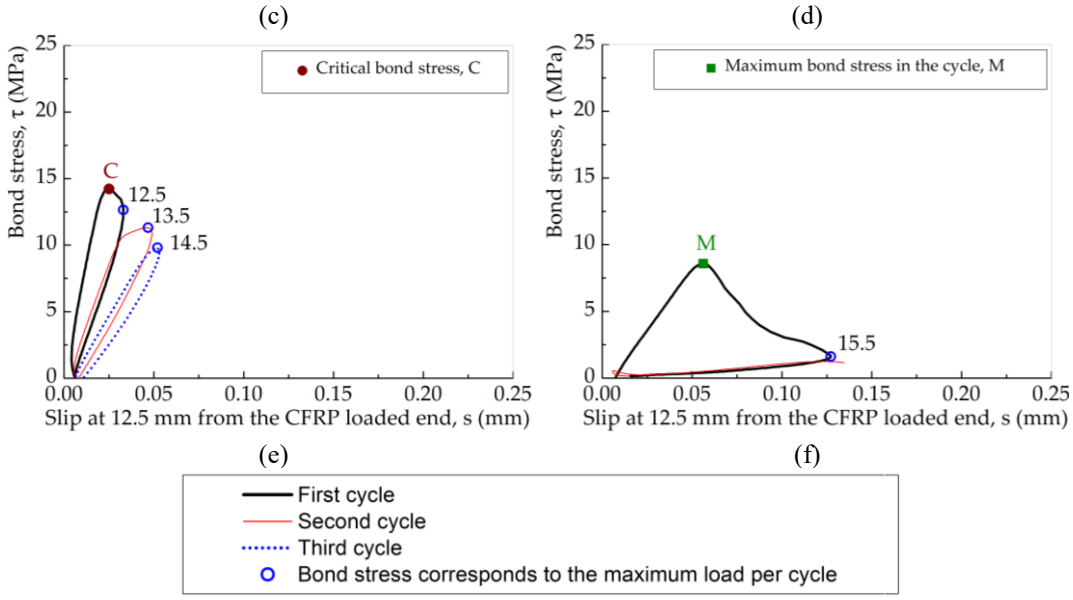

Figure 3.8 - Stages of pseudo-cyclic bond-slip curves.

From the above analysis of the bond-slip relationships, for the finite cycles with maximum load not exceeding the "critical loading" (corresponding to Point C in the pseudo-cyclic bond-slip) no damage occurs. If the load is such that the "critical bond stress" is surpassed, then damage occurs, i.e. the initiation, propagation and consolidation of the micro cracks within the bonded interface lead to the degradation of interfacial stiffness and residual slip become relevant as the cycles approximate the maximum load and debonding failure occurs [86].

Figure 3.9 shows the bond stress vs. slip relationships at 12.5 mm obtained for the monotonic and pseudo-cyclic tests with HIT specimens (in Figure 3.9a) and with SIKA specimens (in Figure 3.9b). The envelope of the pseudo-cyclic bond stress vs. slip curves basically coincided with the monotonic curves. Moreover, it is clear that the stiffness degradation and energy dissipation gradually occurred for the cycles that surpassed the critical bond stress in each curve.

Accumulation of damage above the "critical bond stress", for the cyclic loading, was examined applying 600 cycles to the joints and in the particular case of specimen S-C-03 after applying 1,000 cycles.

Figure 3.10 shows the comparison of the cyclic and monotonic bond-slip curves before and after the cyclic tests, both for HIT (Figure 3.10a) and SIKA (Figure 3.10b) CFRP-to-steel joints. The progress of the bond stress vs. slip curves at 12.5 mm can be interpreted as an indirect measurement of the damage which occurred in the vicinity of the loaded end, i.e. the area limited by the CFRP most loaded end at 0 mm and 12.5 mm. The result of the accumulation of damage is visible. As initially suspected, the increase of the number of cycles led to the increase of the interfacial damage in the vicinity of the CFRP loaded end, pushing the applied load

further along the bonded length. Furthermore, these cyclic bond-slip curves show the cumulative degradation and track gradually the monotonic curves.

Like the monotonic load vs. slip responses after the cyclic tests, the interfacial stiffness of the monotonic bond stress vs. slip curves also followed the same interfacial stiffness determined at the end of the last cycle carried out during the cyclic tests, and then, the bond-slip curve tracked the monotonic one until complete debonding as it can be seen from the experimental results obtained from specimens, e.g., H-CM-02 and S-CM-02. Observing the curve obtained for specimen S-C-03, the complete debonding between the CFRP and the steel plate initiated at point 12.5 mm after 1,000 cycles and therefore, the curve of S-CM-03 (under monotonic loading after being subjected to 1,000 cycles) showed a single and linear stage that can be attributed to the friction between the debonded CFRP laminate and the corresponding part of substrate, i.e. steel and/or adhesive.

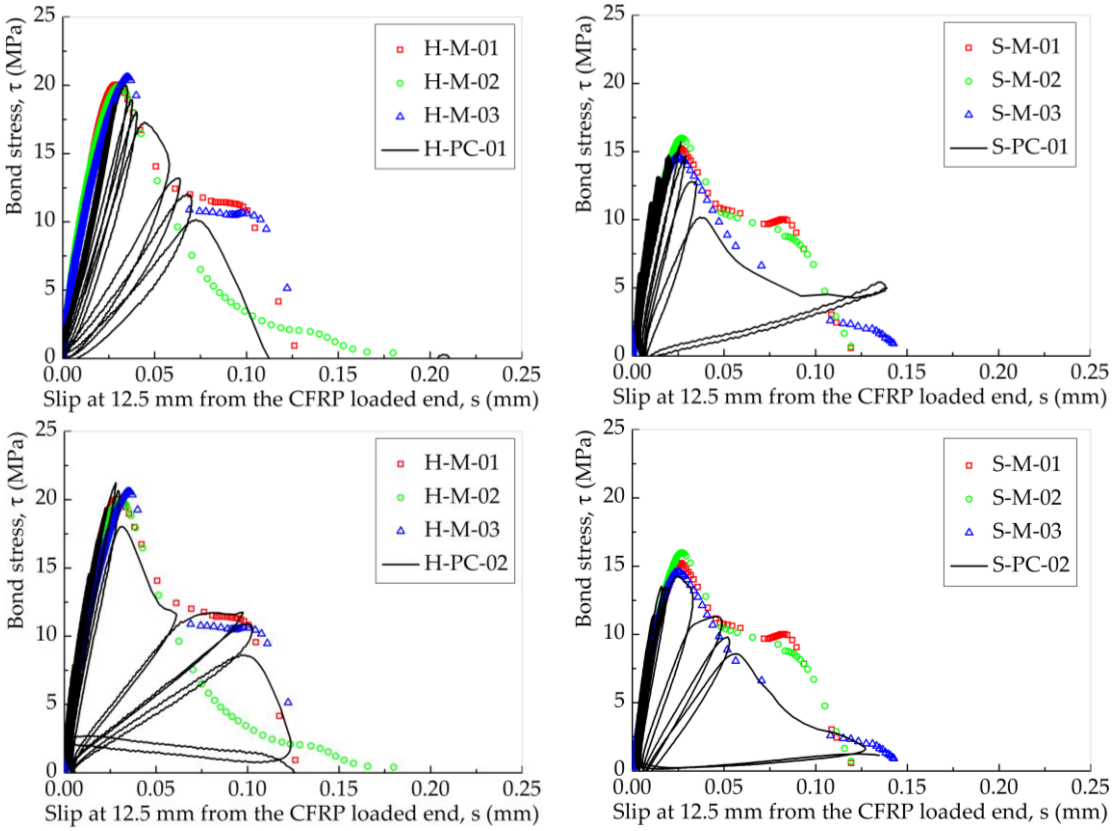

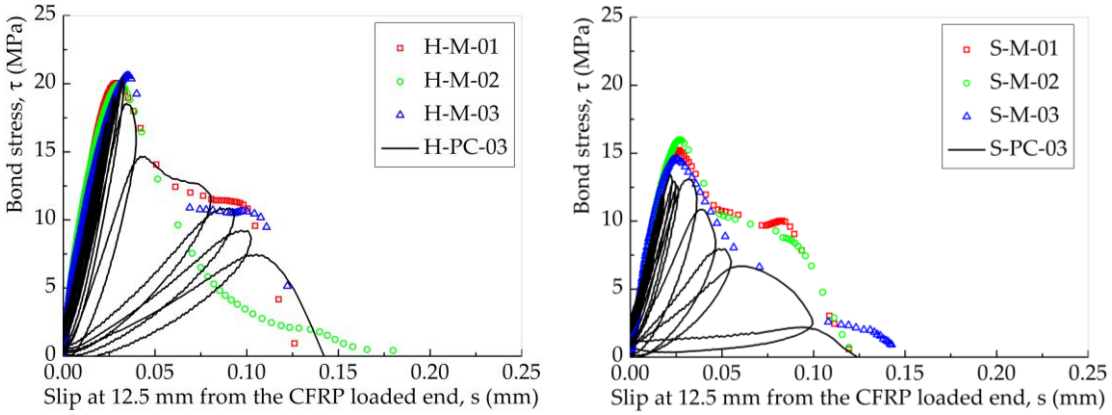

(a) (b)

Figure 3.9 - Monotonic and pseudo-cyclic bond-slip curves: (a) HIT bonded joints; and (b) SIKA bonded joints.

3.4 Analysis of damage

3.4.1 Interfacial damage analysis

As mentioned above, the process of damage, i.e., the initiation and propagation of the micro cracks to debonding failure occurred once the critical bond stress was surpassed and reflected on the degradation of the interfacial stiffness and energy dissipated during its cyclic debonding process. Therefore, the interfacial stiffness and the residual fracture energy decreased with the number of loading/unloading cycles. Thus, it is assumed that the damage parameter (D) can be defined and based on the degradation of the interfacial stiffness, e.g. [86]:

$$D = 1 - \frac{K_{d,i}}{K_e} \tag{3.10}$$

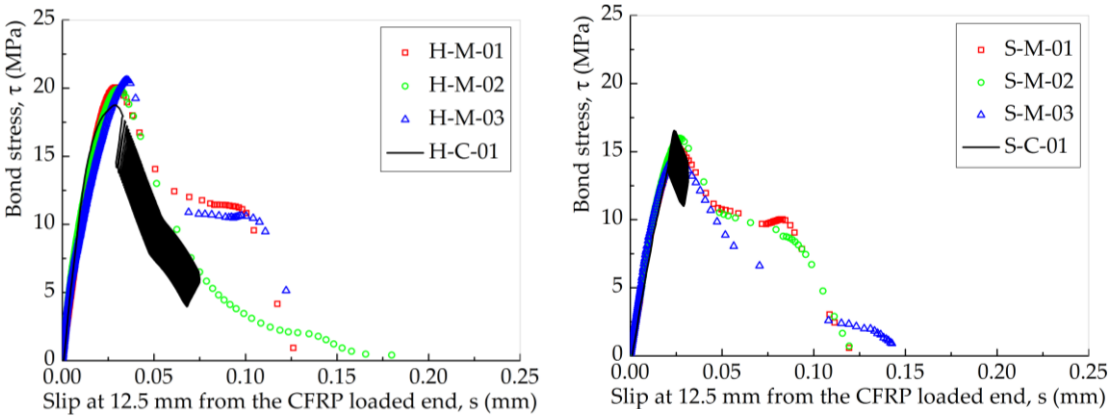

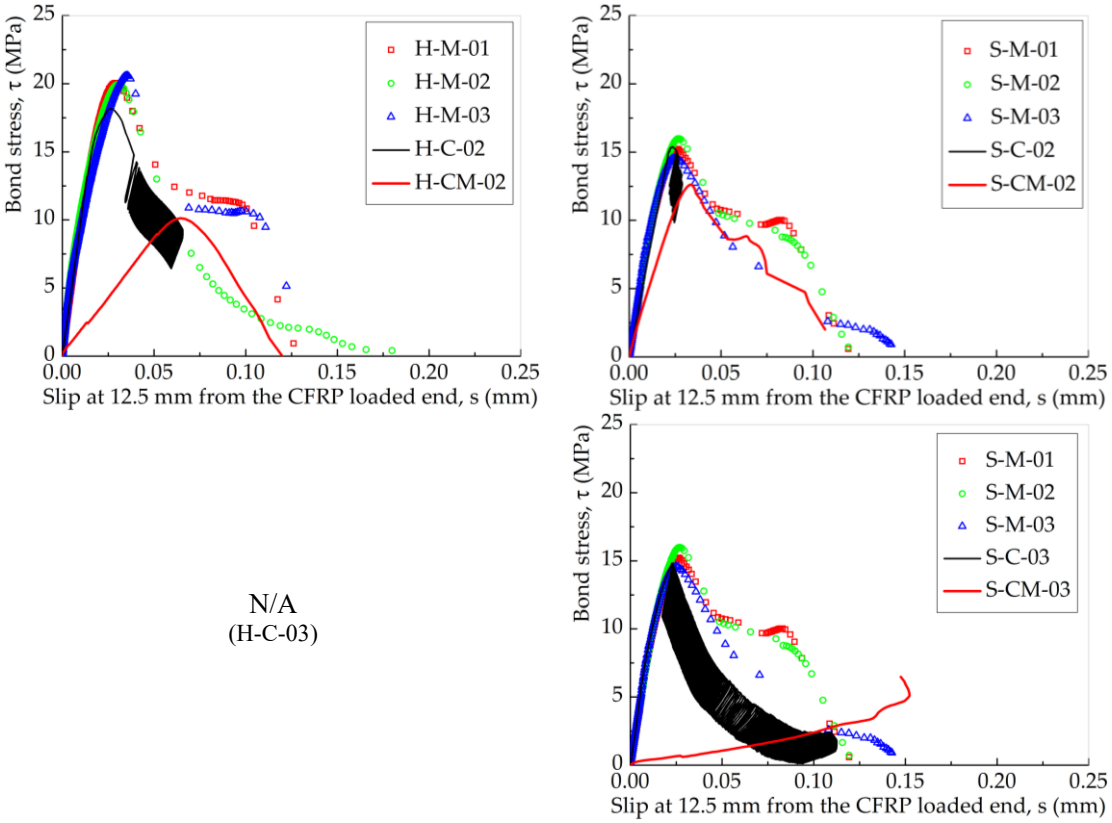

Figure 3.10 - Cyclic bond-slip curve: (a) HIT bonded joint (b) SIKA bonded joint.

where $K_{d,i}$ is the interfacial stiffness at the particular cycle i and K_e is the initial (or elastic) interfacial stiffness, i.e. corresponding to the elastic stage of the bond-slip relationship. Thus, it is reasonable to associate the damage parameter (D) with the ratio between the energy dissipated (w_d) at a particular cycle and the total fracture energy (G_f) of the bonded joint. This damage parameter can be defined as a function of the ratio between the energy dissipated and the fracture energy, or, for simplicity, as a function of the normalized dissipated energy (w_d/G_f):

$$\mathrm{D} = \mathrm{f}\left(\frac{w_d}{G_f}\right) \tag{3.11}$$

where

$$w_d = \int_0^{s_i} \tau(s)ds - \frac{{\tau_i}^2}{2K_{d,i}} \tag{3.12}$$

being s_i and τ_i the slip and the bond stress at cycle i, respectively, and

$$G_f = \int_0^{s_{ult}} \tau(s)ds \tag{3.13}$$

The relationship between the normalized dissipated energy determined from the experimental results and the damage parameter (D) is based on six tests and, consequently, based on the six bond-slip relationships shown in Figure 3.9. The results are shown in Figure 3.11a. As shown in this figure, the damage of the CFRP-to-steel interface increased with the increase of the

normalized energy due to interfacial stiffness decay once the elastic state is surpassed and the cumulative dissipated energy began to increase. The damage vs. normalized dissipated energy relationship is closely associated with the shape of the bond-slip curve and for the present case, with a bi-linear bond-slip relationship, the following mathematical function can be used to represent the experimental results, having a 0.97 of coefficient of determination (R^2):

$$D = -\left(\frac{w_d}{G_f}\right)^2 + 2\left(\frac{w_d}{G_f}\right) \tag{3.14}$$

Eq. (3.14) was also used to numerically predict the damage of CFRP-to-concrete interfaces during their cyclic debonding process [86]. The relationship between the damage parameter (D) and the normalized slip (s/s_{ult}) was also analyzed. The results were based on the same tests and corresponding bond-slip relationships shown in Figure 3.9 and the experimental results are shown in Figure 3.11b. As shown in this figure, for cycles at an elastic stage, i.e., where the bond stress is lower than the critical bond stress, the damage of the interface is almost nonexistent and thus, the damage parameter (D) was assumed to be zero. During the debonding cyclic process, the slip at one of the semi-cycles increased and therefore, the damage parameter (D) analysis associated with the normalized slip (s/s_{ult}) may return meaningful information. Also from Figure 3.11b it can be seen that only when the normalized slip became greater than 0.22 the damage parameter began to increase. These experimental results can be closely approximated through the following mathematical function, the approximation leading to a calculated coefficient of determination (R^2=0.87):

$$D = \begin{cases} 0 & \text{if} \quad \frac{s}{s_{ult}} < 0.22 \\ \sqrt{\frac{s - s_{max}}{s_{ult} - s_{max}}} & \text{if} \quad 0.22 \leq \frac{s}{s_{ult}} < 1 \end{cases} \tag{3.15}$$

where 0.22 can be seen as the damage limit of the bonded interface, D_{limt}. As it will be seen later, the normalized slip (s/s_{ult}) is closely associated to this damage limit and due to the fitting of Eq. (3.15) with the experimental data this indicates that this relation between the damage (D) and the damage limit (D_{limit}) depends on the normalized slip. Similarly to Eq. (3.14) during the cyclic debonding process of the bonded joint the amount of damage developed at each single point of the bonded length was controlled by an unique value of the normalized dissipated energy whereas Eq. (3.15), despite leading to a unique value for the damage of the interface, depended exclusively on the slip at each point. Since the slips of an adhesively bonded interface are usually the unknowns of the debonding problem, once they are found then the interfacial damage can be easily predicted throughout the bonded length.

The normalized dissipated energy can also be written as a function of the normalized slip which, once again, may provide relevant information through the slip distributed within the CFRP-to-

steel interface. Therefore, introducing Eq. (3.14) into Eq. (3.15) and performing a simple mathematical step, it is possible to establish a relationship between the normalized slip and the normalized dissipated energy according to:

$$\frac{w_d}{G_f} = \begin{cases} 0 & \text{if} \quad \frac{s}{s_{ult}} < 0.22 \\ 1 - \sqrt{1 - \left(\frac{s - s_{max}}{s_{ult} - s_{max}}\right)^{0.5}} & \text{if} \quad 0.22 \leq \frac{s}{s_{ult}} < 1 \end{cases}. \tag{3.16}$$

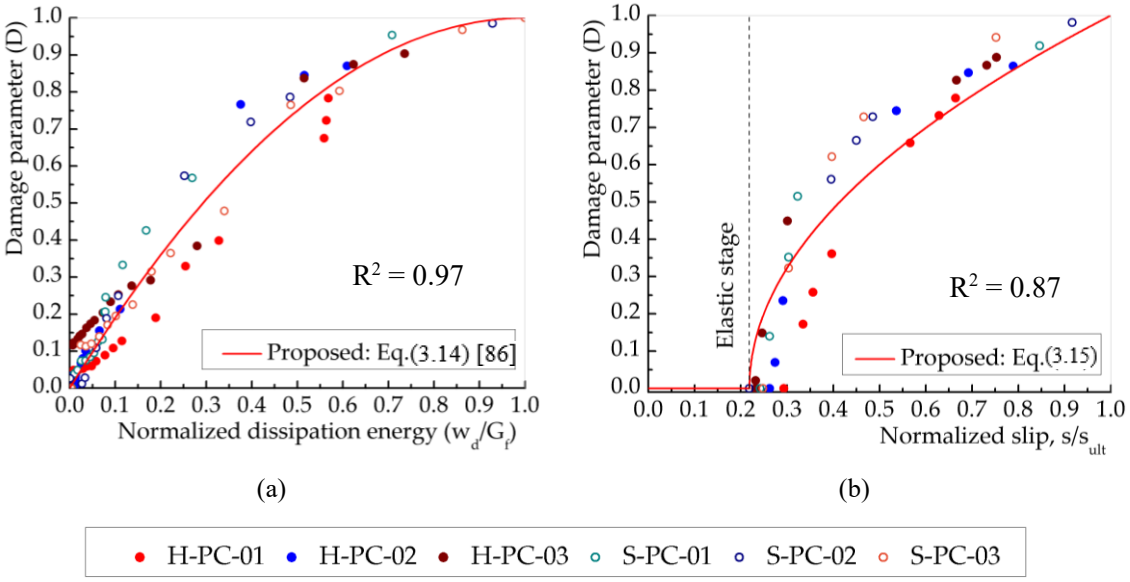

Figure 3.11 - Relation between the damage parameter (D) and: (a) the normalized dissipated energy; and (b) normalized slip.

Figure 3.12 presents the normalized dissipated energy versus the normalized slip obtained from the experimental tests and shows in red the Eq. (3.16). Although it can be seen that the experimental data fits very well with Eq. (3.16), having a 0.95 of coefficient of determination (R^2), a straight line (in black) can be adopted as a simplification of Eq. (3.16) in the following form, with 0.97 as coefficient of determination (R^2):

$$\frac{w_d}{G_f} = \begin{cases} 0 & \text{if} \quad \frac{s}{s_{ult}} < 0.22 \\ \frac{1}{s_{ult} - s_{max}} \cdot (s_{ult} \cdot s - s_{max}) & \text{if} \quad 0.22 \leq \frac{s}{s_{ult}} < 1 \end{cases}. \tag{3.17}$$

Therefore, the normalized dissipated energy can be determined from the slip developed within the CFRP-to-steel interface.

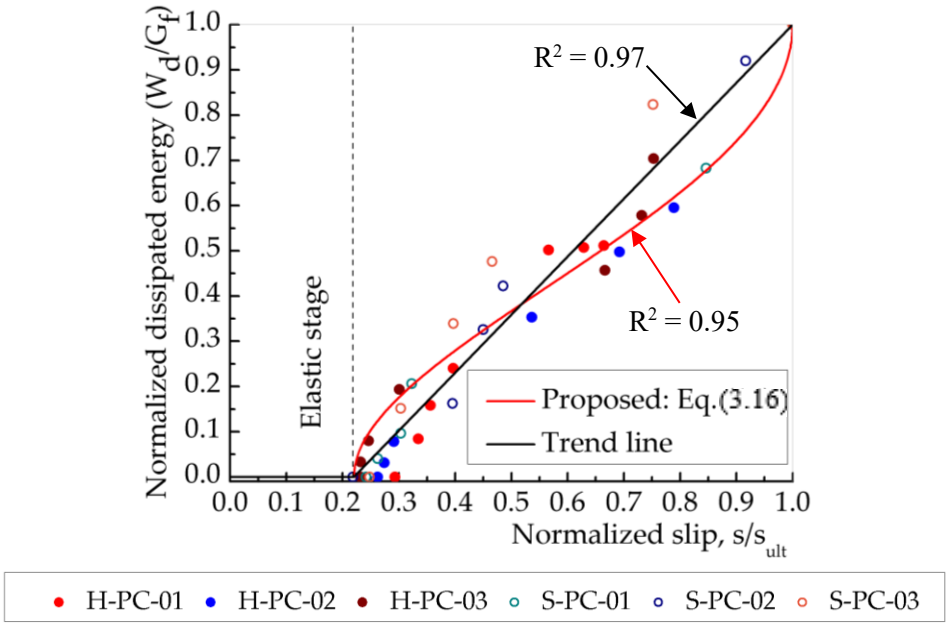

Figure 3.12 - Relation between the normalized dissipated energy and the normalized slip.

From the analysis at every point in the bonded domain of the CFRP-to-steel joints, there exists a "critical bond stress" corresponding to a "critical loading", and the bond behavior is much different before and after that threshold loading is reached. As known, in terms of CFRP-to-steel double strap bonded joints, the force applied to the steel end by the static tensile machine was equally resisted by two reactions each carried by the corresponding CFRP laminate. As shown in Figure 3.13a, the shear stress reaches the stage of "critical bond stress" at the loaded end when $2\times F_{threshold}$ is imposed at the steel end by the static tensile machine, and each CFRP laminate resists $F_{threshold}$. Figure 3.13a also highlights the shear stress distribution in the entire bond at the threshold loading. In the following analysis, the focus of the study is only on one of the bonded sides. When the cyclic maximum load was higher than the "threshold loading", the bond in the loaded end started to deteriorate, and more degradation occurred. Consequently, the damage zone enlarged with the number of cycles and for higher load levels. However, for a maximum load below the "threshold loading", no interfacial damage is detected. Since no interfacial damage occurred before the "threshold loading", the "critical bond stress" is expected to be the same as that determined for the monotonic test and it corresponds to the same "threshold load" illustrated in Figure 3.13 as well. For this particular threshold limit, the experimental results are presented in Figure 3.14 in which the theoretical prediction proposed by Yang et al. [85] for monotonic loading is also shown. The theoretical prediction is based on the average values obtained for each case of the monotonic tests, i.e. for HIT and SIKA CFRP-to-steel bonded joints. Thus, s_{max} = 0.030 mm, τ_1 = 20 MPa, s_{ult} = 0.12 mm correspond to the HIT bonded joints whereas s_{max} = 0.026 mm, τ_1 = 15 MPa, s_{ult} = 0.12 mm correspond to the SIKA bonded joints. Moreover, the axial stiffness ratios are β_{HIT} = 4.98 and β_{SIKA} = 6.38. Based

on these values, the elastic state of the adhesively bonded joint effectively covered a bond length of L_e = 110 mm for HIT joints and L_e = 95 mm for SIKA joints.

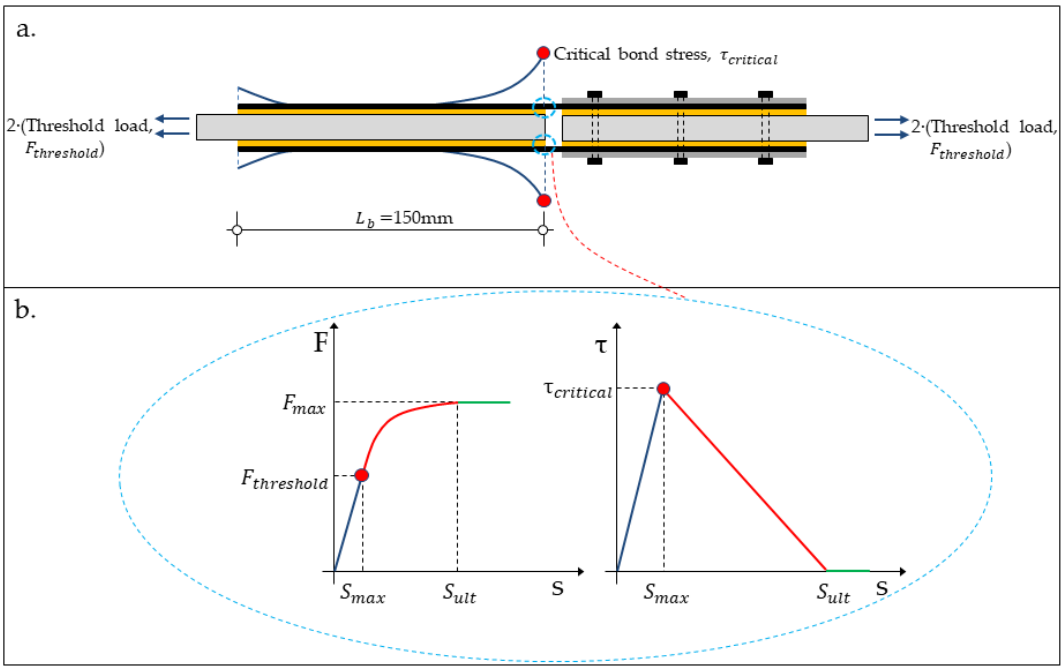

Figure 3.13 - Illustration of bond shear stress distribution at threshold loading state.

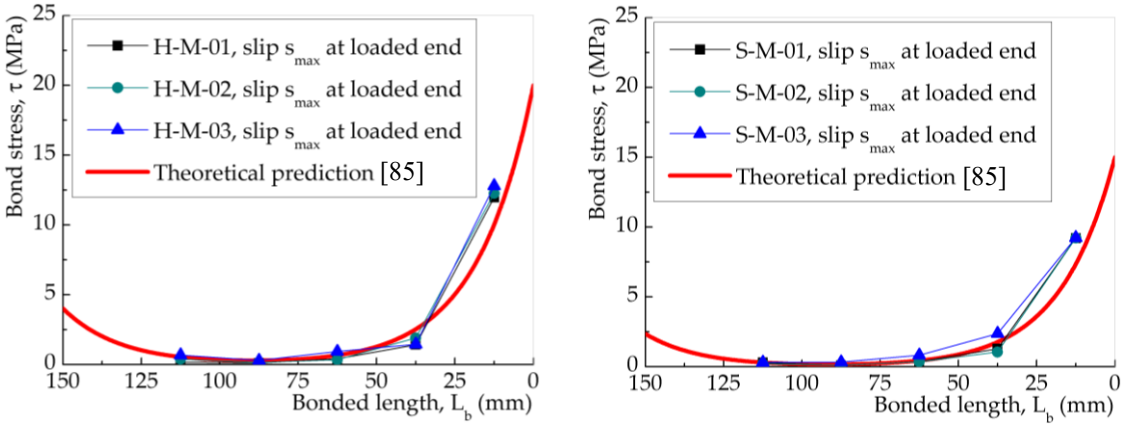

(a) (b)

Figure 3.14 - Bond stress distribution along the bond length at threshold loading state for: (a) HIT; and (b) SIKA bonded joints.

Figure 3.13b illustrates the load vs. slip and the bi-linear bond-stress relationship at the loaded end with the increase of the monotonic loading and the position of the threshold load limit, respectively. All the stages covered by the bi-linear bond-slip relationship (elastic, softening and debonded) are also delimited on the theoretical load vs. slip at the loaded end, where the end of the initial elastic τ-s segment corresponds to the threshold loading in the monotonic loading process.

The ratio between $F_{threshold}$ and F_{max}, here designated as damage limit D_{limit}, was calculated from the data obtained in each set of three samples subjected to the monotonic loading both for HIT and SIKA joints. Figure 3.15 indicates a value of approximately 50% for $F_{threshold}/F_{max}$, related to the "endurance" limit of CFRP-to-steel joints under tensile loading. Comparing these experimental results with the estimations provided from the simplified model proposed by Wu et al. [57]:

$$F_{max} = b_{CFRP} \cdot \sqrt{\tau_{max} \cdot s_{ult} \cdot E_{CFRP} \cdot t_{CFRP} \cdot (1 + 2 \cdot \beta)} \tag{3.18}$$

$$F_{threshold} = b_{CFRP} \cdot \sqrt{\tau_{max} \cdot s_{max} \cdot E_{CFRP} \cdot t_{CFRP} \cdot (1 + 2 \cdot \beta)} \tag{3.19}$$

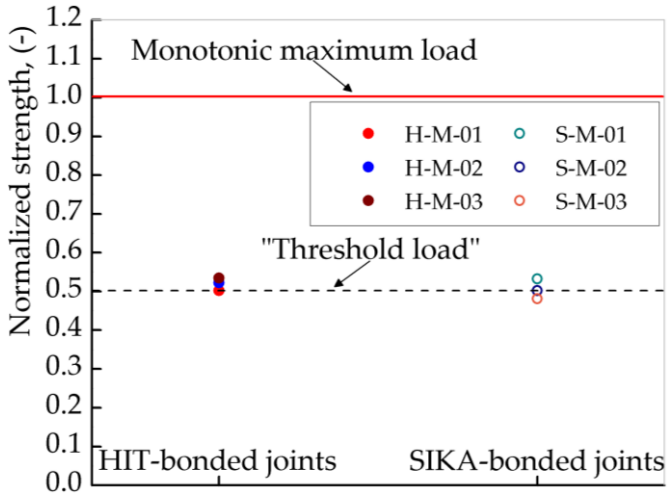

Figure 3.15 - Threshold loading of the joints obtained from the monotonic tests.

where β is the axial stiffness ratio defined in Eq. (3.2) and t_{CFRP}, b_{CFRP} are the thickness and the width of the CFRP laminate; E_{CFRP} is the tensile modulus of the CFRP laminate; τ_{max} and s_{max} are, respectively, the maximum bond stress and the corresponding slip value; s_{ult} is the ultimate slip, and the damage limit is defined by

$$D_{limit} = \sqrt{\frac{s_{max}}{s_{ult}}} \tag{3.20}$$

which leads to F_{max} = 17.43 kN and $D_{limit,\,HIT}$ = 0.5 for HIT bonded joints, and F_{max} = 13.09 kN and $D_{limit,\,SIKA}$ = 0.47 for SIKA bonded joints. It is worth to bear in mind that the value of the damage limit of 0.47 is the same as the square root of the normalized slip of 0.22 already defined in Eq. (3.15) and shown in Figure 3.11 which proves the consistency of the damage analysis beyond the "threshold loading" and/or the "critical bond stress".

3.4.2 Global damage analysis

The dissipated energy, i.e., the area under load vs. slip curve for one cycle (a loading and

unloading process), is associated with the progression of the interfacial damage within the bond between materials. The dissipated energy of the interface between CFRP and steel was calculated from the load-slip curves shown in Figure 3.4 and the results are shown in Figure 3.16.

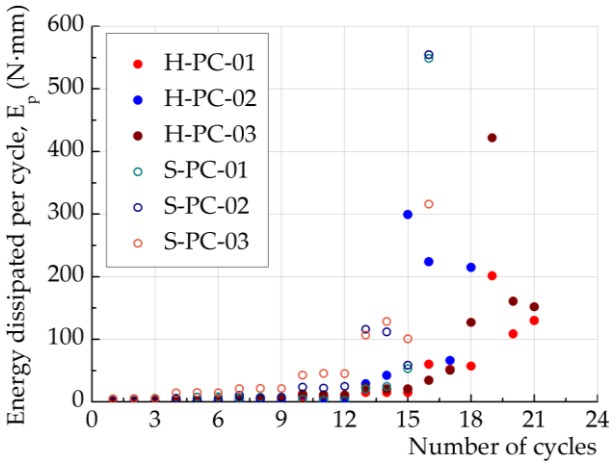

(a) per cycle

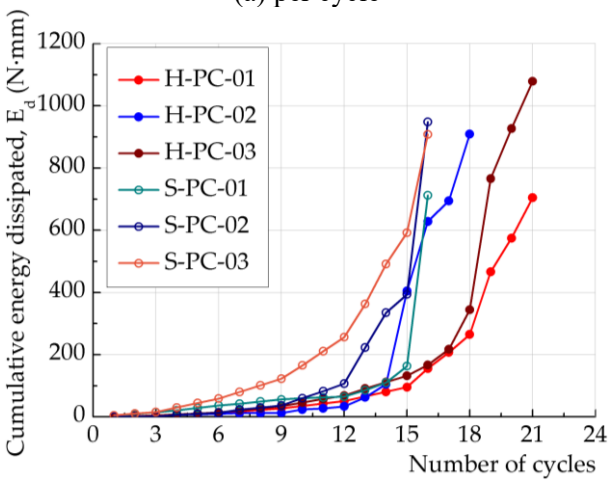

(b) cumulative

Figure 3.16 - Dissipated energy: (a) per cycle; and (b) cumulative.

In Figure 3.16a, the dissipated energy per cycle for HIT and SIKA joints is shown. As it can be seen for the SIKA bonded joints, the dissipated energy can be ignored for the initial cycles and has an important increase after the 6th cycle which corresponds to approximately 50% of the average monotonic load capacity. However, the dissipated energy of HIT bonded joints starts from the 9th cycle which represents approximately 60% of average monotonic load capacity of these specimens. Comparing the CFRP bonded joints from HIT and from SIKA it can be stated that they show a similar variation trend. The dissipated energy of HIT bonded joints can be also found in Figure 3.16b. It should be noted here that specimens H-PC-01, H-PC-02 and H-PC-03, were kept in the laboratory for 2 months more before the pseudo-cyclic tests than specimens H-M-01, H-M-02 and H-M-03 due to unpredicted malfunction of the equipment at that time.

Therefore, the former specimens had a longer cure period that may explain why the samples from H-PC series had a higher strength (see Table 3.1) and, at the same time, the differences on the dissipated energy between both series (H-PC and H-M).

Comparing now the normalized interfacial dissipated energy with the normalized global dissipated energy of the CFRP-to-steel interface, it can be seen from Figure 3.17a that there is a straight relationship between both normalized energies, with 0.93 as coefficient of determination (R^2). The amount of normalized dissipated energy, either globally or locally determined, seems to provide the same value that is, for instance, 50% of normalized interfacial dissipated energy, which corresponds to the same 50% of the normalized global dissipated energy. Therefore, Eq. (3.17) which represents the normalized dissipated energy in the interface versus the normalized slip (w_d/G_f), can also be used for the definition of the normalized global dissipated energy with the normalized slip (E_d/E_t) of the CFRP-to-steel interface. Comparing with the experimental results, Figure 3.17b shows that Eq. (3.17), represented by the trend line, may fairly represent the experimental results, with 0.95 as coefficient of determination (R^2). It is worth to mention also that, for normalized slips lower than 0.22, no dissipated energy was considered which, explains the absence of experimental results at this elastic domain.

3.5 Remarks

Monotonic, pseudo-cyclic and cyclic tests were performed and their results allowed the definition and analyses of bond-slip curves for CFRP-to-steel bonded joints. Thus, based on the results from 24 tests, the following conclusions were taken:

- A "threshold loading" was detected (around 50% of the maximum monotonic load capacity of the joints) that corresponds to a "critical bond stress" in the loaded end below which cyclic loading caused no damage;
- The damage zone which is localized at the vicinity of the CFRP loaded end increased with the number of cycles especially when the maximum load exceeded the "threshold loading". Degradation of the interfacial stiffness of the bond stress vs. slip led to the reduction of the stiffness measured in terms of the load vs. slip response of the bonded joints;

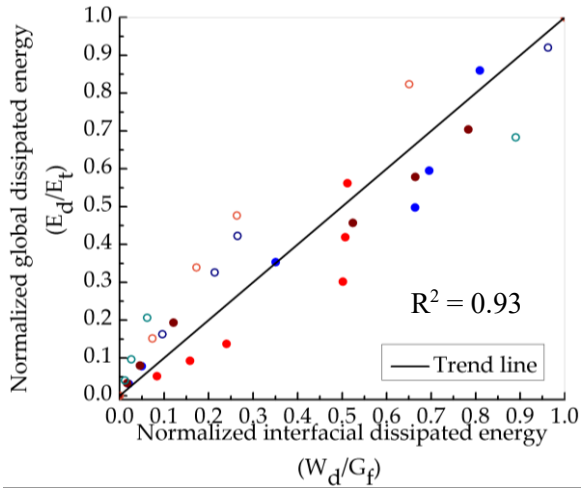

(a)

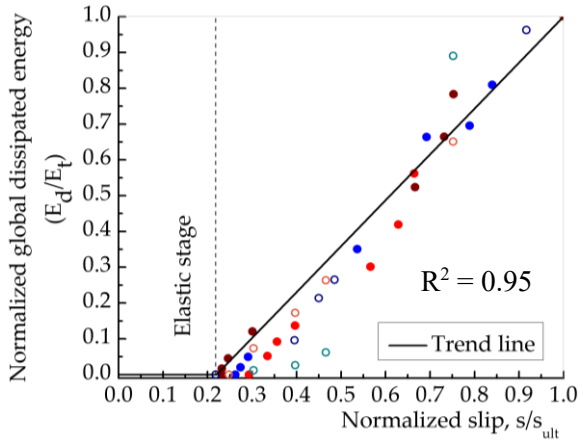

(b)

Figure 3.17 - Relation between: (a) the normalized interfacial and global dissipated energies; and (b) the normalized global dissipated energy and the normalized slip.

- Pseudo-cyclic and cyclic tests under a limited number of cycles had slight effect on the bond strength capacity either on HIT or SIKA CFRP laminates; this fact can be attributed to the bond length longer than the effective bond length;
- The failure modes did not change for the bonded joints previously subjected to pseudo-cyclic or cyclic loading when compared with those monotonically loaded; the maximum bond stress determined from the SIKA bonded joints that had a mixed failure mode is lower than that determined from the HIT bonded joints with cohesive failure mode. However, the bond cyclic damage followed the same way;
- The interfacial stiffness of the adhesively bonded joints degraded with the number of cycles imposed to the specimens and when the samples were monotonically tested; the interfacial stiffness observed on these tests seemed to be almost the same that was previously observed for the last cycle carried out during the cyclic test;
- The normalized dissipated energies determined from the bond-slip relationship (w_d/G_f) or

from the load-slip response (E_d/E_t) had the same trend, i.e. the amount of normalized energy locally and globally dissipated was the same. Nevertheless, in both cases it is possible to establish a relationship with the normalized slip (s/s_{ult}) which, depending on the slip distribution within the CFRP-to-steel interface, allows the determination of the normalized dissipated energies on a local or global point of views;

- The "threshold loading" at the loaded end proposed for the CFRP-to-steel bonded joints could be correlated with an "endurance limit", a topic to clarify in future fatigue tests.

3.6 Summary of this chapter

Pseudo-cyclic (Figure 3.2a) and cyclic loading (Figure 3.2b) were applied to CFRP-to-steel bonded joints built with two different CFRP laminates. In this chapter, the strength capacity (Table 3.1) and bond-slip curves (Figure 3.9 and 3.10) are presented and compared.

The modes of failure are also described and associated with the types of material used, and the observed performances are correlated. The analysis of the results showed a threshold value (see Figure 3.13) for loading and amplitude level, below which the cyclic loading caused no detectable damage. For cycles above that limit, the region of the joints around the loaded end presented degradation, reflected on the bond-slip stiffness and on the increase of residual deformation.

It was found that the normalized dissipated energies either obtained from the bond-slip relationship or from the load-slip response had the same trend (see Figure 3.17a). The experimental data allowed also to establish a relationship between the damage developed within the interface and the normalized slip. A preliminary estimate of fatigue limit based on those data is suggested.

Chapter 4

Bond durability of CFRP-to-steel bonded joints subjected to freeze-thaw

4.1 Introduction

The long-term performance of the CFRP composite reinforced steel systems remains an important concern due to uncertainties on the life cycle of the reinforced system when subjected to long-term severe environmental conditions as described by Buyukozturk *et al*. [87] who published an excellent review on debonding problem of the CFRP bonded steel system and recommended that the bond durability of freeze-thaw environment should be studied. Gholami *et al*. added more data in a more recent review, in 2013, and critically discussed durability research results, and also recommended further studies on freeze-thaw [88].

The weakest links of steel systems reinforced with CFRP are diverse, namely (i) adhesive failure (ii) adhesion failure at either CFRP/adhesive or steel/adhesive interfaces (iv) delamination of CFRP (v) rupture of CFRP, or (vi) mixed failure modes. The degradation of the interface has often been found to be significantly more important than that of the adhesive [23].

Freeze-thaw is a common operating condition for outdoor structures and requires attention to the behavior/durability of externally bonded reinforced systems. Freeze-thaw cycles act on the CFRP-steel bonded system primarily via three processes, (i) diffusion of moisture that can lead to degradation of the adhesive, commonly through plasticization [89], swelling, cracking and hydrolysis [90, 91]; (ii) expansion of the water after freezing generates cracks that degrade the adhesive and interface after repeated cycles; and, (iii) cumulative damage in the bond between CFRP and steel under long-term cyclic shear stress induced by the temperature changes due to the discrepancy of linear thermal expansion coefficient of components [92-94].

The properties of the adhesive influence the shape of the bond-slip curves [41], and the long-term properties of the adhesive also add to the factors that influence the durability of bonded

joints. Studies conducted on different adhesives made by Hand *et al*. [95] showed that coupons of epoxy adhesives at 50°C and 90% relative humidity for 16 days had an maximum moisture absorption near 3.5% with a significant reduction of the strength of the adhesive, 30%-70%. Tensile tests on hot-cured epoxy adhesive coupons exposed at 30°C and 100% relative humidity for 12 weeks by Knox and Cowling [96] showed a 20% decrease in tensile strength and a 10% decrease in Young's modulus. Lesser effects were found by Nguyen *et al*. [97] with Araldite 420 epoxy adhesive after 1,000 h exposure at 50°C and 90% relative humidity. With different adhesives and wet-thermal conditions, the degradation data were not the same, but the plasticization of the adhesives, i.e., more flexibility of their molecular chain with ingress of moisture, was similar. Not many studies regarding adhesive exposure to freeze-thaw cycles exist, one being authored by Agarwal *et al*. [22] who exposed adhesive coupons of SIKA-30 and SIKA-330 to 40 cycles of 16h at -18°C followed by 8h at 38°C and 100% relative humidity, and found 9% and 19% reduction, respectively, on the tensile strength and elastic modulus of SIKA-330 and no significant degradation of strength and 14% reduction of the elastic modulus for SIKA-30. The reduction of modulus occurred primarily during the first 20 freeze-thaw cycles.

Previous studies showed that temperature, moisture and defects inside the material, namely voids, holes and cracks, have an effect on the glass transition temperature (T_g) of the epoxy resin. Yang *et al*. [98] found that initially the temperature accelerates the cross-linking of the molecules and the molecular structure has less mobility and increases the T_g. Opposite to the positive effects of temperature increase, generally, the ingress of moisture reduces molecular interaction and decreases T_g [99]. Xian and Karbhari [99] exposed ambient cured epoxy adhesive to 23°C and 30% relative humidity (RH), having found that T_g increased by 7°C after 12 months aging and slightly decreased after 24 months. The initial increase of T_g indicated that post-curing prevailed over any plasticization effects due to moisture uptake. Inversely, the decrease of the T_g indicated prevalence of moisture with time passing.

There are scarce experiments, Karbhari *et al*. [100] studied bond durability of steel and wet lay-up unidirectional glass and carbon fiber sheets using wedge tests in various environmental conditions. Freeze/thaw exposure (alternating 12 hours cycles between -18°C and 25°C) was found to be the most damaging environment.

Other studies on the CFRP-to-steel single lap joints exposed to different combinations of wet thermal cycle ranges (10°C; 50°C) and sustained loads were reported [101]. The failure mode of specimens exposed to dry thermal cycling under sustained load was delamination of CFRP in the reference specimens while failure took place at the interface of adhesive/steel for wet thermal cycling.

Kim *et al*. [24] showed that steel-to-steel double lap shear joints subjected to 100 freeze/thaw cycles (8h -20°C, 16h room temperature per cycle) had the failure mode changed from cohesive (in the adhesive) at 0 h to adhesive failure.

Recent studies on CFRP-to-steel bonded joints on end-notched flexure specimens previously immersed in distilled water at 45ºC, or in salt water at the same temperature, or exposed to 95% relative humidity at 45°C for 90 days, and then exposed to 250 freeze-thaw cycles [+20°C, -20°C], each cycle taking approximately 12h have been reported by Heshmati *et al*. [25]. The initial slope of the bond shear stress vs. slip (relative deformation between the adherents) remained the same for all the specimens irrespective of the aging condition or the presence of moisture. However, a remarkable reduction of maximum shear stresses was observed for the specimens submitted to freeze-thaw cycles without pre-conditioning.

The failure mode of the pre-conditioned specimens, pre-immersed in either 45°C distilled water or in 45°C salt water for 18 months, remained the same after the freeze-thaw cycles [26]. However, for specimens pre-conditioned in 45°C salt water for 36 months, the failure mode changed from delamination failure of CFRP, started after 125 freeze-thaw cycles, to mixed failure i.e. partial delamination and partial failure in adhesive after 250 freeze-thaw cycles. The cause was attributed to the damage in the adhesive due to the expansion of the salt in the freezing state. Generally, the authors found that moisture had not evident effect on the bond capacity for aging by freeze-thaw cycles. A recent (2015) state of the art review on durability of adhesively bonded FRP/steel joints by Heshmati [23] offers more data on the durability issue.

The initial main objectives of this work were to assess the bond degradation between CFRP laminates adhesively bonded to steel plates after being subjected to freeze-thaw cycles. Therefore, the determination of the local bond-slip relationship after different exposure condition periods is meaningful because it not only helps on the comprehension on how that relationship changes through time (and under successive freeze thaw cycles) but also helps on the interpretation of other results found at different exposure periods such as the debonding load or failure modes. An analytical model is proposed to quantify the interfacial thermal stress developed in the specimens. For the same slip, the analytical model is used to make the comparison between the thermal loading with an equivalent one where an external pulling load is responsible for the debonding. Subsequently, the cumulative damage of the bonded interface under pure cyclic thermal stress is characterized. Through the comparison between the results obtained from the freeze-thaw and pure thermal cycles (from -20ºC to 20ºC), it was found that the degradation mechanism of the CFRP-to-steel bonded joints subjected to the freeze-thaw cycles can be ignored since the interface never exceeded its elastic state.

4.2 Experimental program

In the present chapter, two series of CFRP-to-steel double-strap bonded joints as adopted in the studies of last chapter (chapter 3), each with different kind of CFRP laminates, were made and experimental tests were conducted to try and establish bond constitutive relationship and the variation of bond capacity and failure modes of the bonded joints and the properties of the adhesive coupons. Exposure to freeze-thaw cycles, both of adhesive coupons and joints, for a relatively long-term, was also studied and is described in the following pages. The associated experimental program is described next.

4.2.1 Materials

The materials adopted in present studies are exactly same as in chapter 3. Like in chapter 3, the component materials utilized in the fabrication of the joint specimens include two kinds of CFRP laminates (identified as HIT CFRP and SIKA CFRP as done before), steel plates and a commercial adhesive (SIKADUR 30). Detailed materials information does not repeat here.

4.2.2 Double strap bond specimens

Since the double strap CFRP-steel specimens for current studies are from the same batch used in the last chapter (Chapter 3), some information is not repeatedly described here. After preparation and cured of the specimens as done in chapter 2 and chapter 3, the specimens were mechanically tested (reference specimens at 0 h) or started aging.

4.2.3 Cycles for accelerated aging

Essentially periodic accelerated aging environments were imposed on the specimens, with each cycle lasting 12 hours for freeze-thaw environment, as shown in Figure 4.1. Freeze-thaw cycles from -20ºC to +20°C were imposed in a Fito Clima chamber and are defined in Figure 4.1. The change from -20ºC to +20ºC took 80 minutes at a rate of 0.5 °C/min, decreasing at the same rate from +20ºC to -20ºC avoiding thermal shock. The plateau lasted 4h40min each. The relative humidity (RH) was close to 50%. It is noted that the usual room temperature of 25ºC is higher than the starting temperature of the first freeze-thaw cycle. Some representative temperatures during the entire duration of the freeze-thaw cycles, i.e., +25ºC, +20ºC, +10ºC, -10ºC and -20ºC, are highlighted with letters “i”, “ii”, “iii”, “iv” and “v”, respectively, in Figure 4.1. After curing of the adhesive for 2 weeks at room temperature, most of the coupons were aged for 2,500 h, 5,000 h and 10,000 h.

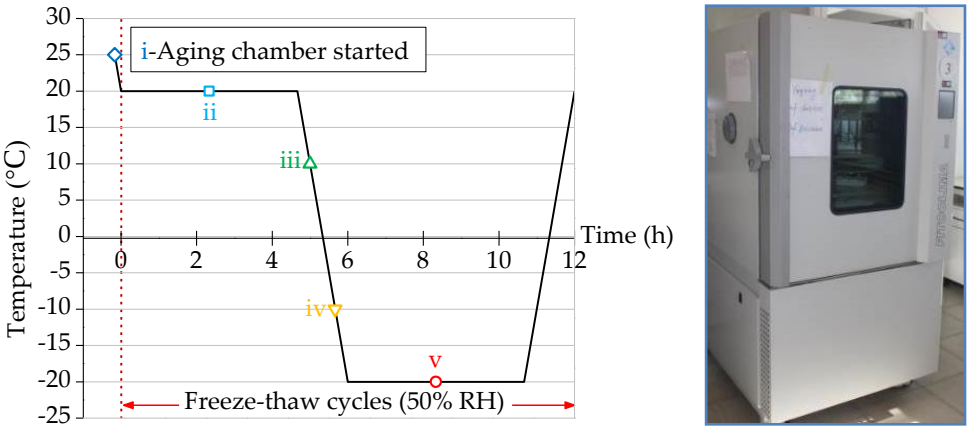

(a) (b)

Figure 4.1 - (a) Freeze-thaw cycle procedure; and (b) aging chamber.

4.2.4 Monotonic and cyclic tensile test set-up

Table 4.1 - ID of the specimens and corresponding conditions of the tests.

Specimen	ID	Aging actions	Exposure (h)	Loaded method	No. of cycles
HIT-bonded joints	REF-H-01 to 03	Reference	0	Monotonic	0
HIT-bonded joints	FT-H-01 to 03	Freeze-thaw	1,000	Monotonic	83 (thermal)
HIT-bonded joints	FT-H-04 to 06	Freeze-thaw	2,500	Monotonic	208 (thermal)
HIT-bonded joints	FT-H-07 to 09	Freeze-thaw	3,500	Monotonic	292 (thermal)
HIT-bonded joints	FT-H-10 to 12	Freeze-thaw	5,000	Monotonic	416 (thermal)
HIT-bonded joints	FT-H-13 to 15	Freeze-thaw	10,000	Monotonic	833 (thermal)
HIT-bonded joints	H-C-01 to 03	Reference	0	Cyclic	833 (mechanical)
SIKA-bonded joints	REF-S-01 to 03	Reference	0	Monotonic	0
SIKA-bonded joints	FT-S-01 to 03	Freeze-thaw	2,500	Monotonic	208 (thermal)
SIKA-bonded joints	FT-S-04 to 06	Freeze-thaw	5,000	Monotonic	416 (thermal)
SIKA-bonded joints	FT-S-07 to 09	Freeze-thaw	10,000	Monotonic	833 (thermal)
SIKA-bonded joints	S-C-01 to 03	Reference	0	Cyclic	833 (mechanical)
Adhesive coupon	REF-A-01 to 03	Reference	0	Monotonic	0
Adhesive coupon	FT-A-01 to 03	Freeze-thaw	2,500	Monotonic	208 (thermal)
Adhesive coupon	FT-A-04 to 06	Freeze-thaw	5,000	Monotonic	416 (thermal)
Adhesive coupon	FT-A-07 to 09	Freeze-thaw	10,000	Monotonic	833 (thermal)

A total of thirty-six CFRP-to-steel bonded joints including aged and control or reference specimens were tested for bond capacity as shown in Table 4.1. The three specimens from H-C series and the three specimens from S-C series were subjected to 833 mechanical cycles with a regular loading-unloading history with amplitudes of 2.9 kN and 2.3 kN, respectively, which represent approximately 17% and 18% of the maximum bond capacity of the specimens monotonically tested, respectively. The purpose of these tests was to compare the bond degradation of the joints subjected to 833 (equivalent to 10,000 h) freeze-thaw cycles with that where an equivalent slip was imposed. These comparisons may help to ascertain the role of the moisture during freeze-thaw aging. The thermal cyclic history of these tests was based on the results obtained from an analytical model which can only reflect the stress state of the bonded joints at initial aging stage, i.e., with aging and materials degradation, the stress state should be

changed (briefly presented in section 5) for estimating the performance of the specimens subjected to freeze-thaw aging conditions, and the results compared with those obtained from the specimens subjected to loading-unloading conditions. The possibility of these cyclic histories to induce, *per se*, damage into the adhesively bonded interface could be therefore, investigated in more detail. All quasi-static tests were performed with a Zwick 50 kN tensile machine according to a low tensile force rate corresponded to a displacement of 1 mm/min.

4.2.5 Glass transition temperature (T_g)

Dynamic mechanical analysis (DMA) of the adhesive was performed in dual cantilever mode using a DMA Q800 in order to obtain the values of the glass transition temperature T_g. The adhesive samples made for DMA experienced the same conditions like the adheisve coupons and CFRP-to-steel bonded joints as shown in Table 4.1. The sample prisms of 60×10×3 mm^3 were tested at a heating rate of 5 °C/min for a temperature range [30; 200]°C under a constant deformation amplitude of 10 μm. The Tg of the adhesive was determined by the temperature corresponding to the peak value of the Tanδ.

4.2.6 Scanning Electron Microscopy (SEM)

Images of the debonding surface of the CFRP laminate and steel plates after tests were obtained with both a Hitachi TM 3030Plus Tabletop and a PRO-X Phenom World Scanning Electron Microscope (SEM). The samples for scanning were cut from the specimens created for tensile and shear tests.

4.3. Results

4.3.1 Adhesive

In order to gain knowledge of the modifications undergone by the adhesive alone, likely important to understand the behavior of the joints, its characterization was carried out on individual flat coupons of SIKADUR 30.

Figure 4.2 shows values of the tensile mechanical properties of adhesive coupons at different aging times, i.e. at 0 h, 2,500 h, 5,000 h and 10,000 h. As shown in Figure 4.2a, the tensile stress-strain curves show non-linear behavior, starting from a major linear response that is lost when rupture is closer to occur.

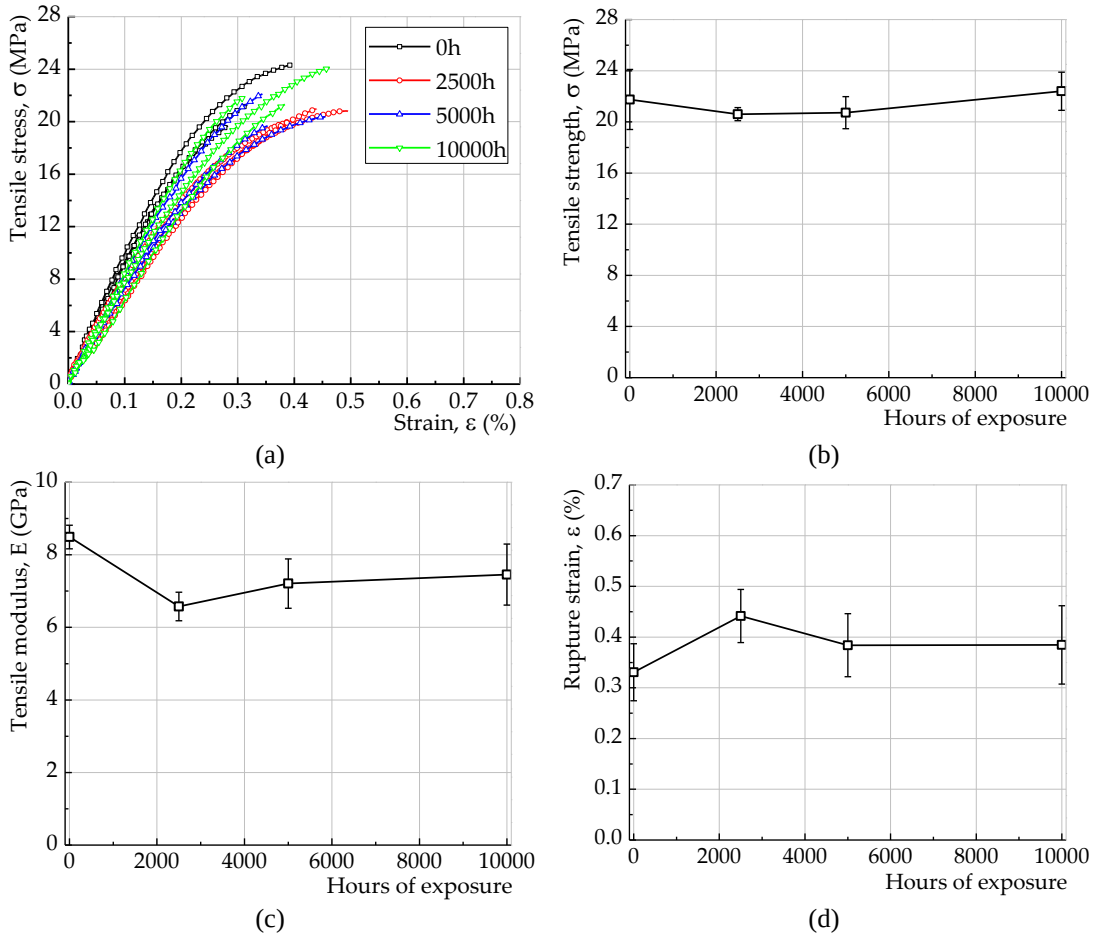

Figure 4.2 - Tensile stress-strain curves of adhesive coupon (a), tensile strength (b), modulus and rupture strain (c) and (d) after different number of freeze-thaw cycles.

Overall, the axial stiffness of the adhesive coupons was higher at 10,000 h than at 2,500 h and 5,000 h (Figure 4.2c), likely due to resin post-curing that proceeded and dominated the process for the entire period of 10,000h of exposure. The tensile fracture morphologies of the adhesive coupon were observed with SEM and are shown in Figure 4.3. The scatter of the results is related to the heterogeneity of the samples, with some "voids" formed inside the sample during their preparation due to the presence of air. Material identified in position "1" corresponds to inorganic filler particles inside the adhesive (e.g., SiO_2, Al_2O_3, etc.), and position "2" locates a void caused by an air bubble.

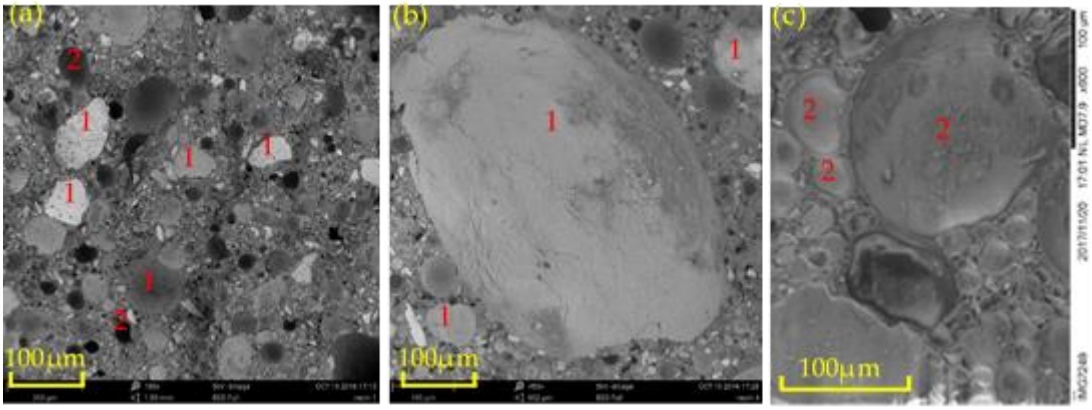

Obs.: The materials identified in the position "1" and "2" correspond to inorganic filler particles inside the adhesive (e.g., SiO_2, Al_2O_3, etc.) and to a void caused by an air bubble, respectively.

Figure 4.3 - SEM images after tensile failure of adhesive coupons at 0 h (a), 1,000 h (b), and 10,000 h (c) freeze-thaw exposure.

The T_g values obtained by DMA are summarized in Table 4.2. At the onset of aging, 0 h, the value of T_g was 67.0°C. An almost same value of T_g (66.8°C) was found after 2,500 h aging that slightly reduced to 64.5°C after 5,000 h aging. The last average value of T_g after 10,000 h of aging increased approximately 4.2ºC.

Table 4.2 - T_g values of adhesive after exposure to freeze-thaw aging.

Time of exposure (h)	T_g (°C)
0	67.0
2,500	66.8
5,000	64.5
10,000	71.2

As recognized in the literature [98, 99], T_g is affected by raising temperature and moisture, but no increase of those values was actually presented in the freeze-thaw cycles. The presence of moisture, however, may have induced microcracking when the negative temperatures led to formation of ice inside the adhesive and caused some lowering of T_g. The increase of 4.2°C after 10,000 h indicates that natural post-curing, after the initial 5,000 h, prevailed over the causes for its decrease.

4.3.2 CFRP-to-steel double strap joints

4.3.2.1 Effects of accelerated aging on the joint strength

The ultimate capacity for monotonic loading of HIT at 0 h, 1,000 h, 2,500 h, 3,500 h, 5,000 h, 10,000 h, and for SIKA at 0 h, 2,500 h, 5,000 h, 10,000 h, is shown in Table 4.3. The bond capacity was slightly affected by freeze-thaw aging, in both types of joints. The ultimate load of HIT bonded joints reached around 17kN, a value considerably higher than that of SIKA joints

that did not exceed approximately 13kN, though submitted to the same conditions. The ultimate load in the table refers to the ultimate load transferred to each of the two CFRP laminates.

Table 4.3 - Ultimate load for joints subjected to freeze-thaw cycles.

ID	Aging actions	Exposure (h)	Ultimate load (kN)	Average (kN)
REF-H-20-01 to 03	Reference	0	16.23/17.90/16.89	17.01
FT-H-20-01 to 03	Freeze-thaw	1,000	19.00/16.34/16.48	17.27
FT-H-20-04 to 06	Freeze-thaw	2,500	17.92/19.18/18.22	18.44
FT-H-20-07 to 09	Freeze-thaw	3,500	17.03/17.11/16.72	16.95
FT-H-20-10 to 12	Freeze-thaw	5,000	15.85/16.46/16.46	16.26
FT-H-20-13 to 15	Freeze-thaw	10,000	16.80/17.30/17.49	17.20
REF-S-20-01 to 03	Reference	0	12.06/13.71/13.03	12.93
FT-S-20-01 to 03	Freeze-thaw	2,500	12.02/15.45/14.76	14.08
FT-S-20-04 to 06	Freeze-thaw	5,000	11.46/14.51/14.01	13.33
FT-S-20-07 to 09	Freeze-thaw	10,000	15.25/12.32/13.41	13.66

Figure 4.4 shows the load-slip responses obtained for all tested specimens. Each load vs. slip curve is characterized by three different branches. The initially one is linear and it is followed by a short and nonlinear branch that makes the transition between the first and the third branches. The last branch is constant and its length depends on the bonded length adopted for the specimens, i.e. the more the bonded length is larger than the effective bond length more ductile the interface will be [70, 63]. These three branches also reflect the three different stages that can be locally identified through the bond-slip relationship. Therefore, the first and linear branch corresponds to the elastic stage of the interface whereas the second and nonlinear branch of the load vs. slip response corresponds to the interfacial softening of the interface. When this softening stage ends, the CFRP-to-steel interface debonds and the load transmitted to the CFRP reaches its maximum value. From that point onwards, and in the case of the bonded length is larger than the effective bond length, a visible plateau in the load vs. slip curves can be seen. Comparing the load vs. slip curves of the specimens subjected to freeze-thaw aging with the reference ones, it can be asseverated that no evident differences can be detected in both types of specimens, i.e. with HIT and SIKA laminates.

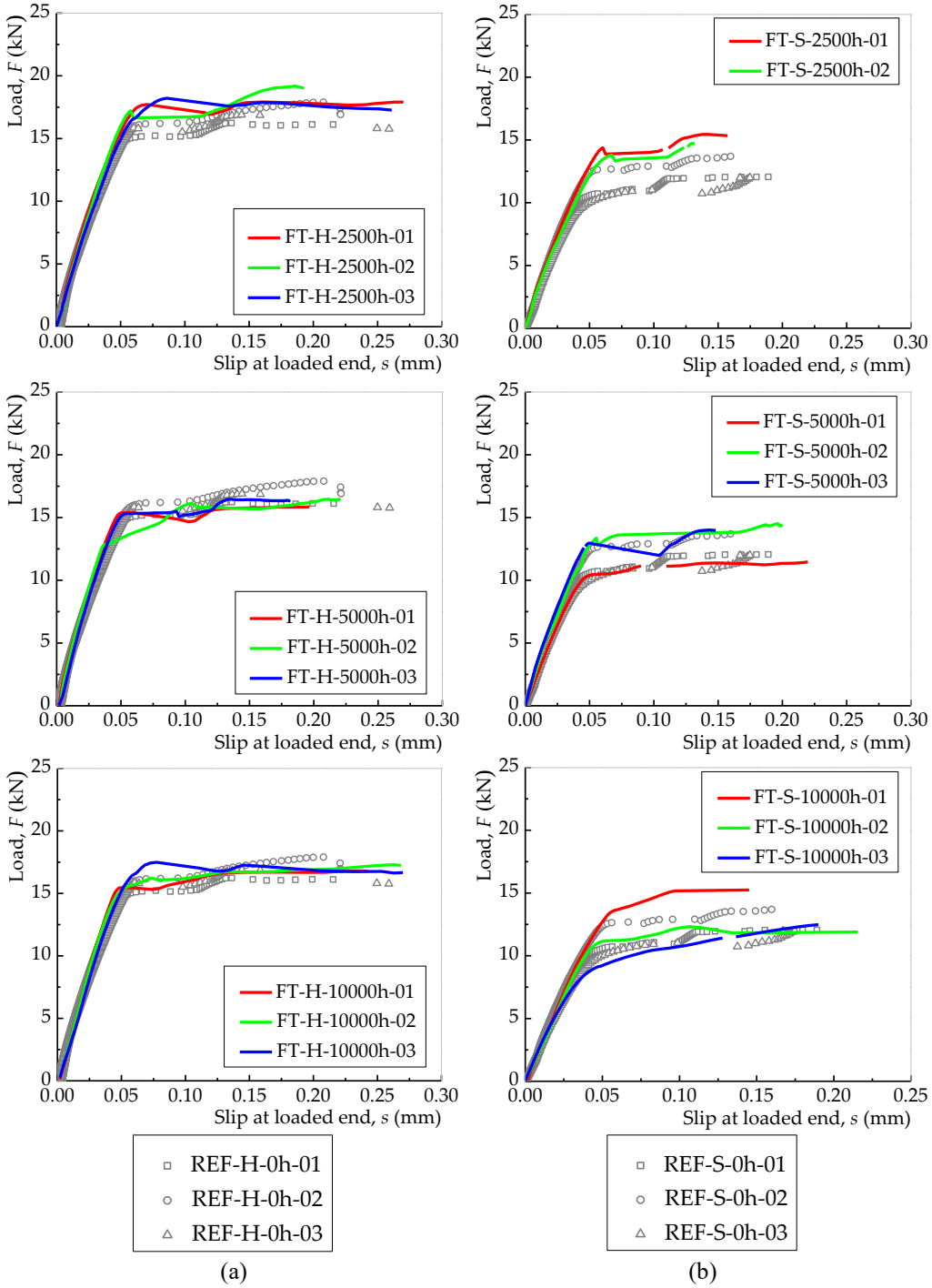

Figure 4.4 - Load-slip responses of the specimens: (a) HIT laminate; and (b) SIKA laminate.

4.3.2.2 Failure modes

The failure modes of the HIT and SIKA bonded joints aged 0 h, 2,500 h, 5,000 h and 10,000 h are shown in Figures 4.5 and 4.6. The failure modes of the joints were analyzed by observing the surface attached to the debonded CFRP laminate and the corresponding surface attached to steel. Figure 4.5a and Figure 4.5b show the failure surface of the CFRP and steel for both types of joints. The images from SEM show different failure modes for the two different CFRP

laminates. For joints with HIT material, the surface of the laminate was totally covered with adhesive, indicating cohesive failure mode. Many small holes could be seen in the adhesive, originated by the preparation of the samples that caused retention of air bubbles in the mixture similar to results published elsewhere [102]. In the case of the joints with SIKA laminates, part of the surface of the CFRP is covered with the adhesive (i.e. cohesive failure) and the remaining part of the CFRP surface is clearly seen (i.e. failure took place at the interface of CFRP and adhesive). Comparison of the fracture morphologies of the adhesive subjected to normal stress (coupon tensile tests, see Figure 4.3) and shear stress (joints Mode-II loading, see Figures 4.5a and 4.5b), showed no apparent difference.

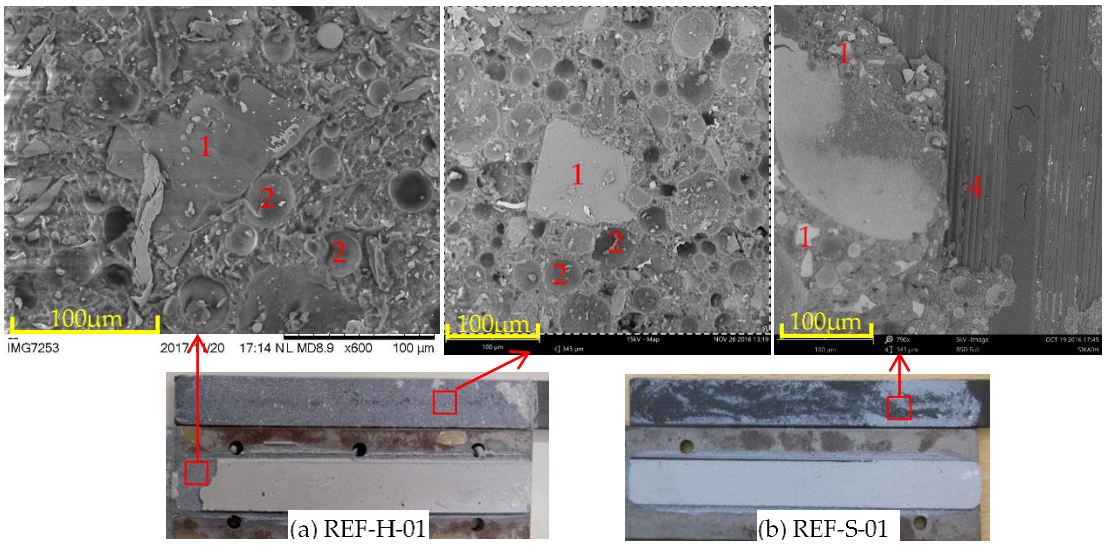

Obs.: The materials identified in the position "1", "3" and "4" correspond to inorganic filler particles inside the adhesive (e.g., SiO_2, Al_2O_3, etc.), steel and carbon fiber, respectively. Position "2" locates a void caused by an air bubble.

Figure 4.5 - Failure modes of the HIT (a) and SIKA (b) bonded joints at 0 h (Reference).

Observing the cohesive failure mode at 0 h, Figure 4.5a, it occurred in the adhesive adjacent to the steel rather than adjacent to the CFRP laminates and was limited to a small area at the free end of the bond length. The steel surface is all covered with adhesive in the small area. After 5,000 h of freeze-thaw cycles, the small area shown in Figure 4.6d became larger and the steel was clearly exposed. After 10,000h freeze-thaw cycles, a much enlarged area, estimated as half of the bonded area, was observed, and SEM revealed that the failure surface, on the interface with steel, had almost no adhesive, Figure 4.6e, indicating that failure occurred at the interface adhesive/steel.

The failure surfaces of the SIKA joints at 2,500 h, 5,000 h and 10,000 h aging are shown in Figure 4.6f-h and no changes could be identified associated with freeze-thaw aging, Figure 4.5b, Figure 4.6f-h. This result indicated that the interface of SIKA CFRP and adhesive was not strong

enough to ensure cohesive failure, and represented the weakest link in the bond after the freeze-thaw cycles.

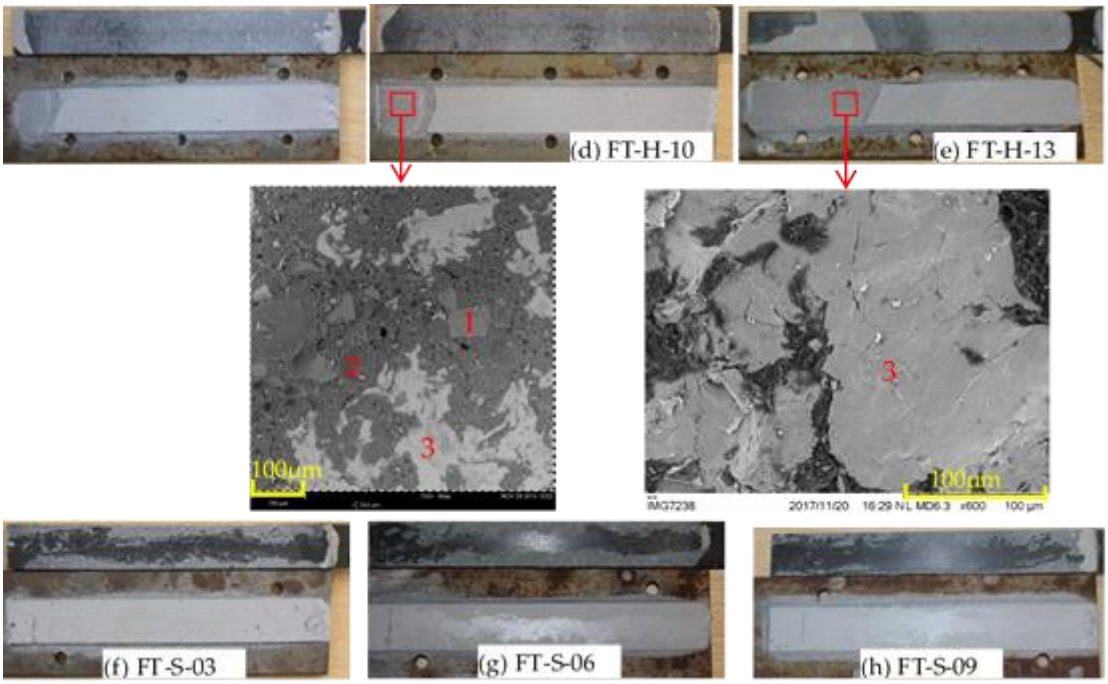

Obs.: The materials identified in the position "1", and "3" correspond to inorganic filler particles inside the adhesive (e.g., SiO_2, Al_2O_3, etc.), and steel, respectively. Position "2" locates a void caused by an air bubble.

Figure 4.6 - Failure modes of bonded joints submitted to 2,500 h, 5,000 h and 10,000 h freeze-thaw cycles for HIT (c)-(e) and for SIKA (f)-(h).

Bond between CFRP and adhesive was strong enough for the HIT joints, both after freeze-thaw cycles or subjected to natural aging. In addition, HIT and SIKA bonded joints showed different failure modes, indicating that the interfacial adhesion between adhesive and HIT laminates was stronger than with SIKA laminates. The freeze-thaw cycles degraded the interfacial adhesion between adhesive and steel, causing failure to occur at the interface in the HIT joints. Similar change of the failure mode due to freeze-thaw aging has been reported in the literature [22, 24].

4.4 Bond-slip relationship of the adhesively bonded joints

4.4.1 Experimental determination

The interfacial bond-slip relationship of the CFRP-to-steel interface, both for monotonic and equivalent cyclic tests, was calculated from the original data collected through the strain gauges mounted on the CFRP laminate along the bond length (the distributions of strain gauges are same as shown in chapter 3). The bond stresses developed within the interface were calculated assuming that they are constant between two consecutive strain gauges, and the following

equation is commonly used

$$\tau(x_{i+1/2}) = E_{CFRP} \cdot t_{CFRP} \frac{\varepsilon_{CFRP,i+1} - \varepsilon_{CFRP,i}}{x_{i+1} - x_i} \quad (4.1)$$

where $\varepsilon_{CFRP,i+1}$ and $\varepsilon_{CFRP,i}$ are, respectively, the strains in the CFRP laminate at point i+1 and point i; and the difference $(x_{i+1} - x_i)$ is the distance between two consecutive points. The calculation of the slip developed within the CFRP-to-steel interface is more complicated when compared to single shear bonded joint. In the case of double strap bonded joints, the deformations in the steel substrate should not be ignored in the caculation of the relative displacements (or slips) between the CFRP and the steel substrate. Thus, as shown in previous publications [85, 103], the slips can be calculated according to

$$s(x_{i+1}) = \int_{x_i}^{x_{i+1}} (\varepsilon_{CFRP} - \varepsilon_{steel})\, dx + s(x_i) \approx \quad (4.2)$$

$$\approx \left[\frac{\varepsilon_{CFRP,i+1} + \varepsilon_{CFRP,i}}{2} - \frac{\varepsilon_{steel,i+1} + \varepsilon_{steel,i}}{2}\right] \cdot (x_{i+1} - x_i) + s(x_i)$$

where $s(x_{i+1})$ is the slip at point x_{i+1} and $\varepsilon_{steel,i+1}$ and $\varepsilon_{steel,i}$ are the strains in the steel plate at points x_{i+1} and x_i, respectively. Since the bond stresses were evaluated at midpoints, the corresponding average value of the slip is

$$s(x_{i+1/2}) = \frac{1}{2}(s_{x_{i+1}} + s_{x_i}) \quad (4.3)$$

where subscript i+1/2 corresponds to the middle point beween i and i+1. The largest slip occurred at the CFRP loaded end where the data for the complete bond-slip curve should be obtained. Typical bond-slip curves at 12.5 mm from the CFRP loaded end (i.e., x = 137.5 mm) were thus chosen and are herein reported. As it will be seen later, the determination of the slip due to temperature only should be made in a different way.

4.4.2 Influence of the freeze-thaw cycles

The interfacial bond-slip curves of boned joints (HIT and SIKA) aged at 0 h, 2,500 h, 5,000 h and 10,000 h were obtained by the method mentioned above and presented in Figure 4.7. As shown in the figures, the HIT bond-slip curves at different time stages (Figure 4.7a-d) are almost similar. In addition, no significant differences are observed in the SIKA bond-slip curves at 0 h, 2,500 h, 5,000 h and 10,000 h of exposure (Figure 4.7e-h). These results corresponded to their bond capacity and despite the knee observed in the softening branches of the results (attributed to some imperfections, i.e. lack of linearity of the specimens that enables the development of compression stresses perpendicular and along the CFRP-to-steel joints), they could be simply approximated by a bilinear bond-slip relationship like did in chapter 3 [103]. In addition, by comparison of the HIT and SIKA bond-slip curves it was found that they had

the same initial stiffness as expected, since both had been used with the same adhesive (SIKA-30), preparation and curing. The maximum bond stresses (approximately 20MPa) for HIT specimens were higher than those obtained for the SIKA laminate (approximately 15MPa) indicating that damage initiation in the bond between the SIKA laminates and steel was much earlier than that of HIT, which is attributed to the interfacial bond strength between HIT laminates and the adhesive that provided a stronger and better adhesion with these CFRP laminates than with SIKA laminates. Overall, weak interfacial bond strength (SIKA with mixed failure mode) led to damage initiation in the interface, whereas strong interfacial bond strength (HIT with cohesive failure mode) led to the damage initiation that occurred in the adhesive and delayed the damage initiation in the bond.

4.5 Influence of the temperature cycles on the bonded interface

4.5.1 Analytical approach

The thermal shear stresses developed in the bonded interface due to the different linear thermal expansion coefficient of CFRP laminates and steel can be a critical factor on the damage of the bonded joints [92-94]. In this section, the interfacial stresses and slips developed in the double strap CFRP-to-steel joints in the case of entire temperature range (i.e., from +25°C to -20°C) of accelerated freeze-thaw environment are predicted. Then, the bond response of the joints when an external pulling load acts on the CFRP loaded end (i.e., at x = 150 mm) is determined and compared with the bond response due to temperature change.

Thus, for the analytical prediction of the temperature influence on the adhesively bonded interface, the equilibrium of segment *dx*, see Figure 4.8, led to

$$\frac{d\sigma_{CFRP}(x)}{dx} - \frac{\tau(x)}{t_{CFRP}} = 0, \tag{4.4}$$

$$\frac{d\sigma_{steel}(x)}{dx} + \frac{2b_{CFRP} \cdot \tau(x)}{b_{steel} \cdot t_{steel}} = 0 \tag{4.5}$$

and

$$2 \cdot \sigma_{CFRP}(x) \cdot b_{CFRP} \cdot t_{CFRP} + \sigma_{steel}(x) \cdot t_{steel} \cdot b_{steel} = 0. \tag{4.6}$$

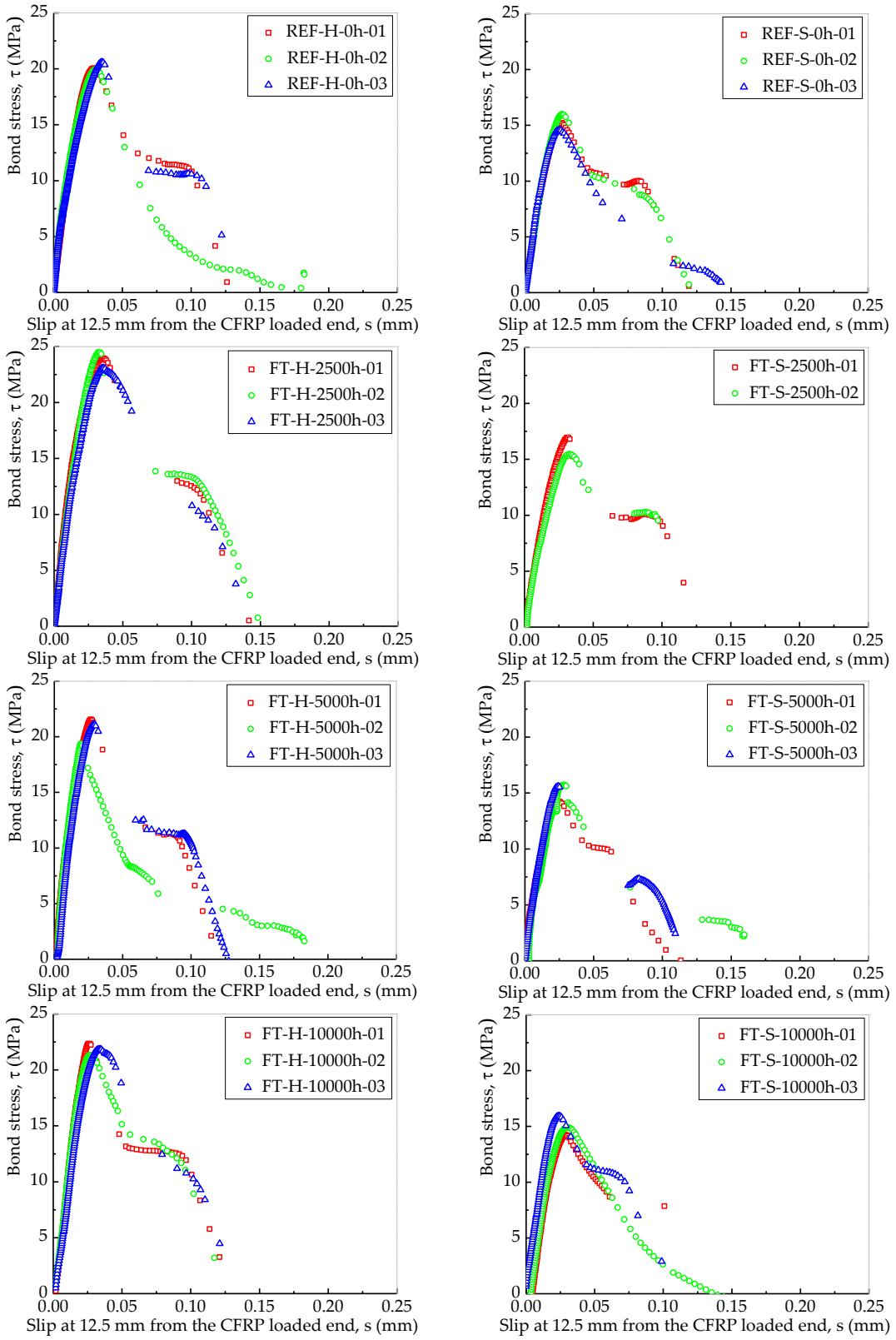

Figure 4.7 - Bond-slip curves with freeze-thaw cycles: (a) HIT laminate; and (b) SIKA laminate.

The strains in both materials (ε), CFRP laminate and steel, can be determined according to:

$$\varepsilon = \varepsilon_F + \varepsilon_{\Delta T} \tag{4.7}$$

where ε_F and $\varepsilon_{\Delta T}$ are the strains in both materials due to the mechanical and temperature actions, respectively. Assuming that during the process of temperature variations, both materials are always in their elastic regime, the axial stresses in the CFRP laminate and steel are, respectively:

$$\sigma_{CFRP}(x) = E_{CFRP} \cdot \left(\frac{du_{CFRP}(x)}{dx} - \alpha_{CFRP} \cdot \Delta T \right) \tag{4.8}$$

and

$$\sigma_{steel}(x) = E_{steel} \cdot \left(\frac{du_{steel}(x)}{dx} - \alpha_{steel} \cdot \Delta T \right) \tag{4.9}$$

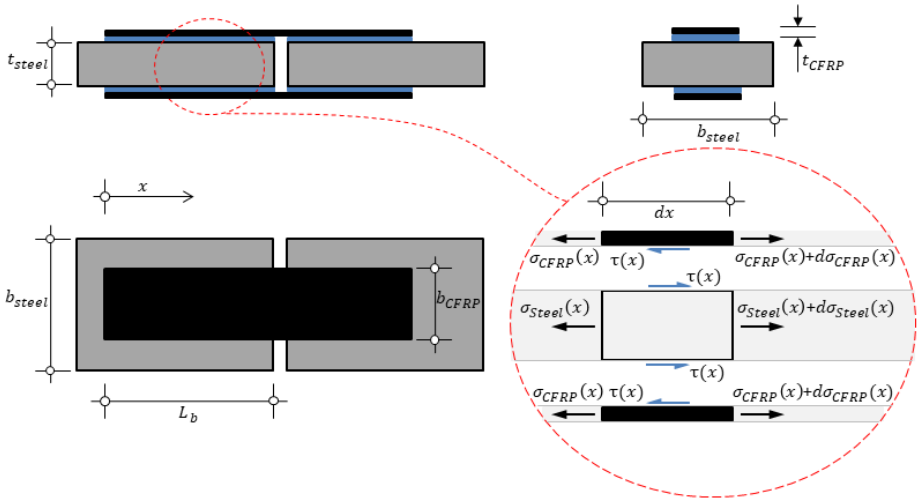

Figure 4.8 - Equilibrium of forces in the CFRP/steel interface under temperature changes.

where E_{CFRP} and E_{steel}, and, α_{CFRP} and α_{steel}, and, u_{CFRP} and u_{steel} are, respectively, the Young's moduli, the linear coefficients of thermal expansion and the displacements of the CFRP laminate and steel; ΔT is the difference between the final temperature (T_f) and its initial value T_i, i.e. $\Delta T = T_f - T_i$; and du_{CFRP}/dx and du_{steel}/dx are, respectively, the axial strains (ε) in the CFRP laminate and in the steel. The relative displacement between CFRP and steel, i.e. interfacial slip (s), is determined according to:

$$s = u_{CFRP} - u_{steel} \tag{4.10}$$

Differentiating Eq. (4.10) with respect to x and introducing Eqs. (4.8) and (4.9) yields:

$$\frac{ds(x)}{dx} = \frac{\sigma_{CFRP}(x)}{E_{CFRP}} - \frac{\sigma_{steel}(x)}{E_{steel}} + (\alpha_{CFRP} - \alpha_{steel}) \cdot \Delta T. \tag{4.11}$$

Differentiating Eq. (4.11), Eqs. (4.4) and (4.6) leads to

$$\frac{d^2s(x)}{dx^2} - \lambda^2 \cdot \tau(x) = 0 \tag{4.12}$$

where

$$\lambda^2 = \frac{1}{E_{CFRP} \cdot t_{CFRP}} + \frac{2 \cdot b_{CFRP}}{E_{steel} \cdot t_{steel} \cdot b_{steel}}. \tag{4.13}$$

Combining Eqs. (4.6) and (4.11), the axial stresses in the CFRP laminate are

$$\sigma_{CFRP}(x) = \frac{E_{CFRP}}{1+2\beta} \cdot \left[\frac{ds(x)}{dx} - (\alpha_{CFRP} - \alpha_{steel}) \cdot \Delta T\right]. \tag{4.14}$$

where β is the axial stiffness ratio between CFRP laminates and steel plate defined as:

$$\beta = \frac{(E \cdot A)_{CFRP}}{(E \cdot A)_{steel}} \tag{4.15}$$

where A_{CFRP} and A_{steel} are the cross-sectional areas of one CFRP laminate and of the steel bar, respectively. From Eq. (4.6)

$$\sigma_{steel}(x) = \frac{2\beta \cdot E_{steel}}{1+2\beta} \cdot \left[(\alpha_{CFRP} - \alpha_{steel}) \cdot \Delta T - \frac{ds(x)}{dx}\right]. \tag{4.16}$$

The solution of Eq. (4.12) depends on the bond-slip law that represents the local behavior of the CFRP laminate-to-steel interface, already defined from monotonic tests on CFRP-to-steel joints, see Figure 4.7.

For small slips, bond-slip can be approximated by a linear ascending law

$$\tau(x) = \frac{\tau_f}{s_1} \cdot s(x) \quad \text{if} \quad 0 \le s(x) \le s_1 \tag{4.17}$$

where s_1 is the slip at τ_f, maximum bond stress developed in the adhesively bonded interface. Introducing Eq. (4.17) into Eq. (4.12) leads to

$$\frac{d^2s(x)}{dx^2} - \gamma^2 \cdot s(x) = 0 \tag{4.18}$$

where

$$\gamma^2 = \frac{\tau_f}{s_1} \cdot \lambda^2. \tag{4.19}$$

Introducing the boundary conditions of $\sigma_{CFRP} = 0$ at $x = 0$ and $x = L_b$ [104, 105], the interfacial slip distribution throughout the bonded length is

$$s(x) = \frac{(\alpha_{CFRP} - \alpha_{steel}) \cdot \Delta T}{\gamma} \cdot \left\{[1 - \cosh(\gamma \cdot L_b)] \cdot \frac{\cosh(\gamma \cdot x)}{\sinh(\gamma \cdot L_b)} + \sinh(\gamma \cdot x)\right\}. \tag{4.20}$$

Then, the interfacial shear stress is

$$\tau(x) = \frac{\tau_f}{s_1} \cdot \frac{(\alpha_{CFRP} - \alpha_{steel}) \cdot \Delta T}{\gamma} \cdot \left\{ [1 - \cosh(\gamma \cdot L_b)] \cdot \frac{\cosh(\gamma \cdot x)}{\sinh(\gamma \cdot L_b)} + \sinh(\gamma \cdot x) \right\}. \tag{4.21}$$

The strain in the CFRP laminate can be found equating Eq. (4.8) to Eq. (4.14)

$$\varepsilon_{CFRP}(x) = \frac{1}{1 + 2\beta} \cdot \left[\frac{ds(x)}{dx} + (2\beta \cdot \alpha_{CFRP} + \alpha_{steel}) \cdot \Delta T \right]. \tag{4.22}$$

Introducing the derivative of Eq. (4.20) with respect to *x* into Eq. (4.22), yields:

$$\varepsilon_{CFRP}(x) = \frac{\Delta T}{1 + 2\beta} \cdot \left\{ (\alpha_{CFRP} - \alpha_{steel}) \cdot \left[(1 - \cosh(\gamma \cdot L_b)) \cdot \frac{\sinh(\gamma \cdot x)}{\sinh(\gamma \cdot L_b)} + \cosh(\gamma \cdot x) \right] + (2\beta \cdot \alpha_{CFRP} + \alpha_{steel}) \right\}. \tag{4.23}$$

The strain distributions in the steel plate is obtained equating Eq. (4.9) to Eq. (4.16):

$$\varepsilon_{steel}(x) = \frac{1}{1 + 2\beta} \cdot \left[(2\beta \cdot \alpha_{CFRP} + \alpha_{steel}) \cdot \Delta T - 2\beta \cdot \frac{ds(x)}{dx} \right] \tag{4.24}$$

leading finally to

$$\varepsilon_{steel}(x) = \frac{2\beta \cdot \Delta T}{1 + 2\beta} \cdot \left\{ \frac{\alpha_{steel}}{2\beta} - (\alpha_{CFRP} - \alpha_{steel}) \cdot \left[(1 - \cosh(\gamma \cdot L_b)) \cdot \frac{\sinh(\gamma \cdot x)}{\sinh(\gamma \cdot L_b)} + \cosh(\gamma \cdot x) \right] \right\}. \tag{4.25}$$

4.5.2 Global interfacial response

The linear coefficients of thermal expansion of the CFRP laminate and steel were α_{CFRP} = -0.3×10^{-6} /ºC [93] and α_{steel} = 12×10^{-6} /ºC [94], respectively. The reference temperature was 25°C and ΔT denotes the uniform temperature variation imposed on the specimens. From the freeze-thaw ageing conditions of the specimens, the temperatures: 25°C, 20°C 10°C, -10°C and -20°C were selected to be shown here and marked with letters “i”, “ii”, “iii”, “iv” and “v” in Figure 4.1 and the corresponding temperature variations (ΔT) were 0°C, -5°C, -15°C, -35°C and -45°C.

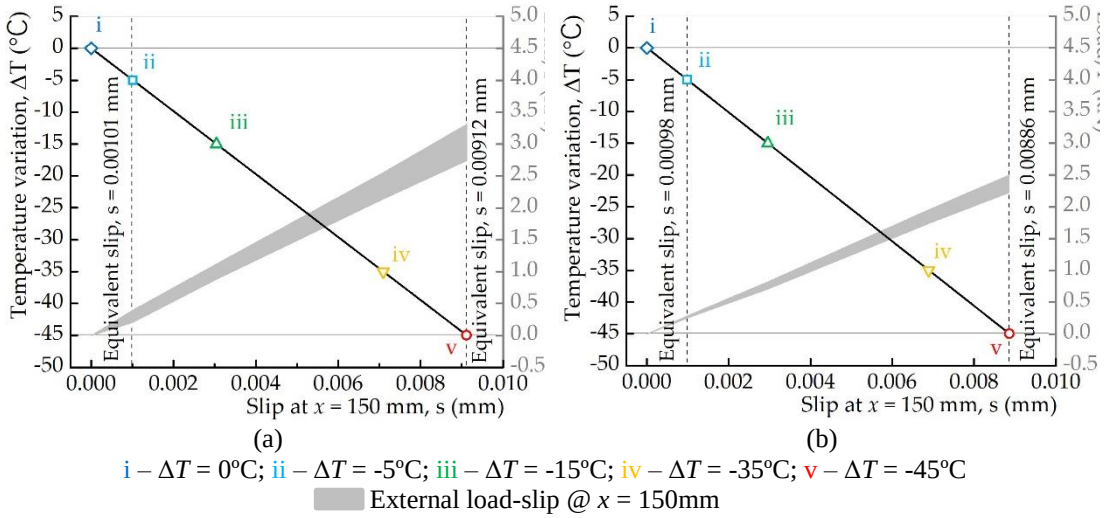

Figure 4.10 - Comparison of global interfacial response of bonded joints induced by temperature changes and from equivalent external load: (a) HIT and (b) SIKA.

The thermal interfacial slip at any of the two CFRP free ends (at x = 0 or 150 mm) induced by temperature change, hereafter called thermal global interfacial response, can be obtained from Eq. (4.20) as previously derived. The thermal interfacial slip at x = 150 mm is illustrated in Figure 4.10a for HIT and Figure 4.10b for SIKA. If a larger temperature variation is considered, then a larger thermal interfacial slip results. Figure 4.9 also displays the external load vs. interfacial slip at the same position, x = 150 mm, obtained from experimental monotonic tests. Figure 4.9 shows the same interfacial slip at x = 150 mm corresponding to temperature variation or to an external load. The global interfacial response at the temperatures marked in Figure 4.1 is highlighted in Figure 4.9, and an external monotonic loading was found that produced the same interfacial slip response independently of the action, thermal or mechanical, that the specimen is subjected to. The global interfacial response obtained from the three unaged HIT specimens shown in Figure 4.9a reached higher load and slip when compared with that for the SIKA joints in Figure 4.9b. That difference may be attributed to the higher modulus of the HIT laminates when compared to the SIKA laminates (see Table in chapter 3). For instance, when ΔT = -45°C, the interfacial slip $s = 9.12\times10^{-3}$ mm for HIT and $s = 8.86\times10^{-3}$ mm for SIKA, corresponding to equivalent loads of 2.9 kN and 2.3 kN, respectively.

4.5.3 Slip and bond stress distributions

The thermal interfacial slip and bond stress were calculated for the selected temperatures of the freeze-thaw cycles, using Eq. (4.20) and Eq. (4.21). Figure 4.10 shows the slip and the interfacial stress distribution along the bond length for HIT (Figure 4.10a-b) and SIKA (Figure 4.10d-e) joints. The thermal interfacial stress and slip exhibit anti-symmetrical distribution about the midpoint of the bond length (i.e., at x = 75 mm). The interfacial stress and slip increased with decreasing temperature, i.e., with the amplitude of the temperature variation.

The modulus of the CFRP laminates applied in the joints had significant importance on the thermal shear stress in the interface CFRP-to-steel. Higher modulus of CFRP led to larger thermal interfacial stress and slips consistent with other results reported in the literature [94].

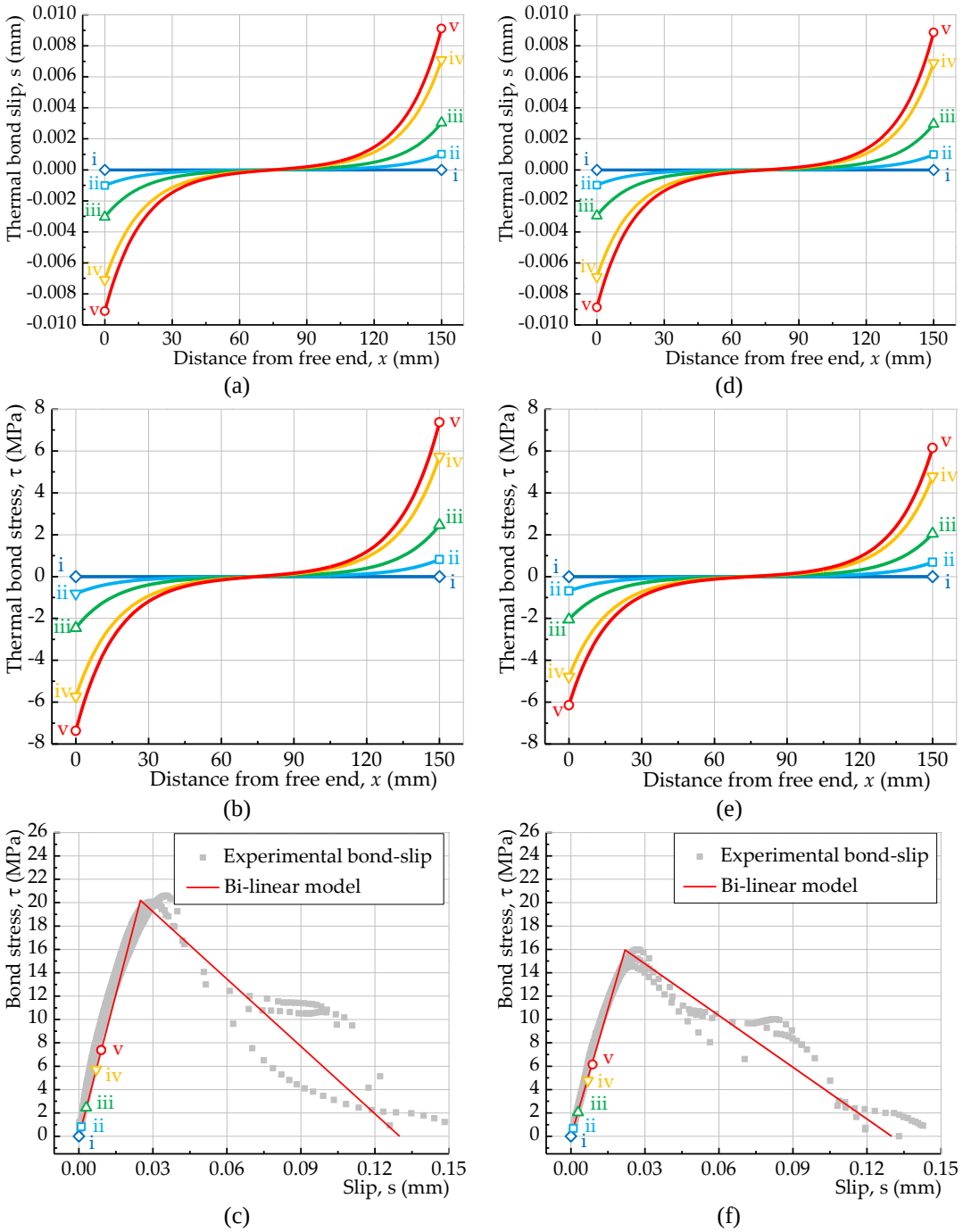

i – ΔT = 0ºC; ii – ΔT = -5ºC; iii – ΔT = -15ºC; iv – ΔT = -35ºC; v – ΔT = -45ºC (from analytical proposed model)

Figure 4.10 - Interfacial stress and interfacial slip distribution at some representative temperatures; and comparison of local interfacial response of bonded joints subjected to external loading and loads induced by temperatures; HIT (a)-(c) and SIKA (d)-(f).

The relationships between the local interfacial stress and slip induced by temperature were also

compared with those induced by experimental monotonic loading. As shown in Figure 4.10c for HIT and Figure 4.10f for SIKA, the local interfacial response of bonded joints due to temperature followed the bond-slip relationship obtained from experimental monotonic loading. From the points highlighted in Figure 4.10c and Figure 4.10f, which correspond to the selected temperatures in Figure 4.1, it can be seen that the thermal interfacial stress vs. slip tracked the experimental bond vs. slip curves and covered a very limited range of the ascending stage (usually designated as *elastic stage*) of the experimental bond-slip curve.

4.5.4 Strain distribution in the CFRP laminate and steel plate

The strain distributions of CFRP laminates and steel plates (obtained from Eq. (4.23) and Eq. (4.25)) have a symmetric development around the middle point of the bond length, i.e. at x = 75 mm. For the previously mentioned selected temperatures, the corresponding strain distributions in the CFRP laminates and steel plate, at temperatures corresponding to the freeze-thaw condition, are illustrated in Figure 4.11a for HIT and Figure 4.11b for SIKA laminates. The negative values of the CFRP laminates and steel plate strain indicate that the two materials actually shrunk during freeze-thaw aging conditions. The strains in the steel plate can be determined from those measured in the CFRP laminate by introducing Eq. (4.8) and Eq. (4.9) into Eq. (4.6) leading to:

$$\varepsilon_{steel}(x) = -2\beta \cdot \varepsilon_{CFRP}(x) + \Delta T \cdot (2\beta \cdot \alpha_{CFRP} + \alpha_{steel}). \tag{4.26}$$

Since the strains developed in the steel plate were not measured, they were obtained from Eq. (4.26), where the strains in the CFRP laminate were actually measured during one freeze-thaw cyclic.

Overall, it can be stated that the estimated strain distributions due to a negative temperature variation was negative, i.e. the steel plate began to shrink. At the same time, a compression force was also installed in the CFRP laminates. At the middle of the bonded end, i.e. at x = 75 mm, since there is no slip within the interface, full compatibility between materials causes the same deformations in CFRP and steel at that point. As slips began to develop throughout the bonded length, the strains developed in the CFRP laminate and in the steel began to diverge. The strains in the steel plate decreased (negative value) whereas the strains in the CFRP increased, reaching the minimum and maximum values in the steel and CFRP laminate at both ends, respectively.

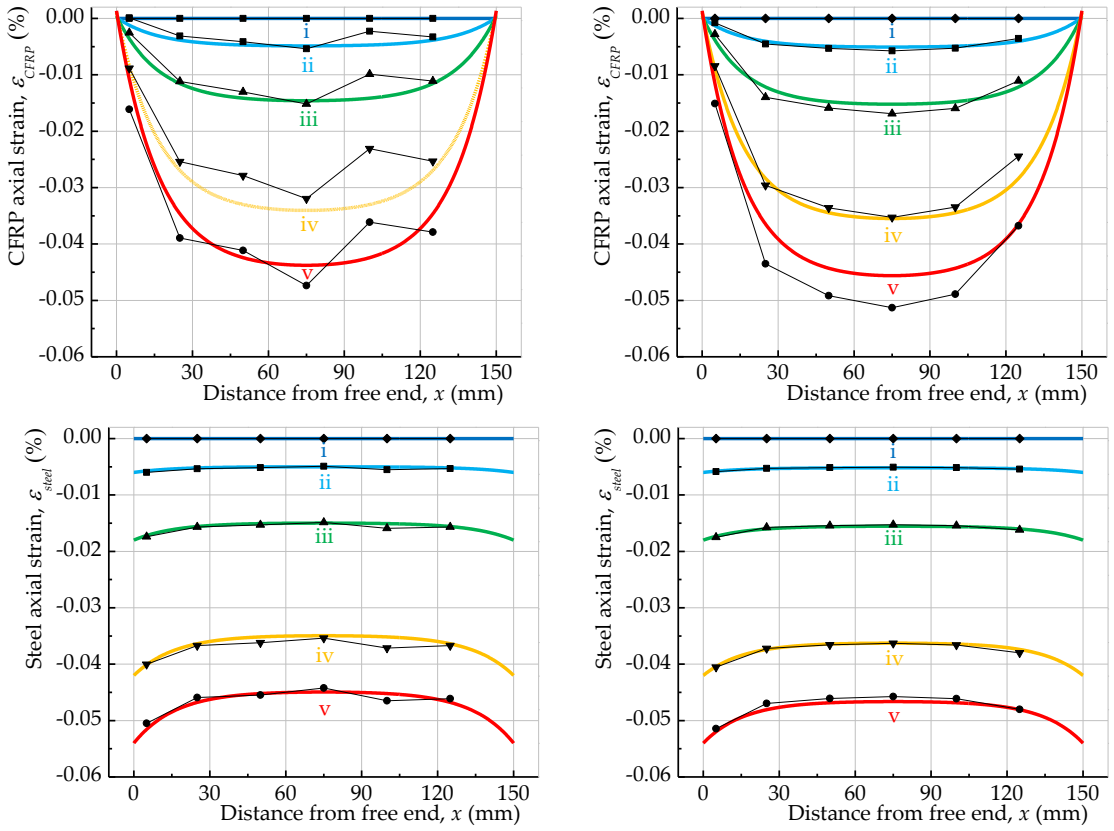

i – ΔT = 0ºC; ii – ΔT = -5ºC; iii – ΔT = -15ºC; iv – ΔT = -35ºC; v – ΔT = -45ºC (from analytical proposed model)

Figure 4.11 - Strain distribution of materials at some representative temperatures during freeze-thaw cycles: (a) HIT bonded joints; (b) SIKA bonded joints.

4.6 Thermal vs. Mechanical cycles

In this section, a comparison between monotonic tests after exposure to freeze-thaw cycles and an "equivalent slip" is made; effects of 833 temperature cycles [20°C; -20°C] of specimens prepared at 25°C room temperature and those caused by mechanical (monotonic) loading are compared. The strains developed in two different specimens, HIT and SIKA laminates were experimentally determined during one freeze-thaw cycle. The bond stresses were calculated according to Eq. (4.1) and the slips according to Eq. (4.22) after integrating *ds*/*dx*. Hence, exclusively due to temperature variation, the slips were numerically calculated according to

$$s(x_{i+1}) = \int_{x_i}^{x_{i+1}} ((1+2\beta)\cdot\varepsilon_{CFRP} - (2\beta\cdot\alpha_{CFRP} + \alpha_{steel})\cdot\Delta T)\,dx + s(x_i) \approx \tag{4.27}$$

$$\approx \left[(1+2\beta)\frac{\varepsilon_{CFRP,i+1} + \varepsilon_{CFRP,i}}{2} - (2\beta\cdot\alpha_{CFRP} + \alpha_{steel})\cdot\Delta T\right]\cdot(x_{i+1} - x_i) + s(x_i).$$

As analyzed in the last section, external loads and temperatures applied on the CFRP loaded end (i.e., at x = 150 mm) cause the same interfacial bond-slip response. Thus, it is reasonable

to assume an equivalency between load and temperature cycles and replace temperature vatiation by an external cyclic loading, in order to find the bond cumulative response of joints subjected to temperature cycles.

For the same equivalent slip developed at x = 150 mm, the minimum and maximum cyclic loading corresponding to the temperatures at 20°C and -20°C, respectively, were 0.32 kN and 2.9 kN for HIT, 0.25 kN and 2.3 kN for SIKA, respectively, as displayed in Figure 4.8a and 8b. Figure 4.12 shows the slip (Figure 4.12a and 4.12c) and bond stress (Figure 4.12b and 4.12d) distributions along the bond length induced by the external loads. These distributions throughout the bonded length of the adhesively bonded joint correspond to final temperatures of 20°C and -20°C and to the corresponding external load 0 kN and 2.9 kN for HIT and external load 0 kN and 2.3 kN for SIKA. In the same conditions, Figure 4.13a and c and Figure 4.13b and d show the strains developed in the CFRP laminates and as well as the strains developed in the steel plate.

The figures show, for instance, that the interfacial stress distribution created by temperature between 75 mm and 150 mm agrees well with that created by the external loads (applied at x = 150 mm) whereas in the other part of the bonded length (between 0 and 75 mm) both actions cause different responses. However, as shown in [73], for low axial stiffness ratios (see Eq. (4.15)) such as those used for the current specimens (with β = 0.20 and β = 0.16 for HIT and SIKA laminates, respectively), the slip and bond stress distributions at those areas and their interfacial responses should be very limited and for such low load levels (2.9 kN and 2.3 kN for HIT and SIKA joints) those bonded regions almost keep their initial undeformed state.

Figure 4.13 also shows the comparison of the strain distributions in both materials induced by temperature variation and external load for HIT and SIKA bonded joints (Figure 4.13a and c) and steel plates (Figure 4.13b and d). The strains developed due to the application of an external load to the specimens and due to temperature are quite different. Actually, in the case of negative temperature variation, the CFRP laminates and steel shrink whereas when subjected to an external load both materials develop positive strains. However, since the thermal coefficient of the steel plate is much larger than that of the CFRP laminates, such difference led the bonded interface to behave similarly to the cases where a load was applied to the CFRP loaded end (i.e., 150 mm), as previously analyzed. So, despite the differences between the strain distributions in both loading situations, thermal and mechanical, such differences do not affect the feasibility of the equivalent slip method, since it is focused on the interfacial bond-slip behavior.

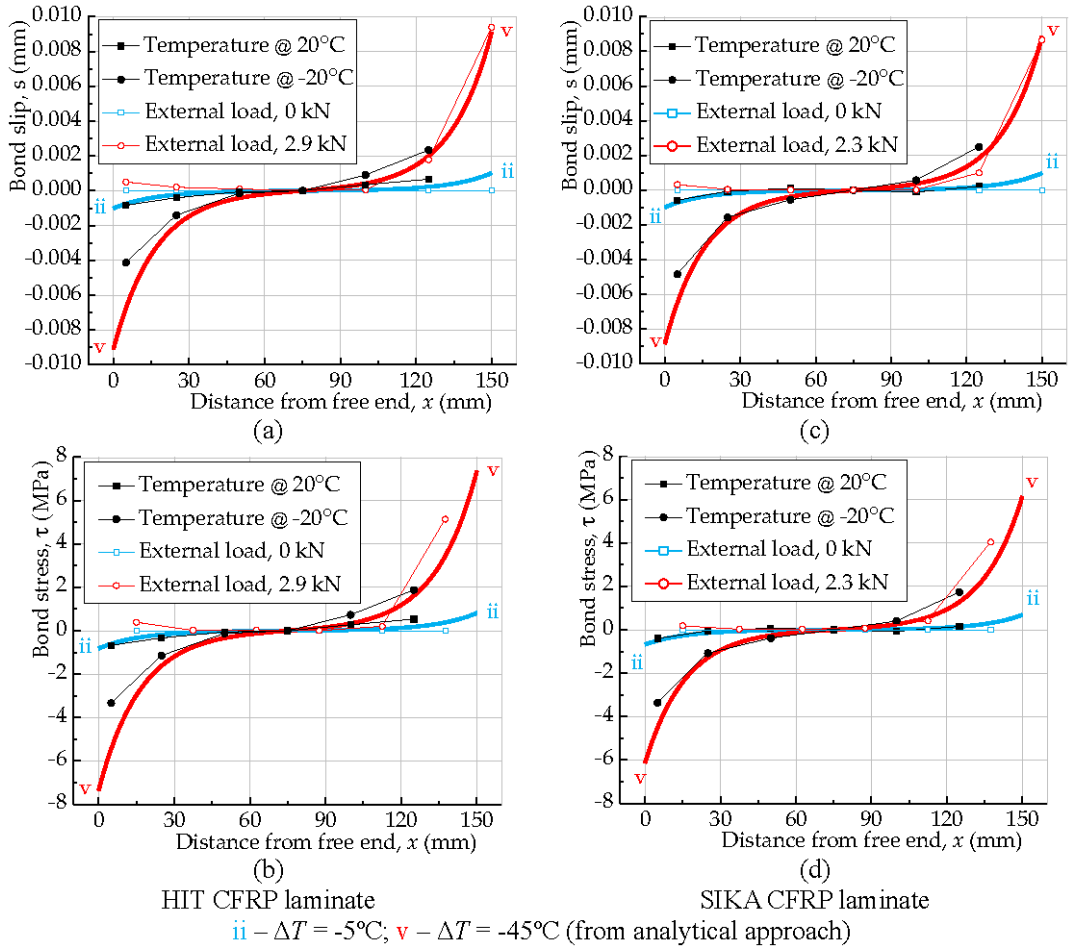

Figure 4.12 - Comparison between slip and bond stress distributions when thermal and mechanical loads are applied to the HIT bonded joint (a)-(b) (specimen H-M-01) and SIKA bonded joint (c)-(d) (specimen S-M-03).

Usually, the variation of the interfacial bond-slip relationship can be used as a macroscopic or indirect characterization of the damage of the joint, e.g., micro-cracks or voids induced by loading. In other words, with these modifications of the adhesive materials or adhesive/adherent interfacial region, with aging, the interfacial bond-slip curve must make corresponding changes, e.g. lower slope, larger hysteresis area (correspondent to dissipated energy per cycle). For the present case, 833 equivalent cycles, each from 0 kN to 2.9 kN for HIT and from 0 kN to 2.3 kN for SIKA, were applied to the CFRP-to-steel joints and the interfacial cyclic bond-slip relationships were obtained and compared with the monotonic bond-slip relationship. Figure 4.14 illustrates the comparison of the equivalent thermal cyclic bond-slip curves (833 cycles) with the experimental monotonic bond-slip curves at the closest measured point of 137.5 mm, i.e. measured between the two consecutive strain gauges closer to the CFRP pulling load and located at the center of the specimen. As shown in Fig. 4.14, the ascent of the cyclic bond-slip curve tracked the monotonic one. Those results show no change of the bond-slip stiffness or no interfacial energy dissipated with the mechanical cycles neither, indicating that no damage

occurred in the interface of the bonded joints when subjected to 833 equivalent thermal cycles. Actually, in chapter 3 [103], a similar conclusion was already obtained: for repeated loading associated with bond stresses below its maximum value, i.e. under the elastic regime of the interface, no damage occurs.

Therefore, it can be stated that unlike what would be the initial expectation, the thermal interfacial cyclic stress induced by temperature cycles between 20°C and -20°C with a 25°C reference temperature had a low impact on the interfacial behavior since the maximum stress could not be reached during these thermal cycles and thus, imposed, *per se*, no damage to the interface. Based on the above analysis, it can be stated that thermal cycles (from -20°C to 20°C) have marginal impact on the bond between the CFRP laminate and the steel substrate. However, it should be mentioned that these temperature cycles are far away from the T_g of the resin that has changed due to the thermal cycle exposure from 64.5ºC (after 5,000 h of exposure) to 71.2ºC (after 10,000 h of exposure), as already shown in Table 4.2.

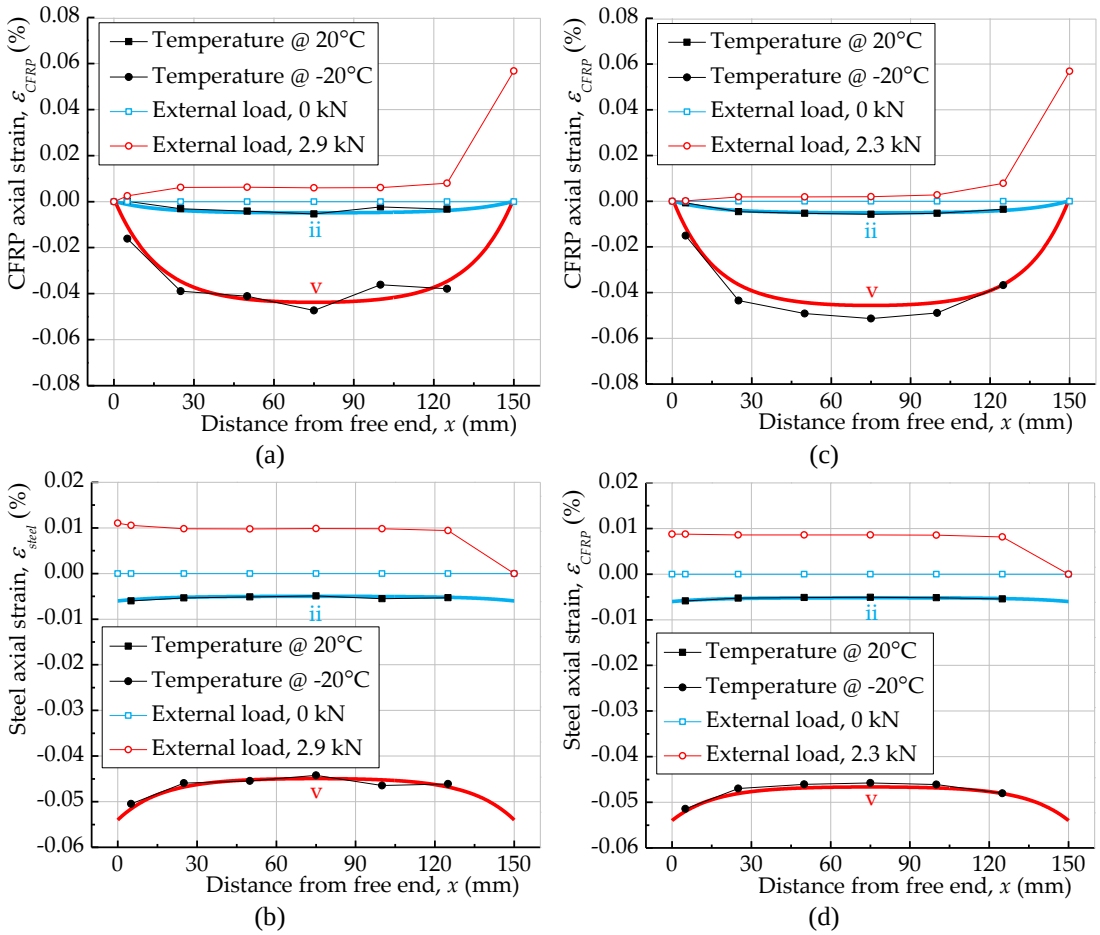

ii – ΔT = -5ºC; v – ΔT = -45ºC (from analytical proposed model)

Figure 4.13 - Comparisons between the strains developed in the CFRP laminates and steel plates when thermal and mechanical loads are applied to the HIT bonded joint (a)-(b) (specimen H-M-01) and SIKA bonded joint (c)-(d) (specimen S-M-03).

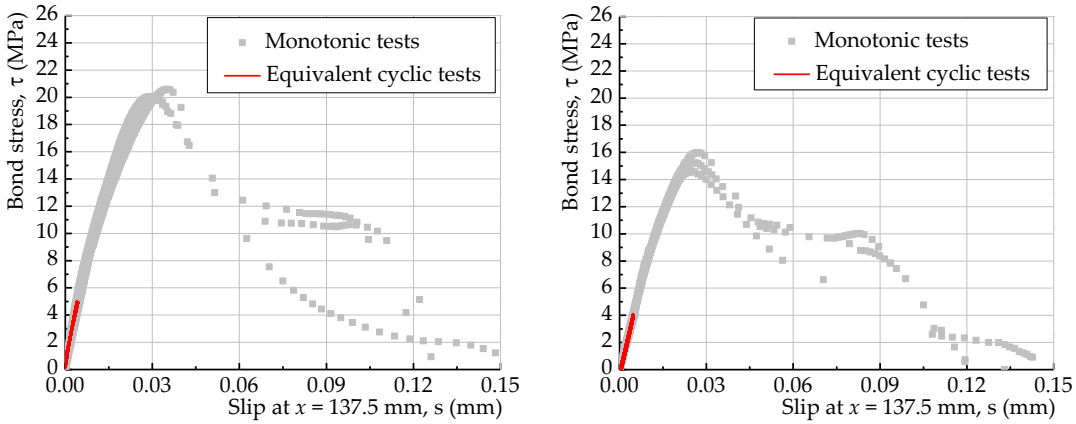

Figure 4.14 - Equivalent thermal cyclic bond-slip curves- after 833 mechanical cycles: (a) HIT (specimen H-C-03) and (b) SIKA (specimen S-C-02).

4.7 Remarks

Two different CFRP laminates were externally bonded with an epoxy resin to steel substrates and double-lap bonded joints and adhesive flat coupons were specially analyzed after being aged to the same freeze-thaw cyclic conditions. Different time periods were considered and after each period the specimens were tested and characterized. Based on the data obtained from the epoxy adhesive and from the double-lap shear tests, the following conclusions about the degradation of the CFRP-to-steel bonded joints can be drawn:

- The bond capacity of CFRP-to-steel bonded joints (HIT and SIKA) and the mechanical properties of the adhesive flat coupons were slightly influenced by the imposed 833 freeze-thaw cycles, between +20°C and -20°C at 50% of RH;
- The degradation of the interfacial bond strength between adhesive and steel with the freeze-thaw cycles for the bonded joints with HIT laminates changed the failure mode from cohesive failure to mixed failure mode, i.e., partially cohesive and another part adhesive at the same interface;
- The weaker interfacial bond strength between CFRP and adhesive, in SIKA bonded joints, led to damage initiation at the interface and it was associated to a lower maximum shear stress and a mixed failure mode. Conversely, HIT bonded joints led to damage initiation at later stages for a higher maximum shear stress in the bond-slip curve and a cohesive failure;
- Approximating the shape of the bond-slip curve by a bi-linear model, the slip and bond stress distributions during the thermal cycles have, throughout one-half of the bonded length (between 75 mm to 150 mm), similar behavior to that found when external loading is applied to the bonded joint; however, the strain in CFRP laminates and steel plate showed quite different behavior compared to that from mechanical loading.

- Thermal interfacial stress and slip distributions, with temperature variations from 25°C (reference temperature) to 20°C and from 25°C to -20ºC were illustrated. Comparing to the mechanical loading and for the same thermal slip developed at x = 150 mm, the HIT laminates produced an equivalent load of 2.9 kN whereas in the SIKA laminates the corresponding equivalent load reached 2.3 kN;
- The strain distributions throughout the bonded length due to the thermal action are completely different from those expected to occur when the CFRP laminates are subjected to a mechanical load. In the thermal conditions, the maximum strains (negative value) in the CFRP laminate develop at the middle of the bonded length (at x = 75 mm) reaching, in the present case, approximately 0.05% in both HIT and SIKA laminates whilst under the mechanical load, the same equivalent slip led to a maximum strain at x = 150 mm of approximately 0.06%, in both HIT and SIKA laminates;
- Moisture is a critically important factor in the freeze-thaw cycles. Thermal interfacial cyclic bond-slip curves were obtained from the equivalent cyclic loading tests and confirmed that cumulative damage within the interface due to freeze-thaw does not arise exclusively from thermal cycles. For the present case, with temperature cycles between 20ºC and -20ºC, only the elastic regime of the adhesively bonded interface was reached.

4.8 Summary of this chapter

The degradation mechanisms of bonded joints between CFRP laminates and steel substrates under severe environmental conditions require more durability data and studies to increase the database and better understand their causes. Studies on bond properties of double-strap CFRP-to-steel bonded joints with two different composite materials as well as adhesive coupons subjected to freeze-thaw cycles for 10,000 h were conducted to reduce that gap. In addition, the equivalent to the number of thermal cycles and their slips induced in the CFRP laminates was replicated by an equivalent (mechanical) loading-unloading history condition imposed by a static tensile machine.

The mechanical properties of the adhesive coupons and the strength capacity of the bonded joints were only slightly changed by artificial aging (see Figure 4.2 and Table 4.3). It was confirmed that the interfacial bond strength between CFRP and adhesive is critically related to the maximum shear stress and failure mode. The interfacial bond strength between adhesive and steel degraded with aging (see Figure 4.6). However, the equivalent thermal cyclic bond stress caused no detectable damage on the bond because only the interfacial elastic regime was actually mobilized (see Figure 4.14), which confirmed that pure thermal cycles aging, *per se*, at the level imposed, have low impact on the degradation of CFRP-to-steel bonded joints.

Chapter 5

CFRP-to-steel joints behaviour after salt fog exposure: monotonic and cyclic loads

5.1 Introduction

As known, CFRP/steel bond properties are decisive in the effectiveness of the reinforced system [39] but the bond between both materials is the result of interaction of the adherent materials and the bonded interfaces, CFRP-to-adhesive and steel-to-adhesive, being complex to predict its behavior. In addition, long-term service conditions, e.g. aggressive environmental conditions [88, 23] and/or repeated loading [39] may be demanding and increase the uncertainties in the design of CFRP/steel bonding systems. Thus, more experimental results are required to increase the database and enhance the confidence for application of this strengthening technique, especially when the structures are subjected to harsh environmental conditions.

Among the latter, exposure to salt fog is likely to cause significant degradation in mechanical properties including the bond between the FRP composite and the steel substrate and the literature on this topic is scarce. The existing knowledge on the bond durability between FRP composites and concrete after salt fog exposure allows a cautious extrapolation to the CFRP/steel joints. In this matter, Silva and Biscaia [106] studied the causes for the changes of the bond created by the external bond of CFRP and GFRP sheets to the soffit of small reinforced concrete (RC) beams after immersed in salte water and after exposed to salt fog cycles. Results of four points bending tests on the un-aged and aged specimens indicated that the bond damage initiation occurred in the concrete substrate for un-aged beams, while for the aged beams the failure was observed in the adhesive/concrete interface. The bond strength, i.e. the maximum bond stress, unexpectedly increased with aging, behavior attributed to improvement of the characteristics of concrete, namely its tensile and compressive strengths.

Possible causes of degradation in CFRP bonded steel systems under immersion in salt water and salt fog are briefly reviewed next. Common cause is the action of salt crystals eventually

formed in the interfaces and in the adhesive. One study on bond durability of CFRP/steel joints after salt fog exposure under peeling loads conducted by Teixeira de Freitas et al. [102] concluded that salt water penetrated the joints along the interface, from the edges towards the inner side of the bond area, causing changes in the failure mode and progressive reduction on peel strength.

Another study reports that the degradation of the adhesive due to the moisture absorption caused a reduction of 17% and 26% in the initial loading carrying capacity of CFRP/steel bonded joints after 12 months under immersion in salt water at 20ºC and 50ºC, respectively [97].

Alternative route of deterioration in carbon fiber/matrix interface due to moisture and temperature was reported by Heshmati et al. [107]. The authors reported that after CFRP/steel double strap joints were subjected to immersion in salt water at 45°C, for 210 to 840 days, the failure mode of the bonded joints changed from cohesive (in adhesive) to a mixed failure mode with primary damage observed at the carbon fiber/matrix interface and severe degradation in the bond strength of the samples.

Dawood and Rizkalla [108] immersed CFRP-to-steel double strap joints in salt water with 5% of NaCl at 38°C for 6 months. The authors [108] found that the load capacity was severely reduced by 60% from its initial value at 0 hours of exposure due to the partial corrosion of the steel substrate near the edge of the bonded area.

In addition to the descriptions made above, the degradation of the CFRP/steel joints may be due to galvanic corrosion that commences when the bonded CFRP materials are in direct contact with the steel [32, 33].

Repeated loading below the monotonic strength capacity of the bonded joints may lead to cumulative damage that may produce catastrophic and unexpected brittle failures. The global response (force *vs*. deformation of the bonded joints) under fatigue loading has been studied [19, 20, 18]. Colombi and Fava [19] assessed the fatigue behavior of CFRP-to-steel double strap joints through the observation of the interfacial crack initiation, progression and debonding up to failure. Other fatigue studies conducted by Liu et al. [20] and Wu et al. [18] focused on the effects of different level fatigue loads on the residual load carrying capacity of bonded joints. The former found that post-fatigue strength was not evidently affected when the maximum fatigue load was less than approximately 35% of the ultimate static strength, when the reduction was below 10%. The latter found that the interfacial damage under fatigue loading was limited to an area around the loaded end that approximated 1% of the entire bonded area.

A direct characterization method to correlate the bond response with the corresponding interfacial damage under repeated loading is necessary to improve the current knowledge on the bond cumulative damage mechanism. As already mentioned, the bond behavior is often

represented by a bond-slip relationship that can incorporate interfacial damage initiation, progression and debonding under repeated loading with reflections on the stiffness degradation, dissipated energy and slip increase. Thus, the acquisition and collection of experimental data to represent the cyclic bond-slip curve is necessary to go deeply into the correct analysis of the bond cyclic behavior. In a previous Chapter [103], pseudo-cyclic and cyclic loading tests were carried out with unaged CFRP-to-steel bonded joints and two different CFRP laminates were considered. The bond cyclic behavior was analyzed based on the data collected from pseudo-cyclic and cyclic tests and subsequent results allowed the determination of the corresponding bond-slip curves.

The present work is part of an extensive experimental program carried out by the authors regarding the bond behavior and durability of CFRP-to-steel bonded joints when subjected to repeated loading and aggressive environmental conditions. The current study complements the work already developed by in Chapter 3 [103]. In this study, an analysis of the bond durability is conducted through applying the same cyclic tests philosophy carried out in chapter 3 [103] to salt fog aged specimens and comparisons with the un-aged specimens are presented, in order to investigate the cause-effect of salt fog aging conditions on the monotonic and cyclic behavior of CFRP-to-steel bonded joints.

5.2 Experimental program

The current work is complementary to the works performed in chapter 3 [103], where the bond monotonic and cyclic behavior were studied and focused on the un-aged bonded joints. In this chapter, a deep analysis of bond durability data is conducted through applying the same cyclic tests philosophy carried out in Chapter 3 to salt-fog aged bonded joints and compared with that from the un-aged bonded joints, to investigate the effects of salt fog aging on the monotonic and cyclic bond behavior.

5.2.1 Materials and bonded joints

In the current chapter, the materials adopted are the same as before (chapter 2, 3 and 4), i.e., HIT CFRP and SIKA CFRP, steel and adhesive SIKADUR 30, were chosen for the study.

The preparation process of the adhesive coupon for mechanical measurement and the fabrication of bonded joints were well described in the last three chapters. Here this is not repeated but some images on bonded joints (Figure 5.1) are given. As illustrated in Figure 5.1b, the bonded joints used 25mm width of CFRP laminates and 55mm width of steel plates, which are not the same as before, where 10mm width CFRP laminates and 50 mm width steel plate were adopted in chapter 2, while 20mm width CFRP laminates were considered in chapter 3

and 4. The methods to obtain the mechanical properties of CFRP laminates, adhesive and steel are also available in last three chapters.

A total of twenty-four CFRP-to-steel bonded joints were made; among those, twelve of which were produced with HIT CFRP laminates and the other twelve specimens with SIKA CFRP laminates. Three specimens were prepared each case with different initial condition (aged and un-aged) and loading type (monotonic, pseudo-cyclic, and cyclic). For the unaged specimens, as previously mentioned, relevant experiments under monotonic, pseudo-cyclic, cyclic and monotonic after cyclic loading history were already carried out in chapter 3 [103]. Therefore, only the tests under monotonic loading history were considered herein and are referred and identified as reference specimens. For aged specimen, three specimens failed during the pre-scheduled cyclic loading history, while the other three specimens did not fail until the end of cyclic loading. Thus, these latter specimens were reused to evaluate their bond behavior when subjected to a monotonic loading history until rupture (monotonic after cyclic).

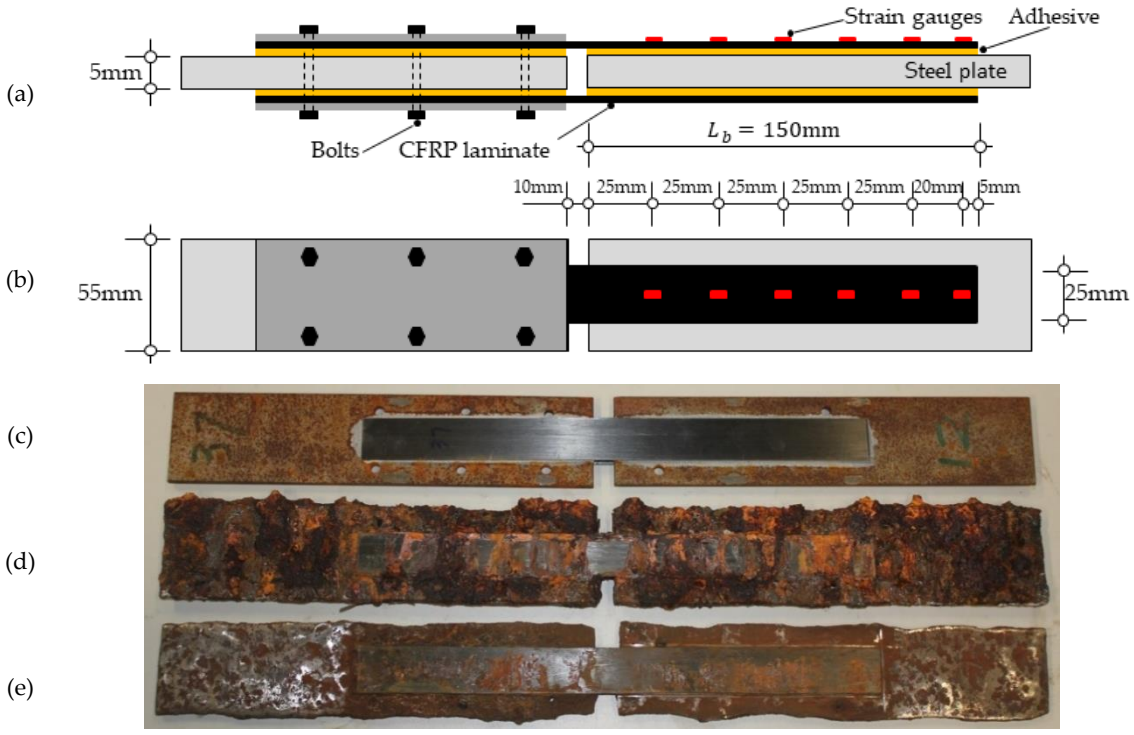

Figure 5.1 - Schematic view of bonded joints: (a) side view; (b) front view; and images of bonded joints with: (c) reference; (d) corroded; and (e) cleaned.

Table 5.1 summarizes the information of the tested CFRP-to-steel bonded joints, including their designation (ID), initial condition (aged or not aged), time period exposed to aging conditions, loading type and the corresponding number of loading cycles carried out in each test. The tested specimens are designated in the form "X-Y-Z-n", where "X" indicates the aging condition (REF = un-aged, SF = salt fog), "Y" corresponds to the type of CFRP laminate used (H = HIT, S =

SIKA), "Z" indicates the type of loading history adopted in the test (M = monotonic, PC = pseudo-cyclic, C = cyclic and CM = monotonic loading history after cyclic test with no rupture of the specimen) and "n" is a sequential ID number to distinguish the repeated tests in each class with the exception of the CM series where "n" is associated to the same "n" number of the C series. As an example, the following designation REF-H-M-02 means that the specimen is un-aged and it corresponds to the 2nd specimen carried out under a monotonic loading history of HIT CFRP-to-steel bonded joint.

Table 5.1 ID of the CFRP-to-steel bonded joints, aging conditions and loading types.

ID	Aging condition	Exposure (h)	Loading type	Number of cycles
REF-H-M-01	Reference	0	Series #1	-
REF-H-M-02				-
REF-H-M-03				-
SF-H-M-01	Salt fog	5000	Series #1	-
SF-H-M-02				-
SF-H-M-03				-
SF-H-PC-01			Series #2	22
SF-H-PC-02				22
SF-H-PC-03				20
SF-H-C-01			Series #3	57
SF-H-C-02				174
SF-H-C-03				600
SF-H-CM-03			Series #4	-
REF-S-M-01	Reference	0	Series #1	-
REF-S-M-02				-
REF-S-M-03				-
SF-S-M-01	Salt fog	5000	Series #1	-
SF-S-M-02				-
SF-S-M-03				-
SF-S-PC-01			Series #2	22
SF-S-PC-02				22
SF-S-PC-03				26
SF-S-C-01			Series #3	600
SF-S-C-02				600
SF-S-C-03				3
SF-S-CM-01			Series #4	-
SF-S-CM-02				-

5.2.2 Adopted cycles in the accelerated aging conditions

A salt fog aging condition was artificially created within the chamber of a corrosion box (see Figure 5.2). The accelerated aging condition was imposed with a cyclic procedure for 5,000 hours long and each cycle consisted of 6 hours of salt fog spray followed by 18 hours in dry conditions at a constant temperature of 35°C. The salt water used to artificially produce the salt fog spray had a salt concentration of 5% of NaCl. The specimens were kept in the chamber in a lying position and separated between them with enough space to ensure that all bonded surfaces could be in perfect contact with the salt fog when salt fog spraying.

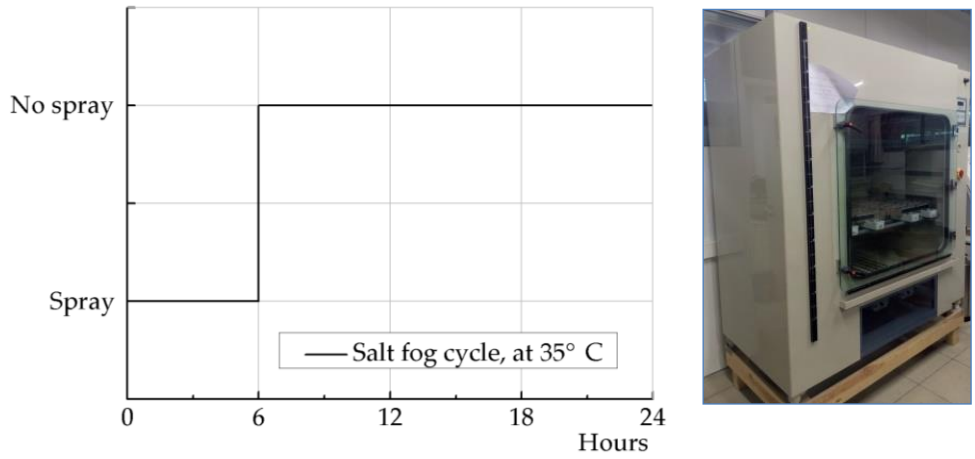

Figure 5.2 - Salt fog cycle procedure and corrosion chamber.

5.2.3 Loading history and test set up

Monotonic, pseudo-cyclic and cyclic test philosophies are the same as shown in chapter 3 [103] for the un-aged bonded joints (while here aged specimens are considered), to facilitate the comparison of the two cases. It should be noted that, for the normalization of the loading force, with direct consequences on the cyclic loading history, the average maximum monotonic load obtained to the aged specimens were considered here.

5.3 Failure modes and load carrying capacity

In addition to what is graphically presented in Figure 5.3, the failure modes of HIT and SIKA bonded joints were correlated with acronyms that are summarized in Table 5.2. As it can be seen from Figure 5.3a, the reference HIT bonded joints (REF-H-M-01) exhibit cohesive failure mode after monotonic tests, i.e. with rupture within a small layer of the adhesive which is listed with “C” (for Cohesive) in Table 5.2. While reference SIKA bonded joints (REF-S-M-01) exhibit mixed failure mode combining CFRP/adhesive interface failure with cohesive failure in the adhesive, which is listed with “C+A” (for Cohesive plus Interfacial) in Table 5.2. These observations indicate that the interfacial bond between HIT CFRP laminates and adhesive may be stronger enough to induce cohesive rupture rather than interfacial ones, while the SIKA CFRP laminates may exibit a not so strong adhesion with the adhesive which fails in some regions of the bonded area. These failure modes observed from the monotonic tests are the same as those observed in a previous work of Chapter 3 [103]. Actually, in that work in chapter 3 [103], it was reported that the failure modes of the un-aged bonded joints were not associated with the loading history, i.e. the failure modes observed from the un-aged bonded joints that have been subjected to monotonic, pseudo-cyclic or post-cyclic loading histories had no evident differences between them.

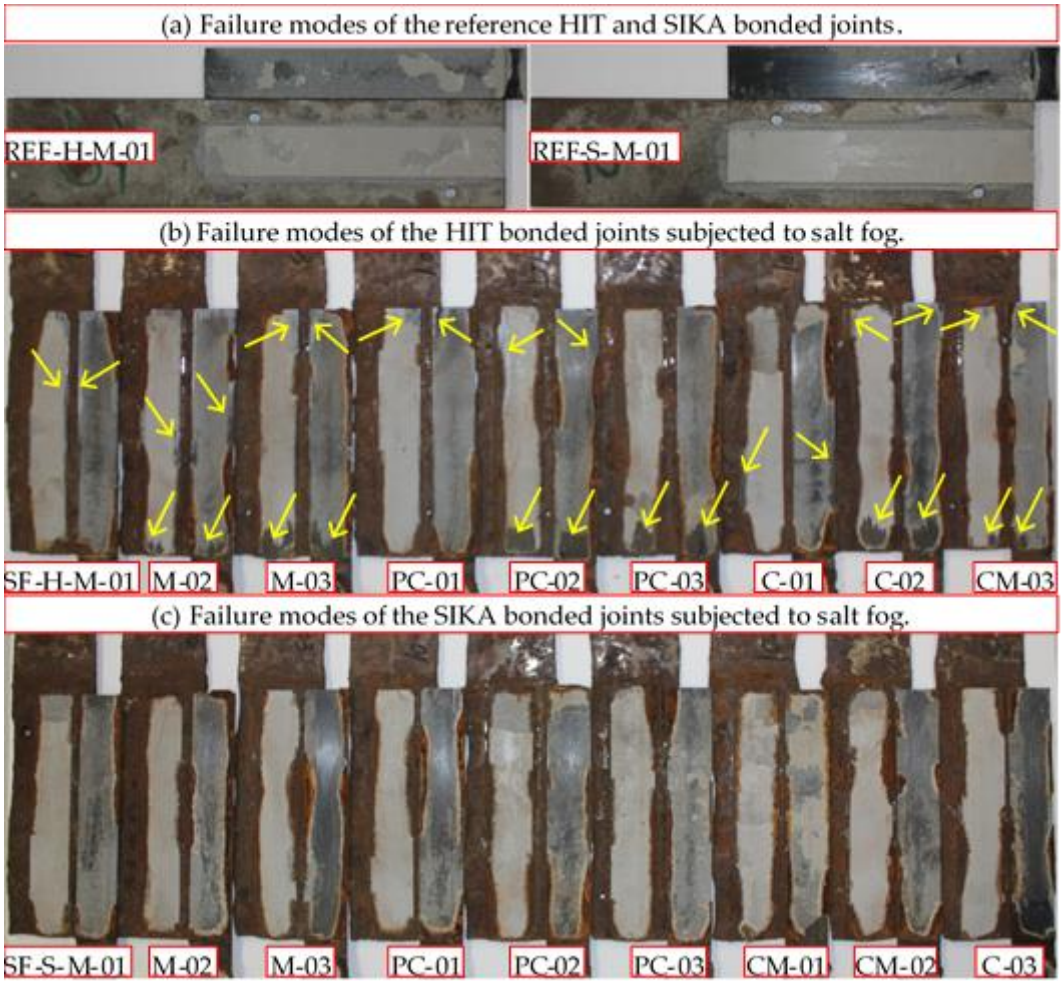

Figure 5.3 - Failure modes of (a) the reference and aged bonded joints with (b) HIT and (c) SIKA.

Figure 5.3b shows the monotonic (SF-H-M-01/02/03), pseudo-cyclic (SF-H-PC-01/02/03), cyclic (SF-H-C-01/02) and monotonic after cyclic (SF-H-CM-03) failure modes of the HIT bonded joints after salt fog aging conditions. As it can be seen for all the bonded joints, the regions around the edges of the bonded areas were seriously corroded due to the presence of the salt water, which became the weakest link and potentiated the rupture due to the rust developed at those regions. Observing the surfaces of the debonded CFRP laminates and the corresponding separated part of the steel bar (see Figure 5.3b), it can be seen that the CFRP has delaminated in some regions of the bonded area and it is possible to observe some CFRP material still bonded to the adhesive. Those damages were mainly concentrated on some particular bonded regions closed to the CFRP loaded end and also at some edges of the bonded area (see the regions marked with an arrow in Figure 5.3b). The delamination of the CFRP in those regions was attributed to the degradation of the carbon fiber/resin interface due to galvanic corrosion. In addition, after aging, it seems that the degradation within the CFRP/adhesive interface occurred and eventually increased the exposure area of the HIT CFRP when compared

the CFRP debonding surfaces associated to unaged and aged bonded joints. Based on the above described inspection and analysis, the failure mode of the HIT bonded joints was represented by "C+A+R+D" (for Cohesive plus Interfacial plus Rupture inside the corrosion Rust plus Delamination) in Table 5.2.

Table 5.2 - ID of joints, failure load, maximum bond stress and failure mode type.

ID	Number of cycles	Failure load F[(1)] (kN)	Avg. Failure loads F (kN)	Max. Bond stress (MPa)	Avg. Max. Bond stress (MPa)	Failure Mode[(2)]
REF-H-M-01	-	20.29		20.12		
REF-H-M-02	-	22.37	21.26	19.96	20.22	C
REF-H-M-03	-	21.11		20.59		
SF-H-M-01	-	16.11		9.57		
SF-H-M-02	-	16.87	17.27	12.59	12.59	C+A+R+D
SF-H-M-03	-	18.83		15.61		
SF-H-PC-01	22	18.11		11.71		
SF-H-PC-02	22	17.71	17.66	14.00	12.59	C+A+R+D
SF-H-PC-03	20	17.15		12.05		
SF-H-C-01	57	14.01	14.11	11.27	13.40	C+A+R+D
SF-H-C-02	174	14.20		13.63		
SF-H-C-03	600	-	-	15.29		-
SF-H-CM-03	-	19.20	19.20	1.77	-	C+A+R+D
REF-S-M-01	-	17.48		17.55		
REF-S-M-02	-	19.86	18.25	18.42	17.60	C+A
REF-S-M-03	-	17.40		16.82		
SF-S-M-01	-	17.87		12.89		
SF-S-M-02	-	16.87	14.39	9.90	10.07	C+A+R
SF-S-M-03	-	8.43		7.41		
SF-S-PC-01	22	15.26		8.38		
SF-S-PC-02	22	15.03	16.31	N/A	10.66	C+A+R
SF-S-PC-03	26	18.64		12.94		
SF-S-C-01	600	-	-	N/A	11.23	-
SF-S-C-02	600	-		8.60		-
SF-S-C-03	3	12.22	12.22	13.86		
SF-S-CM-01	-	16.97	15.47	N/A	-	C+A+R
SF-S-CM-02	-	13.96		2.65		

Note: [(1)] the failure load F refers to the load transmitted to a single CFRP laminate; and [(2)] the acronyms C, A, R, D are associated to Cohesive failure mode (i.e., rupture inside the adhesive), Interfacial rupture between the CFRP and the adhesive, Rupture inside the corrosion Rust, and Delamination of the CFRP, respectively.

Figure 5.3c shows the failure modes of the monotonic (SF-S-M-01/02/03), pseudo-cyclic (SF-S-PC-01/02/03), cyclic (SF-S-C-03) and monotonic after cyclic (SF-S-CM-01/02) observed from the SIKA bonded joints after salt fog aging conditions. As it can be seen, there are no evident differences in the failure modes between SIKA bonded joints and HIT besides that SIKA failed without delamination of CFRP material. Therefore, the failure mode of the SIKA bonded joints was characterized by a hybrid failure mode consistent with an adhesive rupture, i.e. within the CFRP/adhesive interface, combined with a rupture inside the corrosion rust which was designated as C+A+R (for Cohesive plus Interfacial plus Rupture inside the

corrosion Rust) in Table 5.2.

From the observations made before, it can be primarily stated that the bonded joints subjected to salt fog aging conditions were seriously deteriorated due to the corrosion in the steel substrate mainly developed at the edges of the bonded area, which triggered the rupture of the bond within the corrosion rust at those regions when subjected to the mechanical loading. Moreover, like the un-aged bonded joints tested in chapter 3 [103], the failure modes of the aged bonded joints herein tested also revealed that the loading histories have not direct implications on the failure modes of CFRP-to-steel bonded joints.

The strength capacity of the reference and aged bonded joints, i.e. the load carrying capacity of the bonded joints, both for HIT and SIKA under different loading types (monotonic, pseudo-cyclic and monotonic after cyclic loading) are detailed in Table 5.2 for each specimen. As reported in this table, the reference HIT bonded joints have a calculated average maximum capacity of 21 kN whereas the SIKA bonded joints reached an average maximum capacity of 18 kN. The probable causes for this difference of 3 kN between joint types were associated to different bond strengths achieved in both cases due to different damage initiation (see failure modes in Figure 5.3a), different elastic modulus and thickness between both CFRP laminates.

The load carrying capacity of the aged bonded joints has larger scatter results due to the randomized formation of corrosion. However, it can be seen that the average carrying capacity of the bonded joints after aging conditions reduced from 21 kN to 17 kN in HIT CFRP bonded joints whilst a reduction from 18 kN to 15 kN were determined for SIKA CFRP bonded joints, which represent a load capacity reduction of 19% and 21%, respectively. These degradations of the load capacity are mainly attributed to the corrosion of the steel substrate around the bonded area as it can be seen from Figure 5.3b-c.

5.4 Load vs. slip and bond vs. slip

The global bond response of the bonded joints, at a designated location along the bond length, is often associated with a global relationship between an external load transmitted to the CFRP laminates and the corresponding relative displacements between bonded materials (or slips). The load transmitted to the CFRP laminate can be calculated from the strain gauges previously mounted on the CFRP surface and then, considering the constitutive relation of the CFRP laminates, the load in the CFRP at a certain point of the bonded length can be calculated according to:

$$\mathrm{F}(x_i) = E_{CFRP} \cdot \varepsilon_{CFRP,i} \cdot t_{CFRP} \cdot b_{CFRP} \quad (5.1)$$

where $F(x_i)$ is the load transferred to the CFRP laminate at point x_i; E_{CFRP} is the Young modulus

of the CFRP laminate; $\varepsilon_{CFRP,\,i}$ is the CFRP axial strain measured at point x_i; t_{CFRP} and b_{CFRP} are the thickness and the width of the CFRP laminate.

From a practical point of view, it is assumed that the transferred loads and the strains between two consecutive strain gauges have a linear distribution and thus, at a designated position x_i, e.g. at the midpoints between two consecutive strain gauges, the transferred load can be calculated according to:

$$\mathrm{F}\left(x_{i+1/2}\right) = \frac{1}{2}\left(F_{x_{i+1}} + F_{x_i}\right) \tag{5.2}$$

where $F(x_{i+1/2})$ and $F(x_{i+1})$ are the loads transferred to the CFRP laminate at points $x_{i+1/2}$ and x_{i+1}, respectively. However, the calculation of the developed slips within the CFRP-to-steel interface is a more complex task to carry out when compared to those cases where a single shear bonded test is considered [73]. In the case of pull-pull double strap bonded joints, the deformations in the steel substrate cannot be ignored and the slips at the CFRP free end are not zero. Therefore, when integrating the strains, the formula derived for the calculation of the slips should consider the strains developed in the steel as suggested in the literature, e.g. [103, 85]:

$$\mathrm{s}(x_{i+1}) = \int_{x_i}^{x_{i+1}} (\varepsilon_{CFRP} - \varepsilon_{steel})\, dx + s(x_i) \approx$$

$$\approx \left[\frac{\varepsilon_{CFRP,i+1}+\varepsilon_{CFRP,i}}{2} - \frac{\varepsilon_{steel,i+1}+\varepsilon_{steel,i}}{2}\right] \cdot (x_{i+1} - x_i) + s(x_i) \tag{5.3}$$

where $s(x_i)$ and $s(x_{i+1})$ are the slips at point x_i and x_{i+1}; $\varepsilon_{CFRP,i}$, $\varepsilon_{CFRP,i+1}$ and $\varepsilon_{steel,i}$ $\varepsilon_{steel,i+1}$ are the axial strains in the CFRP laminate and in the steel bar at points x_{i+1} and x_i, respectively. Since the forces or the strain are measured between points i+1 and i, an average value of the slip is determined at point i+1/2 according to:

$$\mathrm{S}\left(x_{i+1/2}\right) = \frac{1}{2}\left(s_{x_{i+1}} + s_{x_i}\right). \tag{5.4}$$

The local bond response is quantified through an interfacial relationship that correlates bond stresses developed within the interface with the slips developed at the same measured point. The bond stresses developed within the interface are calculated assuming a uniform distribution between two consecutive strain gauges. Therefore, the following equation, usually used in these circumstances, was used to calculate the bond stresses:

$$\tau\left(x_{i+1/2}\right) = E_{CFRP} \cdot t_{CFRP} \frac{\varepsilon_{CFRP,i+1}-\varepsilon_{CFRP,i}}{x_{i+1}-x_i} \tag{5.5}$$

where the difference (x_{i+1}- x_i) is the distance between two consecutive points i+1 and i. Then, the load *vs*. slip or the bond stress *vs*. slip relationships can be established by associating the slip with the corresponding load or bond stress at the same measured point.

The largest calculated slips were found to occur at the CFRP loaded end (at x = 0 mm) where

the complete load-slip curves can be defined and therefore, this is herein reported in the following subsections. However, it should be noted that the load-slip curves will be used in Section 5 to analyse the global interfacial damage measured at position x = 12.5 mm which is the measured closest point to the CFRP loaded end. Typical bond-slip curves, herein also determined at 12.5 mm from the CFRP loaded end, were also chosen to obtain the most complete interfacial response of the CFRP-to-steel joints.

All the global load *vs*. slip and local bond stress *vs*. slip relationships of the CFRP-to-steel interfaces (monotonic, pseudo-cyclic and cyclic tests) were calculated from the original data collected from the strain gauges previously bonded on the CFRP laminates throughout the bonded length, and the load transferred to the bonded joints was measured by the tensile machine.

5.4.1 Monotonic tests

The monotonic force *vs*. slip response of the reference and aged HIT and SIKA bonded joints is shown in Figure 5.4a-b. To make easier to compare with the aged specimens, the results obtained from the three reference specimens in each case are presented in a grey area which is limited by the highest and lowest loads obtained in all three reference specimens. The same was adopted to show the bond *vs*. slip relationships.

At a low load magnitude, the reference and the aged specimens have the same initial force *vs*. slip relation which means that the stiffness of both HIT (see Figure 5.4a) and SIKA (see Figure 5.4b) CFRP joints have not changed due to the ageing conditions that the specimens were exposed to. This fact is consistent with the local bond *vs*. slip response where during the initial stage (see Figure 5.5a-b) the reference and the aged specimens have a similar local bond response.

The failure loads of the bonded joints after aging were evidently reduced mainly due to the corrosion of the steel developed on the bonded area. The average failure loads in the HIT and SIKA bonded joints reduced by 19% and 21%, respectively. In one case, SF-S-M-03, a plastic plateau in the force *vs*. slip response could not be identified, contrary to all the remaining test results. In this specimen, failure was brittle rather than ductile meaning that unlike the other specimens, the debonding progress was suddenly interrupted. It should be mentioned that a load capacity of 8.43kN was recorded for the brittle rupture sample, SF-S-M-03, much lower than the other two aged samples that almost kept unchanged from the unaged samples, as listed in Table 5.2.

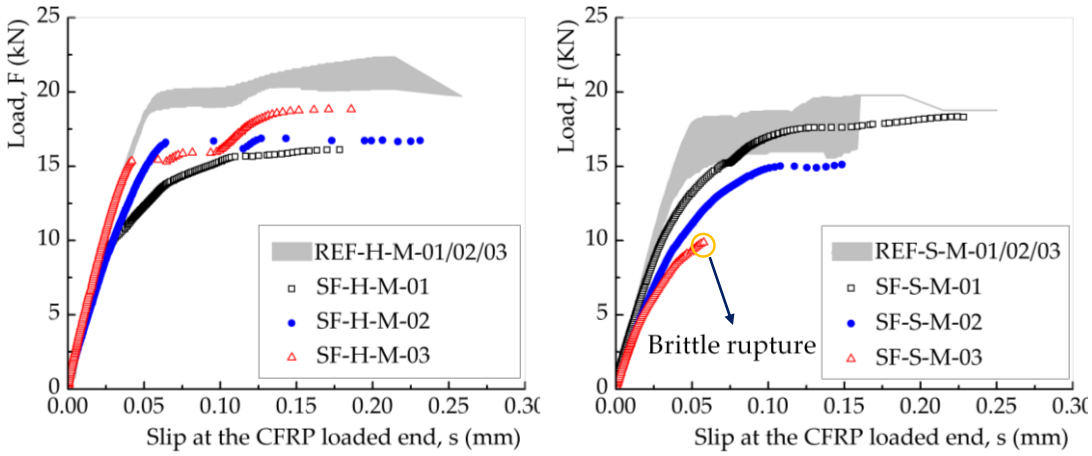

(a) (b)

Figure 5.4 - Force *vs*. slip curves from reference and aged joints; (a) HIT and (b) SIKA.

The monotonic bond *vs*. slip response of the reference and aged bond joints (HIT and SIKA) are shown in Figure 5.5. The reference HIT and SIKA bonded joints had approximately the same initial slope, while the maximum bond stress reached in both cases was different. The same initial slope was attributed to the use of the same adhesive (SIKADUR-30) in both series and also with the same thickness. Thus, the results allowed determination of an average maximum bond stress of 21 MPa and 17 MPa for the HIT CFRP and SIKA CFRP bonded joints, respectively. This difference of 4 MPa was attributed to the damage initiation within the adhesive for HIT CFRP while for the SIKA CFRP the damage initiation occurred within the CFRP/adhesive interface (see failure modes in Figure 5.3a).

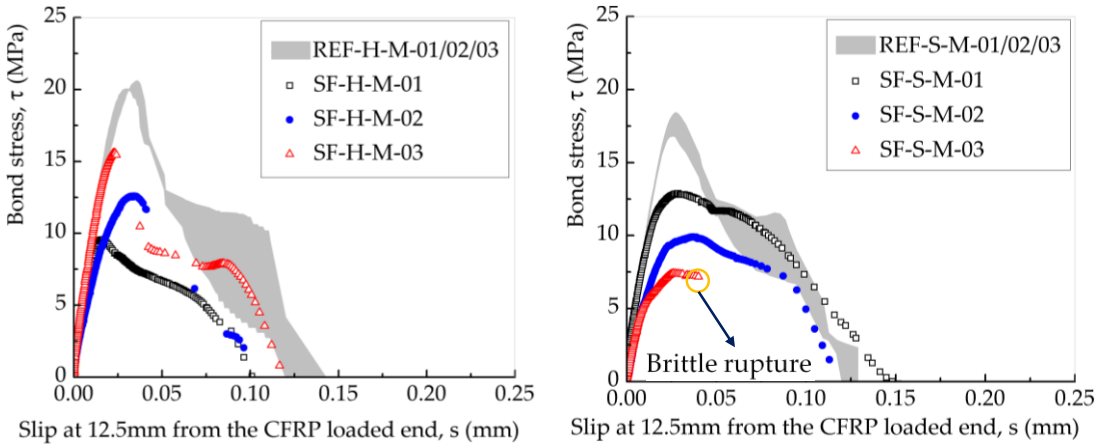

(a) (b)

Figure 5.5 - Bond *vs*. slip curves from reference and aged joints; (a) HIT and (b) SIKA.

Despite the fact that aged and un-aged bonded joints showed a similar initial stiffness, an evident lower maximum bond stress obtained in the SIKA CFRP bonded joints was probably caused by damage initiation within the corrosion rust in steel/adhesive interface. The values of

the maximum bond stress determined for each specimen are listed in Table 5.2. After exposed to the aging conditions, the average maximum bond stresses determined for the HIT CFRP and SIKA CFRP bonded joints reduced about 38% and 43%, respectively. Once the maximum bond stress was reached, the interfacial damage initiation started and progressed towards the complete debonding of the CFRP-to-steel joints, which is reflected in all bond-slip curves by a quasi linear descent stage.

Only one specimen (SF-S-M-03) showed a major ascending stage (see Figure 5.5b), which indicates that, at a distance of 12.5 mm from the CFRP loaded end, the damage progression process developed too fast and led to a rapid and brittle rupture of the entire bonded joints. In this case, the corrosion process may have induced peeling stresses that caused not only the lowest maximum bond stress developed within the joint but also promoted premature failure as explained in the literature [109, 110].

5.4.2 Pseudo-cyclic tests

In order to compare the bond response of the un-aged bonded joints under pseudo-cyclic loading reported in chapter 3 [103], the same pseudo-cyclic test procedures were adopted for the current aged bonded joints. The particular force *vs*. slip curve of specimen SF-S-PC-02 was not obtained because a malfunction of the data acquisition data logger turned impossible to save correctly the data collected from the strain gauges. For this reason, the corresponding bond *vs*. slip curve of this specimen is not shown here.

The curves obtained for the load *vs*. slip at the CFRP loaded end, both for monotonic and pseudo-cyclic loading, are shown in Figure 5.6. The envelope curves of the pseudo-cyclic tests from both aged HIT (Figure 5.6a) and SIKA (Figure 5.6b) CFRP joints followed their monotonic responses, respectively. A similar observation was also found for the un-aged HIT and SIKA CFRP bonded joints in chapter 3 [103] and therefore, it may be stated that the monotonic force *vs*. slip curves, independently of being aged or not, track the envelope of their corresponding pseudo-cyclic curves.

Like the un-aged bonded joints, the aged bonded joints showed similar trends. In every comparison on the force *vs*. slip curves, the pseudo-cyclic and monotonic curves were almost coincident at the initial cycles, showing approximately the same stiffness with no meaningful dissipated energy associated at this earlier stage. At a later stage, the degradation of the stiffness and the increase of the dissipated energy calculated at the point closest to the CFRP loaded end became evident with the increase of the number of cycles. This degradation of the stiffness and increase of the dissipated energy are attributed to the deterioration of the interfacial region at the vicinities of the CFRP loaded end and increased with the number of cycles and, consequently, higher load amplitudes.

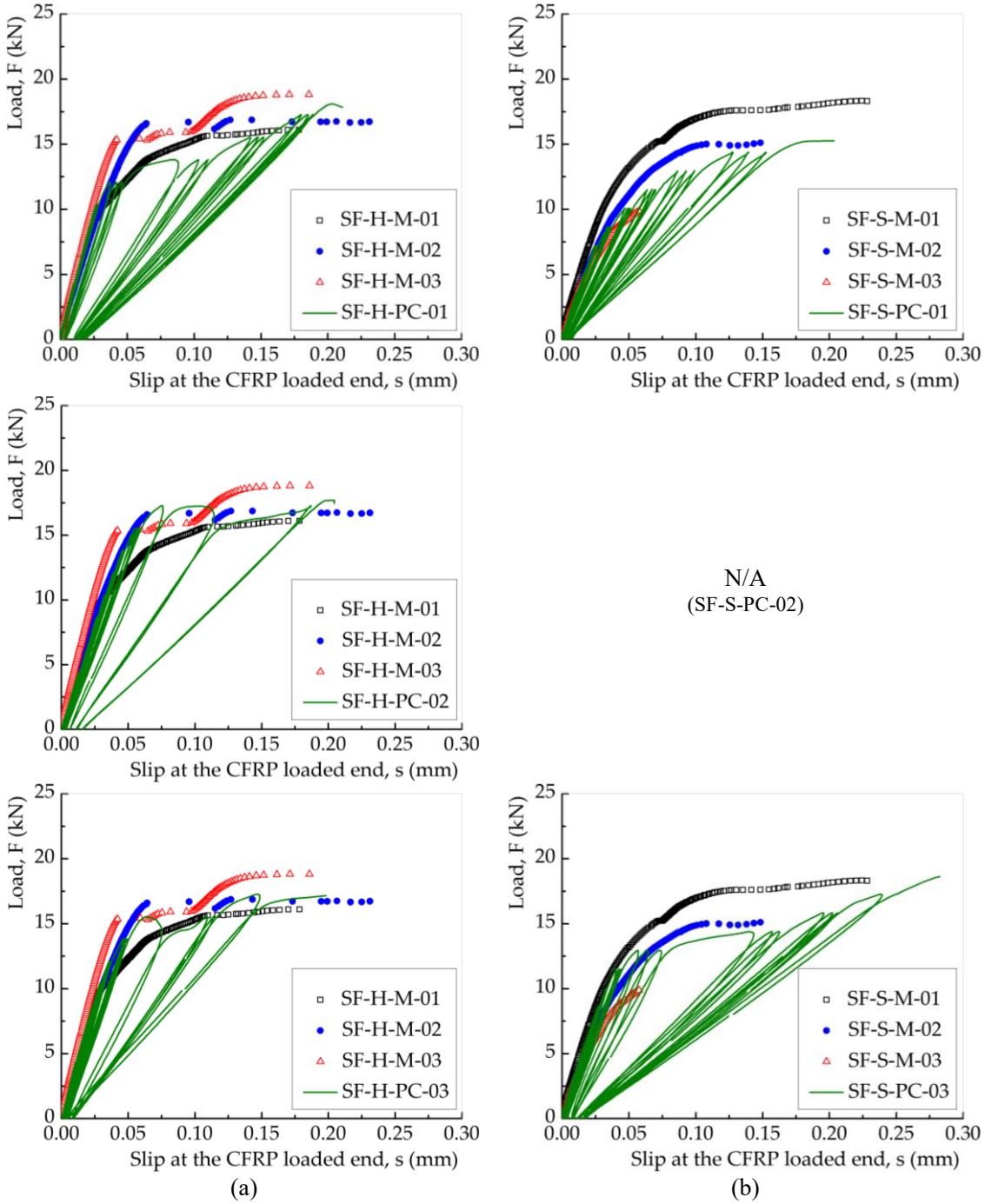

Figure 5.6 - Pseudo-cyclic force *vs*. slip curves (a) aged HIT and (b) aged SIKA joints.

The available pseudo-cyclic bond *vs*. slip curves of the aged bonded joints at 12.5 mm from the CFRP loaded end are compared with their corresponding monotonic curves in Figure 5.7. As shown in this figure, the monotonic bond *vs*. slip curves of the aged specimens can be also simplified into a bi-linear relationship, which coincides with observations made for un-aged specimens in chapter 3 [103], as well as the bond *vs*. slip relationship obtained for CFRP-to-steel bonded joints reported by other authors in the literature [13]. An overall observation of the bond *vs*. slip relationships showed that the envelope of the pseudo-cyclic curves basically

coincided with the monotonic ones. Still, like for the unaged bonded joints, the ascending and the descending branches corresponded to several and complete loading and unloading processes and are almost coincident with the monotonic curves in the initial cycles. These showed no stiffness degradation nor dissipated energy when the maximum bond stresses were lower than the "critical bond stress", i.e. the maximum bond stress reached in the monotonic curve. However, when this "critical bond stress" was exceeded, the loading and unloading cycles associated to the pseudo-cycles followed different paths than those observed from the descending branches of the monotonic bond *vs*. slip curves. These differences tend to aggravate at later stages, where the accumulated degradation of the interfacial stiffness and the dissipated energy increased with the number of cycles and larger load amplitudes.

5.4.3 Cyclic tests

The same cyclic test methodology adopted in chapter 3 [103] was adopted for un-aged bonded joints and 600 cycles, with a higher maximum cyclic loading applied to the aged CFRP bonded joints. With the aim of examining the local and global interfacial cumulative responses when the maximum bond stress is exceeded, tests were firstly carried out in a monotonic load history until 85% of the maximum load capacity of the monotonic tests was reached. The results were then compared with the un-aged bonded joints subjected to the same loading conditions. A malfunctioning of the data logger acquisition made impossible to acquire the data provided by the strain gauges due to the long duration demanded by this type of tests. For this reason, the results from the tests of specimens SF-S-C-01 and SF-S-CM-01 did not allow the correct determination of the force *vs*. slip curves nor the bond *vs*. slip curves and, therefore, those graphs are not presented.

Nevertheless, for the available data, Figure 5.8 makes the comparison between the cyclic load *vs*. slip responses at the CFRP loaded end and their corresponding responses of the CFRP aged bonded joints under monotonic load conditions. Figure 5.8a, it is shown the results obtained from the HIT CFRP bonded joints whereas Figure 5.8a shows the results obtained from the SIKA CFRP bonded joints. From an overall appreciation of all load *vs*. slip responses, it can be stated that a gradual reduction of stiffness of the bonded joints occurred with the loading cycles. However, there are some exceptions such as in the cases of specimens SF-H-C-01, SF-H-C-03 and SF-S-C-02 where, during some particular cycles, an "accelerated progress" caused a rapid increase in slip which was associated to a reduction of stiffness, probably due to stress concentrations on some regions of the bonded area where the formation of corrosion rust took place. This "accelerated progress" was never detected on the un-aged specimens in chapter 3 [103], which exhibited gradual damage progress during all the loading cycle history. In addition, looking at Table 5.2, it can be seen that the cyclic tests of specimens SF-H-C-01, SF-H-C-02 and SF-S-C-03 reached only 57, 174 and 3 cycles until failure, respectively. However,

comparing with the un-aged specimens, no one failed after 600 cycles, which may indicate that the cumulative damage of the CFRP-to-steel joints under cyclic loading accelerated after the specimens were exposed to aging conditions.

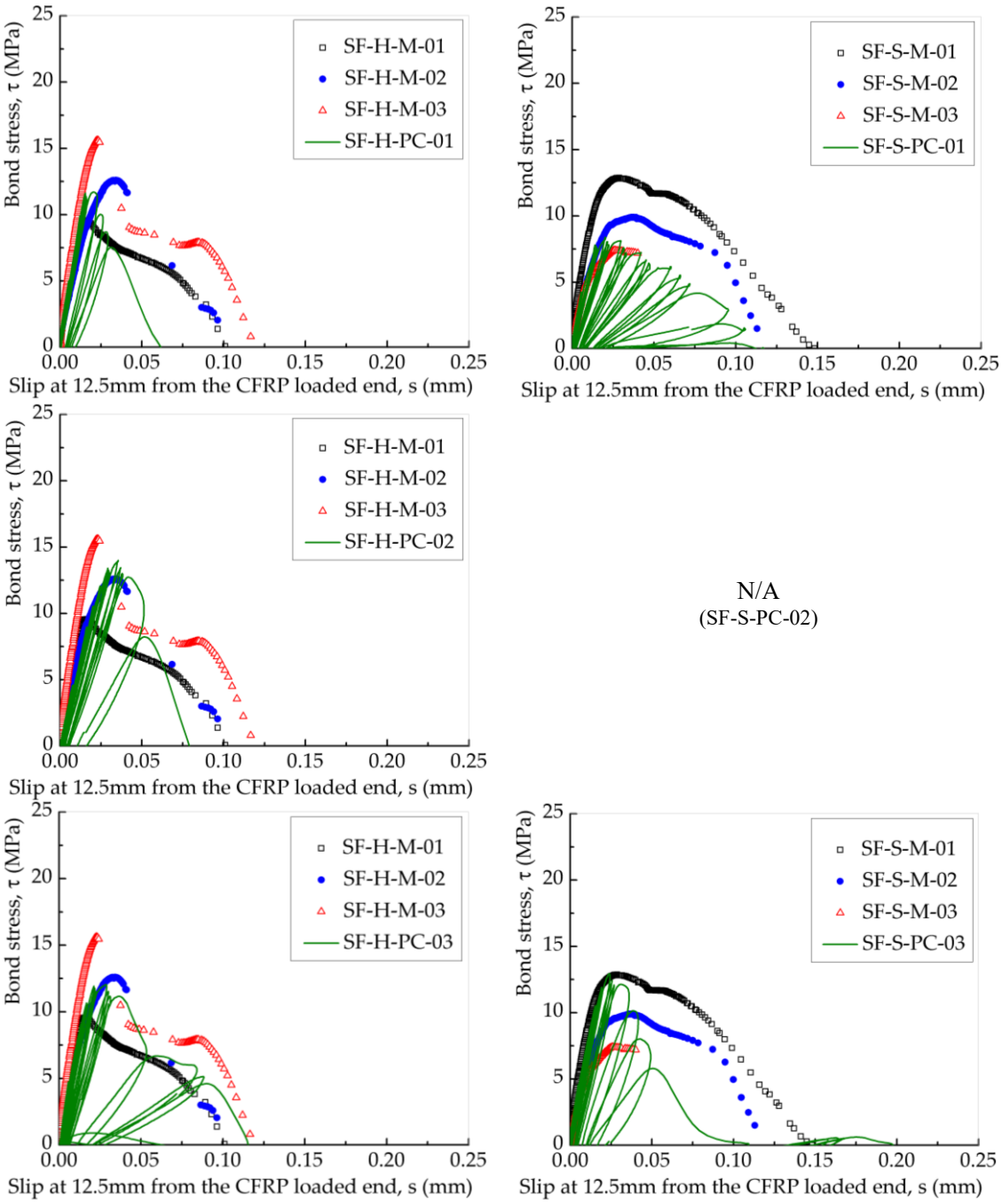

Figure 5.7 - Pseudo-cyclic bond stress *vs*. slip curves (a) aged HIT and (b) aged SIKA joints.

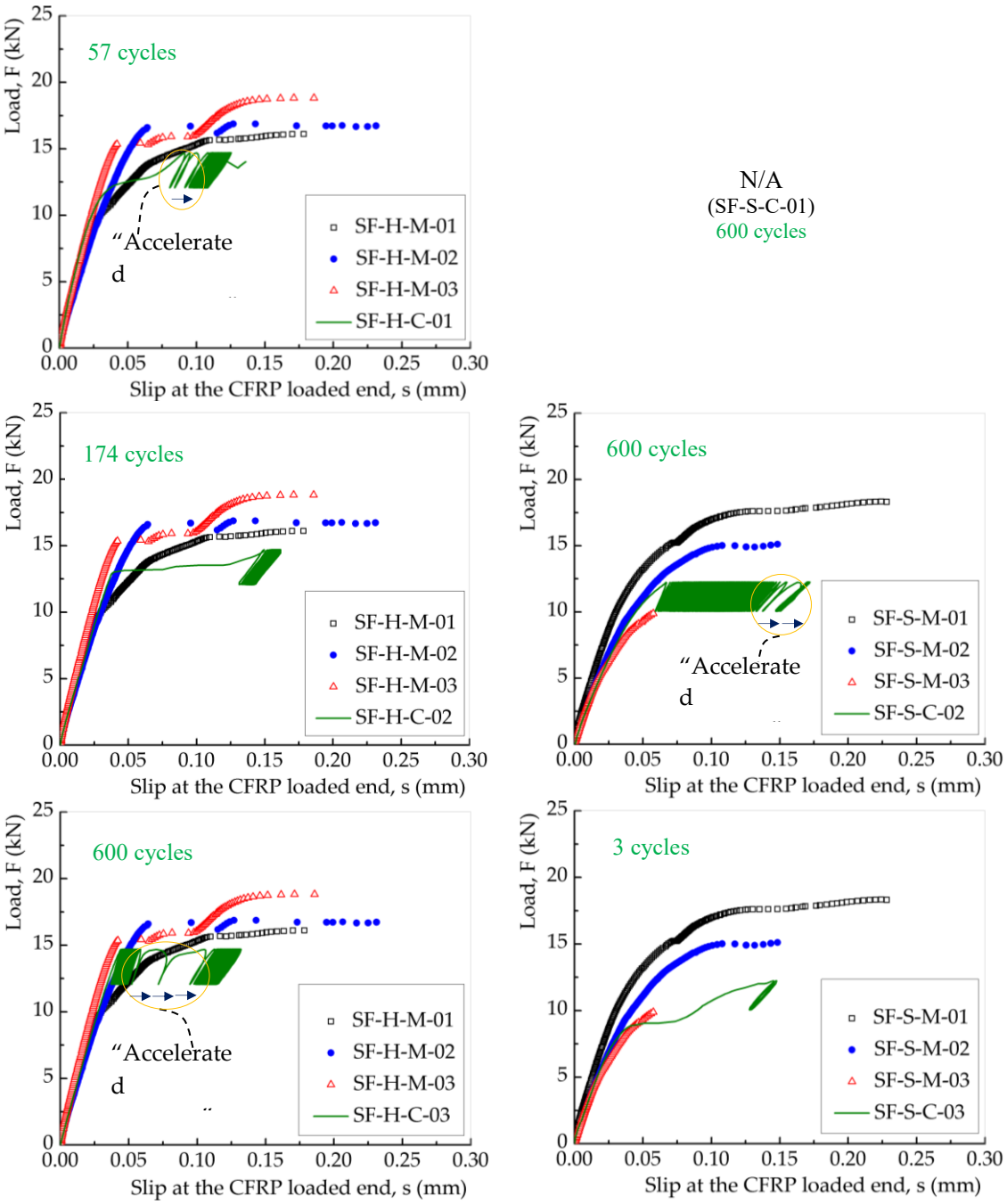

Figure 5.8 - Cyclic force *vs*. slip curves (a) aged HIT and (b) aged SIKA joints.

Figure 5.9 compares the cyclic bond *vs*. slip curves with the monotonic ones for the aged HIT (Figure 5.9a) and SIKA (Figure 5.9b) CFRP bonded joints. As expected, 85% of the average monotonic failure load applied to the CFRP loaded end, provided a load that, at 12.5 mm from the CFRP loaded end the maximum bond stress developed within the interface exceeded its "critical bond stress" value. Then, with the repeated loading and unloading cycles, the gradual cumulative damage is determined from the bonded interfacial region delimited by the bonded region between 0 mm and 12.5 mm. Therefore, the interfacial cumulative damage at those

regions (0 to 12.5 mm) may reflect on the gradual damage progress of the cyclic bond *vs*. slip curves, which exhibited cumulative degradation in stiffness but basically tracked the monotonic bond *vs*. slip curves.

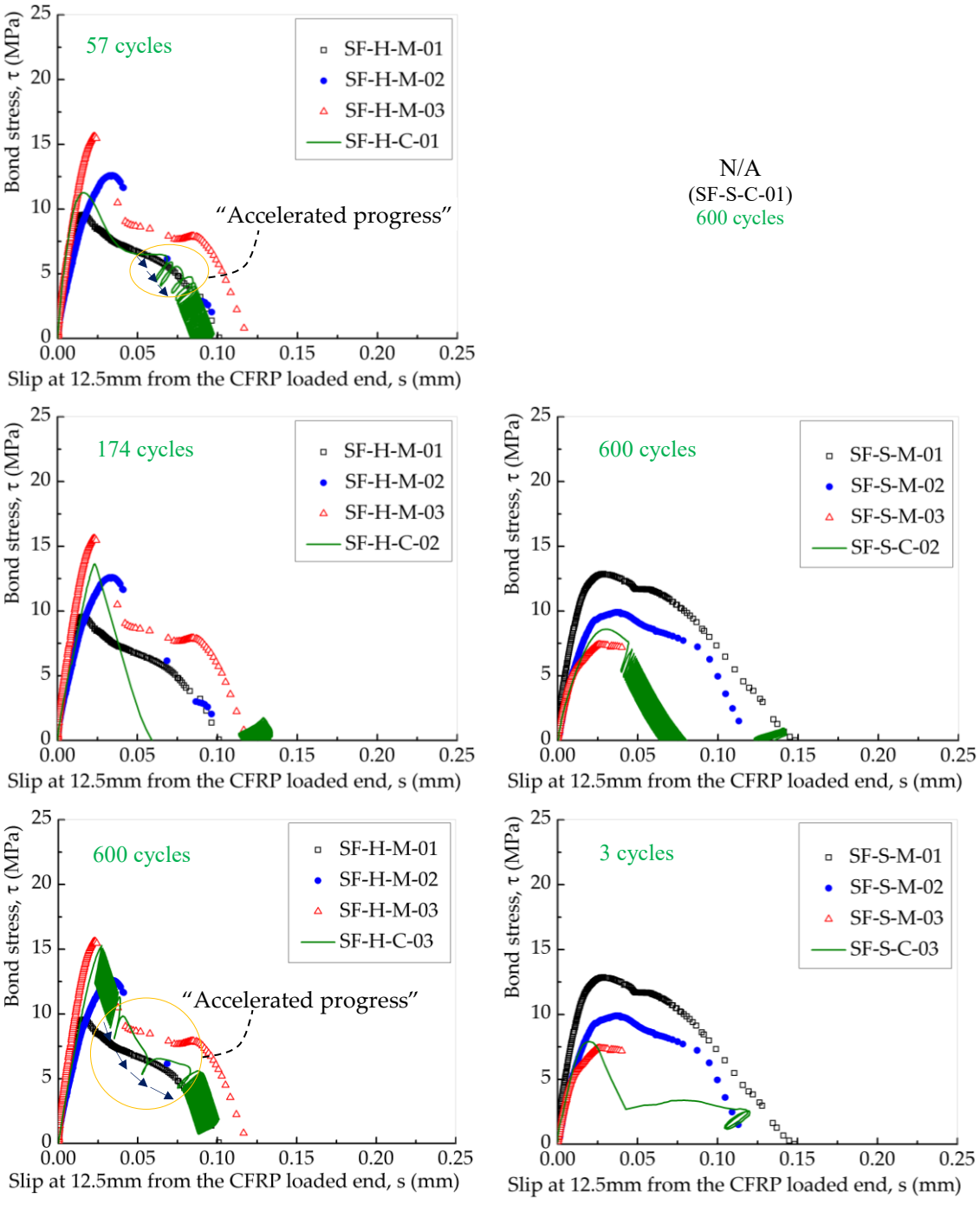

Figure 5.9 - Cyclic bond *vs*. slip curves (a) aged HIT and (b) aged SIKA joints.

Like to the force *vs*. slip curves, the accelerated damage probably induced by stress concentrations in some bonded regions due to interfacial corrosion rust may explain the

"accelerated progress" of the cyclic bond *vs*. slip curves observed from the results obtained in the tests of the SF-H-C-01 and SF-H-C-03 specimens. However, the accelerated damage observed from force *vs*. slip response of the SF-S-C-02 specimen (marked in Figure 5.8b with "accelerated progress") was not observed in the bond *vs*. slip response (see Figure 5.9b). These results indicated that the stress concentration region is associated with the corrosion rust which is distributed in the bonded region beyond the range of 0 to 12.5 mm from the CFRP loaded end. In addition, a single descending stage without any cycles was obtained from SF-H-C-02 specimen (see Figure 5.9a), which may indicate that the maximum load imposed by the cyclic test procedure was not transferred to the point where the bond *vs*. slip curve was generated, i.e., at x = 12.5 mm.

5.4.4 Some monotonic tests after cyclic loads

As shown in the last section, some aged bonded joints did not fail after subjected to 600 cycles such as specimens SF-H-C-03, SF-S-C-02 and SF-S-C-02. Likely to the un-aged specimens, monotonic tests were performed for those specimens that did not collapsed. The results obtained from these tests are presented in Figure 5.10, where the monotonic and the cyclic force *vs*. slip responses of those bonded joints are also shown with the purpose of helping the comparison between different responses to different loading history conditions.

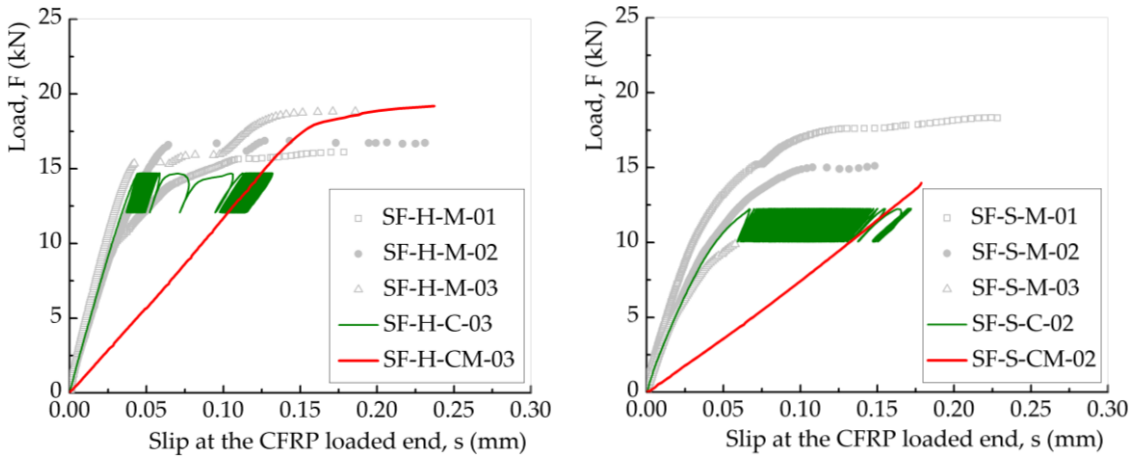

(a) (b)

Figure 5.10 - Monotonic force *vs*. slip curves after cyclic tests (a) aged HIT and (b) aged SIKA joints.

Based on these results, the stiffness of the bonded joints that previously experienced a cyclic loading history almost followed the same stiffness that they had at the end of 600th cycle. Therefore, the results obtained from specimens SF-H-CM-03 and SF-S-CM-02 were similar to the unaged samples, as also observed in chapter 3 [103], which indicates that the cumulative

interfacial damage due to cyclic loading is irrecoverable. In addition, the monotonic force *vs*. slip curves obtained for the specimens SF-H-CM-03 have a long plastic plateau while SF-S-CM-02 only has an ascending stage, which indicates that cyclic loading may change the failure mode of bonded joints from ductile to brittle due to the change of the initial value of the effective bond length of the CFRP-to-steel interface.

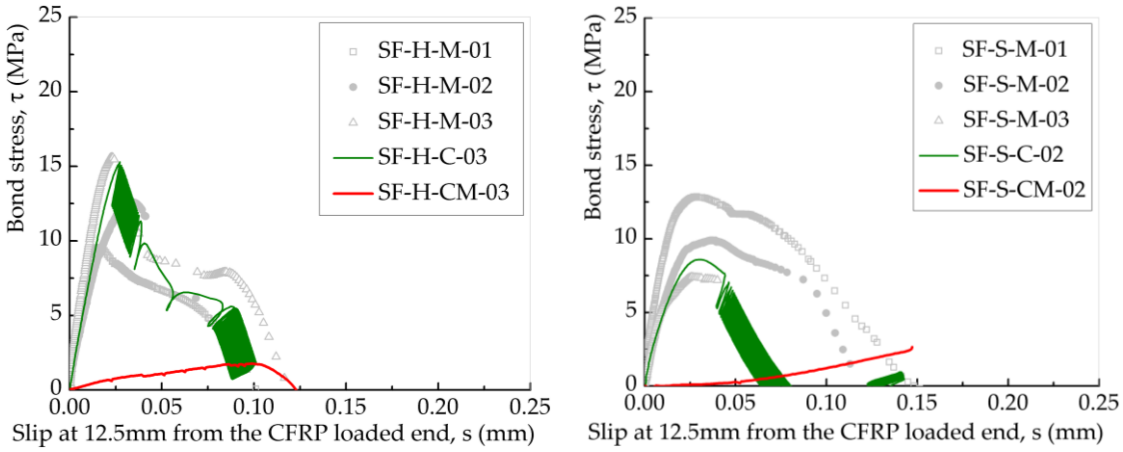

(a) (b)

Figure 5.11 - Monotonic bond *vs*. slip curves after cyclic tests (a) aged HIT and (b) aged SIKA joints.

From a local point of view, Figure 5.11 compares the monotonic bond *vs*. slip curves obtained for the aged CFRP-to-steel bonded joints previously subjected to a cyclic loading history with the results obtained for the monotonic and cyclic tests. As it can be seen from this figure, the monotonic bond response of the joints after cyclic tests depended on the damage of the interface previously caused by the cyclic tests. After the cyclic tests, the initial slope obtained for the subsequent monotonic bond *vs*. slip curve approximately followed the same slope determined at the end of the 600th cycle. The measured results directly confirmed that the cumulative damage of aged bonded joints subjected to cyclic loading cannot be recovered, like in the unaged bonded joints in chapter 3 [103].

After the cyclic test, the monotonic bond *vs*. slip obtained for the SF-S-CM-02 specimen exhibited a single and linear stage that was associated to a new elastic stage (but with a lower stiffness) originated by the damage previously imposed to the bonded joint by the cyclic loading test. In this particular test, the damage bonded region of the substrate when monotonically reloaded did not show a softening stage as typically revealed in the other specimens under monotonic and cyclic loading conditions.

5.5 Damage analysis of the pseudo-cyclic tests

5.5.1 Local dissipated energy and slip increment

The performance of an adhesively bonded joint is closely related to its local behavior. As analyzed in chapter 3 [103] where un-aged CFRP-to-steel bonded joints were analyzed, no damage takes place within the bonded interfacial region if the bond stress does not overpass its "critical" value, i.e. the maximum bond stress. Consequently, in the linear-elastic bond *vs*. slip stage shown in Figure 5.12a, no stiffness degradation (same slope) nor energy dissipation (no hysteresis area) are detected (see Figure 5.12b). When the bond stresses exceed the "critical" value, some micro cracks initiate and propagate until the complete debonding failure of the joint. This crack initiation and growth is, in the case of the CFRP-to-steel bonded joints, locally reflected through a descending branch of the bond *vs*. slip curve (see Figure 5.12a), and, in this stage, the degradation of the stiffness (lower slope in the cycle than that occurred in the previous one) and the cumulated dissipated energy tend to increase with the number of cycles and/or load amplitude.

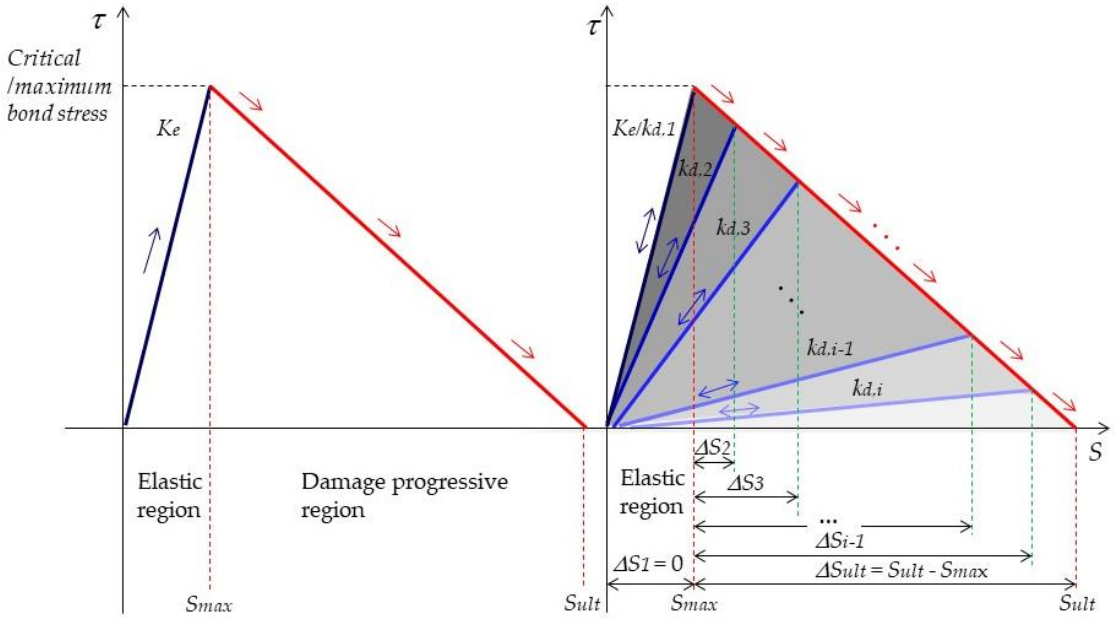

Figure 5.12 - Local interfacial response under: (a) monotonic; and (b) cyclic loading.

As already mentioned, if the maximum bond stress does not exceed the "critical bond stress", no meaningful damage is expected to occur in the adhesively bonded interface. However, damage initiation occurred due to the corrosion rust, which consequently induced that the bond stress surpassed the "critical bond stress" and propagated until debonding failure, eventually presenting mixed failure modes which differ from the rupture modes associated to the unaged bonded joints. The interfacial damage process for aged bonded joints was also reflected in the

degradation of the bond *vs*. slip stiffness (ratio between the bond stress and slip) and dissipated energy (area limited by the loading and unloading of one cycle). Thus, the damage parameter (D) can be defined as a function of the interfacial stiffness, as did in chapter 3 [103]:

$$D = 1 - \frac{k_{d,i}}{K_e} \tag{5.6}$$

where $k_{d,i}$ is the interfacial stiffness at the particular cycle i, K_e is the initial (or elastic) interfacial stiffness, i.e., corresponding to the elastic stage of the bond *vs*. slip relationship (see Figure 5.12). The interfacial damage can be related also with the ratio between the dissipated energy (W_d) determined at a particular cycle and the total interfacial fracture energy (G_f). For easier analyses and interpretation, it is assumed a normalized dissipated energy defined through the ratio of the dissipated energy by the total interfacial fracture energy, i.e. W_d/G_f, and the damage of the CFRP-to-steel interface defined through a function according to:

$$D = \mathrm{f}\left(\frac{W_d}{G_f}\right) \tag{5.7}$$

where

$$W_d = \int_0^{s_i} \tau(s)ds - \frac{{\tau_i}^2}{2k_{d,i}} \tag{5.8}$$

and s_i and τ_i are the slip and the bond stress developed at cycle i, respectively. The total interfacial fracture energy is defined as follows:

$$G_f = \int_0^{s_{ult}} \tau(s)ds. \tag{5.9}$$

The normalized dissipated energy (W_d/G_f) and the damage parameter (D) were experimentally determined, i.e. based on the results obtained for the bond *vs*. slip relationships obtained for the un-aged situation in chapter 3 [103] plus the same relationships obtained for the salt fog aged condition and depicted in Figure 5.7. The subsequent relationship between the damage and the normalized dissipated energy is presented in Figure 5.13. As shown, the damage parameter (D) increased with the increase of the normalized dissipated energy (W_d/G_f), what can be attributed to the degradation of the interfacial stiffness and increase of the cumulative dissipated energy as the load amplitude transmitted to the CFRP laminate increased.

In addition, a trend could be found between the damage parameter (D) and the normalized dissipated energy, which reflected a faster increase of the damage in the first half stage of this relationship that tended to smooth in the second half stage. In order to fit the experimental data of the un-aged and aged specimens, the following mathematical function is proposed:

$$D = \frac{1-e^{\left(r\cdot\left(\frac{W_d}{G_f}\right)\right)}}{1-e^{r}} \tag{5.10}$$

where, for the data collected from the un-aged and aged bonded joints, r = -2.66 and -2.24, respectively.

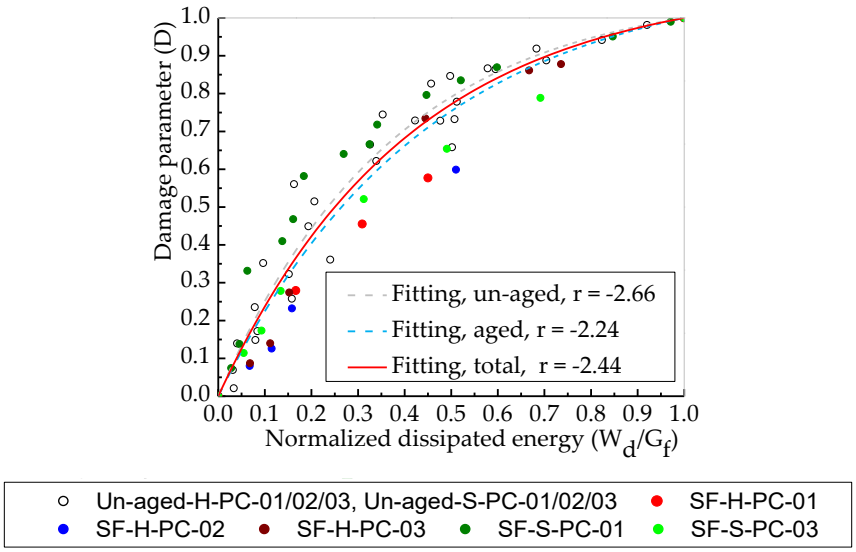

Figure 5.13 - Relation between the damage parameter (*D and*) the normalized dissipated energy (W_d/G_f).

Since the results do not show significant differences between the aged and un-aged bonded joints, an additional fitting procedure was performed for the CFRP-to-steel bonded joints (both aged and un-aged) using Eq. (5.10). The subsequent output led to r = -2.44, placed between the un-aged (r = -2.66) and aged (r = -2.24) cases, as can be graphically confirmed in Figure 5.13. Therefore, it is reasonable to adopt the same mathematical function to represent the damage evolution with the normalized dissipated energy of CFRP-to-steel bonded joints independently of their aging condition (un-aged or aged with salt fog).

As analyzed in chapter 3 [103] for un-aged CFRP-to-steel bonded joints, the damage parameter can also be related to the interfacial slip (see Figure 5.12b). In this case, once the bond stress in the interface exceeded the "critical bond stress" i.e. the slip (s) in the interface became larger than s_{max} the damage in the interface was triggered. Thus, to analyze the evolution of the damage in function to the slips, the experimental results obtained from the aged and un-aged specimens were used. In the present analysis, $\Delta S = s - s_{max}$ was considered.

It was also possible to establish relationships between the ratio of the slip increment ($\Delta S = s - s_{max}$) and the maximum slip increment ($\Delta S_{ult} = s_{ult} - s_{max}$), as seen in Figure 5.12b, permitting to correlate the damage parameter (D) with the normalized slip increment ($\Delta S/\Delta S_{ult}$). Since two different ways allowed the definition of the damage parameter, the normalized slip increment ($\Delta S/\Delta S_{ult}$) and the normalized dissipated energy (W_d/G_f) were coupled and a relationship between both was established. For the former case, the experimental results are

presented in Figure 5.14 whereas for the latter one the results are shown in Figure 5.15.

The relations between the damage parameter (D) and the slip increment ($\Delta S/\Delta S_{ult}$) exhibited similar trend for the un-aged and aged CFRP-to-steel bonded joints (see Figure 5.14). Such relationship can be closely approximated through the same type of exponential function already defined for the relation between the normalized dissipated energy (W_d/G_f) and damage parameter (D) defined in Eq. (5.10), with W_d/G_f replaced by $\Delta S/\Delta S_{ult}$

$$D = \frac{1-e^{\left(r\cdot\left(\frac{\Delta S}{\Delta S_{ult}}\right)\right)}}{1-e^{r}} \tag{5.11}$$

where, once again, the value for r is based on the experimental data and obtained through a fitting procedure where the experimental data from the un-aged, aged and total specimens provided the following output r = -3.67 with a 0.99 of coefficient of determination (R^2), -2.83 with 0.99 of R^2 and -3.16 with 0.98 of R^2, respectively. These three corresponding mathematical functions are graphically represented in Figure 5.14 and it seems reasonable to consider the same variation trend for the un-aged and aged CFRP-to-steel bonded joints, with r = -3.16. Based on this consideration, the relation between the normalized slip increment ($\Delta S/\Delta S_{ult}$) and the normalized dissipated energy (W_d/G_f) was empirically established as a linear relationship where Eq. (5.10) with r = -2.44 and Eq. (5.11) with r = -3.16 were used. The results then obtained are presented in Figure 5.15 which fairly confirms that linear trend.

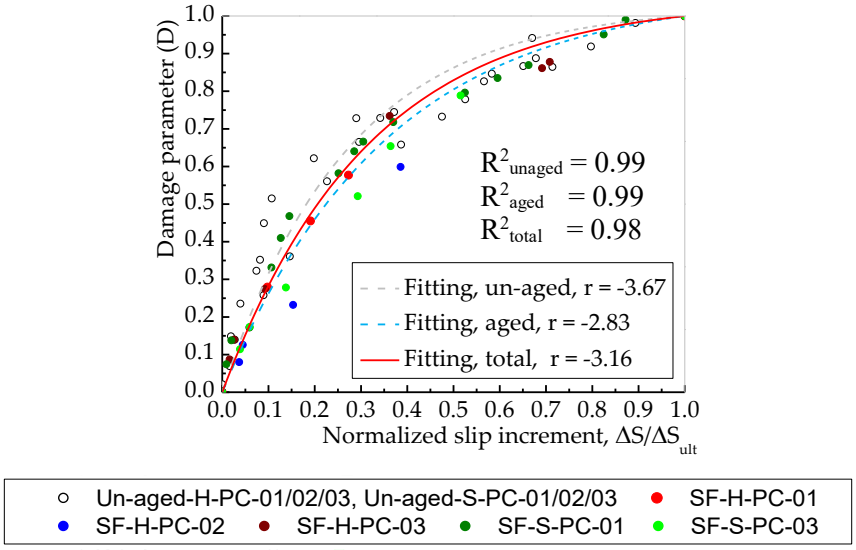

Figure 5.14 - Relation between the damage parameter (D) and the normalized slip increment ($\Delta S/\Delta S_{ult}$).

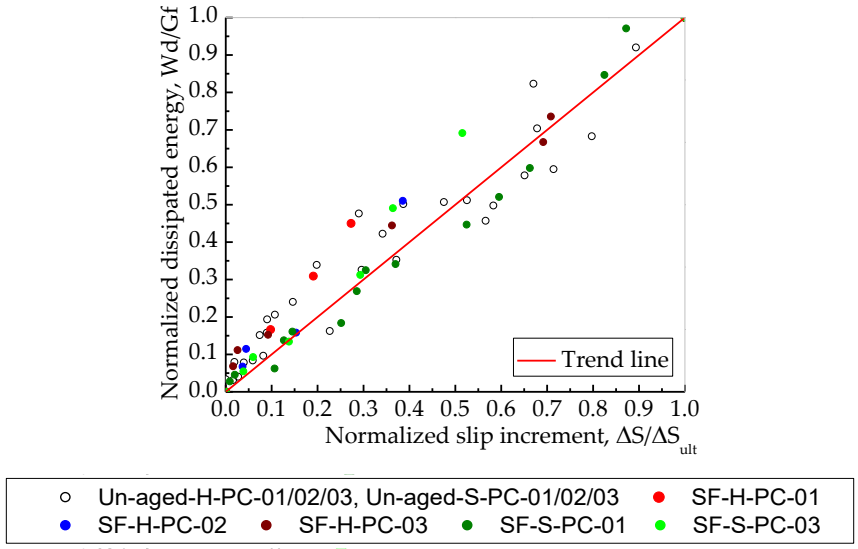

Figure 5.15 - Relation between the normalized dissipated energy (W_d/G_f) and the normalized slip increment ($\Delta S/\Delta S_{ult}$).

5.5.2 Damage global analysis

The global interfacial damage is reflected on the global interfacial dissipated energy, i.e., the area under the force *vs*. slip curve for one cycle (during the loading and unloading process) and the global interfacial dissipated energies of the aged joints based on the experimental force *vs*. slip responses in Figure 5.6, led to results presented in Figure 5.16.

Figure 5.16a shows the global interfacial dissipated energy per cycle (Ep) for aged HIT and SIKA CFRP bonded joints. The global dissipated energy could be ignored in the initial cycles and started to increase at a particular cycle until the complete debonding failure of the joints. The same observation was made by authors when un-aged CFRP-to-steel bonded joints were tested under a cyclic loading history in chapter 3 [103]. Therefore, all the points of the bonded regions under the elastic regime were ignored since their corresponding values will not have impact on calculation of the global interfacial dissipated energy in higher cycles. Consequently, the global interfacial dissipated energy only had meaningful increase when the damaged interfacial regions of the joint increased. This trend can also be seen in Figure 5.16b, where the cumulative global interfacial dissipated energy (E*d*) obtained from the pseudo-cyclic tests of the specimens is presented.

The experimental results of the normalized local interfacial dissipated energy (W_d/G_f) and their corresponding normalized global interfacial dissipated energy (E_d/E_t) are shown in Figure 5.17a. The two seem to have a linear relationship, as seen in the figure. In the previous section, the experimental results of the normalized slip increment ($\Delta S/\Delta S_{ult}$) and the normalized local interfacial dissipated energy (W_d/G_f) also exhibited a linear relationship. Therefore, it is reasonable that the normalized global interfacial dissipated energy (E_d/E_t) and the normalized

slip increment ($\Delta S/\Delta S_{ult}$) be linearly correlated as, in fact, the experimental results seemed to confirm, as shown in Figure 5.17b.

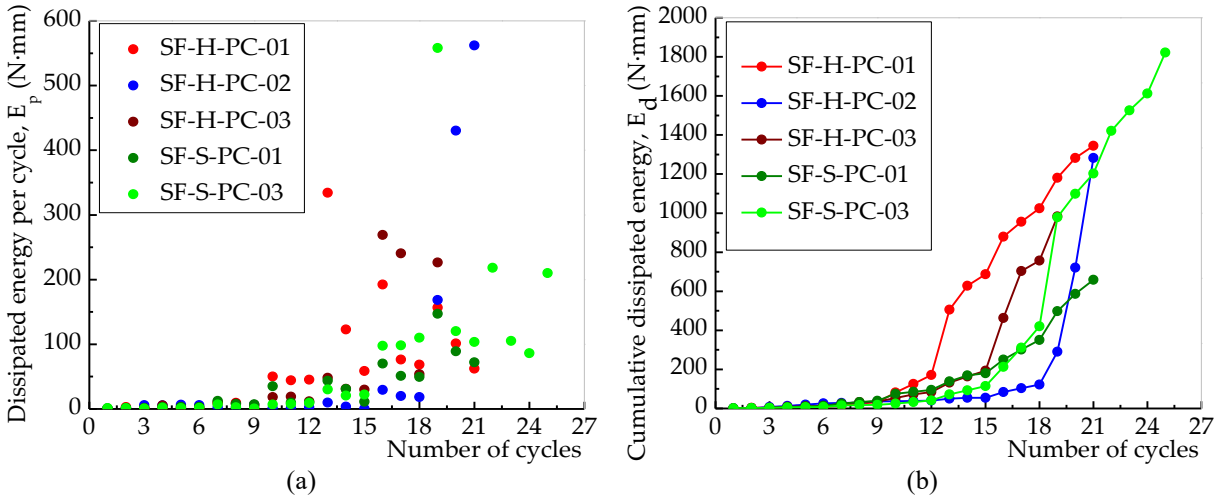

Figure 5.16 - Dissipated energy: (a) per cycle; and (b) cumulative.

From the previous analysis, the results confirmed that normalized slip increment ($\Delta S/\Delta S_{ult}$), normalized local and global interfacial dissipated energy (W_d/G_f) and (E_d/E_t), may be linearly correlated. This is an important aspect since it allows a simple estimation of the global interfacial damage according to the local interfacial damage or to the normalized slip increment.

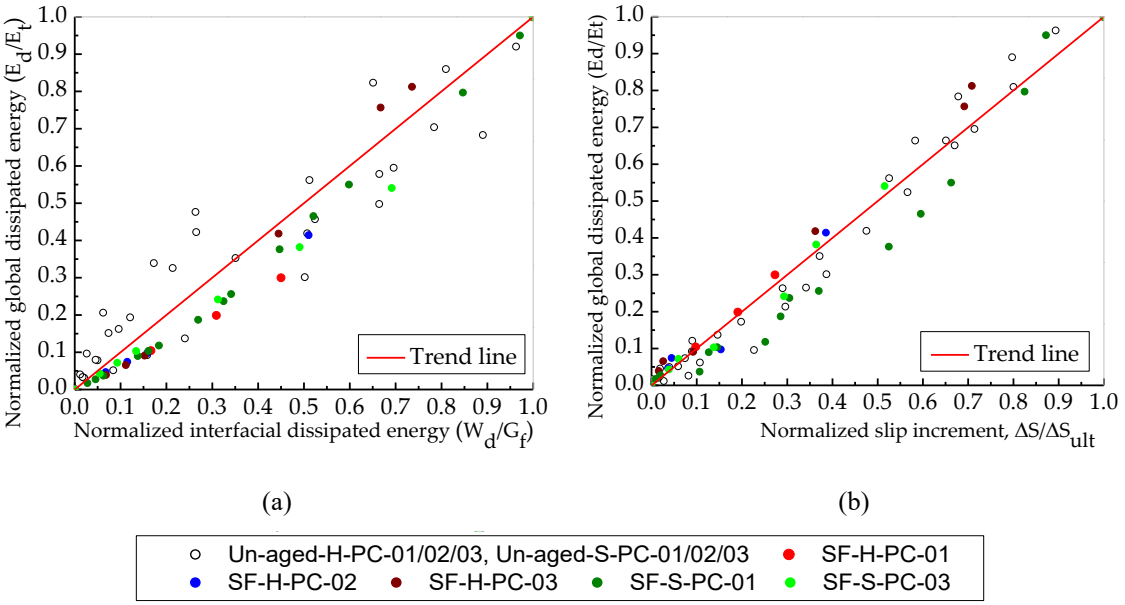

Figure 5.17 - Relations between: (a) normalized interfacial and normalized global dissipated energies; and (b) normalized slip increment and normalized global dissipated energies.

For instance, a 60% of normalized interfacial slip increment of the CFRP-to-steel joint indicates

a 60% of the local interfacial damage and a 60% of global interfacial damage. Despite these values cannot allow quantification of the debonding progression, they show, at a particular point of the bonded joint, how the global interfacial damage develops. Thus, the analyses based on the normalized interfacial slip increment ($\Delta S/\Delta S_{ult}$) are important because through this index it is possible to estimate the damage progress of an interfacial region through a particular interfacial slip increment that is correlated to a particular local or global interfacial damage of the adhesively bonded joint including both unaged and aged.

5.5.3 Influence of the salt fog

In order to highlight the effects of salt fog aging on the interfacial damage of the specimens, the external mechanical loading and the local response of the CFRP-to-steel interface are analyzed, before and after the salt fog aging, during the damage propagation process. The load transmitted to the CFRP at the loaded end, the interfacial dissipated energy (measured at 12.5 mm from the CFRP loaded end) and the slip increment (measured at 12.5 mm), for either un-aged or aged joints, were normalized by their corresponding un-aged value (control value). Thus, the normalized load, the normalized interfacial dissipated energy and normalized slip increment are defined, respectively, from hereafter as follows:

$$\overline{F} = \frac{F_i}{F_{max,0}}, \tag{5.12}$$

$$\overline{W_d} = \frac{W_{d,i}}{G_{f,0}} \tag{5.13}$$

and

$$\overline{\Delta S} = \frac{\Delta S_i}{\Delta S_{ult,0}} \tag{5.14}$$

where, F_i is the load transmitted to the CFRP loaded end, either un-aged or aged bonded joints; $F_{max,0}$ is the average value of the maximum cyclic load of un-aged bonded joints (at 0 h); $W_{d,i}$ is the local dissipated energy measured, in this case, at 12.5 mm from the CFRP loaded end, for either un-aged or aged bonded joints; $G_{f,0}$ is the average fracture energy associated to the un-aged bonded joints (at 0h); ΔS_i is the slip increment of bonded joints either aged or un-aged; and $\Delta S_{sult,0}$ is the average value of the maximum slip increment of the un-aged bonded joints (at 0 h).

The changes of the normalized load ($F_i/F_{max,0}$) during the damage propagation process were calculated and the results are shown in Figure 5.18 for un-aged and aged bonded joints (HIT and SIKA). From the curves shown in Figure 5.18a, it is possible to verify that approximately 61% to 72% of maximum load is transmitted to the aged CFRP loaded end in the HIT bonded

joints, a value much lower than the 85% to 100% observed in the un-aged bonded joints, which have caused the damage initiation and the debonding of the CFRP-to-steel interface at 12.5 mm away from the CFRP loaded end. As the damage increase, the transmitted load to the CFRP laminate seems to increase linearly and therefore, linear fitting curves were assumed to define the variation of the normalized load with the damage of the interface. However, it should be noticed that the experimental results have a scatter trend, especially those obtained from the aged HIT CFRP specimens (see Figure 5.18a).

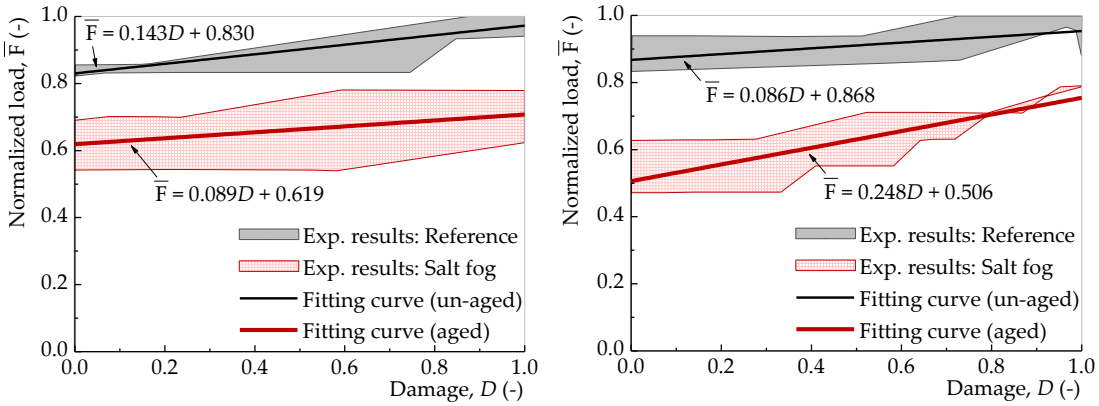

Figure 5.18 - Relation between the normalized load transmitted and the damage parameter (D) for: (a) HIT CFRP specimens; and (b) SIKA CFRP specimens

Like to the HIT CFRP bonded joints, after salt fog exposure, the SIKA CFRP-to-steel interfaces also need a much smaller load to reach debonding (measured at 12.5 mm away from the CFRP loaded end). As showed in Figure 6.18b, 55% to 79% of the maximum load is transmitted to the aged CFRP loaded end in the SIKA CFRP bonded joints, values much lower than the 87% to 100% detected in the corresponding un-aged bonded joints.

Figure 5.19a shows the D *vs.* $\overline{W_d}$ and the D *vs.* $\overline{\Delta S}$ curves for un-aged and aged HIT and SIKA CFRP bonded joints. From this figure, it can be seen that a much lower interfacial dissipated energy, as well as a much shorter relative deformation between the CFRP and the steel bar, were needed to produce the debonding at 12.5 mm. In other words, a value of 42% of the average rupture energy and of 60% of the slip increment in the aged HIT CFRP bonded joints were enough to cause the debonding at 12.5 mm, compared with the 100% needed for the corresponding un-aged bonded joints. In the case of the SIKA CFRP bonded joints, smaller dissipated energy and relative deformation between the CFRP laminate and the steel bar can also be observed from Figure 5.19b. It is also possible to verify that approximately 71% of the average rupture energy and 71% of the slip increment in the aged SIKA CFRP bonded joints were enough to cause the debonding at 12.5 mm, instead of the 100% needed for the

corresponding un-aged bonded joints.

The proposed Eq. (5.10) can be used herein to estimate the experimental D *vs.* $\overline{W_d}$ curves of the un-aged specimens (with r = is -2.44). However, to represent the experimental D *vs.* $\overline{W_d}$ curves of the aged specimens the following expression is proposed:

$$D = \frac{1 - e^{\overline{W_d} \cdot r}}{1 - e^{\alpha_E \cdot r}} \tag{5.15}$$

where α_E is a coefficient that considers the exclusive influence of the salt fog in the CFRP-to-steel bonded joints. The environmental coefficient α_E was obtained from a similar minimization process as previously followed to obtain parameter r. Thus, for the HIT CFRP specimens, an environmental coefficient of $\alpha_E = 0.44$ was determined whilst for the SIKA CFRP specimens $\alpha_E = 0.71$.

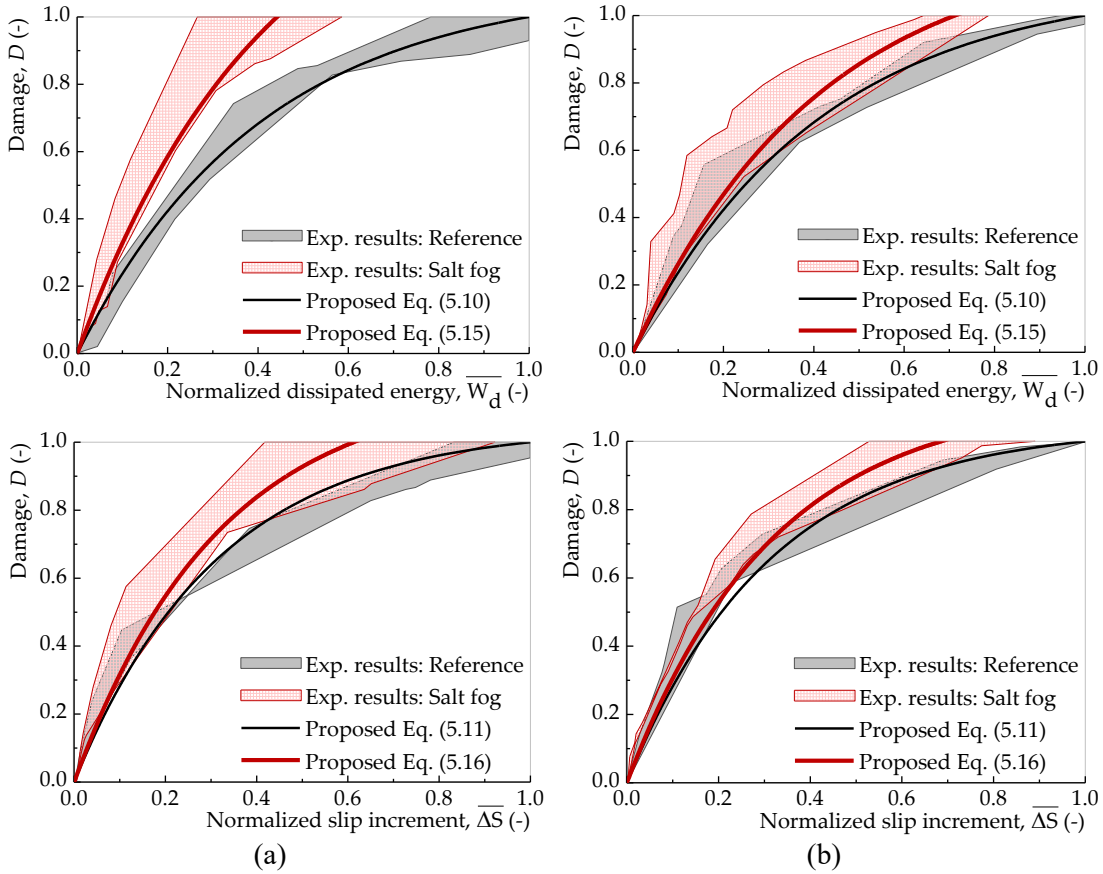

Figure 5.19 - Relations between the dissipated energy and the slip increment (measured at 12.5 mm away from the CFRP loaded end) and the damage parameter for: (a) HIT CFRP specimens; and (b) SIKA CFRP specimens.

Similarly, the proposed Eq. (5.11) was used (with r = -3.16) to predict the damage of the un-aged CFRP-to-steel specimens where ΔS_{ult} in that equation is herein replaced by $\Delta S_{ult,0}$. Thus,

to predict the D *vs*. $\overline{\Delta S}$ curves of the aged specimens, the following exponential function was used:

$$D = \frac{1 - e^{\overline{\Delta S} \cdot r}}{1 - e^{\beta_E \cdot r}}$$

(5.16)

where β_E is a coefficient that takes into account the influence of the salt fog environmental condition. Hence, the minimization procedure carried out to calculate parameter β_E allowed to fit Eq. (5.16) with the experimental results in which $\beta_E = 0.61$ and $\beta_E = 0.69$ were found for the HIT CFRP specimens and for the SIKA CFRP specimens, respectively.

5.6 Remarks

The bond durability of CFRP-to-steel bonded joints was evaluated by applying monotonic and cyclic loadings to different specimens' series after being exposed to 5,000 hours of salt fog cycles (208 cycles). The failure loads and failure modes were recorded and described. Local bond *vs*. slip and global force *vs*. slip relationships were calculated and, based on these, the damage of the CFRP-to-steel bonded joints was analyzed. The results and analyses achieved allow us to enumerate the following conclusions:

- After 5,000 hours of salt fog cycles, the failure mode of the double strap CFRP bonded joints changed from cohesive (in the adhesive) to mixed failure mode. In this latter case, a combination of several ruptures throughout the bonded area was observed. Some parts of the bonded area revealed a partial rupture of: (i) the adhesive; (ii) the CFRP/adhesive interface; (iii) corroded steel substrate; and (iv) the delamination of CFRP in the edges of the bonded area that only was observed in the HIT CFRP-to-steel bonded joints;
- The bond capacity of the bonded joints degraded after salt fog exposure. The reduction of the load capacity of the HIT and SIKA CFRP bonded joints was mainly caused by corrosion of the steel substrate. Damage initiation occurred at the corroded points of the steel substrate which was also associated to a lower maximum bond stress;
- The relationship between the local damage parameter (D) and the normalized local dissipated energy (W_d/G_f) and normalized slip increment ($\Delta S/\Delta S_{ult}$) exhibited the same trend for the bonded joints independently of the environmental exposition that they were exposed to;
- The normalized slip increment ($\Delta S/\Delta S_{ult}$), the normalized local and global dissipated energies (W_d/G_f and E_d/E_t, respectively) can be correlated through a linear relationship between them;
- Some specimens subjected to the cyclic loading had an "accelerated progress" during the

test which was attributed to some stress concentration developed in the interface that was caused by the formation of local corrosion on the steel substrate. Therefore, in these particular points, the damage mechanics of the interface was triggered and the damage progress in those points was "accelerated". As result, the bond *vs*. slip or force *vs*. slip curves had sudden slip increases that were clearly observed at particular cycles;

- The monotonic bond capacity of the joints after being subjected to 600 cycles was reduced, which may indicate that the cumulative damage process of the interface was accelerated;
- Local corrosion points observed on the steel substrate were associated to brittle rupture failure modes for both tests carried out under a monotonic or under a cyclic loading history.
- Approximately 61% to 72% of the average maximum loads were transmitted to the aged CFRP loaded end*s* of HIT bonded joints, a much lower value than the 85% to 100% of the un-aged HIT bonded joints that causes the damage initiation and debonding at 12.5 mm from the aged CFRP loaded end. An approximately 42% of the dissipated energy and 60% of the slip increment were enough to cause the debonding at 12.5 mm of the aged HIT bonded joints. Similarly, 55% to 79% of the maximum load was transmitted to the aged CFRP loaded end, a much lower value than the 87% to 100% of the un-aged SIKA bonded joints. Approximately 71% of the average dissipated energy and 71% of the average slip increment were also observed.

5.7 Summary of this chapter

Deterioration of adhesively bonded CFRP/steel systems in salt fog environment, i.e., deicing salts and ocean environments, has to be taken into account in the design of steel strengthened structures. In the present work, monotonic and cyclic loading were applied to CFRP-to-steel double strap joints for two kinds of CFRP laminates after being aged for a period of 5,000 hours to evaluate the bond behavior. The bonded joints exposed to salt fog had a different failure mode than that observed in the control specimens (0 hours of exposure), see Figure 5.3. The severe reduction of the maximum bond stress resulted from damage initiation that occurred in the corrosion region of the steel substrate, associated with final partial rupture on the corroded steel substrate around the edge of the bonded area: it was also correlated with reduced load carrying capacity. Results of pseudo-cyclic tests showed that the relationship between the local interfacial damage parameter (D) and normalized local interfacial dissipated energy (W_d/G_f) and the normalized interfacial slip increment ($\Delta S/\Delta S_{ult}$) exhibited almost the same trend in the un-aged and aged bonded joints, see Figure 5.13-5.15. The normalized interfacial slip increment can be seen as a direct indicator for the local and global interfacial damage for the un-aged and aged bonded joints, see Figures 5.17. However, monotonic and cyclic tests results revealed that the stress concentration formed by local corrosion of steel substrate could lead to brittle rupture

or accelerated cumulative damage once the aged bonded interface has become weaker. The bonded joints have exhibited also a smaller relative deformation capacity between CFRP and steel, see Figure 5.19.

Chapter 6

CFRP-to-steel joints degradation after salt fog exposure

6.1 Introduction

The absorption of moisture by adhesive and fiber reinforcement polymer (FRP) is a known cause of degradation of some properties and ultimately reduction of life cycle of structures that employ them.

The modification of properties of adhesive subjected to salt moisture materialized, for instance, by water fog cycles includes reduction of elasticity modulus and tensile strength, increase in ductility [111, 107] as well as increase in its Mode-II fracture energy [112] and may severely affect the material durability. Nguyen, et al. [111] immersed Araldite 420 epoxy adhesive in 20°C and 50°C salt water for 12 months and the tensile strength and the elastic modulus were severely reduced. The stress-strain relationship changed from linear to non-linear with an increase of ultimate strain. The degradation primarily occurred in the early stages and was closely related to water absorption. Heshmati, Haghani and Al-emrani [107] exposed epoxy adhesive STO®BPE Lim 567 to salt water at 20°C and 45°C for 260 and 530 days respectively, and the results showed that there was a direct relationship between the moisture content and the mechanical properties. At the highest levels of moisture, the loss of elastic modulus and tensile strength was around 32% and 19% respectively, while the ultimate strain increased approximately 40%.

Accelerated aging tests conducted on CFRP composite materials by immersion in distilled water, salt water or exposure to salt fog, coupled with selected temperatures [111, 113-116] led to degradation primarily attributed to plasticization, swelling and hydrolysis in the matrix as well as weakening of the adhesion between fiber and resin with limited reduction in fiber dominated mechanical properties (tensile strength and modulus) and evident reduction in resin and

interfacial dominated mechanical properties (interlaminar shear strength). Accelerated aging tests with corrosion agents such as an alkaline solution, led to irrecoverable and more severe degradation in the resin and reduction of interface dominated mechanical properties in CFRP laminates [117, 118].

An additional concern results from the eventual contact of carbon fiber reinforced polymer composite materials (acting as a cathode) with most metals as anodes in the presence of an electrolyte e.g. from salt water, and the creation of galvanic coupling [119-123]. Galvanic coupling has been found to degrade the CFRP composite itself besides resulting in more severe metallic corrosion [119-123].

Steel bridges and other structures strengthened with CFRP laminates along the seaside and the use of deicing salts in the cold regions may bring serious deterioration of the structural systems. However, there are scarce durability studies of adhesively bonded CFRP/steel systems under salt fog spray, although some can be found on salt water effects. Salt water ingress into the joints along the interface between the adhesive and steel was found to cause changes in the failure mode and progressive reduction on peel strength [102]. CFRP-to-steel double strap joints immersed in salt water at 38°C and 5% NaCl for 6 months by Dawood and Rizkalla [108] increased bond strength after 1 month immersion and reduced it by 60% after 6 months immersion. The increase was attributed to post-curing while partial corrosion of the steel near the edges of the bonded area and the ingress of salt water along the interface adhesive-steel caused the reduction. Nguyen et al. [111] reported that the tensile strength of CFRP-to-steel double strap joints, after 12 months immersion in 20°C and 50°C salted water exposure, reduced by 17% and 26% respectively. The reduction trend was similar to that of the tensile strength of adhesive coupons and the bond capacity degradation was attributed to the degradation of adhesive. Recent studies on CFRP-to-steel double strap bonded joints reported by Heshmati, Haghani and Al-emrani [107], with the joints immersed in 20°C and 45°C salt water for 36 months, showed that steel significantly corroded but no corrosion was found in the bonded areas. For the immersion in 20°C salt water, the failure mode remained cohesive and the bond strength increased by a maximum of 17% after 1 year immersion followed by a slight reduction. While in 45°C salt water, the failure mode shifted along time and primary failure was due to the damage of fiber/matrix, with a severe degradation of the bond strength.

Different degradation mechanisms were described by Kim, Bumadian and Park [124] who investigated the effects of galvanic coupling on the bond durability of CFRP-to-steel joints and found that the steel acting as anode was significantly corroded in the edges of the bonded areas and debonding failure of CFRP took placed. The authors indicated that the adhesive layer impeded galvanic interaction between the steel and conductive carbon fibers. Recent studies on accelerated corrosion of CFRP-to-steel bonded joints by Batuwitage et al. [32, 33] found that

failure of the joints changed from interfacial failure between adhesive and steel to CFRP rupture failure, and a significant reduction in tensile strength of CFRP. Increasing the number of CFRP layers increased the durability of the bonded joints.

In the present study, two series of CFRP-to-steel bonded joints each made with a different CFRP laminate, as well as adhesive coupons, were exposed to artificial salt fog cycles. Strength capacity of CFRP-to-steel joints was measured under Mode-II loading and the observed failure modes were associated with the properties of the materials. The mechanical properties of the adhesive coupon were analyzed in terms of their influence on the behavior of the bonded joints.

6.2 Materials and bonded joints

In the current chapter, the materials adopted as before (chapter 2, 3, 4 and 5), i.e., HIT CFRP and SIKA CFRP, steel and adhesive SIKADUR 30, were chosen for the study. Since the studies in present chapter primarily focused on the behavior of materials, more detailed and relevant data are provided as possible in the next. The HIT CFRP laminate was produced using epoxy resin system and carbon fiber by pultrusion in the lab of the Harbin Institute of Technology (HIT) in China. The carbon fiber used was PAN-based carbon fibers (TC-36s, Tairyfil Brand carbon fiber) manufactured by the Formosa Plastics Group Production (Taiwan, China). The epoxy resin, diglycidyl ether of bisphenol-A (DGEBA), was procured from Xing-Chen Chemicals Co. Ltd (Wuxi, China). The curing agent used was methyl tetrahydrophthalic anhydride (MeTHPA) procured from Qing-yang Chemistry Co. Ltd (Jiaxing, China). The accelerator was a tertiary amine (tris dimethylaminomethyl) phenol (DMP30) procured from Shan-Feng Chemical Industry Co. Ltd (Changzhou, China). The detailed chemical structures of epoxy resin, curing agent, accelerator and cured epoxy resin are shown in Figure 6.1 [98].

The SIKA CFRP laminates were acquired from SIKA Corporation, and the detailed components information of the fiber and epoxy resin is limited to the product data sheet made available by the supplier to the public.

Same batch of CFRP-to-steel bonded joints were fabricated, some without aging were as reference specimens and the rest went to the corrosion chamber for accelerated salt fog aging. Part of the them (un-aged and aged) were used for bond response measurement as shown in chapter 5 and part of them were used for materials characterization in the present chapter. As such, the information on CFRP-to-steel bonded joints is not repeated here, but some images on adhesive (Figure 6.2a and b) and bonded joints (Figure 6.2c and d) are given.

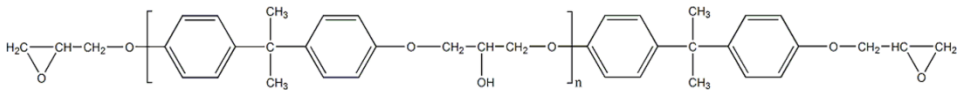

DGEBA (epoxy resin)

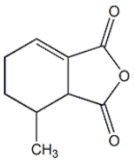

MeTHPA (curing agent)

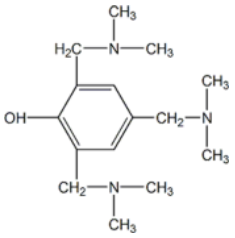

DMP30 (accelerator)

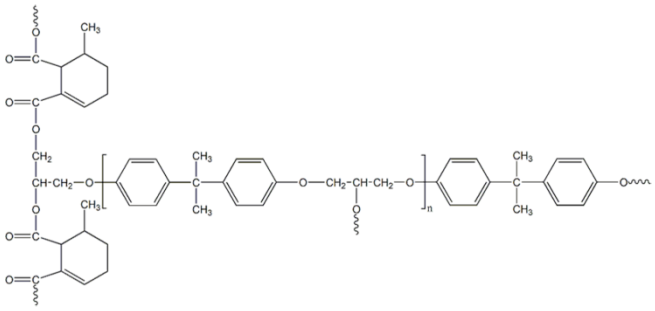

CURED EPOXY

Figure 6.1 - Chemical structure of epoxy resin, curing agent and cured structures in HIT CFRP laminates.

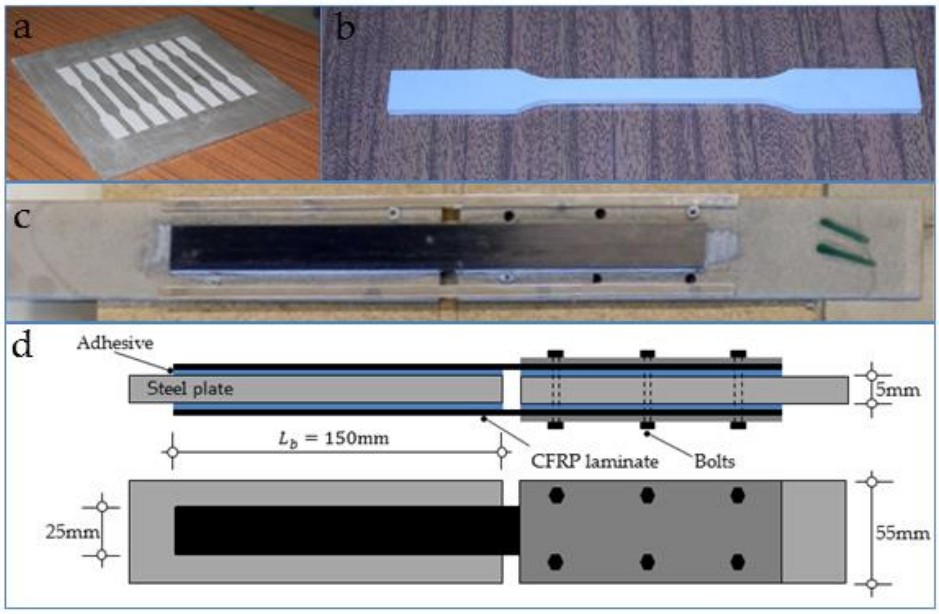

Figure 6.2 – Joint specimens: (a) plate to shape adhesive coupons (b) adhesive coupon (c) and (d) CFRP-to-steel bonded joints.

6.3 Experimental program

6.3.1 Accelerated aging program

The salt fog aging procedure was the same as described in chapter 5. Different stages of aging were considered, 2500 h, 5000 h and 10,000 h, to characterize and compare the properties after aging with those of the reference or control specimens.

6.3.2 Monotonic shear test plan for joints

A total of thirty-six specimens, 24 CFRP-to-steel bonded joints and 12 adhesive coupons, were tested. Three specimens were tested for each condition, as shown in Table 6.1

Table 6.1 - ID of specimens to test and types of environmental exposure.

Specimen	ID	Aging actions	Exposure time (h)
HIT-Bonded Joints	REF-H-01/02/03	Reference	0
HIT-Bonded Joints	SF-H-01/02/03	Salt fog cycles	2500
HIT-Bonded Joints	SF-H-04/05/06	Salt fog cycles	5000
HIT-Bonded Joints	SF-H-07/08/09	Salt fog cycles	10000
SIKA-Bonded Joints	REF-S-01/02/03	Reference	0
SIKA-Bonded Joints	SF-S-01/02/03	Salt fog cycles	2500
SIKA-Bonded Joints	SF-S-04/05/06	Salt fog cycles	5000
SIKA-Bonded Joints	SF-S-07/08/09	Salt fog cycles	10000
Adhesive coupon	REF-A-01/02/03	Reference	0
Adhesive coupon	SF-A-01/02/03	Salt fog cycles	2500
Adhesive coupon	SF-A-04/05/06	Salt fog cycles	5000
Adhesive coupon	SF-A-07/08/09	Salt fog cycles	10000

All the monotonic tests were performed with a Zwick tensile machine with a maximum load capacity of 50kN, Figure 6.3, in the laboratory of the civil engineering department at FCT/UNL. A loading displacement of 1 mm/min was applied to the CFRP-to-steel bonded joints, Figure 6.3a, and adhesive coupons (Figure 6.3b). The axial strain at the narrower section of the adhesive coupon was obtained using a clip-on strain gauge.

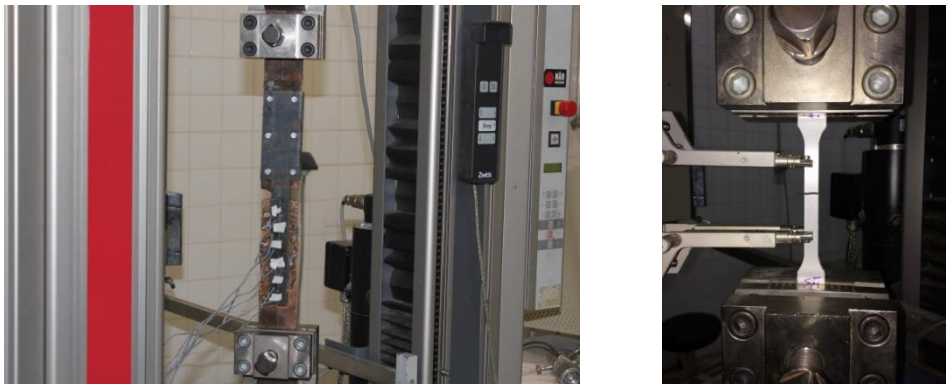

Figure 6.3 - Set-up for tests of (a) CFRP-to-steel joints and (b) adhesive coupon

6.3.3 Dynamic mechanical analysis (DMA)

Dynamic mechanical analysis was chosen to obtain the glass transition temperature (T_g), a property often used to attempt explaining mechanisms of degradation of epoxy adhesive. Yang et al [98] suggested that further cross-linking of the molecular segments induced by temperature rise, in the initial period of post-curing, led to enhancement of the molecular structure causing less mobility that reflected on an increased T_g.

The energy dissipation of FRP composites, interpreted by the area under tanδ curve, is closely related to the properties of the interface between fiber and matrix. Changing the interface properties between fiber and matrix e.g. due to fatigue loading [125], fiber surface modifications [126-128] or environmental aging [129] leads to changes of the energy dissipation of FRP composites, detected by DMA. A degraded fiber-matrix interface dissipated more energy, conversely, an improved interface reduced the energy dissipated. The samples for DMA were prepared by cutting the adhesive coupon and CFRP laminates into prisms of 60x10x3mm^3 for adhesive and 60x10x1.46mm^3 and 60x10x1.26mm^3 for HIT and SIKA laminates. The tests were performed in dual cantilever mode using TA Instruments equipment Q800, at a heating rate of 5°C/min for a temperature range [30; 200]°C with a frequncy of 1Hz.

6.3.4 Scanning electron microscope (SEM) and Attenuated Total Reflectance-Fourier transform infrared spectroscopy (ATR-FTIR)

The tensile failure morphologies of the adhesive coupon and bonded joints, as well as the polished section area of CFRP laminate, were observed with a Hitachi TM 3030Plus Tabletop and a PRO-X Phenom World Scanning Electron Microscope (SEM). The chemical structures of CFRP laminates surface, primarily included the cured epoxy resin, were analyzed using ATR-FTIR spectroscopy over a wave number range of 4000 to 500 cm^{-1} obtained by FTIR-Thermo Nicolet 6700 FTIR spectrometer with ATR attached.

6.4 Results and discussion

6.4.1 Adhesive tensile properties

The tensile properties of the adhesive coupons are shown in Figure 6.4. The tensile stress-strain curves of reference specimen (0h) and aged specimen after salt fog exposure for 2,500h, 5,000h and 10,000h are presented in Figure 6.4a. The stress-strain relationship was initially almost linear, with aging time increasing it became elasto-plastic with a clear plastic plateau, increase of strain and reduction of modulus. The degradation of the tensile properties tended to stabilize after 2,500h aging.

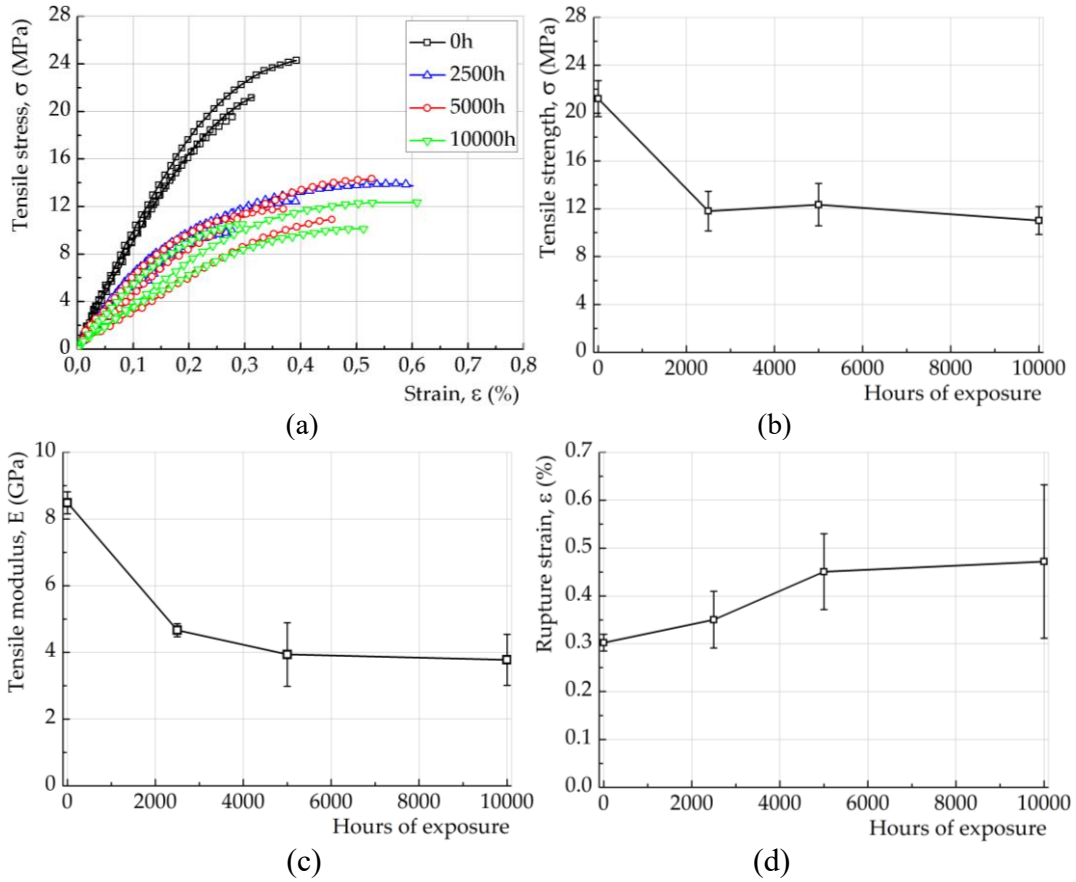

Figure 6.4 - Tensile properties of adhesive coupon with aging; stress-strain curves with aging (a); tensile strength (b); tensile modulus (c); rupture strain (d).

Figure 6.4b shows the variation of the tensile strength of the adhesive coupon with aging time. The degradation of the tensile strength at 2,500h reached 44% and then remained practically constant. Similar trend could be observed for the tensile modulus of the adhesive coupon in Figure 6.4c. As shown in the figure, the tensile modulus decreased by 45% after 2500h aging and then changed only slightly for larger values of time. Figure 6.4d shows the evolution of rupture strain with the aging time, increasing by 16% and 49% at 2,500h and 5,000h, respectively, and then remaining constant at 10,000h.

The reduction of the tensile strength and modulus and the increase of the rupture strain can be primarly attributed to the plasticization due to water that ingressed into the epoxy adhesive, and led to greater flexiblity of the molecular chains. In addition, the degradation of the tensile properties occurred primarily during the first 2500h and these results indicated that the salt water in the adhesive reached dynamic saturation, i.e., the absorption of the salt water equaled the desorption, during the salt fog cycles (6h salt fog spray and 18h no spray in each cycle) after 5000h aging.

Figure 6.5 displays the tensile failure morphologies of the adhesive coupons resulting from 0h,

5000h and 10000h salt fog cycles by SEM images. As shown in the figures, some “voids” were formed inside the sample during their preparation due to the presence of air. The material identified by “1” corresponds to inorganic filler particles inside the adhesive (e.g., SiO_2, Al_2O_3 etc), and by “2” locates a void caused by an air bubble. No significant differences could be observed.

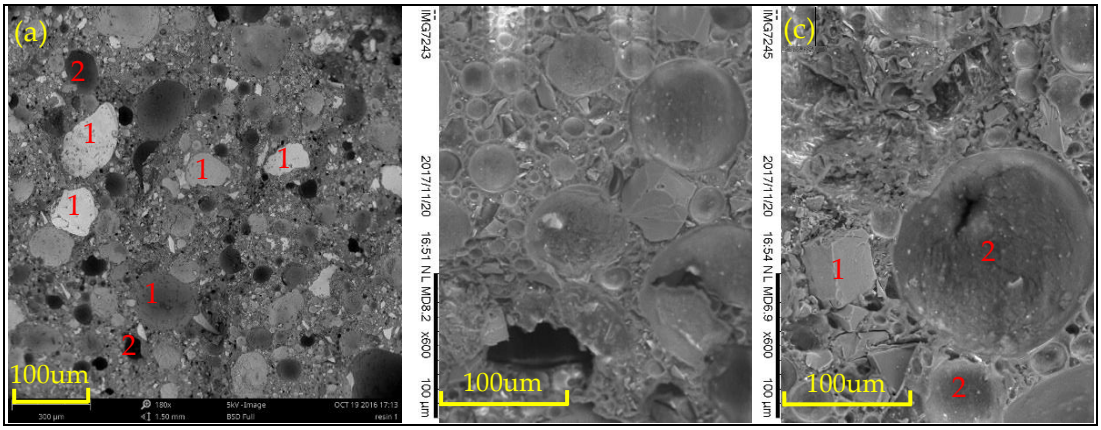

Figure 6.5 - Tensile fracture surface of adhesive coupon with aging; (a) 0h (b) 5,000h (c) and (d) 10,000h

6.4.2 Adhesive glass transition temperature

Figure 6.6 presents the tanδ curves of reference and aged adhesive specimens for various aging times. The T_g of the adhesive was determinded from the temperature main tanδ peak. As shown in the figure, T_g increased from 67°C (reference specimen) to 71°C (salt fog cycles, 2500h+ ambient temperature,5000h of delay tests), and decreased to 65°C (both salt fog cycles, 5000h and 10000h). Besides the main tanδ peak, it is noted that a weak shoulder peak emerged at higher temperature for specimens aged 5000h and became more evident at 10000h.

The T_g of the ambient cured epoxy system after 12 months of ambient exposure increased due to the prevalence of the postcuring versus plasticization and, conversely, it decreased later due to the dominance of the plasticization after immersion in salt water, as reported also in [99]. The constant value of T_g from 5000h to 10000h indicated that the salt water in the adhesive reached dynamic saturation, during the salt fog cycles (6h salt fog spray and 18h no spray in each cycle) after 5000h. The weak shoulder peak is thought to be associated with a higher temperature transition in the specimen surface due to rapid evaporation during the DMA test.

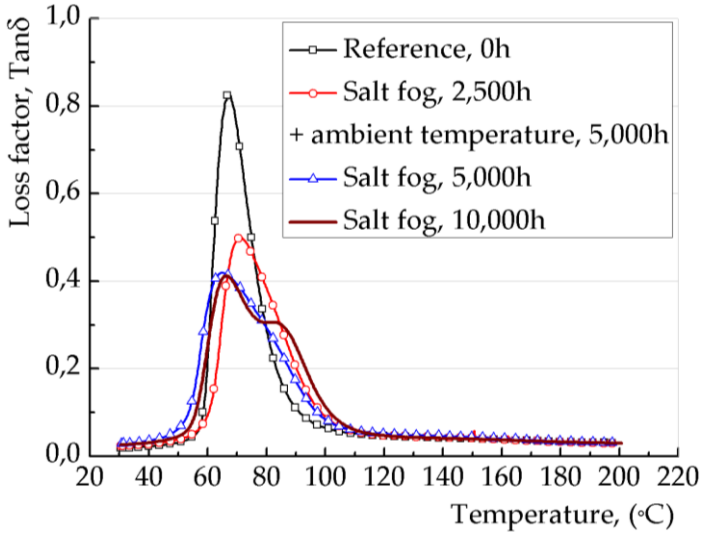

Figure 6.6 - Curves of Tanδ of adhesive for different exposure times

6.4.3 Reduction of joints capacity

The changes of bond capacity of the joints due to aging are graphically presented in this section and matched with the corresponding failure modes.

The normalized failure loads, i.e., the ratios between the bond capacity of samples subjected to 0h, 2500h and 5000h aging by that found at 0h, are presented in Figure 6.7. Around 15% increase in HIT bonded joints and 7% increase in SIKA bonded joints after 2500h aging, were followed by approximately 19% and 21% reduction after 5000h aging. Both kinds of bonded joints suffered corrosion debonding failure in the chamber prior to opening the chamber at 10,000h**.** The increase of the bond capacity was attributed to additional curing of the samples, similar to an increase of 17% reported by Heshmati et al [107]. The reduction in the present case was primarily attributed to corrosion of the steel in the bonded area was much larger than reported elsewhere [107, 111] where the reduction was attributed to the degradation of adhesive or CFRP after immersion in the salt water. Even before reaching 10,000h exposure in the chamber, the steel was severely corroded and debonding took place.

The failure modes of the HIT and SIKA bonded joints aged at 0h, 2500h and 5000h of freeze-thaw cycles are shown in Figures 6.8 and 6.9. The analysis of failure modes was conducted by observing the surface of the debonded CFRP laminates and the corresponding surface in steel to see whether or not either or both had adhesive.

Figure 6.8 shows the tensile failure modes of the HIT bonded joints after 0h, 2500h and 5,000h aging. At 0h, failure occurred inside the adhesive, the surface of the debonded CFRP all are coved with adhesive. However, after 2,500h aging, partial exposure of CFRP and the remaining area was covered with adhesive as seen by SEM. Very little of the edges of the bonded area

were corroded. Samples after 5,000h aging showed severe steel corrosion and intermittent debonding along the edges. Local delamination of CFRP was also observed at the edges after 2500h and 5000h aging. The surface of the carbon fiber from the delamination CFRP was observed by SEM and showed no attachments to the surface of the carbon fiber.

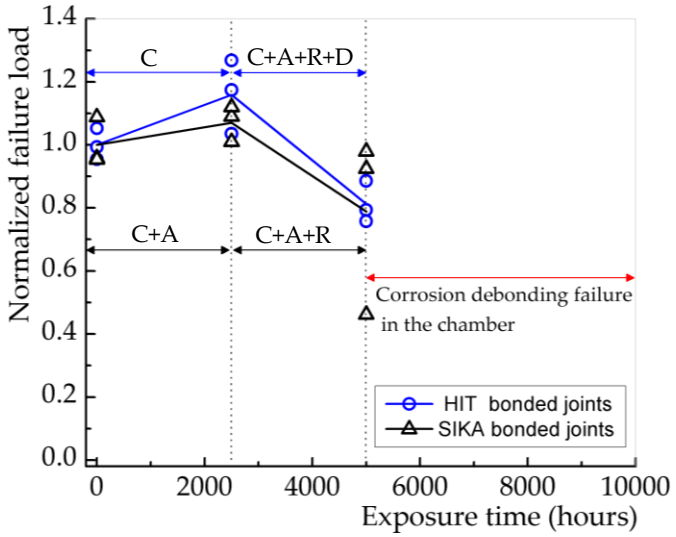

Letters C, A, R, D correspond to cohesive failure mode, failure in the CFRP/adhesive interface, failure in the corrosion rust, and delamination of the CFRP, respectively.

Figure 6.7 - Effects of accelerated salt fog aging on the bond capacity of CFRP-to-steel joints.

Figure 6.9 shows the failure modes of the SIKA bonded joints after 0h, 2500h and 10,000h aging. At 0h they exhibited mixed failure mode combining rupture inside the adhesive and CFRP/adhesive interface debonding. This failure mode was different from the HIT bonded joints at 0h, a fact explained by the weak interfacial bond strength between SIKA CFRP and adhesive, as reported in chapter 3 [103]. At 2,500h the steel substrate at the edges of the bond area was corroded and became more severely so at 5,000h. However, no debonding was observed with aging on SIKA CFRP laminates.

6.4.4 Degradation of the CFRP laminates

CFRP coupons were cut from the bonded joints for 0h and 5000h of salt fog cycles exposure such that the eventual modification of chemical structure by FTIR, thermal mechanical properties by DMA and direct damage by SEM could be studied.

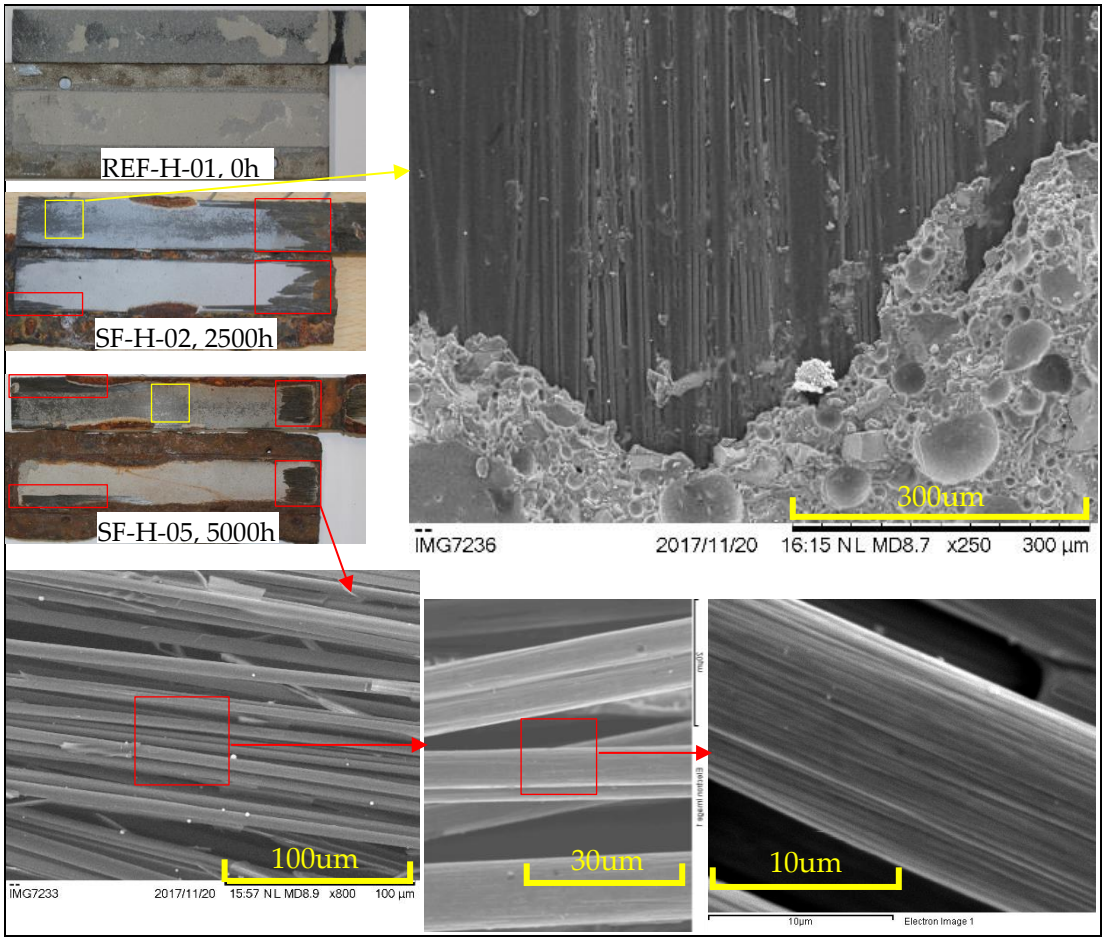

Figure 6.8 - Images of failure surfaces of bonded joints for HIT CFRP.

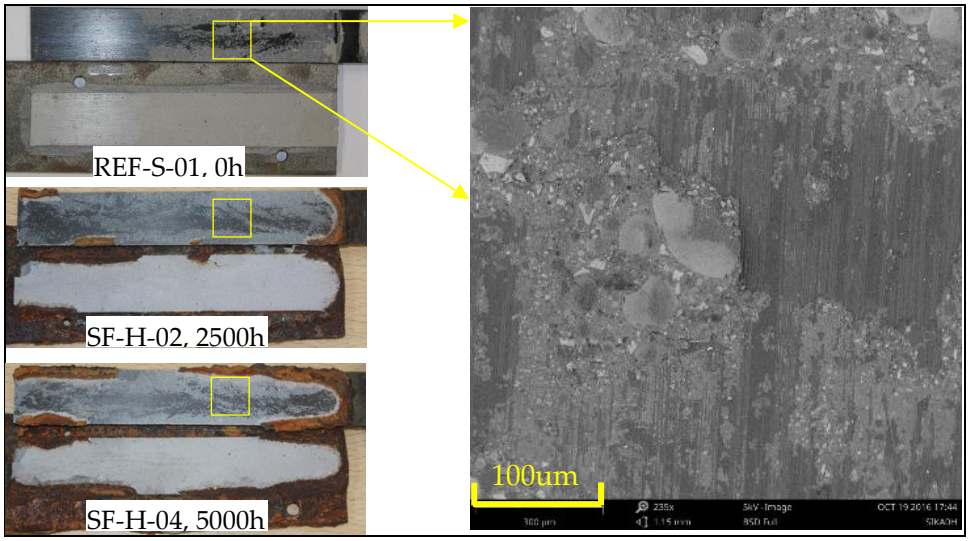

Figure 6.9 Images of failure surfaces of bonded joints for SIKA CFRP.

6.4.4.1 Chemical structure (ATR-FTIR)

The attenuated total reflection Fourier transform infrared (ATR-FTIR) spectra of HIT and SIKA CFRP at 0h (reference) or aged for 5,000h are presented in Figure 6.10. The ATR-FTIR spectra for the CFRP primarily represent the response of its cured epoxy resin. The characteristic

absorption bonds in the spectra of the reference coupon of HIT laminates were divided in three groups identified in Table 6.2. The first group includes an intensity of bond near 3400cm^{-1}corresponding to the O-H stretching vibrations, and indicated the presence of water in the reference HIT CFRP [118, 130]. The second group of bonds located in the region 2750-3400cm^{-1} is related to the stretching vibration of the C-H group of epoxy [118, 130]. The third group of bonds is detected below 2000cm^{-1}. The bands near 1739 and 1280cm^{-1} are characteristic of the stretching vibration of the C=O and C-O groups in the ester group [123, 98]. The presence of bands around 1612 and 1509cm^{-1} was attributed to C=C stretching in alkenes and aromatics, respectively [130]. The bonds near 1042 and 1239cm^{-1} correspond to the symmetric and asymmetric stretching vibration of C-O-φ (φ representing the benzene ring) [98]. The assignment of C-O and C-H aromatic ring stretching was made at 1182cm^{-1} [131]. The band at 827cm^{-1} was attributed to C-H bending in the benzene ring [130].

Comparing the ATR-FTIR spectra of the reference and aged HIT CFRP in Figure 6.10, there are no obvious changes in the FTIR spectra. Figure 6.10 also shows the FTIR spectra of reference SIKA CFRP, which are similar to those of HIT, but the assignment of functional groups is not easy due to lack of data on their chemical composition. Nonetheless, no obvious changes could be observed in the ATR-FTIR spectra obtained through measuring the small area located on the surface of the reference and aged SIKA CFRP coupons, Figure 6.10. Despite CFRP laminates being composed of carbon fibers, matrix and interface, the ATR-FTIR technogly measurements were located in a limited area and the results could not represent the properties of the entire area, nor reflect tiny changes on the matrix adjacent to the fiber-matrix interface when measurements are made in the bulk matrix. It may, nevertheless, be stated that no severe degradation occurred in the epoxy matrix.

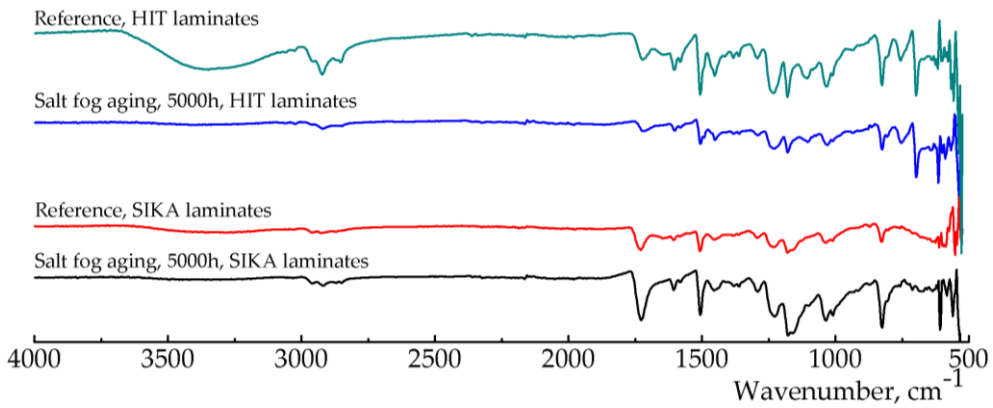

Figure 6.10 - ATR-FTIR spectra for reference CFRPs and aged; HIT and SIKA.

Table 6.2 - Assignment of the characteristic absorption bonds in the FTIR spectra for the reference HIT laminates.

Groups	Absorption bands (cm^{-1})	Assignments
First group	3400	O-H stretch [118, 130]
Second group	2850-2950	Stretching vibration of C-H group of epoxy [118, 130]
Third group	1739	Ester C=O stretch [123, 98]
	1610	C=C stretch bond (alkene) [130]
	1510	C=C (aromatic nucleus) [130]
	1280	Ester C-O stretch [123]
	1239	Asymmetric stretching vibration of C-O-φ [98]
	1182	C–O and C-H aromatic ring stretching [131]
	1042	Symmetrical stretching vibration of C-O-φ [98]
	827	Out of plane bending of C–H in benzene ring [130]

6.4.4.2 Tg results (DMA)

The thermal mechanical properties of the resin matrices (HIT and SIKA) at 0h and after 5000h salt fog aging are presented in Figure 6.11. Fig. 6.11a shows the comparison of the tanδ curve and storage modulus curve of HIT CFRP laminates at 0h and 5000h aging. The reference and 5000h aged specimens exhibited similar storage modulus, and the T_g for reference and 5000h aged specimen were 105°C and 106°C, respectively. However, energy dissipation increased i.e., there was a much higher area under tan δ after aging.

Figure 6.11b shows the comparison of the tanδ curve and storage modulus curve of SIKA CFRP laminates at 0h and 5000h aging. There are two tanδ peaks over the temperature range, and the lower temperature tanδ peak was the T_g of the resin in the CFRP laminates and the higher one was the T_g of the interphase between carbon fiber and resin [125, 132]. For reference and aged specimens, the lower T_g was always 104°C and the higher T_g were 167°C and 165°C, respectively, and the storage modulus and energy dissipation (tanδ curve) were also similar

The measued Tg in the laminates mainly reflected the properties of its matrix, and almost the same Tg was obtained for reference and 5000h aged CFRP laminates indicating that no major chemical change took place in the epoxy matrix.

In the DMA technique, energy dissipation can be measured from the response of the specimen to a low-strain periodic deformation. The energy dissipation of the fibers can be ignored and the deformaton energy dissipated in CFRP is mainly due to the molecular chain motions in the matrix and the interphase region [125-129]. If matrix, fiber volume fraction and fiber orientation are identical, then the energy dissipation can be used to assess the fiber-matrix interfacial properties. A poorer interface causes more energy dissipation since the weak interaction between fibers and matrix increase the mobility of the molecular chains of the fiber-matrix interface during testing [125-129].

Then, since the epoxy matirx in the HIT and SIKA laminates before and after aging were

unaltered, a higher energy dissipation for aged HIT CFRP laminates indicates a poorer fiber-matrix interface. In aged and reference SIKA laminates with no alterations in the fiber-matrix interface properties there was similar energy dissipation. The approximately equal storage moduli can be attributed to the fact that the fiber-matrix interfacial strength had little effect on fiber dominated properties, in agreement with previous experimental results [125].

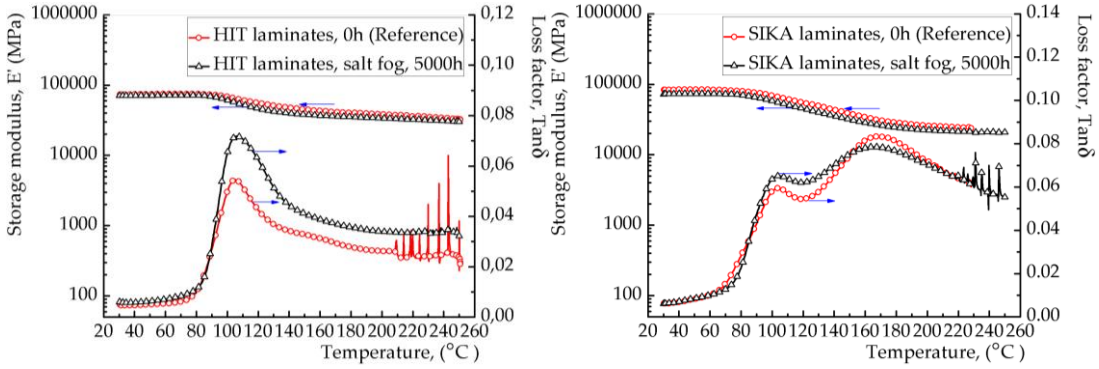

(a) (b)

Figure 6.11 - Storage modulus and tanδ for CFRP laminates with aging; HIT(a); SIKA(b).

As mentioned above, the energy dissipation of carbon fibers can be ignored, thus energy dissipation in the composites primarily occured at the fiber-matrix interface and matrix can be quantitatively estimated using the formula [125-129]:

$$\tan\delta_{int} = \tan\delta_c - \frac{(1-V_f)\cdot E_m \cdot \tan\delta_{mat}}{E_c} \quad (6.1)$$

where, $\tan\delta_{int}$ is the energy dissipation in the interface; $\tan\delta_c$ and $\tan\delta_{mat}$ are the energy dissipation in the fiber reinforced polymer composites and their matrices, respectively; v_f is the fiber fraction; E_c and E_m are the elastic modulus of composites and matrix, respectively.

In the case of HIT CFRP, $\tan\delta_c$ equaled 0.051 at 0h and 0.073 at 5,000h aging, as shown in Figure 6.11a and $\tan\delta_{mat}$= 0.96 [98], v_f= 69%, E_c= 180.5GPa, E_m= 2.75GPa [129]; which leads to $\tan\delta_{int}$= 0.047 at 0h and 0.069 after 5,000h aging; Therefore, the interface energy dissipation of HIT laminates increased by 47%, after aging, which further confirmed the severe degradation of the interface.

Overall, it can be stated that the salt fog cycles degraded the carbon fiber-matrix interface of HIT laminates while no evident similar degradation occurred in the SIKA CFRP laminates.

6.4.4.3 SEM images

Some HIT and SIKA laminates samples were cut from the bonded joints at 0h and after 5000h of salt fog exposure for SEM observation. The cross sections were polished using 1000-4000 grit sandpaper and uniform hand loading.

Figure 6.12 shows the SEM images for 6 samples, including two HIT reference samples and two after 5000h exposure, one SIKA reference and one after 5000h exposure, identified by“1”,

"2", "3", "4", "5", "6". As seen in the images, HIT CFRP (sample 1 and 2) had a smooth surface after polish. However, after 5000h exposure, the carbon fibers in the edge of the sectional area were evidently peeled out, and the damage had a trend of extending towards the center of the laminates. Further observation showed that the surface of the peeled carbon fiber had nothing attached, and the resin separated from the carbon fiber showing no cracking, but a significant separated area, Figure 6.13. No significant difference was observed in SIKA samples 5 and 6. Severe degradation occurred in the interface between carbon fiber and matrix in HIT laminates. These results correlate well with the findings of FTIR and DMA.

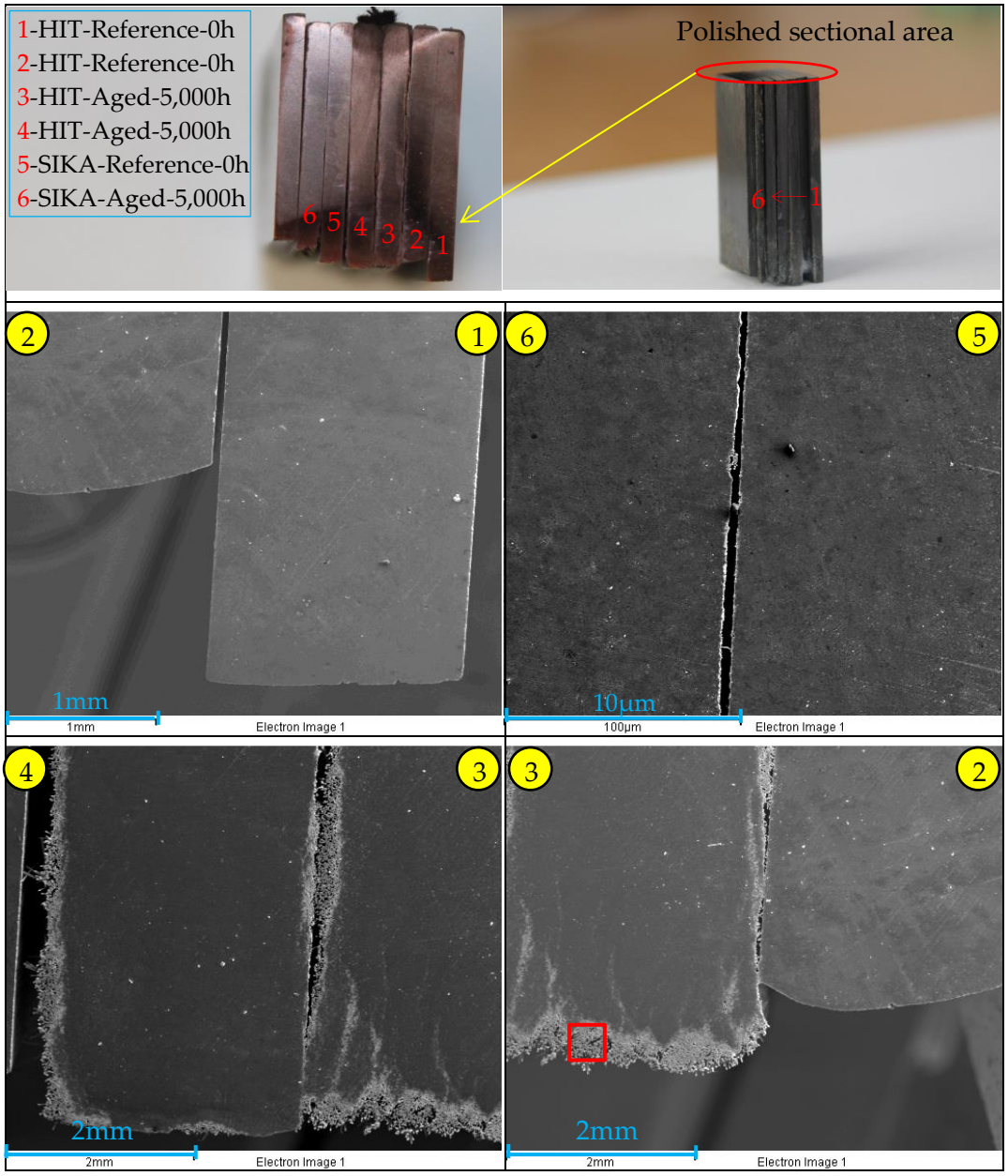

Figure 6.12 - SEM images of sectional area from reference and aged after polished.

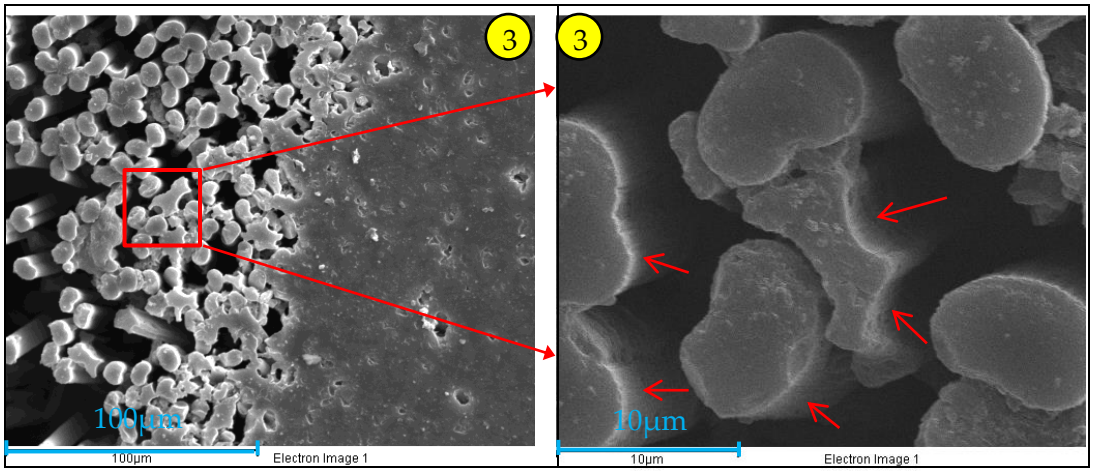

Figure 6.13 - Amplified SEM images of sectional area from HIT laminate aged 5,000h.

6.4.5 Corrosion mechanism of the CFRP-to-steel system under salt fog exposure

In the salt fog aging chamber, electrochemical corrosion occurred in the presence of salt water spray around the CFRP/steel bonded system. Figure 6.14 illustrates the overall corrosion mechanism occurring in the CFRP-to-steel bonded joints under those conditions of exposure.

At the beginning of the essay, the iron corrosion developed by uniform corrosion in the steel plate. In this aerated solution, the iron oxidation should be mainly supported by the cathodic reaction of oxygen reduction at the metallic alloy surface:

$$O_2 + 2H_2O + 4e^- \rightarrow 4OH^- \quad (6.2)$$

Further chemicals equilibriums generated several iron corrosion products, such as:

$$3Fe + 4H_2O \rightarrow Fe_3O_4 + 8H^+ + 8\ e^- \quad (6.3)$$

$$2Fe + 3H_2O \rightarrow Fe_2O_3 + 6H^+ + 6\ e^- \quad (6.4)$$

A galvanic corrosion between steel and CFRP laminates starts when the corrosion products, comprising magnetite (Fe_3O_4) with a higher electric conductivity, precipitated on the joint of CFRP/steel, electrically connecting the metal to the carbon fibers. Due to the higher electrochemical potential of the carbon fibers, the cathodic reduction of oxygen is partially localized to the exposed carbon fibers and to carbon fiber-resin interfaces. This will increase the pH inside the CFRP laminates.

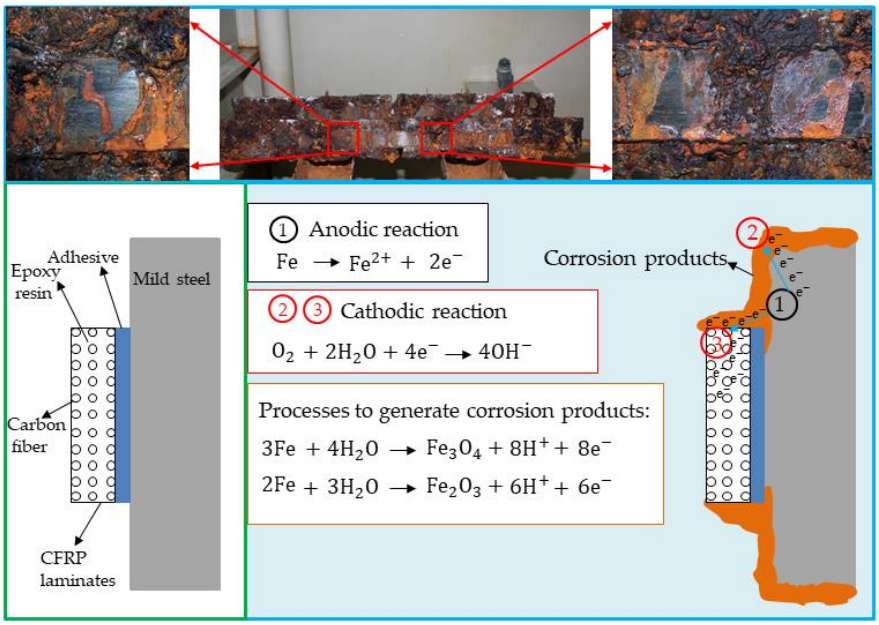

Figure 6.14 - Galvanic corrosion mechanism of the CFRP-to-steel bonded joints under salt fog exposure.

With all these conditions satisfied, one possible damage mechanism was associated by Sloan and Talbot [123] on their study of galvanic corrosion of a graphite fiber polymer composite,with an epoxy matrix that exhibited–ester bond and showed severe degadation in the composite material. The reason was attributed to the disruption of the ester bond in the epoxy matrix attacked by the OH^- produced due to cathodic reaction near the carbon fiber. Their conclusion was verified by FTIR results. However, in the present case, no obvious degradation found in the epoxy matrix based on the FTIR and DMA analysis. Therefore, tiny damage of the epoxy matrix near the fiber-matrix interface due to the same mechanism described above and broken ester linking may have been enough to cause severe damage in fiber-matrix interface. Another possibility was that an osmotic pressure formed within the carbon fiber-matrix interface with production of the OH^- [120, 121], the stress produced by osmotic pressure could damage the interface. It also was possibility that above two combined.

Thus, galvanic corrosion caused damage of carbon fiber-matrix interface in the HIT laminates as analyzed by FTIR and DMA and observed by SEM. However, no degradation of SIKA CFRP was observed. This suggests a lack of intrinsic CFRP conditions to form galvanic corrosion in this composite. As an example, no degradation in CFRP composites after potentiostatic polarisation treatment was observed by Liu et al. [133]. So, material conditions, such as carbon fiber surface treatments, polymer matrix composition, interfacial qualities between carbon fiber and polymer matrix and manufacturing processes are important [120-123].

6.5 Remarks

Durability of CFRP-to-steel joints subjected to artificial salt fog aging was assessed through a series of experimental tests pre and after aging by salt fog spray cycles. Mode-II loading of the joints was used as well as techniques of materials engineering to characterize and interpret their behavior. Based on the analysis of the results, the following conclusions can be stated:

- Bond capacity of joints was greatly affected by cycles of salt fog aging, with approximately 20% decrease after 5,000h aging.
- Specimens aging for 10,000h were found debonded in the chamber, the failures being primarily associated with corrosion of steel.
- The mechanical and thermal-mechanical properties of the adhesive degraded fast in the initial 2,500h aging and remained almost unaltered after that.
- The delamination of HIT laminates started along the edges, and deterioration progressed from there towards the inner part of the CFRP laminates.
- Severe degradation in the interface between HIT carbon fibers and resin matrix was found. No such degradation was detected in the SIKA laminates.
- Galvanic coupling between CFRP and steel developed due to the corrosion product depositions over the components, acting as electric bridges, leading to the degradation of the HIT laminates.

6.6 Summary of this chapter

Environmental effects on CFRP-steel joints are studied via accelerated aging by salt fog. Mode-II tests were conducted to assess bond capacity of CFRP-to-steel in double strap joints for two different types of laminates after 10,000 hours of salt fog aging. Different degradation mechanisms are analyzed. The results show initial increase of the bond capacity of the joints, followed by decrease at later stages (Figure 6.7). Corrosion debonding took place in the chamber prior to 10,000h and without loading. Combined Attenuated Total Reflectance-Fourier transform infrared (FTIR) spectroscopy (Figure 6.10) and Dynamic Mechanical Analysis (DMA) results (Figure 6.11) only showed severe degradation at interface of carbon fibers and resin for one type of the laminates used. Galvanic corrosion was also detected and analyzed (Figure 6.14).

Chapter 7

Conclusions, recommendation and further research

7.1 General

The effectiveness of CFRP laminates strengthening steel structures with adhesively bond technology directly depends on their bond performance. A CFRP-to-steel double strap bonded joints, as a simplified model, was adopted throughout the entire process of the research to study bond response under mechanical loading namely monotonic and repeated loading, as well as to assess durability when subjected to severe conditions. Therefore, briefly, the present work can be divided into two parts. The first part of the work describes some monotonic and cyclic tests on the CFRP-to-steel bonded joints to study the interfacial stress transfer mechanism and propose an interfacial constitutive model under monotonic loading; it further examines the bond response under different repeated load levels of amplitude to find the bond cumulative damage mechanism. The second part of the work assesses the durability of the CFRP/steel bonded system subjected to relative long-term artificial accelerated aging (freeze-thaw cycles and salt fog spray). Materials and bond properties were characterized and their modifications with aging were examined. Based on those, their degradation mechanisms were described. The results of analytical and experimental characterization associated with various service conditions, i.e., monotonic, cyclic, freeze-thaw and salt fog of this systematic research work were presented in five chapters (including five journal articles), which promote the progress of this field in CFRP laminates strengthening steel structures. The following conclusions were taken based on the series of analysis and experimental work.

7.2 Conclusions

7.2.1 Materials degradation

The tensile mechanical properties and thermal mechanical properties of adhesive flat coupon have been slightly changed after the current freeze-thaw cycles i.e., 833 cycles (with 10,000 h

of exposure to temperature variation between +20°C and -20°C under 50% of RH); However, after salt fog exposure, due to the plasticization of the moisture, the mechanical and thermal-mechanical properties of the adhesive degraded fast in the initial 2,500h aging and remained almost unaltered after that.

The galvanic corrosion of HIT CFRP laminates, that was fabricated in the adhesively bonded joints with steel plate under salt fog exposure, was detected through FTIR, DMA and SEM characterization. Severe degradation occurred within the fiber/resin interfacial region However, no such degradation detected in SIKA CFRP laminates.

7.2.2 Failure mode of bonded joints

The failure modes of the CFRP-to-steel bonded joints test in the current thesis are summarized in Table 8.1. The control bonded joints with HIT CFRP laminates have cohesive failure mode. With the freeze-thaw cycles, that changes to mixed failure mode (I+C) due to the degradation of the steel/adhesive interface. With the salt fog exposure, that changes to mixed failure mode (C+A+R+D) due to the degradation of the adhesive/CFRP interface and corrosion of the steel substrate and galvanic corrosion of the CFRP laminates.

The control bonded joints with SIKA CFRP laminates have mixed failure mode (A+C) due to the weak link between CFRP and adhesive. With the freeze-thaw cycles, the failure mode remained the same. With the salt fog exposure, that changed to mixed failure mode (A+C+R) due to the corrosion of the steel substrate.

The failure modes did not change for both the unaged and salt fog aged bonded joints previously subjected to pseudo-cyclic or cyclic loading when compared with those monotonically loaded;

7.2.3 Bond strength and load carrying capacity of bonded joints

The bond strength, i.e., maximum bond stress, is associated with the damage initiation within the bonded joints. HIT bonded joints have a much higher bond strength than SIKA, cause that in the former the damage initiation occurred inside the adhesive, while in the latter damage occurred within the CFRP/adhesive interface. That also is the main cause that the former has a much higher loading carry capacity than the latter.

Damage initiation occurred in the corroded points of steel substrate, which was associated to a much lower maximum bond stress. This is also the main cause that the loading capacity of the bonded joints after salt fog exposure evidently decreased.

Pseudo-cyclic and cyclic tests under a limited number of cycles had slight effect on the load carrying capacity either on unaged HIT or SIKA CFRP laminates, while some monotonic load capacity of aged HIT and SIKA bonded joints after cyclic tests seems reduced. This fact can be attributed to a residual bond length longer than the effective bond length in terms of unaged

bonded joints but shorter in terms of aged bonded joints, causing that the accelerated cumulative damage process.

Table 7.1 Failure mode of the bonded joints test in current thesis.

Specimen	Aging condition	Duration (h)	Loading type	Failure mode
HIT	Control	0	Monotonic	C
			Pseudo-cyclic	C
			Cyclic	No Failure
			Monotonic after cyclic	C
	Freeze-thaw	2500	Monotonic	C
		5000		I+C
		10000		I+C
	Sat fog	2500	Monotonic	C+A+R+D
		5000	Monotonic	C+A+R+D
			Pseudo-cyclic	C+A+R+D
			Cyclic	C+A+R+D
			Monotonic after cyclic	C+A+R+D
		10000	Monotonic	C+A+R+D
SIKA	Control	0	Monotonic	A+C
			Pseudo-cyclic	A+C
			Cyclic	No Failure
			Monotonic after cyclic	A+C
	Freeze-thaw	2500	Monotonic	A+C
		5000		A+C
		10000		A+C
	Salt fog	2500	Monotonic	C+A+R
		5000	Monotonic	C+A+R
			Pseudo-cyclic	C+A+R
			Cyclic	C+A+R (Part failure)
			Monotonic after cyclic	C+A+R
		10000	Monotonic	C+A+R

Note: C means that the rupture occurred inside the adhesive (cohesive failure); A means that it occurred within the interface between CFRP and adhesive; I refers to the rupture occurred within the interface between steel and adhesive; R refers to the rupture occurred inside the steel corrosion rust; D means delamination of the CFRP;

7.2.4 Closed-form solutions

The stress transfer mechanism of CFRP-to-steel double strap bonded joints (pull-pull tests) with different bond lengths was well explained through closed-form solutions. The interfacial thermal stress under temperature changes can be obtained through closed-form solutions.

7.2.5 Damage analysis

A "threshold loading" was detected (around 50% of the maximum monotonic load capacity of the joints) that corresponds to a "critical bond stress" in the loaded end below which cyclic loading caused no damage.

Moisture is a critically important factor for the freeze-thaw cycles, if present. Cumulative damage within the bonded interfacial region, with temperature cycles between 20ºC and -20ºC, can be ignored because only the elastic regime of the adhesively bonded interface is mobilized.

The relationship between the local interfacial damage parameter (D) and normalized local interfacial dissipated energy (w_d/G_f) and normalized interfacial slip increment ($\Delta S/\Delta S_{ult}$) exhibited the same trend for the bonded joints included the un-aged and aged.

The normalized interfacial slip increment ($\Delta S/\Delta S_{ult}$), normalized local and global interfacial dissipated energy (w_d/G_f) and (E_d/E_t) have a straight relationship with each other. The normalized interfacial slip increment is an important index to characterize damage of the interfacial region.

The stress concentration points formed due to local corrosion of the steel substrate may lead to accelerated damage or brittle rupture failure under monotonic and cyclic loading.

Galvanic coupling between CFRP and steel develops due to the corrosion product depositions over the components, acting as electric bridges and leading to the degradation of the HIT laminates.

7.3 Recommendations

After the studies carried out in the current PhD thesis, the knowledge obtained from the laboratory work and theoretical analysis allows to make some recommendations for the real application of this technology in civil engineering, i.e., strengthening or repair steel elements with CFRP using adhesively bonded technology.

7.3.1 Design of the application of the CFRP to steel substrate

In order to reach the maximum load carrying capacity and fully use this bond technology, increase the safety storage, the bond length of the CFRP should be long enough, i.e., longer than the effective bond length, if the space allows.

When adopting ultimate-high modulus CFRP, due to a higher value of the axial stiffness ratio, β, the damage initiation, propagation and even debonding could be occur from the bonded free end.

The maximum bond stress within the CFRP/steel interface, developed under service loading conditions on a reinforced steel structure subjected, should be controlled within the elastic stage, i.e., less than the critical bond stress defined in current PhD study, in order to avoid cumulative damage.

7.3.2 Conditions to execution of the CFRP to steel substrate

The bonded surfaces of the steel and CFRP must be well prepared. In terms of steel substrate, normally, the cleaning methods adopted in the thesis are fundamental. The surface of the steel substrate should be prepared by grit-blasting, dust removing and cleaning with acetone to eliminate grease and other contaminants prior to application of the adhesive. However, a special chemical coupling agent should be applied to improve the adhesive/steel interface service conditions of the bonded system at cold and wet environment.

To avoid the interface failure of bonded joints, as observed in one kind of CFRP (SIKA) in the current study. Prior to application, the bonded surface of the CFRP laminates should be slightly polished with a fine sand paper and then cleaned with acetone to make a stronger interface between CFRP and adhesive, as much as possible.

7.3.3 Inspection, maintenance

Epoxy polymer adhesives are susceptible to a loss of their mechanical properties when the temperature surpasses the T_g. Moreover, the T_g of the adhesive applied in the civil engineering is quite lower because of the low temperature and site cured condition. For example, the T_g of the SIKA-30 utilized in current study is around 60ºC. Therefore, high temperatures should stay far away from the bonded area.

In addition to above, it should be paid attention to the issue of steel corrosion, which may lead to galvanic corrosion of the CFRP. Therefore, regular inspection is necessary and maintenance could be executed, for instance, application of anti-corrosion coating.

7.3 Further research

7.3.1 Mechanical response

a) The CFRP-to-steel double strap bonded joints model adopted in the current study has a low value of the axial stiffness ratio, β. Further experimental tests and analytical solutions on CFRP-to-steel double strap bonded joints model with a higher value of the axial stiffness ratio, β, should be conducted to consider the effects of the ultimate high modulus CFRP laminates utilized in strengthening engineering.

b) The bond mechanism between CFRP laminates and adhesive should be well understood.

The surface treated methods for the CFRP laminates need to be improved to ensure a cohesive failure mode.

c) Fatigue tests can be conducted to obtain S-N curves; the corresponding obtained fatigue endurance may be used for verifying the proposed threshold load in cyclic tests.

d) Since the cumulative damage analysis is based on the static cyclic tests, dynamic tests can be carried out to consider the effects of loading velocity.

e) Numerical modeling can be developed, introducing different failure criteria to compare the failure modes obtained from experiments

f) The bond behavior and global response of a full-scale steel girder strengthened with CFRP laminates could provide useful information.

7.3.2 Durability

a) As analyzed in the article of freeze-thaw aging, moisture may a vital factor for the freeze-thaw cycles. Further freeze-thaw cycles with high relative humidity (RH) should be conducted to directly assess this effect.

b) High temperature with high humidity service conditions should be considered.

c) Different CFRP laminates can be produced with different kinds of fiber, fiber surface treated agent, resin and fiber-resin interfacial properties. Corrosion circle to ascertain its effect on the galvanic corrosion.

Chapter 8

References

[1] Bjorn Paulsson, Tan Olofsson, Hans Hedlund, Brian Bell, Bjorn Talsten, Lennart Elfgren. “Sustainable Bridges - Results from a European Integrated Research Project”. 34th International Symposium on Bridge and Structural Engineering, Venice, September 2010 DOI: 10.2749/222137810796024727

[2] “Status of the Nation’s Highways, Bridges, and Transit: Conditions & Performance”. REPORT TO CONGRESS. U.S. Department of Transportation, Federal Highway Administration, Federal Transit Administration. 2013

[3] Tao X-Y Zhang Y-L, Service life evaluation experience for existing railway steel bridge in China. Advanced steel construction 2015; 11:347-358

[4] Karbhari VM. Rehabilitation of civil infrastructure using Fiber reinforced polymer (FRP) composites. 2014

[5] Al-Zubaidy HA, Zhao X-L, Al-Mahaidi R. Experimental evaluation of the dynamic bond strength between CFRP sheets and steel under direct tensile loads. International Journal of Adhesion& Adhesives 2012; 40:89–102.

[6] Hollaway LC, Cadei J. Progress in the technique of upgrading metallic structures with advanced polymer composites. Prog Struct Eng Mater 2002; 4(2):131–48.

[7] Kumar P, Chandrashekhara K, Nanni A. Structural performance of a FRP bridge deck. Constr Build Mater 2004; 18(1):35-47.

[8] Yi C, Julio F. Accelerated aging test for evaluations of durability performance of FRP reinforcing bars for concrete structures. Compos Struct 2007; 78:110–1.

[9] Uomoto T. Use of fiber-reinforced polymer composites as reinforcing material for concrete. J Mater Civil Eng 2002; 14(3):191-209.

[10] da Silva LFM, Ochsner A, Adams RD. Handbook of adhesion technology. Heidelberg: Springer; 2011.

[11] National Research Council Advisory Committee. Guidelines for design and construction of externally bonded FRP systems for strengthening existing structures-metallic structures. Rome, Italy: National Research Council; 2007.

[12] Al-Mosawe A, Al-Mahaidi R, Zhao X-L. Effect of CFRP properties, on the bond characteristics between steel and CFRP laminate under quasi-static loading. Construction and Building Materials, 2015; 98:489-501.

[13] Yu T, Fernando D, Teng J, Zhao X. Experimental study on CFRP-to-steel bonded interfaces. Composites Part B: Engineering, 2012; 43:2279-2289

[14] Xia SH, Teng JG. Behaviour of FRP to steel bonded joints. In: Chen JF, Teng JG, editors. Proceedings of the international symposium on bond behaviour of FRP in structures 2005. p. 419-426.

[15] Teng JG, Fernando D, Yu T and Zhao XL. "Treatment of Steel Surfaces for Effective Adhesive Bonding". CICE 2010 - The 5th International Conference on FRP Composites in Civil Engineering September 27-29, 2010, Beijing, China.

[16] Fernando D, Yu T, Teng J. Behavior of CFRP laminates bonded to a steel substrate using a ductile adhesive. J Compos Constr 2014; 18:04013040

[17] Fawzia S, Zhao XL, Al-Mahaidi R. Bond-slip models for double strap joints strengthened by CFRP. Composite Structures, 2009; 92(9):2137-2145.

[18] Wu C, Zhao XL, Duan WH, Al-Mahaidi R. Bond characteristics between ultra high modulus CFRP laminates and steel. Thin Walled Structures 2012; 51:147-157.

[19] Colombi P, Fava G. Fatigue behaviour of tensile steel/CFRP joints. Compos Struct 2012; 94(8):2407-17.

[20] Liu HB, Zhao XL, Al-Mahaidi R. The effect of fatigue loading on bond strength of CFRP bonded steel plate joints. In: Proceedings of international symposium on bond behaviour of FRP in structures (BBFS), 2005. p. 459-64.

[21] Wu C, Zhao XL, Chiu WK, Al-Mahaidi R, Duan WH. Effect of fatigue loading on the bond behaviour between UHM CFRP plates and steel plates. Compos Part B 2013; 50:344-53.

[22] Agarwal A, Foster SJ, Hamed E, Ng TS. Influence of freeze-thaw cycling on the bond strength of steel-FRP lap joints. Compos Part B-Eng 2014; 60:178-85.

[23] Heshmati M, Haghani R, Al-Emrani M. Environmental durability of adhesively bonded FRP/steel joints in civil engineering applications: state of the art. Compos Part B-Eng 2015; 81:259-75.

[24] Kim YJ, Hossain M, Yoshitake I. Cold region durability of a two-part epoxy adhesive in double-lap shear joints: experiment and model development. Constr Build Mater 2012; 36:295-304.

[25] Heshmati M, Haghani R, Al-Emrani M. Dependency of cohesive laws of a structural adhesive in Mode-I and Mode-II loading on moisture, freeze-thaw cycling, and their synergy. Mater Des 2017; 122:433-47.

[26] Heshmati M, Haghani R, Al-emrani M. Durability of CFRP/steel joints under cyclic wet-

dry and freeze-thaw conditions. Compos Part B-Eng 2017; 126:211-226.

[27] I. Kafodya, G.J. Xian, H. Li, Durability study of pultruded CFRP plates immersed in water and seawater under sustained bending: Water uptake and effects on the mechanical properties, Compos. Part B Eng. 70 (2015) 138-48.

[28] W.C. Tucker, R.B.T.J. Rockett, S.K. Miriyala, Blistering of graphite/polymer composites galvanically coupled with metals in sea water, in: Annual Report. 1992.

[29] M. Tavakkolizadeh, H. Saadatmanesh, Galvanic corrosion of carbon and steel in aggressive environments, J. Compos. Constr. 5 (2001) 200-10.

[30] F.E. Sloan and J.B. Talbot, Corrosion of graphite fiber-reinforced composites-1-galvanic coupling damage, Corros. 48 (1992) 830-38.

[31] Y.J. Kim, I. Bumadian, J.S. Park, Galvanic current influencing interface deterioration of CFRP bonded to a steel substrate, J. Mater. Civ. Eng. 28 (2016) 28:04015129.

[32] C. Batuwitage, S. Fawzia, D. Thambiratnam, R. Al-Mahaidi, Durability of CFRP strengthened steel plate double-strap joints in accelerated corrosion environments, Compos. Struct. 160 (2017).

[33] C. Batuwitage, S. Fawzia, D. Thambiratnam, R. AlMahaidi, Evaluation of Bond Properties of Degraded CFRP-strengthened Double Strap Joints, Compos. Struct. 173 (2017) 144-155.

[34] Fam A, MacDougall C, Shaat A. Upgrading steel-concrete composite girders and repair of damaged steel beams using CFRP laminates. Thin-walled Structures, 2009; 47:1122-1135.

[35] Al-Saidy AH, Klaiber FW and Wipf, TJ. Repair of steel composite beams with carbon fiber-reinforced polymer plates. Journal of Composites for Construction, 2004; 8(2):163-72.

[36] Ghafoori, E, Motavalli, M, Botsis, J, Herwig, A, Galli, M. Fatigue strengthening of damaged metallic beams using prestressed unbonded and bonded CFRP plates. International Journal of Fatigue, 2012; 44:303-15.

[37] Colombi, P and Fava, G. Experimental study on the fatigue behaviour of cracked steel beams repaired with CFRP plates. Engineering Fracture Mechanics, 2015; 145:128-142.

[38] Yu, QQ and Wu, YF. Fatigue strengthening of cracked steel beams with different configurations and materials. Journal of Composite for Construction, ASCE, 2017; 21(2):04016093.

[39] Kamruzzaman M, Jumaat MZ, Ramli Sulong N, Islam A. A review on strengthening steel beams using FRP under fatigue. Scientific World Journal, 2014; 2014:1-21.

[40] Akbar I, Oehlers DJ, Ali MM. Derivation of the bond-slip characteristics for FRP plated steel members. Journal of Constructional Steel Research, 2010; 66:1047-1056.

[41] He, J and Xian, G. Debonding of CFRP-to-steel joints with CFRP delamination.

Composites Structure, 2016; 153:12-20.

[42] Biscaia HC, Chastre C, Borba IS, Silva C, Cruz D. Experimental evaluation of bonding between CFRP laminates and various structural materials. Journal of Composites for Construction, ASCE, 2015:04015070.

[43] Fawzia S, Al-Mahaidi R, Zhao XL. Experimental and finite element analysis of a double strap joint between steel plates and normal modulus CFRP. Composite Structures, 2006; 75(1-4):156-162.

[44] Teng JG, Fernando D, Yu T, Zhao XL. Debonding failures in CFRP-strengthened steel structures. In: Proceedings third Asia-Pacific conference on FRP in structures (APFIS2012); 2012 [Japan].

[45] Hosseini A, Mostofinejad D. Effective bond length of FRP-to-concrete adhesively-bonded joints: experimental evaluation of existing models. International Journal of Adhesion & Adhesives, 2014; 48:150-158.

[46] Sweedan, AMI, El-Sawy, KM and Alhadid, MMA. Interfacial behavior of mechanically anchored FRP laminates for strengthening steel beams. Journal of Constructional Steel Research, 2013; 80:332-345.

[47] Yuan H, Teng JG, Seracino R, Wu ZS, Yao J. Full-range behavior of FRP-to-concrete bonded joints. Engineering Structures, 2004; 26(5): 553-564.

[48] Teng, JG, Yu, T and Fernando, D. Strengthening of steel structures with fiber-reinforced polymer composites. Journal of Constructional Steel Research, 2012; 78:131-143.

[49] Zhao XL, Zhang L. State-of-the-art review on FRP strengthened steel structures. Engineering Structures, 2007; 29(8):1808-1823.

[50] ASTM D. 3039/D 3039-00. Standard test method for tensile properties of polymer matrix composite materials. 2000, p. 10.

[51] ISO Standard. Plastics - Determination of tensile properties - Part 2: Test conditions for moulding and extrusion plastics. Reference ISO 527-2, 1993(F).

[52] EN 10025: 2004 “Hot rolled products of non-alloy structural steels.” Euronorm standard.

[53] Chen, J F and Teng, JG. Shear capacity of FRP-strengthened RC beams: FRP debonding. Construction and Building Materials, 2003; 17:27-41.

[54] Ouezdou, MB, Belarbi, A and Bae, SW. Effective bond length of FRP sheets externally bonded to concrete. International Journal of Concrete structures and Materials, 2009; 3(2):127-131.

[55] Biscaia, HC, Micaelo, R, Teixeira, J and Chastre, C. Numerical analysis of FRP anchorage zones with variable width. Composites Part B: Engineering, 2014; 67:410-426.

[56] Biscaia, HC, Cruz, D and Chastre, C. Analysis of the debonding process of CFRP-to-timber interfaces. Construction and Building Materials, 2016; 113:96-112.

[57] Wu ZS, Yuan H, Niu HD. Stress transfer and fracture propagation in different kinds of adhesive joints. Journal of Engineering Mechanics, ASCE 2002; 128(5):562–73.

[58] Nakaba, K, Kanakubo, T, Furuta, T and Yoshizawa, H. Bond behavior between fiber-reinforced polymer laminates and concrete. ACI Structural, 2001; 98(3):359-367.

[59] Ferracuti B, Savoia M, Mazzotti C. Interface law for FRP-concrete delamination. Composite Structures, 2007; 80:523-31.

[60] Al-Shawaf, A. Influence of fibres' stiffness on wet lay-up CFRP/steel joints' behaviour under subzero exposures. Composites Part B: Engineering, 2015; 73:61-71.

[61] Ceroni, F, Ianniciello, M and Pecce, M. Bond behavior of FRP carbon plates externally bonded over steel and concrete elements: Experimental outcomes and numerical investigations. Composites Part B: Engineering, 2016; 92:434-446.

[62] Biscaia, HC, Silva, MAG and Chastre, C. Factors influencing the performance of externally bonded reinforcement systems of GFRP-to-concrete interfaces, Materials and Structures, 2015;48(9):2961-2981.

[63] Biscaia H, Chastre C, Silva, MAG. Linear and nonlinear analysis of bond-slip models for interfaces between FRP composites and concrete. Composites: Part B Engineering, 2013; 45(1):1554-1568.

[64] Dai JG, Ueda T, Sato Y. Development of the nonlinear bond stress-slip model of fiber reinforced plastics sheet-concrete interfaces with a simple method. Journal of Composites for Construction, 2005; 9:52-62.

[65] Ren, FF, Yang, ZJ, Chen, JF, Chen, WW. An analytical analysis of the full-range behaviour of grouted rockbolts based on a tri-linear bond-slip model. Construction and Building Materials, 2010; 24(3):361-370.

[66] Biscaia, HC, Chastre, C, Cruz, C and Viegas, A. Prediction of the Interfacial performance of CFRP laminates and old timber bonded joints with different strengthening techniques. Composites: Part B Engineering, 2017; 108:1-17.

[67] Carrara, P, Ferretti, D, Freddi, F and Rosati, G. Shear tests of carbon fiber plates bonded to concrete with control of snap-back. Engineering Fracture Mechanics, 2011; 78:2663-2678

[68] Teng, JG, Lu, XZ, Ye, LP and Jiang, JJ. Bond-slip models for interfaces between externally bonded FRP and concrete. FRP Composites in Civil Engineering - CICE 2004, pp. 55-68.

[69] Cornetti, P and Carpinteri, A. Modelling the FRP-concrete delamination by means of an exponential softening law, Engineering Structures, 2011; 33(6):1988-2001.

[70] Biscaia, HC, Borba, IS, Silva, C and Chastre, C. A nonlinear analytical model to predict the full-range debonding process of FRP-to-parent material interfaces free of any mechanical anchorage devices, Composite Structures, 2016; 138: 52-63.

[71] Wu, YF, Xu, XS, Sun, JB and Jiang, C. Analytical solution for the bond strength of externally bonded reinforcement. Composite Structures, 2012; 94:3232-3239.

[72] Al-Mosawe, A, Al-Mahaidi, R and Zhao, XL. Experimental and Numerical Study on Strengthening of Steel Members Subjected to Impact Loading Using Ultrahigh Modulus CFRP. Journal of Composites for Construction, 2016; 20(6):04016044, 1-10.

[73] Biscaia HC, Chastre C. Theoretical analysis of fracture in double overlap bonded joints with FRP composites and thin steel plates. Eng. Fract. Mech. 2018; 190:435-60.

[74] Neubauer, U and Rostásy, FS. Design aspects of concrete structures strengthened with externally bonded CFRP-plates. Proceedings of the 7th International Conference on Structural Faults and Repairs, Vol. 2**,** 1997, pp. 109-118.

[75] Zhou H, Doroudi Y and Fernando D. Cyclic bond behaviour of FRP-to-Steel bonded joints. International Conference on Performance-based and Life-cycle Structural Engineering, 2015.

[76] Buyukozturk O, Gunes O, Karaca E. Progress on understanding debonding problems in reinforced concrete and steel members strengthened using FRP composites. Constr Build Mater 2004; 18(1):9-19.

[77] Diab HM, Wu Z, Iwashita K. Theoretical solution for fatigue debonding growth and fatigue life prediction of FRP-concrete interfaces. Adv Struct Eng 2009; 12(6):781-92.

[78] Nigro E, Di Ludovico M, Bilotta A. Experimental investigation of FRP-Concrete debonding under cyclic actions. J Mater Civil Eng 2011; 23(4):360-71.

[79] Bizindavyi L, Neale KW and Erki MA. Experimental investigation of bonded fiber reinforced polymer-concrete joints under cyclic loading. J Compos Constr 2003; 7(2):127-134.

[80] Martinelli E, Caggiano A. A unified theoretical model for the monotonic and cyclic response of FRP strips glued to concrete. Polymers 2014; 6(2):370-381.

[81] Chen JF, Xie JK, Tao Y, Li XQ. A review of FRP strengthened concrete structures under extreme loading. International Conference on Performance-based and Life-cycle Structural Engineering. 2015.

[82] Ko H, Sato Y. Bond stress-slip relationship between FRP sheet and concrete under cyclic load. J Compos Constr 2007; 11(4):419-26.

[83] Caggiano, A, Martinelli, E. A fracture-based interface model for simulating the bond behavior of FRP strips glued to a brittle substrate. Composite Structures 2013; 99:397-403.

[84] Caggiano, A, Schicchi, DS. A thermo-mechanical interface model for simulating the bond behavior of FRP strips glued to concrete substrates exposed to elevated temperature. Engineering Structures 2015; 83:243-251.

[85] Yang Y, Biscaia H, Chastre C and Silva MAG. Bond characteristics of CFRP-to-steel

bonded joints. J Constr Steel Res 2017; 138:401-419.

[86] Zhou H, Fernando D, Chen G, Kitipornchai S. The quasi-static cyclic behaviour of CFRP-to-concrete bonded joints: An experimental study and a damage plasticity model. Eng Struct 2017; 153:43-57.

[87] Buyukozturk O, Gunes O, Karaca E. Progress on understanding debonding problems in reinforced concrete and steel members strengthened using FRP composites. Constr Build Mater 2004; 18(1):9-19.

[88] Gholami M, Sam ARM, Yatim JM, Tahir MM. A review on steel/CFRP strengthening systems focusing environmental performance. Constr Build Mater 2013; 47:301-10.

[89] Karbhari VM. Durability of composites for civil structural applications. Woodhead Pub; 2007.

[90] Chin JW, Nguyen T, Aouadl K. Effects of environmental exposure on fiber-reinforced plastic (FRP) materials used in construction. J Compos Technol Res 1997; 19(4):205-13.

[91] Boer P, Holliday L, Kang TH-K. Independent environmental effects on durability of fiber-reinforced polymer wraps in civil applications: a review. Constr Build Mater 2013; 48:360-70.

[92] Yoshitake I, Tsuda H, Itose J, Hisabe N. Effect of discrepancy in thermal expansion coefficients of CFRP and steel under cold temperature. Constr Build Mater 2014; 59:17-24.

[93] Korta J, Mlyniec A, Uhl T. Experimental and numerical study on the effect of humidity-temperature cycling on structural multi-material adhesive joints. Compos Part B-Eng 2015; 79:621-30.

[94] Yoshitake I, Tsuda H, Kim YJ and Hisabe N. Effect of thermal distress on residual behavior of CFRP-strengthened steel beams including periodic unbounded zones. Polym 2015; 7:2332-43.

[95] Hand H, Arah C, McNamara D, Mecklenburg M. Effects of environmental exposure on adhesively bonded joints. Int J Adhes Adhes 1991; 11:15-23.

[96] Knox E, Cowling M. Durability aspects of adhesively bonded thick adherend lap shear joints. Int J Adhes Adhes 2000; 20:323-31.

[97] Nguyen TC, Bai Y, Zhao XL, Al-Mahaidi R. Durability of steel/CFRP double strap joints exposed to sea water, cyclic temperature and humidity. Compos Struct 2012; 94:1834-45.

[98] Yang YM, Xian GJ, Li H, Sui LL. Thermal aging of an anhydride-cured epoxy resin. J Polym Dreat Stab 2015; 118:111-9.

[99] Xian GJ, Karbhari VM. DMTA based investigation of hygrothermal ageing of an epoxy system used in rehabilitation. J Appl Polym Sci 2007; 104:1084-94

[100] Karbhari VM, Shulley SB. Use of composites for rehabilitation of steel structures

determination of bond durability. J Mater Civ Eng 1995; 7:239-45.

[101] Agarwal, A, Foster, SJ and Hamed E. Testing of new adhesive and CFRP laminate for steel-CFRP joints under sustained loading and temperature cycles. Compos Part B-Eng 2016; 99:235-247.

[102] Teixeira de Freitas S, Banea MD, Budhe S, de Barros S. Interface adhesion assessment of composite-to-metal bonded joints under salt spray conditions using peel tests. Compos Struct 2017; 164:68-75.

[103] Yang YM, Silva MAG, Biscaia HC，Chastre C. CFRP-to-steel bonded joints subjected to cyclic loading: An experimental study. Compos Part B-Eng 2018; 146:28-41.

[104] Biscaia HC, Chastre C, Viegas A, Franco N. Numerical modelling of the effects of elevated service temperatures on the debonding process of FRP-to-concrete bonded joints. Compos Part B-Eng 2015; 70:64-79.

[105] Gao WY, Teng JG, Dai JG. Effect of temperature variation on the full-range behavior of FRP-to-concrete bonded joints. J Compos Constr 2012;16(6):671-83.

[106] Silva MAG, Biscaia H. Degradation of bond between FRP and RC beams. Compos Struct 2008; 85:164-74.

[107] Heshmati M, Haghani R, Al-Emrani M. Durability of bonded FRP-to-steel joints: effects of moisture, de-icing salt solution, temperature and FRP type. Compos Part B Eng 2017; 119:153-67.

[108] Dawood M, Rizkalla S. Environmental durability of a CFRP system for strengthening steel structures. Constr Build Mater 2010; 24:1682-9.

[109] Biscaia HC, Chastre C, Silva MAG. Bond-slip model for FRP-to-concrete bonded joints under external compression. Compos Part B Eng 2015; 80:246-259.

[110] Biscaia HC, Chastre C. Design method and verification of steel plate anchorages for FRP-to-concrete bonded interfaces. Compos Struct 2018; 192:52-66.

[111] T.C. Nguyen, Y. Bai, X.L. Zhao, R. Al-Mahaidi, Durability of steel/CFRP double strap joints exposed to sea water, cyclic temperature and humidity, Compos. Struct. 94 (2012) 1834-45.

[112] P. Fernandes, G. Viana, R. Carbas, et al, The influence of water on the fracture envelope of an adhesive joint, Theor Appl Fract Mech. 89 (2017) 1-15.

[113] P.M.G. Fernandes, P.M. Silva, L.L.G. Correia, J. Sena-Cruz, Durability of an epoxy adhesive and a CFRP laminate under different exposure conditions, In: Proceedings of SMAR2015-Third Conference on Smart Monitoring, Assessment and Rehabilitation of Civil Structures. Antalya, Turkey, Conference 07-09 Sept. 2015, Conference 2015. p. 8.

[114] H.S. Seo, H.Y. Jang and I. Lee, Experimental investigation of salt fog effect on the CFRP laminates, Adv. Compos. Mater. (2016).

[115] B. Hong, G.J. Xian, Z.K. Wang, Durability study of pultruded carbon fiber reinforced polymer plates subjected to water immersion, Adv. Struct. Eng. (2017).

[116] V.M. Karbhari, G.J. Xian, Hygrothermal effects on high VF pultruded unidirectional carbon/epoxy composites: Moisture uptake, Compos. Part B Eng. 40 (2009) 41-49.

[117] S. Cabral-Fonseca, J.P. Nunes, M.P. Rodrigues, M.I. Eusebio. Durability of carbon fibre reinforced polymer laminates used to reinforced concrete structures. Sci. Eng. Compos. Mater. 18 (2011) 201-7.

[118] Z.K. Wang, X.L. Zhao, G.J. Xian, G. Wu, R.K. Singh Raman, S. Al-Saadi, Durability study on interlaminar shear behaviour of basalt-, glass- and carbon-fibre reinforced polymer (B/G/CFRP) bars in sea water sea sand concrete environment, Constr. Build. Mater. 156 (2017) 985-1004.

[119] I. Kafodya, G.J. Xian, H. Li, Durability study of pultruded CFRP plates immersed in water and seawater under sustained bending: Water uptake and effects on the mechanical properties, Compos. Part B Eng. 70 (2015) 138-48.

[120] W.C. Tucker, R.B.T.J. Rockett, S.K. Miriyala, Blistering of graphite/polymer composites galvanically coupled with metals in sea water, in: Annual Report. 1992.

[121] J. Qin et al, The effect of carbon fiber type on the electrochemical degradation of carbon fiber polymer composites. NACE International Conference CORROSION/95, March 26–31, 1995, Orlando, FL, U.S.A., Proceed. Paper No 275.

[122] M. Tavakkolizadeh, H. Saadatmanesh, Galvanic corrosion of carbon and steel in aggressive environments, J. Compos. Constr. 5 (2001) 200-10.

[123] F.E. Sloan and J.B. Talbot, Corrosion of graphite fiber-reinforced composites-1-galvanic coupling damage, Corros. 48 (1992) 830-38.

[124] Y.J. Kim, I. Bumadian, J.S. Park, Galvanic current influencing interface deterioration of CFRP bonded to a steel substrate, J. Mater. Civ. Eng. 28 (2016) 28:04015129.

[125] A. Afaghi-Khatibi, Y.W. Mai, Characterisation of fibre/matrix interfacial degradation under cyclic fatigue loading using dynamic mechanical analysis, Compos. Part A Appl. Sci. Manuf. 33 (2002) 1585-92.

[126] Q.B. Zhang, G.S. Wu, F. Xie, et al, Mechanical properties of carbon fiber composites modified with nano-SiO2 in the interphase, J. Adhes. Sci. Technol. 28 (2014) 2154-2166.

[127] M. Jacob, B. Francis, K.T. Varughese, S. Thomas, The Effect of Silane Coupling Agents on the Viscoelastic Properties of Rubber Biocomposites, Macromol Mater Eng 291 (2006) 1119-26.

[128] M.J. John, R.D. Anandjiwala, Chemical modification of flax reinforced polypropylene composites, Compos. Part A Appl. Sci. Manuf. 40 (2009) 442-8.

[129] Z.K. Wang, G.J. Xian, X.L. Zhao, Effects of hydrothermal aging on carbon fibre/epoxy composites with different interfacial bonding strength, Constr. Build. Mater.

[130] Y. Ngono, Y. Maréchal, N. Mermilliod, Epoxy-amine reticulates observed by infrared spectrometry. I: hydration process and interaction configurations of embedded H_2O molecules, J. Phys. Chem. B. 103 (1999) 4979-4985.

[131] K.E. Chike, M.L. Myrick, R.E. Lyon, S.M. Angel, Raman and near-infrared studies of an epoxy resin, Appl. Spectrosc. 47 (1993) 1631–1635.

[132] Z.Y. Lu, G.J. Xian, H. Li, Effects of exposure to elevated temperatures and subsequent immersion in water or alkaline solution on the mechanical properties of pultruded BFRP plates, Compos. Part B Eng. 77 (2015) 421-430.

[133] Z. Liu, M. Curioni, P. Jamshidi, A. Walker, P. Prengnell, G.E. Thompson, P. Skeldon, Electrochemical characteristics of a carbon fibre composite and the associated galvanic effects with aluminium alloys, Appl. Surf. Sci. 314 (2014) 233-240.

Appendix A

In this appendix, the solutions of the differential equations stated throughout Section 2.4 (Eqs. (2.17), (2.33) and (2.49)) are presented in more detail. The boundary conditions used in each state and the integration constants determined for each solution are presented next.

A.1 Elastic state

The general solution of Eq. (2.17) is:

$$s_E(x) = C_1 \cdot \cosh(\alpha_1 \cdot x) + C_2 \cdot \sinh(\alpha_1 \cdot x) \tag{A.1}$$

where C_1 and C_2 are constants that must be determined from the boundary condition at $x = 0$:

$$\begin{cases} F_{CFRP} = F \\ F_{steel} = 0 \end{cases} \tag{A.2}$$

and from the second boundary condition at $x = L_b$ where:

$$\begin{cases} F_{CFRP} = 0 \\ F_{steel} = F \end{cases}. \tag{A.3}$$

Thus, regarding Eq. (2.9), the load in the CFRP laminate can be written as:

$$F_{CFRP} = E_{CFRP} \cdot A_{CFRP} \cdot \frac{du_{CFRP}}{dx} \tag{A.4}$$

where A_{CFRP} is the cross section of the CFRP laminate. Introducing Eq. (2.12) into Eq. (A.4), the load in the CFRP laminate can be rewritten as:

$$F_{CFRP} = E_{CFRP} \cdot A_{CFRP} \cdot \left(\frac{du_{steel}}{dx} - \frac{ds}{dx} \right). \tag{A.5}$$

However, from the boundary condition stated in (A.2) and regarding Eq. (2.9) yields:

$$\frac{ds}{dx} = -\frac{F}{E_{CFRP} \cdot A_{CFRP}}. \tag{A.6}$$

On the other hand, the load on the steel plate is:

$$F_{steel} = E_{steel} \cdot A_{steel} \cdot \frac{du_{steel}}{dx} \tag{A.7}$$

and from the boundary condition stated in (A.3) and regarding Eq. (2.10), Eq. (A.7) can be rewritten as:

$$F_{steel} = E_{steel} \cdot A_{steel} \cdot \left(\frac{du_{CFRP}}{dx} + \frac{ds}{dx} \right).$$

(A.8)

However, due to the second boundary condition of the problem, the following expression is valid at $x = L_b$:

$$\frac{ds}{dx} = \frac{F}{E_{steel} \cdot A_{steel}}$$

(A.9)

where A_{steel} is the cross section of the steel plate. Hence, from the first derivative of Eq. (A.1) with respect to x, constants C_1 and C_2 are respectively determined and defined as:

$$C_1 = -\frac{F}{\alpha_1 \cdot \sinh(\alpha_1 \cdot L_b)} \cdot \left(\frac{1}{E_{steel} \cdot A_{steel}} + \frac{\cosh(\alpha_1 \cdot L_b)}{E_{CFRP} \cdot A_{CFRP}} \right) \tag{A.10}$$

and

$$C_2 = -\frac{F}{\alpha_1 \cdot E_{CFRP} \cdot A_{CFRP}}. \tag{A.11}$$

With some mathematical simplifications, the slip distribution in the Elastic state $s_E(x)$ is then defined accordingly to Eq. (2.19).

A.2 Softening-Elastic state

In this state, the general solution of Eq. (2.33) is:

$$s_S(x) = C_3 \cdot \cos(\alpha_2 \cdot x) + C_4 \cdot \sin(\alpha_2 \cdot x) + \frac{a}{\alpha_2^{\,2}} \tag{A.12}$$

where C_3 and C_4 are constants that should be found from the boundary conditions of this S-E state. Furthermore, for the elastic region of the interface, the general equation stated in (A.1) remains valid. Thus, beyond the boundary conditions previously stated in (A.2) and (A.3) and denoting L_S by the softening length, the following compatibility boundary conditions are used to find constants C_1, C_2, C_3 and C_4:

$$@\, x = L_S : \begin{cases} s_S = s_E = s_1 \\ \left. \dfrac{du_{CFRP}}{dx} \right|_{Left} = \left. \dfrac{du_{CFRP}}{dx} \right|_{Right} \end{cases}. \tag{A.13}$$

Hence, constants C_1, C_2, C_3 and C_4 are defined according to:

$$C_1 = -\frac{F}{\alpha_1 \cdot E_{steel} \cdot A_{steel} \cdot \tan(\alpha_2 \cdot L_b)} \cdot \left(\frac{1}{\beta} + \frac{1}{\cos(\alpha_2 \cdot L_S) \cdot \cosh(\alpha_1 \cdot (L_b - L_S))} \right) + \frac{s_1 \cdot \alpha_1 \cdot \tanh(\alpha_1 \cdot (L_b - L_S))}{\alpha_1 \cdot \sin(\alpha_2 \cdot L_S)}, \tag{A.14}$$

$$C_2 = -\frac{F}{\alpha_2 \cdot E_{CFRP} \cdot A_{CFRP}}, \tag{A.15}$$

$$C_3 = \frac{s_1 \cdot \cosh(\alpha_1 \cdot L_b)}{\cosh(\alpha_1 \cdot (L_b - L_S))} - \frac{F \cdot \sinh(\alpha_1 \cdot L_b)}{\alpha_1 \cdot E_{steel} \cdot A_{steel} \cdot \cosh(\alpha_1 \cdot (L_b - L_S))}, \tag{A.16}$$

and

$$C_4 = -\frac{s_1 \cdot \sinh(\alpha_1 \cdot L_b)}{\cosh(\alpha_1 \cdot (L_b - L_S))} + \frac{F \cdot \cosh(\alpha_1 \cdot L_b)}{\alpha_1 \cdot E_{steel} \cdot A_{steel} \cdot \cosh(\alpha_1 \cdot (L_b - L_S))}. \tag{A.17}$$

The slip distributions in the Elastic state $s_E(x)$ and in the Softening state $s_S(x)$ are then determined through Eqs. (2.36) and (2.37), respectively, after some mathematical simplifications.

A.3 Constant-Softening-Elastic state

The general solution of Eq. (2.49) is a second order polynomial function defined as:

$$s_C(x) = \alpha_3 \cdot \frac{x^2}{2} + C_5 \cdot x + C_6 \tag{A.18}$$

where C_5 and C_6 are constants that must be defined by imposing adequate boundary conditions of this C-S-E state. In addition to the boundary conditions previously defined in (A.2) and (A.3) and denoting $L_{S,\max}$ and L_C as the maximum softened length of the CFRP-to-steel interface and as the length with a constant bond stress τ_2, respectively, the following compatibility conditions should be used:

$$@\, x = L_{S,\max} + L_C : \begin{cases} s_S = s_E = s_1 \\ \left. \frac{du_{CFRP}}{dx} \right|_{Left} = \left. \frac{du_{CFRP}}{dx} \right|_{Right} \end{cases} \tag{A.19}$$

and

$$@\, x = L_C : \begin{cases} s_S = s_E = s_2 \\ \left. \frac{du_{CFRP}}{dx} \right|_{Left} = \left. \frac{du_{CFRP}}{dx} \right|_{Right} \end{cases}. \tag{A.20}$$

Therefore, constants from C_1 to C_6 are defined as:

$$C_1 = \frac{s_1 \cdot \cosh(\alpha_1 \cdot L_b)}{\cosh(\alpha_1 \cdot (L_b - L_C - L_{S,\max}))} - \frac{F \cdot \sinh(\alpha_1 \cdot (L_C + L_{S,\max}))}{\alpha_1 \cdot E_{steel} \cdot A_{steel} \cdot \cosh(\alpha_1 \cdot (L_b - L_C - L_{S,\max}))}, \tag{A.21}$$

$$C_2 = \frac{F \cdot \cosh(\alpha_1 \cdot (L_C + L_{S,\max}))}{\alpha_1 \cdot E_{steel} \cdot A_{steel} \cdot \cosh(\alpha_1 \cdot (L_b - L_C - L_{S,\max}))} - \frac{s_1 \cdot \sinh(\alpha_1 \cdot L_b)}{\cosh(\alpha_1 \cdot (L_b - L_C - L_{S,\max}))}, \tag{A.22}$$

$$C_3 = \frac{\alpha_1 \cdot s_1 \cdot \cos(\alpha_2 \cdot L_C) \cdot \tanh(\alpha_1 \cdot (L_b - L_C - L_{S,\max})) + L_C \cdot \alpha_2 \cdot \cos(\alpha_2 \cdot (L_C + L_{S,\max}))}{\alpha_2 \cdot \sin(\alpha_1 \cdot L_{S,\max})}$$
$$- \frac{F \cdot \sinh(\alpha_1 \cdot L_b)}{\alpha_2 \cdot \sin(\alpha_2 \cdot L_{S,\max})} \cdot \left[\frac{\cos(\alpha_2 \cdot (L_C + L_{S,\max}))}{E_{CFRP} \cdot A_{CFRP}} + \frac{\cos(\alpha_2 \cdot L_C)}{E_{steel} \cdot A_{steel} \cdot \cosh(\alpha_1 \cdot (L_b - L_C - L_{S,\max}))} \right] \tag{A.23}$$

$$C_4 = \frac{\alpha_1 \cdot s_1 \cdot \sin(\alpha_2 \cdot L_C) \cdot \tanh(\alpha_1 \cdot (L_b - L_C - L_{S,\max})) + L_C \cdot \alpha_2 \cdot \sin(\alpha_2 \cdot (L_C + L_{S,\max}))}{\alpha_2 \cdot \sin(\alpha_1 \cdot L_{S,\max})}$$
$$- \frac{F \cdot \sinh(\alpha_1 \cdot L_b)}{\alpha_2 \cdot \sin(\alpha_2 \cdot L_{S,\max})} \cdot \left[\frac{\sin(\alpha_2 \cdot (L_C + L_{S,\max}))}{E_{CFRP} \cdot A_{CFRP}} + \frac{\sin(\alpha_2 \cdot L_C)}{E_{steel} \cdot A_{steel} \cdot \cosh(\alpha_1 \cdot (L_b - L_C - L_{S,\max}))} \right] \tag{A.24}$$

$$C_5 = -\frac{F}{E_{CFRP} \cdot A_{CFRP}} \tag{A.25}$$

and

$$C_6 = s_2 - \alpha_3 \cdot \frac{{L_C}^2}{2} + \frac{F \cdot L_C}{E_{CFRP} \cdot A_{CFRP}}. \tag{A.26}$$

After some mathematical simplifications, the slip distributions in the Elastic state $s_E(x)$, in the Softening state $s_S(x)$ and in the Constant state $s_C(x)$ are then defined according to Eqs. (2.51), (2.52) and (2.53), respective.